PSFC/RR-10-3 **DOE/ET-54512-371**

Lithium Pellet Injection into High Pressure Magnetically Confined Plasmas

Böse, B.D.

May 2010

Plasma Science and Fusion Center
Massachusetts Institute of Technology
Cambridge MA 02139 USA

This work was supported by the U.S. Department of Energy, Grant No. DE-FC02-99ER54512-CMOD. Reproduction, translation, publication, use and disposal, in whole or in part, by or for the United States government is permitted.

Lithium Pellet Injection into High Pressure Magnetically Confined Plasmas

by

Brock Böse

Submitted to the Physics
in partial fulfillment of the requirements for the degree of

Doctor of Philosophy

at the

MASSACHUSETTS INSTITUTE OF TECHNOLOGY

June 2010

Author .....
Physics
March 29, 2010

Certified by .....
Earl Marmar
Senior Research Scientist
Thesis Supervisor

Accepted by .....
Krishna Rajagopal
Associate Department Head for Education

Lithium Pellet Injection into High Pressure Magnetically Confined Plasmas

by

Brock Böse

Submitted to the Physics
on March 29, 2010, in partial fulfillment of the
requirements for the degree of
Doctor of Philosophy

Abstract

The ablation of solid pellets injected into high temperature magnetically confined plasmas is characterized by rapid oscillations in the ablation rate, and the formation of field aligned filaments in the ablatant. High speed imaging of the ablation ($> 250,000$ frames/second) during the 2003-2004 campaign revealed that these filament move away from the pellet primarily in the poloidal direction with a characteristic speeds of $\sim 5\mathrm{k}m/s$. Significant differences appeared in the filament drifts in RF heated H-mode plasmas compared to ohmic L-mode plasmas. Filaments in ohmic L-mode plasmas moved in both the electron and ion diamagnetic directions while filaments in H-mode move only in the electron diamagnetic direction. Furthermore, the motion of the filaments in L-mode plasmas appeared to be semi-random, with the direction changing randomly from shot to shot, but with a distinct preferred direction during each shot. The susceptibility of the filament's motion to variations in the background plasma conditions indicate that the drift is a result of interactions with the background plasma, and not a result of the internal dynamics of the ablation cloud. Furthermore, the chaotic, or semi-random, nature of the filament drift suggests that the drift could be due to ExB flows resulting from plasma turbulence.

A stereoscopic imaging system was installed on Alcator C-Mod to make a detailed study of three dimensional evolution of the filaments. By examining a large number of pellet injections into ohmically heated L-mode plasmas, we were able to demonstrate that filaments do indeed move primarily along flux surfaces, and that the filament flow direction is correlated for sequential filaments. Additionally, a statistical examination of the trajectory data revealed that filaments have a wider distribution of speeds at lower values of the local safety factor, q.

The measurements of the stereo-imaging system were compared with the implied turbulent ExB drifts determined by the gyrokinetic solver GYRO. Simulations conducted using profiles consistent with both pre-pellet and post-pellet conditions demonstrate that the filament drifts are more consistent with the turbulent conditions prevalent after the injection, indicating the filament drifts are most likely the result of turbulence generated by the modified plasma profiles from injection process

itself.

Thesis Supervisor: Earl Marmar
Title: Senior Research Scientist

Acknowledgments

I would like to give a sincere thanks to all the people who lent a shoulder in helping to bring this work to completion. To Earl Marmar for his guidance in all aspects of this work. To Miklos Porkolab and Bruno Coppi for their time and patience in guiding my education. To David Mikkelsen, without whom the numerical portions of this work would never have been attempted. To Martin Greenwald, Paul Bonoli, and Peter Cato for their help understanding the theoretical aspects of this work. I would also like to thank Stewart Zweben, Jim Terry, and Brian Lombard for their help in the design of the experiment and especially Ed Fitzgerald and Tom Toland without whom my experimental plan could never have been implemented. Finally Anne White, whose confidence, optimism, and knowledge proved invaluable during the preparation for my defense.

I would also like to pay special thanks to all of the students at the PSFC, past, present and future, who helped me endure the challenges of research, and shared with me their inspiration, wonder and triumphs. In no particular order, Noah Smick, Liang Lin, Balint Veto, Eric Edlund, Ken Marr, Aaron Bader, Andréa Schmidt, Greg Wallace, Alexandre Parisot, Alex Ince-Cushman, Rachael McDermott, Matt Reinke, Vincent Tang, Kirill Zurovich, Jerry Hughes, Howard Yuh, John Liptac, Yunxing Ma, Daniel Brunner, Geoff Olnyk, Robert Mumgaard, and Mike Garret.

Finally, I would like to thank the members of the MIT Rugby Club, the staff and management of the Muddy Charles, and my beloved fiancée, and future wife, Sarah Forrest for the good times and emotional support over these past seven years.

For Sarah

Contents

List of Figures

List of Tables

Chapter 1

Introduction

The aim of this research is to further the development of controlled nuclear fusion. The history of mankind has been marked by the perpetual search for, and exhaustion of, energy resources. In recent decades, this process has been complicated further by the realization that many of our current energy sources have potentially damaging effects on the environment or increase the risks of nuclear weapons proliferation. With a near limitless fuel supply, fusion presents a permanent solution to our energy problems. Fusion is even more attractive when one considers that it produces no green house gases, and when compared with nuclear fission, should produce dramatically reduced radioactive waste, and makes the clandestine production of weapons-grade fissionable materials extremely difficult.

From the beginning of the fusion energy program, one of the primary obstacles to achieving controlled nuclear fusion in magnetically confined plasmas was limiting the loss of particles and heat so that the plasma could reach the temperatures and densities necessary to sustain the reaction. Classical theory predicts losses that could be orders of magnitude lower than what is observed in typical plasma discharges. The anomalous transport, that above the classical predictions, is dominantly caused by turbulence within the plasma.

Lithium pellet injection experiments in 2003 and 2004 on Alcator C-Mod, measuring the properties of the pellet ablation, indicated that the pellet ablation process may be affected by the local plasma turbulence, and hence might provide a diagnos-

tic capable of making direct measurements of the turbulence. This thesis has two primary aims: 1. to catalog these previously undocumented plasma phenomena; and 2. to explore the relationship between these phenomena and the plasma turbulence. What follows is organized on the following outline. The remainder of this chapter is dedicated to a brief background in plasma physics, the tokamak containment device and a review of the motivating research, an outline what we expected to accomplish with this work, and a summary of the main results. Chapter 2 gives a brief review of what is known about pellet ablation physics. Chapter 3 delves into a review on plasma turbulence and flow. Chapter 4 covers the design, execution, and results from an extensive survey of pellet injection experiments. Chapter 5 reviews the results from a series of non-linear gyrokinetic simulations that were used to characterize the properties of the plasma turbulence. We conclude in chapter 6 with comparisons of the results from chapters 4 & 5, and a discussion of their significance.

1.1 Fusion Overview

In a fusion reactor, energy is produced by fusing two light nuclei to form a heavier one. The initial mass of the reactants is fractionally larger than that of the products, with the difference converted into the kinetic energy of the fusion products. The most promising reaction for a future reactor is the the deuterium-tritium (D-T) reaction, given by

$$D + T \longrightarrow {}^4He + n + 17.6MeV \tag{1.1}$$

This is because the of relatively large cross section, shown in figure 1-1 as a function of the reactants' relative energy. As might be expected due to the coulomb repulsion of the positively charged nuclei, the cross section peaks at high energies, $\sim 100\text{k}eV$. For comparison, figure 1-1 also shows the total cross section for coulomb scattering. Even at its peak, the DT cross section is approximately an order of magnitude smaller than the coulomb cross section, with the immediate consequences that at every interaction between deuterium and tritium they are much more likely to scatter via

coulomb repulsion than to undergo fusion. For this reason, it is necessary to confine the energetic particles so that they undergo a large number of interactions before leaving the reactor and thus have many opportunities to fuse. The resulting repeated interactions leads to the thermalization of the reactants and a characteristic Gaussian distribution of particle velocities. The further key advantage of this method, termed thermonuclear fusion, is that particles in the wings of the distribution, where energies are the highest, are able fuse, and thus the plasma only requires temperatures of the order 10keV.

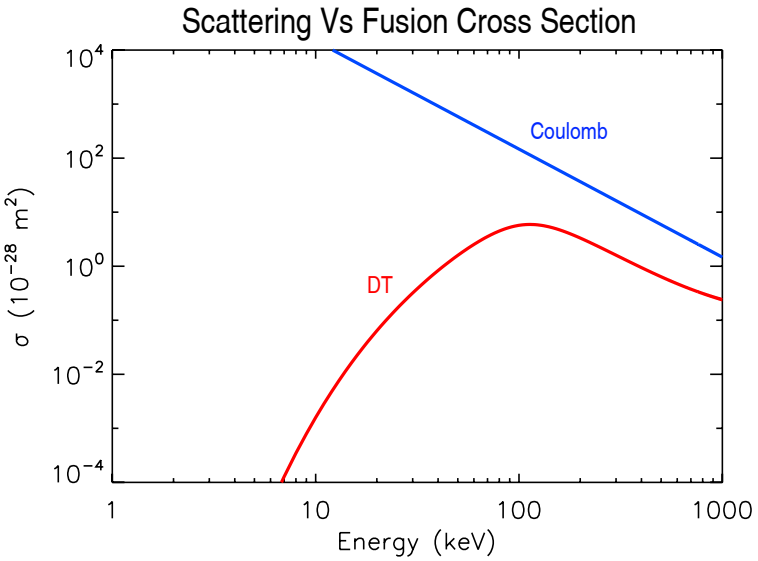

Figure 1-1: The DT fusion (red) and coulomb scattering (blue) cross section.

The extremely large energy of the reactants, tens of thousands of times larger than the ionization energy of the hydrogenic species, means that the reactants exist in a plasma state where the electrons are no longer bound to their nuclei. The high energy density of the plasma additionally means that it is necessary to keep it away from any solid material surface, both because no solid surface can long withstand contact with something that energetic, and because the solid surface would rapidly cool the plasma to the point where fusion is no longer possible. There are three principle methods of confining a plasma: gravitationally, as is the case with the sun; inertially, as in thermonuclear explosions, and magnetically. It is this last case with which we are here concerned.

The basis for magnetically confining a plasma lies in the fact that the plasma is composed of a sea of moving ions and electrons, which are subject to the Lorentz force exerted by electric ($\vec{E}$) and magnetic ($\vec{B}$) fields on charged particles moving with velocity ($\vec{v}$).

$$\vec{F} = m\frac{\mathrm{d}\vec{v}}{\mathrm{d}t} = q\left(\vec{E} + \vec{v} \times \vec{B}\right) \tag{1.2}$$

where q is the particle's charge, and m its mass. In the case where there are no perpendicular electric fields, this force leads to the particle spiraling around the magnetic field line as shown in figure 1-2, with a characteristic radius known as the Larmor or gyro radius given by,

$$\rho = \frac{mv_{\perp}}{qB} \tag{1.3}$$

and characteristic frequency, known as the gyro frequency, given by,

$$\omega_c = \frac{qB}{m} \tag{1.4}$$

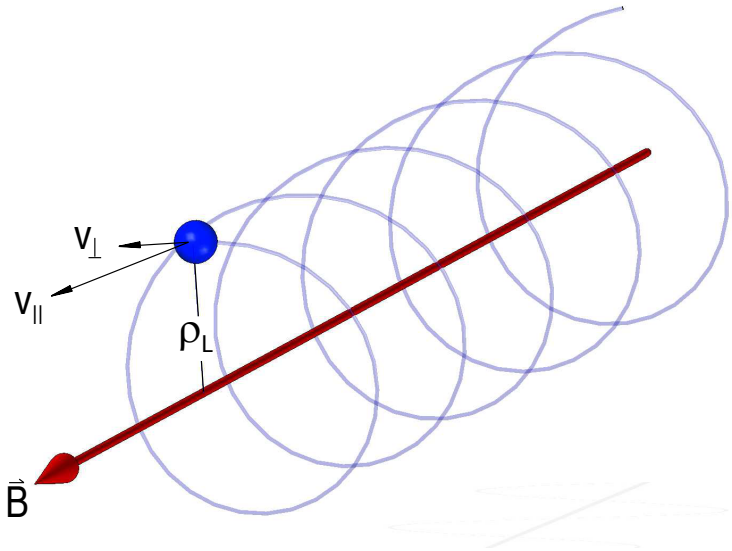

Figure 1-2: Blue particle confined by magnetic field. From the direction of the spiral the particle must be negatively charged.

To zeroth order, particles follow the magnetic field lines. In general, any force that acts on the particle perpendicular to the direction of the magnetic field causes

the orbit to distort, leading to a particle drift perpendicular to both the direction of the magnetic field, and the direction of the applied force. The general form of this drift is given by,

$$\vec{v}_D = \frac{1}{q}\frac{\vec{F}_g \times \vec{B}}{B^2} \tag{1.5}$$

where F_g is the generalized force.

One of the more important drifts, and the one with which this thesis is intimately concerned, is that derived from the force exerted by an electric field ($\vec{F}_g = q\vec{E}$). Known as the ExB drift, it is given by,

$$\vec{v}_{\mathrm{E\,xB}} = \frac{\vec{E} \times \vec{B}}{B^2} \tag{1.6}$$

Additionally, inhomogenities in the magnetic field can lead to a similar distortion of the the Larmor orbit. This leads to what is known as the ∇B drift, which is given by,

$$\vec{v}_{\nabla B} = \frac{mv_\perp^2}{2qB}\frac{\vec{B} \times \vec{\nabla} B}{B^2} \tag{1.7}$$

and unlike the ExB drift, the direction and magnitude of the motion resulting from this effect are charge dependent.

1.2 The Tokamak

To date, the most successful concept for magnetic fusion is the tokamak. The term tokamak is a Russian abbreviation for Toroidal Chamber with Magnetic Coils, and originates from its initial development in the Soviet Union during the 1950's. What follows is a basic overview of sufficient to understand the remainder of the thesis; for a more complete description the reader is directed to the review by Wesson [1].

The tokamak solves the problem of confinement, by creating a magnetic geometry in which the field lines containing the plasma never come into contact with material surfaces, as shown in figure 1-3.

As can be observed from figure, the geometry of a tokamak is toroidal, or donut

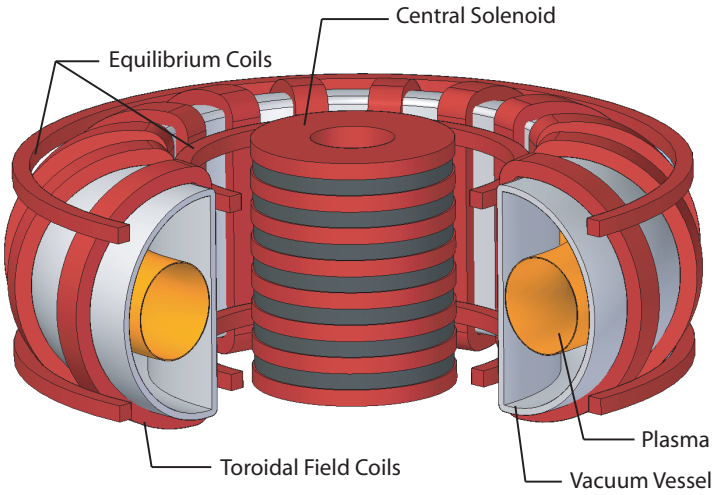

Figure 1-3: Diagram labeling basic tokamak features.

shaped. The long way around the torus is referred to as the toroidal direction, while the short way around is referred to as the poloidal direction. There are two coordinate systems that are commonly applied to describe locations in the torus. The first is the familiar cylindrical coordinate system (R, ϕ, Z) ,where Z is the distance above the mid-plane of the reactor, R, often referred to as the major radius, is the distance from the symmetry access of the torus, and ϕ, referred to as the toroidal angle, is the angle about the symmetry axis. Another commonly used coordinate system is (r, θ, ϕ), where r is the distance from the plasma axis, θ is the angle subtended from the mid-plane to the minor radius, and ϕ is again the toroidal angle. Both coordinate systems are shown in figure 1-4 along with a plasma pressure contour.

The primary component of the magnetic field in a tokamak is provided by the toroidal field coils, quite literally a solenoid that has been bent into a donut shape, which creates a field that wraps around the torus in the toroidal direction. Unlike in an infinite straight solenoid, the magnetic field from the toroidal field coils is not constant inside the coils, as application of Ampere's law with a loop that runs in the toroidal direction will show, but rather drops as $1/R$. This inhomogeneity in the magnetic field gives rise to vertical ∇B drifts that are oppositely directed for

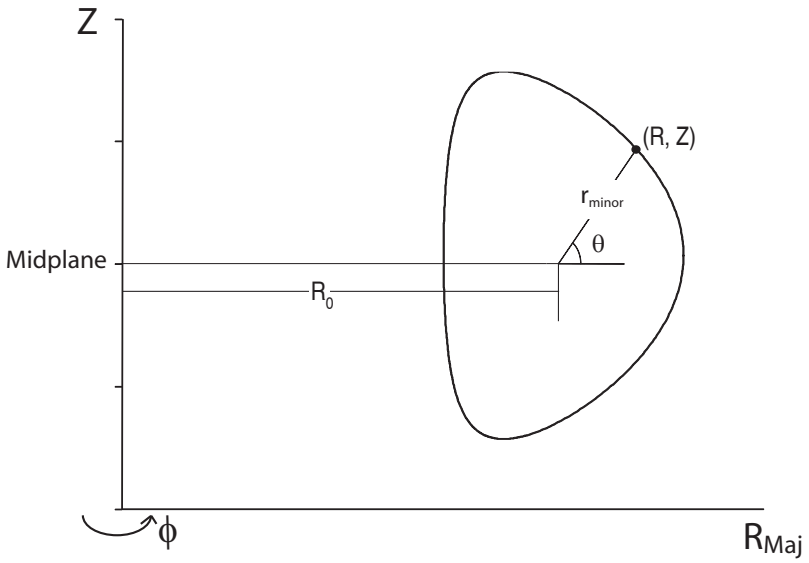

Figure 1-4: Common coordinate systems used to describe locations in the torus. The location (R, Z) is shown in both (R, ϕ, Z) and (r, θ, ϕ) coordinates.

electrons and ions. To avoid polarization of the plasma, and the outward ExB drifts that would result, a poloidal component is added to the magnetic field by driving a current in the toroidal direction. This current is driven either inductively, by ramping a solenoid that runs through the center of the torus, or by electromagnetic waves which accelerate electrons in a preferential direction.

The poloidal component of the magnetic field causes the field lines to "spiral" around the plasma as shown in figure 1-6, causing the vertical particle drifts to average out. For example, when ions are above the mid-plane, their drift takes them away from the center of the plasma, to larger minor radius; conversely, when they are below the mid-plane they drift towards the center of the plasma. The ratio of the number of times the field spirals around in the toroidal direction to the number of times in the poloidal direction is denoted as q, and is referred to as the safety factor[1]. For a typical tokamak the ratio of the poloidal to toroidal field at the mid minor radius is about $1:10$.

[1]The term safety factor refers to the important role this ratio plays in current driven instabilities.

Table 1.1: Alcator Operating Parameters

Parameter	**Symbol**	**Value**
Major Radius	R_0	$0.67m$
Minor Radius	a	$0.21m$
Toroidal Field[a]	B_T	$2.6 - 8.1T$
Plasma Current	I_p	$0.8 - 2MA$
Auxiliary Heating[b]	P_{ICRF}	$6MW$
LH Current Drive	LHCD	$1.5MW$
Electron Density	n_e	$1 \times 10^{19} - 1 \times 10^{21} m^3$
Electron Temperature	T_e	$\leq 9keV$
Max Pulse Length		$5s$
Plasma Volume	V_p	$\sim 1m^3$

[a] On axis value.
[b] Maximum Delivered

1.3 Alcator C-Mod

The experimental research performed for this thesis was conducted on the Alcator[2] C-Mod tokamak at MIT's Plasma Science and Fusion Center. Alcator C-Mod is a compact, high magnetic field, high density, shaped, diverted tokamak. Although it is significantly smaller than many of the other tokamaks currently operating, Alcator is particularly well suited to fusion research due to its high magnetic field which allows it to reach temperatures, densities, and scale lengths that are reactor relevant. Figure 1-5 shows a cutaway of Alcator C-Mod with a typical D shaped plasma, and table 1.1 lists some of the important parameters that characterize the system.

1.4 Diagnostics

On Alcator, numerous diagnostics are employed to ascertain the state and dynamics of the plasma. Although we will discuss only those systems essential to the research contained in this thesis, the reader is directed to the overview by Basse [2] for more thorough description of the complete diagnostic complement, and Hutchinson's book [3] for a detailed discussion of the physics principles underpinning the diagnostic

[2] Alcator is an abbreviation for Alto Campo Torus, Italian for High Field Torus.

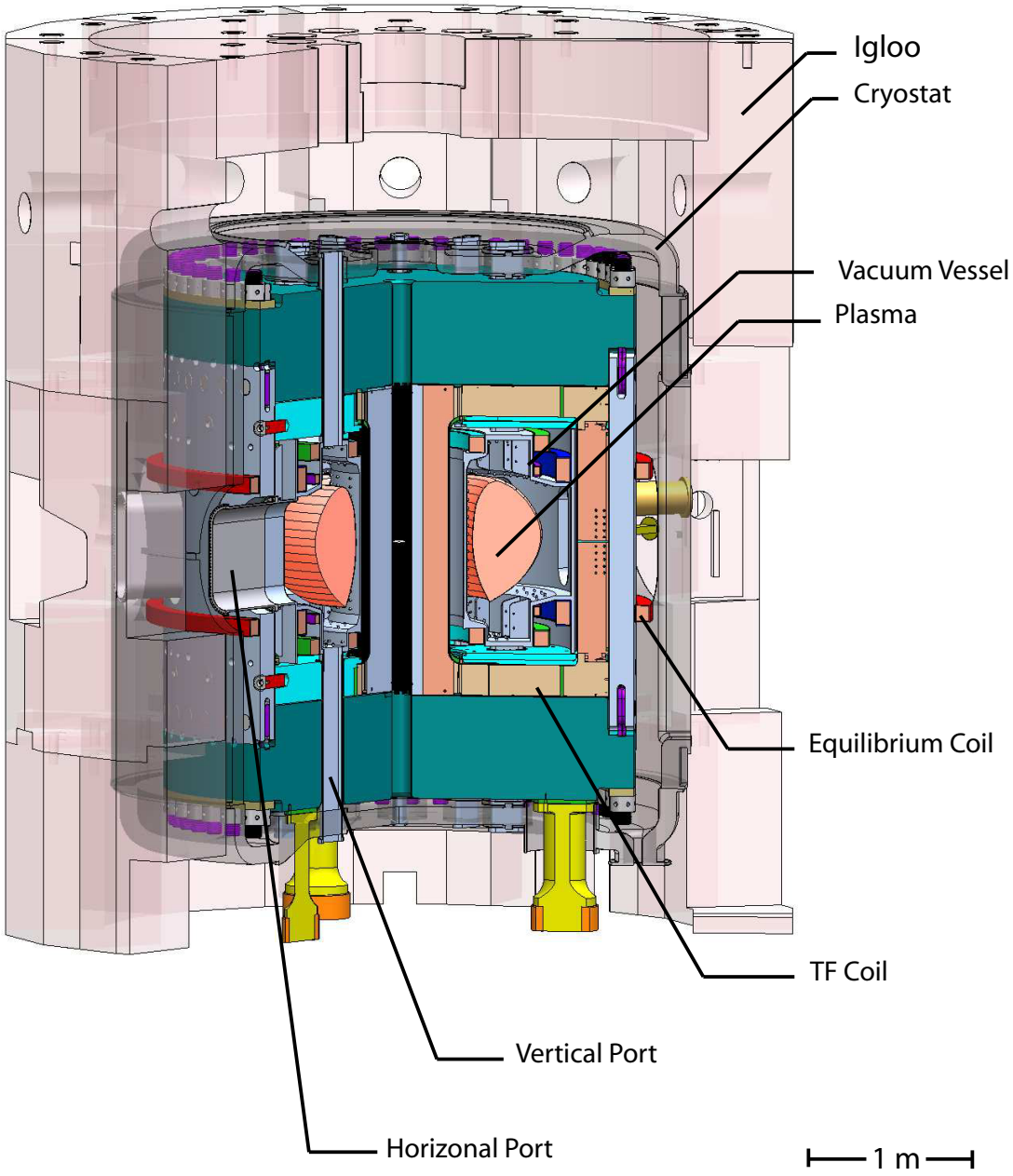
Alcator C-Mod
Igloo
Cryostat
Vacuum Vessel
Plasma
Equilibrium Coil
TF Coil
Vertical Port
Horizonal Port
1 m

Figure 1-5

techniques.

On Alcator C-Mod the electron temperature is diagnosed using four separate diagnostics, three of which are based on cyclotron emission from plasma electrons.

ECE

Electron Cyclotron Emission diagnostics, known as ECE, works by observing the thermalized cyclotron radiation emitted from plasma electrons. Plasma electrons, which oscillate about the magnetic field lines, emit radiation at frequencies which are integer multiples of the cyclotron frequency, as given in equation 1.4. Since all electrons in the same region of the plasma oscillate with nearly the same frequency, the cyclotron radiation is also absorbed strongly due to high optical depth at C-Mod parameters. Thus the emission intensity follows a black body distribution and carries information about the local plasma temperature. Since the cyclotron frequency is a function of the local magnetic field, the choice of frequency also allows localization of the temperature measurement. The success of this technique requires that the electron have a maxwellian velocity distribution, and the presence of a high energy tail, as occurs during lower hybrid current drive, can lead to artificially high emission which prevents use as a electron temperature diagnostic in these circumstances.

The ECE diagnostics on Alcator utilize second harmonic X-mode[3] emission; the higher second harmonic usually prevents the signal from falling below the plasma frequency and thus being cutoff during the discharge. The Michelson ECE uses a large-scan interferometer to obtain a full radius temperature scan with a repetition rate of $33Hz$. Higher time resolution is obtained with the GPC (Grating PolyChromators) ECE diagnostics, which use grating diffraction for frequency differentiation to observe distinct locations in the plasma. GPC can obtain a time resolution of $10\mu s$, with a spatial resolution of $\sim 1cm$ and an uncertainty of approximately $10eV$. Higher spatial resolution still can be obtained using the heterodyne FRCECE (Fusion Research Center ECE) system, which has a spatial resolution of $\sim 4mm$.

[3]X-mode refers to an electromagnetic wave whose $\vec{k}$ is perpendicular to the tokamaks magnetic field, and whose electric field is also polarized perpendicular to the background plasma magnetic field. More details of wave propagation in a plasma can be found in Stix [4]

Thomson Scattering

The Thomson scattering diagnostic provides profile measurements of both electron temperature and density in both the core and edge region of the plasma. The diagnostic makes its measurements by observing light scattered from an Nd:YAG laser ($\lambda_0 = 1064nm$) which is directed vertically through the plasma. From a physics perspective, the diagnostic can make simultaneous measurements of the temperature and density because the line width of the scattered light is a function of the electron velocities, through Doppler broadening, and the intensity of scattered light is proportional to the density of scattering centers. Spatial localization of the measurement is a result of the intersection of the line-of-sight of the viewing optics and the laser. The Thomson diagnostic has a time resolution of $8ns$, a repetition rate of $60Hz$ and a spatial resolution of approximately $1cm$ in the core and $2mm$ in the edge region. The diagnostic is capable of making temperature measurements between $0.05 \leq T_e \leq 10keV$ (core) and $15 \leq T_e \leq 800eV$ (edge) and density measurements between $.5 \leq n_e/10^{20} \leq 30$ (core) and $.3 \leq n_e/10^{20} \leq 5$ (edge).

Two Color Interferometry

Additionally to measure the plasma density, Alcator employs a Two Color Interferometer (TCI), which determines the line integrated density by measuring the plasma induced phase shift for laser light traversing the plasma. A $10.6\mu m$ CO_2 laser measures the phase caused by the plasma, while an overlapping $632nm$ $HeNe$ laser, for which the plasma introduces negligible phase shifts due to its high frequency, is used to correct for vibrations. Measurements are taken through 10 vertical chords located between major radii of $.6 - .8m$ at rates that range from $5 - 10kHz$, though burst data can be taken at a rate of up to $1MHz$.

Ion Temperature

Although Alcator possess a diagnostic which can make direct measurements of the ion temperature profile, via the HIREX X-ray spectrometer, data from this diagnostic

was not available for the research in this thesis. Rather, the ion temperature was inferred from the total neutron production rate due to D-D fusion. The neutron production rate can be related to the deuterium density and temperature through the relation,

$$R_{DD} = \frac{n_D^2}{2} \langle \sigma v \rangle_{DD} \tag{1.8}$$

where n_D can be inferred from n_e, through quasi-neutrality[4] and the effective charge of plasma ions, Z_{eff}. $\langle \sigma v \rangle_{DD}$, the D-D fusion cross section averaged over the velocity distribution [1], can be approximated as

$$\langle \sigma v \rangle_{DD} \approx 2.33 \times 10^{-14} T_i^{-2/3} \mathrm{e}^{-18.76 T_i^{-1/3}} \tag{1.9}$$

The ion temperature is determined by assuming a Gaussian ion temperature profiles, and then adjusting the peak ion temperature until the predicted and observed neutron rate match [5].

The neutron flux is determined from two systems. The first consists of 12 fission chambers, four BF_3 counters and four ^3He detectors with a time resolution of $1ms$, and is absolutely calibrated with Cf^{252} and D-D fusion neutrons from Alcator C-Mod. The second system provides fast measurements with a time resolution of $0.1ms$ and is cross calibrated with the first system.

Magneto-hydro Dynamics

It's convenient at this time to briefly discuss the magneto-hydro dynamic (MHD) equations that govern the gross behavior of plasma as it will introduce several key terms and concepts that are central to research on a fusion device. A complete treatment of ideal MHD can be found in Freidberg [6]. Ideal MHD models the plasma as a single perfectly conducting fluid. In steady state these equations take the form [6]

[4]Quasi-neutrality expresses the tendency for the plasma to be electrically neutral due to the large mobility of the electrons.

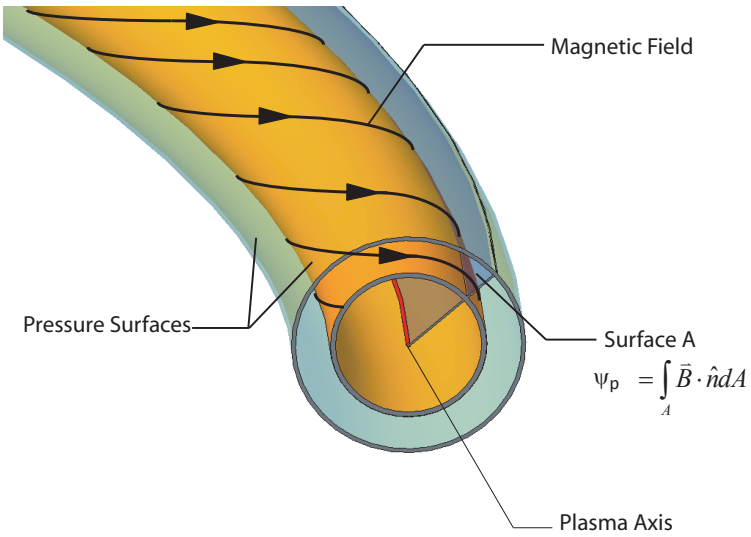

Figure 1-6: Diagram showing the equivalence of flux surfaces and pressure surfaces. The normal to surface A, $\hat{n}$, selects on the poloidal component of the magnetic field.

$$\vec{J} \times \vec{B} = \vec{\nabla} p \tag{1.10}$$

$$\vec{E} + \vec{v} \times \vec{B} = 0 \tag{1.11}$$

$$\vec{\nabla} \times \vec{B} = \mu_0 \vec{J} \tag{1.12}$$

$$\vec{\nabla} \times \vec{E} = 0 \tag{1.13}$$

$$\vec{\nabla} \cdot \vec{B} = 0 \tag{1.14}$$

Taking the inner product of equation 1.10 with $\vec{B}$, we see immediately that $\vec{B} \cdot \vec{\nabla} p = 0$, i.e. that magnetic fields lie within surfaces of constant pressure. Playing the same trick with the current density, $\vec{J}$, we see that $\vec{J} \cdot \vec{\nabla} p = 0$, or that the current also lies within surfaces of constant pressure. For a tokamak, the contours of constant pressure are nested toroidal surfaces. It can be shown that these surfaces of constant pressure are also surfaces of constant poloidal flux[6], as shown in figure 1-6. In general, these surfaces are refered to as flux surfaces and are labeled by the poloidal magnetic flux per unit toroidal angle, ψ.

Many quantities, such as the safety factor q, are flux functions. Since magnetic

field lines are confined to flux surfaces, transport along the surface is usually relatively fast compared to transport across the surface. As a result, quantities such as temperature and density are also nearly constant on a flux surface. As a consequence, flux surfaces make a convenient reference for the plasma equilibrium. Quantities which are constant, or nearly constant, on a flux surface are often plotted as a function of flux, or as a function of the minor radius on the outboard midplane, which can be directly related to the flux profile.

The overall magnetic magnetic configuration of a toroidally symmetric plasma is governed by the Grad-Shafranov equation, which is given by,

$$R^2\vec{\nabla}\cdot\left(\frac{\vec{\nabla}\psi}{R^2}\right) = -RB_\phi\frac{\partial RB_\phi}{\partial\psi} - \mu_0 R^2\frac{\partial p}{\partial\psi} \tag{1.15}$$

An example of the poloidal projection of a solution to the Grad-Shafranov equation is shown in figure 1-7 for Alcator C-Mod; the curves are contours of constant flux.

1.5 Summary of Results

It has been well known since the first high speed images were taken of ablating pellets that plasmoid filaments parallel to the magnetic field form during the injection of solid light element pellets into magnetic fusion devices [7]. The research for this thesis was primarily motivated by a series of observations of this phenomenon during the 2003-2004 campaign on Alcator C-Mod. At the time, a pneumatic gun was configured to inject lithium pellets radially inward into Alcator's plasma at the midplane as shown in figure 1-8.

A high speed, 500k $frames/sec$ CCD camera viewed the injection from behind, down the trajectory of the pellet. In the images that resulted the filaments could be observed to move in the vertical direction. Using an array of vertical diodes to track the location of the pellet along the major radius of the tokamak and assuming the filaments moved purely in the vertical direction, the velocity of the filaments was estimated for each injection.

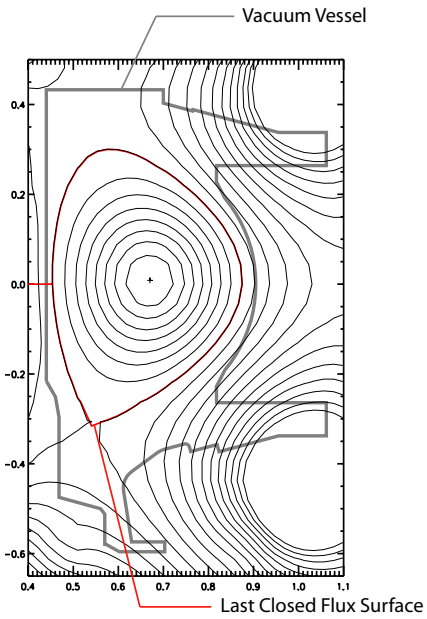

Figure 1-7: EFIT reconstruction of flux surfaces for Alcator Shot 1070503036. The vacuum vessel and last closed flux surface are labeled. As one might note, all flux surfaces are infact closed in a geometric sense in accordance with Maxwell's equation, but in the parlance of fusion research the term closed flux surface is reserved for those that do not intersect a material surface. Thus since magnetic fields are confined to flux surfaces, and the plasma is confined to the magnetic fields, the last closed flux surface marks the boundary of the confined plasma.

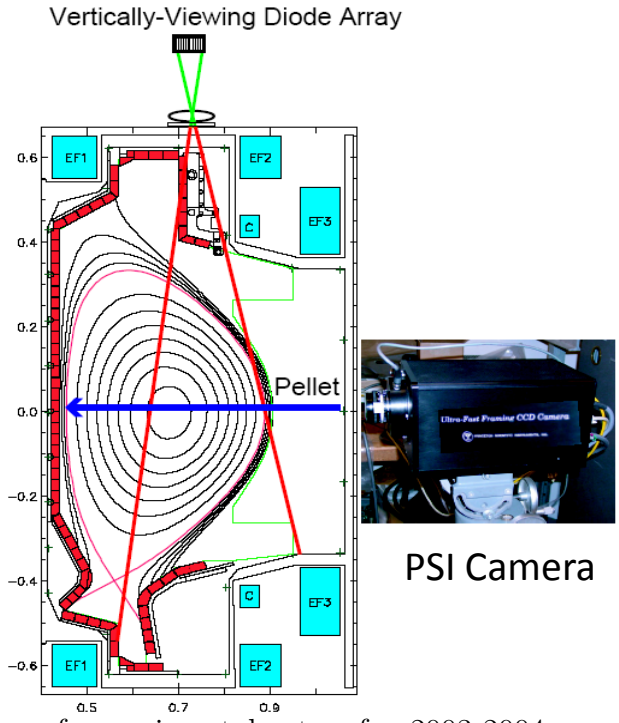

Figure 1-8: Diagram of experimental setup for 2003-2004 campaign. The PSI-IV camera has a frame rate of 500k $frames/sec$ and views the pellet from behind.

Though the data set was limited, some interesting properties of the filaments started to emerge. The most obvious was that if the filaments are indeed moving parallel to the flux surface, then they are moving with velocities over $1000m/s$. Additionally, it was observed that the direction of the filaments motion, either up or down, was only semi-random in the sense that if a filament was emitted in one direction, then there was greater than 50% probability that the next filament would be emitted in the same direction, as shown in figure 1-9. This persistence of direction appeared to last approximately $20-30\mu s$, or given that the pellets were traveling at radially $\sim 500m/s$ the persistence of direction stretched over a distance of $1-2cm$; for a 1keV deuterium plasma and a magnetic field of $5T$, this corresponds to $10-20$ ion gyro radii.

The direction of the filament motion was distinctly different between ohmically heated L-mode plasmas, and RF heated H-mode plasmas[5]. Plots of the measured filament velocities, versus the major radius of the pellet at the time of filament emis-

[5]L-mode and H-mode refer to low (L) and high (H) confinement regimes of the plasma.

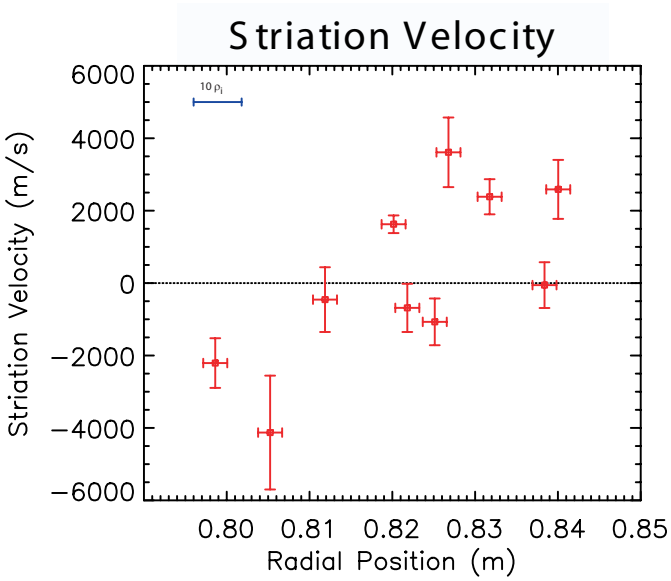

Figure 1-9: Plot of filament velocities as a funciton the pellet's location at the time of emission for shot 1020827021.

sion, are shown in figure 1-10. As can be seen, the velocities in ohmic L-mode plasmas range in both the positive and negative direction, while the velocities in the RF heated H-mode plasmas range in only the negative direction.

These observations suggested some interesting possibilities. First, the fact that the filament properties are different in ohmic L-mode and RF H-mode plasmas indicates that the filaments are affected by the background plasma conditions and are not merely an intrinsic property of the ablation process. Second, since the filaments are affected by the background plasma conditions, their subsequent trajectory after emission is most likely the result of ExB drifts that exist in the background plasma (either prior to the pellets appearance or drifts generated subsequent to the injection). Finally, the semi-random nature of the drifts is consistent with the chaotic properties of electrostatic plasma turbulence, which will be discussed further in chapter 3. Taken as a whole then, the investigation of the filament properties represents not only an opportunity to gain a greater understanding of the ablation process, but also holds the possibility of opening a new window into our understanding of plasma turbulence.

To explore the properties of the ablation filaments, and their possible connection

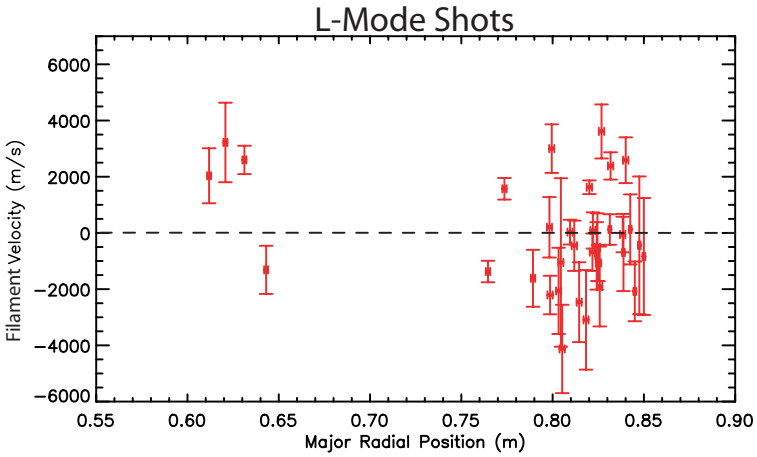

(a) L-mode Filament Velocities

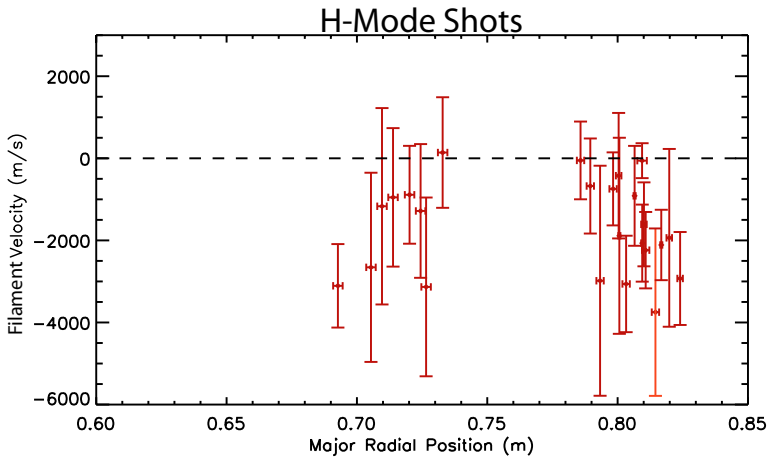

(b) H-mode Filament Velocities

Figure 1-10: Filament velocities for L-mode (a) and H-mode (b) shots.

to plasma turbulence, we explored two avenues of investigation. The first concerned measuring the trajectories of the ablation filaments under a wide variety of plasma conditions to more fully understand their properties and the second concerned the determination of the turbulence properties from direct numerical calculation. To measure the filament trajectories, we constructed a stereoscopic imaging system which was able to track the three dimensional evolution of the filaments. During the 2007-2008 campaign we used this imaging system to record the trajectories of filaments formed during 122 pellet injections into ohmic L-mode discharges. This study corroborated our previous observation that the filaments move along flux surfaces, and any given filament has a tendency to move in the same direction as the preceding filament. Furthermore, the database also revealed that there is a preferential drift direction for the filaments in ohmic L-mode, in the electron diamagnetic direction. A statistical analysis of the database, relying on binned distributions of the filament velocities, revealed that the standard deviation of the filament velocities is a decreasing function of the local safety factor q.

To make a comparison of filament properties to the plasma turbulence we used the nonlinear gyrokinetic solver GYRO to simulate electric fields generated by the plasma turbulence. Our investigation focused on two main cases. The first investigated the turbulence under ambient, pre-pellet, plasma conditions, while the second attempted to model the turbulent conditions during the injection. For the pre-pellet simulations we performed a series of flux-tube simulations at five separate locations in the plasma, chosen so that they covered a region in q space from $q = 1.25 - 2.25$, in an attempt to observe a dependence in the turblent electric fields analogous to the dependence of the filament velocities. These simulations revealed that the turbulent electric fields, and the implied ExB drifts, are approximately an order of magnitude smaller than the drifts observed in the filaments, and lack any obvious dependence on the local safe factor. For the post-pellet plasma conditions, global simulations were used to capture the nonlocal effects of pellet's modification to the plasma profiles on the turbulence. These simulations indicate that the electric fields generated during the injection are approximately a factor of three larger than during the pre-pellet conditions and thus

more consistent with the drifts observed in the filaments. Thus it appears that the filament drifts are a result of the turbulence generated during the pellet injection.

Chapter 2

Review of Pellet Ablation

The investigation of the injection of solid pellets into plasma began early during the fusion program as a fueling mechanism. These investigations were additionally motivated by the discovery of the pellet's transient effect of improving plasma confinement [8, 9], in what have been come to be known as pellet enhanced mode. Since that time, pellet injection has come to be considered the leading fueling technique for the future generation of fusion reactors [10], as well as for applications in controlling ELMs [11] (edge localized ejections of high energy plasma that can have a deleterious effect on plasma facing components), internal transport barrier formation, current modification [11] for advanced tokamak scenarios, and fast alpha diagnostics for fusion alphas.

The following section has three aims. First, to give the reader a basic understanding of the process as a solid pellet ablates in a plasma. The second is to introduce the reader to the generally accepted theories that attempt to explain the formation and evolution of the striations. Finally, I give a brief but comprehensive overview of the phenomenology of the plasma response to the injection, and thus introduce different effects that might come into play in determining the drift of filaments formed during pellet ablation. For a more in-depth explanation I direct the reader to the excellent reviews such as those by Pégourié [10], Milora [11], and Chang [9].

2.1 Ablation Physics

Pellet ablation can be broken roughly into two distinct processes, erosion of the pellet by the plasma followed by the homogenization of the pellet material in the plasma. The first step in understanding the erosion process is to understand the interaction of the pellet with the hot plasma. This process determines the rate at which the pellet is eroded by the plasma, and hence the depth of penetration of the pellet, as well as the properties of the ablation cloud.

When a pellet first enters a plasma it is initially bombarded by hot plasma electrons and ions flowing along the magnetic field. These particles strike the pellet, eroding the surface and forming a cold dense spherical cloud of neutrals around the pellet. This process occurs on a timescale of $10^{-11} - 10^{-7}$ seconds. As the ablatant expands and heats up, it eventually ionizes and is constrained to move along the magnetic field line, thus giving the ionized ablatant its characteristic cigar-like shape as shown figure 2-1. Measurements from frozen deuterium injections into PLT [12, 13] and TFTR [12] in the 1980's and early 1990's indicate electron densities and temperatures in the neutral cloud close to the pellet of $n_e \sim 10^{25} - 10^{26} m^{-3}$ and $T_e \sim 1 - 3eV$ with the densities falling to $10^{23} - 10^{24} m^{-3}$ in the ionized region and the temperatures rising to $10 - 20eV$.

The ablation rate, the rate at which the pellet's surface is eroded, is determined by the balance of the energy flux of plasma species reaching the surface and the energy required to remove particles from the pellet's surface, heat them, ionize them and carry them away. The ablation can be thought of as a self regulatory process whereby the shielding mechanisms adjust themselves so that the energy reaching the pellet surface is sufficient to maintain the pellet shielding. Chief among the mechanisms that play a role in shielding the pellet are magnetic shielding, electrostatic shielding, and neutral gas dynamics/plasma shielding.

The least important mechanism is magnetic shielding, due to the partial expulsion of the magnetic field from the ablation cloud due to finite conductivity of the ablatant during its expansion. Due to the relatively low magnetic Reynolds number of the

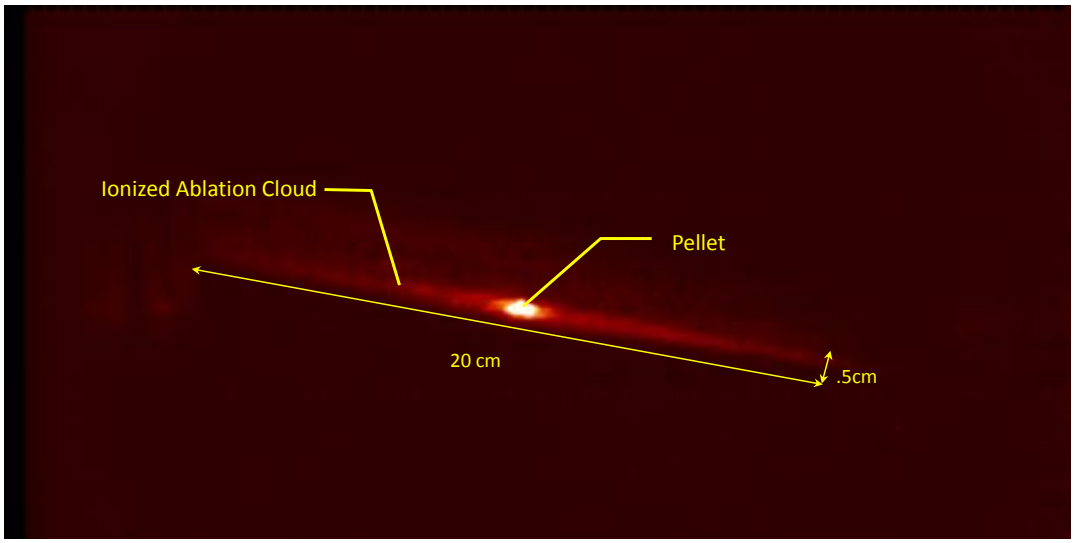

Figure 2-1: Image from a lithium pellet injected into Alcator C-Mod Shot 1030709018, filtered at $672nm$ with a $10nm$ bandpass filter and 10^{-3} neutral density filter. The ablation cloud is approximately 20cm long and .5 cm in diameter.

ablatant, this diversion of the field lines around the pellet, and the particle flux associated with it, results in an almost negligible amount of shielding in present day experiments, $\sim$ 1% of total shielding[10]. The magnetic Reynolds number ($R_M \sim v_{ablatant} r_{pellet}/\eta$), measures the ratio of magnetic advection of the field to magnetic diffusion, where $v_{ablatant}$, is the flow velocity of the ionized ablatant, r_{pellet} is the characteristic size of the pellet, and $\eta = {}^{1}/_{\sigma\mu_0}$ is the magnetic diffusivity. Using $4 \times 10^3 \, {}^{A}/_{V-m}$ for the conductivity of the ablatant for a hydrogen pellet [14], the ion thermal velocity at 1eV for $v_{ablatant}$, and a characteristic dimension of the pellet to be $1mm$, we get $R_m \approx .02$. Quite simply, the ionized ablatant is resistive enough, and the flow slow enough that the magnetic field lines can diffuse through the ablatant faster than the flow can push them away. Thus there is little distortion of the magnetic field lines, and little alteration of the energy flux reaching the surface of the pellet. In future experiments, with larger temperatures and densities, the ablatant is expected to be hotter and more highly conductive, with the consequence that magnetic shielding may play a more significant role.

Electrostatic shielding, which constitutes the next most effective shielding mech-

anism, results from negative charge that builds up in the ablation cloud with respect to the background plasma. The negative charge results from the highly collisional nature of the cold and dense ablation cloud. As background plasma electrons and ions pass through the cloud, they are scattered from their trajectory parallel to the magnetic field due to collisions and begin to collect in the cloud. Because the electrons are lighter, and consequently more mobile, initially there is a greater flux of electrons to the clouds than ions. The electrons accumulate in the ablation cloud until an electrostatic sheath develops which is sufficient to balance the flux of ions and electrons entering the cloud. This process, which is similar to the dynamics of a solid probe in a plasma, will be discussed further in section 2.2 regarding filament formation. The net effect of the sheath formation is to retard the progress of the electrons and accelerate the ions in their approach to the cloud. The ionized portion of the ablation cloud is totally opaque to the ions, and thus the ions deposit almost all of their energy prior to reaching the pellet surface, so that their acceleration has little effect on the ablation rate. The electrons on the other hand, are able to penetrate the ablation cloud and are thus the primary carriers of energy to the pellet surface. Consequently, their screening by the electrostatic sheath can significantly reduce the energy flux reaching the pellet.

The gas dynamic/plasma shielding mechanism, which results from incident electron and ion collisions with the cold ablatant, constitutes the largest source of shielding for the ablating pellet. These collisions, which heat and eventually ionize the ablatant, significantly reduce the incident heat flux from the plasma, ${}^{q_p}/_{q_\infty} \approx 0$ for hydrogen pellets and ${}^{q_p}/_{q_\infty} \approx .3 - .7$ for impurity pellets[1], where q_p is the energy flux at the surface of the solid pellet, and q_∞ is the expected unshielded energy flux. The significance of the ionized portion of the ablation cloud in shielding can easily be seen in pellet injection experiments in reverse field pinches (RFP), where the high transport of the RFP reduces the density in the ionized portion of the cloud to lev-

[1]The primary difference in the ablation dynamics between frozen Hydrogen pellets and impurity pellets results from the enormous difference in their sublimation energies, $0.005eV/atom$ for H_2 and $1.6eV/atom$ for lithium [15]. Because the atoms are more difficult to ablate, more energy must reach the surface to cause ablation. Thus the shielding cloud must also be less dense so that a higher energy flux may reach the pellet.

els significantly lower than those in comparable tokamak and stellerator injections, $n \sim 10 \times 10^{21} m^{-3}$ in the ionized ablatant of the RFP compared with $n \sim 10 \times 10^{23} m^{-3}$ for ablatant in a tokamak or stellerator. Consequently ablation rates as much as twice as high as those seen in tokamaks are observed [16]. Furthermore, the importance of the gas dynamic mechanism in pellet shielding is demonstrated by the remarkable success of the Neutral Gas Shielding model (NGS), which, although simple, accurately predicts ablation rates and pellet penetration depths in a wide array of plasma conditions [17].

2.1.1 Neutral Gas Shielding Model

NGS is a steady state model describing the ablation process in frozen hydrogen and deuterium pellets [18, 14], and later extended to light impurity pellets [15, 19]. The model is characterized by three central approximations: the shielding is dominated by the gas dynamic mechanism mentioned above; the cloud expansion is taken to be purely spherical; and the distribution of incident particles is taken to be mono-energetic. Following the above assumptions, the instantaneous speed at which the pellet's surface is eroded is shown to go like $\dot{r}_{pellet} \sim -r_{pellet}^{-2/3} n_{\infty}^{1/3} T_{\infty}^{1.64}$, which can then be used to determine instantaneous ablation rate, and penetration depth. It should be noted that the NGS model ignores magnetic and electrostatic shielding, the effects of non-uniform heat flux at the pellet surface, atomic processes in the cloud, the cross-field dynamics of the cloud expansion, the effects of a Maxwellian distribution of incident particles, and the dynamics leading to the formation of the cloud. Despite the absence of what appear to be significant contributors to the ablation and shielding mechanisms, the NGS model correctly predicts the pellet penetration depth and ablation rate with a high degree of accuracy in plasmas so long as there is a minimal amount of auxiliary heating or lower hybrid current drive. [2]

[2]Deviation from the NGS scaling in auxiliary heated plasmas is due to the presence of high energy ions in ICRH and neutral beam plasmas and high energy electrons in ECRH and lower hybrid discharges. The high energy ions are able to penetrate the collisional gas shield, and thereby make contributions to the energy reaching the solid pellet surface and thus increase the ablation rate. High energy electrons on the other hand, are able to pass through both the neutral cloud and solid pellet material, depositing energy uniformly throughout the pellet. This can lead to

The solution to the apparent mystery of the NGS model's success, despite its approximations, partially lies in the balance that occurs between each of the neglected mechanism. For instance, taking full account of the Maxwellian distribution of electrons increases the ablation rate by a factor of $\sim 3-5$ [10], while the effects of non-uniform heat fluxes at the pellet surface reduce the ablation rate by ~ 2 [20]. Inclusion of the electrostatic shielding reduces ablation rate by an additional factor of two [10], while including atomic processes in the ablation cloud reduces the ablation rate by an additional 25-50% [21]. Despite its success, the NGS model is only appropriate for calculating ablation rates and penetration depths. To determine the properties of the ionized portion of the cloud, including the formation of ablatant filaments, one must turn to more sophisticated models.

2.1.2 Homogenization

Redistribution of the ablated material over the flux surface begins to occur approximately 5-10 μs after the material is deposited by the pellet and is globally completed in less than $1ms$ [10]. It begins with the expansion of the ablated material along the magnetic field lines of the plasma, which according to measurements on TFTR, occurs at a rate of approximately $2 \times 10^5\, m/s$ for the first $200\mu s$ before slowing to $3 \times 10^4\, m/s$ [22].

Concomitant with the expansion along the field, an outward drift of the ionized ablatant is generally observed during injection experiments [23, 24, 25, 26, 27] which is usually manifested by an outward shift in the major radial direction of the measured density increment after an injection relative to that predicted by the ablation profile determined from light emission from pellet neutrals during ablation. The drift is believed to be caused by the polarization of the ablated material due to the non-homogeneous magnetic field of the tokamak. The $^1/_R$ dependence of the toroidal magnetic field gives rise to oppositely directed curvature drifts for the ions and electron, resulting in a current that goes like $J_{\nabla B;ablatant} = 2P_{ablatant}/RB$.

complete vaporization when the average energy deposited per molecule is greater than the molecular sublimation energy.

Due to the pressure difference between the ablatant and the background plasma, a current difference exists, that goes like $J_{\nabla B} = 2(P_\infty - P_{ablatant})/RB$, resulting in the polarization of the ionized ablatant. The vertical electric field associated with the polarization gives rise to an ExB drift of the ablatant down the magnetic gradient of the tokamak which continues until the pressure of the ablatant equilibrates with the background plasma [28]. During low field side injections, this drift tends to expell the ablatant from the plasma, while for high field side injection the drift helps the ablated material to penetrate more deeply into the discharge. Measurements on ASDEX-U, $R \sim 1.65m$, $B \sim 2T$, $T_e \sim 2keV$ indicate drift velocities of $\sim 10^4\, {}^m/_s$ [24, 23].

2.2 Filament Formation

During the earliest experiments involving the injection of solid pellets into hot magnetized plasmas it was noted that the ablatant did not form a smooth continuous trail, but rather formed a pattern of light and dark striations parallel to the magnetic field [29, 30]. As can be seen in figure 2-2b high resolution time integrated images of ablating pellets in Tore Supra show distinct light and dark field aligned regions. Fast diode measurements of the neutral light emitted from the ablating pellet [30], often used as a proxy for the instantaneous ablation rate since the intensity of emitted light should be roughly proportional to the ionization rate in the neutral cloud surrounding the pellet, exhibit corresponding fluctuations in intensity, figure 2-2a. Measurements on Asdex Upgrade [24] have demonstrated that the light fluctuations are correlated with density fluctuations in the ionized portion of the ablation cloud and the periodic ejection of ablated material from the ablation cloud. Additionally, our measurements on Alcator C-Mod utilizing a high-speed CCD, have captured the formation and ejection of field aligned filaments from the ablation cloud during Lithium pellet injections [31] figure 2-3.

Initial attempts to explain the striated structure of the ablatant, and the associated fluctuations in the ablation rate, focused on the variation in energy reservoir in flux tubes on flux surfaces with a rational or irrational safety factor q [33]. Recall,

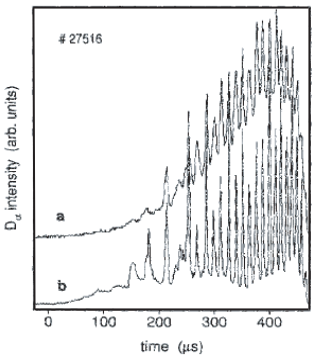

(a) Light Fluctuation vs Time

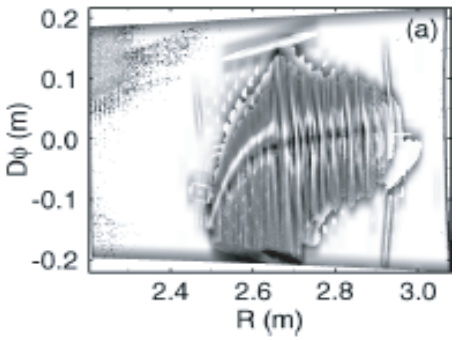

(b) Light Fluctuation in Space

Figure 2-2: a) Trace a, and b present different views of light emission from a 4% neon-doped deuterium pellet on ASDEX [29]. b) Striations are clearly visible on this image of the ablation pattern from a frozen hydrogen pellet injected into Tore Supra [32]. The image is taken using a 512×512 pixel CCD camera integrated over the duration of the pellet injection. The camera is looking down from $2.1m$ above the equitorial plane, resulting in a spatial resolution of $1.2mm \times 1.2mm$. The pellet enters from the right on the low field side, and the vertical axis is along the toroidal direction.

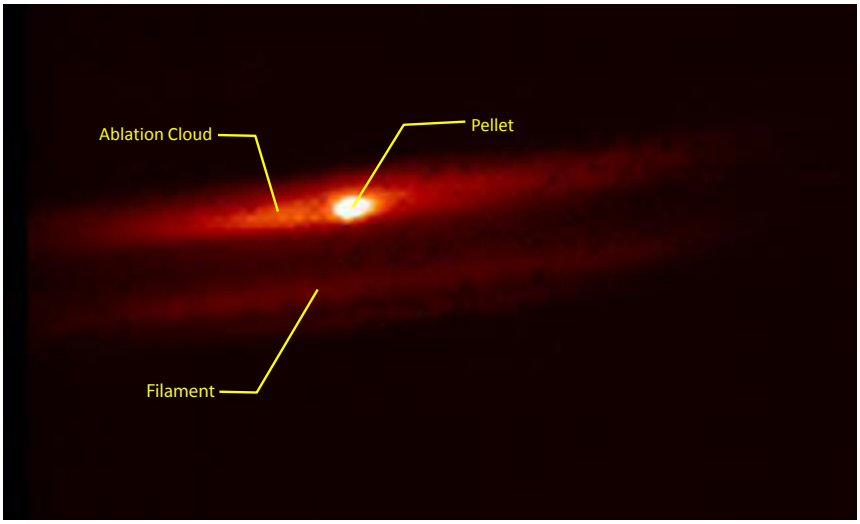

Figure 2-3: Image from Li-injection on Alcator C-Mod shot 1020827021. Light is primarily from the $1s^2 2p$ to $1s^2 2s$ transition in Li^+ using a band pass filter, central wavelength: $548nm$, width: $10nm$ and a 10^{-3} neutral density filter. Note the filament below the primary ablation cloud.

$q \simeq {}^{rB_\phi}/_{RB_\theta}$, is the number of toroidal circuits the magnetic field makes per poloidal circuit. If q is a low order rational number, $q = {}^{m}/_{n}$, where $\{m, n\} = 1, 2$ or 3, then the magnetic field loops back onto itself after only a few transits around the torus. On the other hand, if q is a high order rational number, or irrational, the magnetic field effectively never loops back on itself. As soon as a pellet intersects a magnetic field line on a low order rational surface, it begins to drain electrons. If the residence time of the pellet in the field line, $\tau = r_{pellet}/v_{pellet}$, is of the order the time it takes the field line to drain all of its electrons, $\tau_{drain} \sim {}^{L_B}/_{v_{T_e}} \sim {}^{2\pi[m^2R^2+n^2r^2]^{1/2}}/_{v_{T_e}}$ (where L_B is the length of the field line), then at this surface we would expect a decrease in the incident heat flux to the pellet. Measurements of the neutral emission from pellets crossing the $q = 2/1$, and $q = 3/2$ support this hypothesis, but this observation is only reproducible at very low order rational surfaces and cannot account for the majority of the fluctuations. Furthermore, the spatial and temporal characteristics of the periodic fluctuations in the ablation rate exhibit the same behavior in stellarators, which owing to their low magnetic shear possess few low order rational surfaces, indicating that this can not be the only mechanism driving the striations.

Currently, prevailing theory [10] holds that the fluctuations in ablation rate are caused by the periodic modulation of the ionized portion of the ablation cloud, either due to the pellet's periodically leaving the protection of the ionized portion of the ablation cloud or due to periodic ejections of material from the ablation cloud. During periods of lower density in the ablation cloud, the pellet is less shielded from the background plasma and thus there is a resulting burst in the ablation rate.

At this time it is convenient to consider the dynamics which govern the relative motion of the pellet and the ablation cloud. As material is blown off the surface of the pellet, the ions and electrons have an average velocity equal to the pellet velocity. This average velocity causes the ionized portion of the ablation cloud to polarize in the background magnetic field until the magnetic and electric forces on the electrons and ions balance $E_{polarization} = v_{pellet} \times B$. If an open circuit situation exists, in which the charge accumulation in the cloud cannot be balanced by charge flowing in from the plasma, then the electric field arising from the polarization causes the ablation cloud

to ExB drift along with the pellet, $v_{\mathrm{E\times B}} = {}^{E_{polarization}}/_{B} = v_{pellet}$. In this situation one would expect that the periodic shedding of the ablation cloud must arise from a mechanism internal to the dynamics of the pellet and cloud. In the other extreme, if a closed circuit situation prevails, in which the charge separation in the cloud is negated by charge flowing in from the background plasma, then the ablatant would become "pinned" to the magnetic field lines as soon as it begins to ionize [11]. Thus in this situation the pellet could be stripped of the ablation cloud by the dynamics of the background plasma, such as an E_rxB rotation of the plasma, or a drift of the low temperature magnetized material down the magnetic field gradient of the tokamak [10].

2.2.1 Internal Instability Theory

The most generally accepted model, proposed by Parks in 1996 [34], contends that the striations are a result of a Rayleigh-Taylor instability that occurs in the ablation cloud while it is still surrounding the pellet. This model gives rise to a characteristic time scale for the fluctuations, and is capable of reproducing the main dependences of the fluctuation frequency on electron temperature and magnetic field.

Parks' theory begins by assuming that the ablation cloud moves with the pellet across the magnetic flux surfaces. In a manner similar to probe theory the cloud acquires a net negative charge due to absorption of the more mobile plasma electrons. The exact electrostatic distribution is determined by balancing the fluxes of 1) electrons from the plasma, 2) ions from the plasma, 3) electrons emitted from the ablation cloud, and 4) shine through electrons that come from the background plasma and pass through the ablation cloud without stopping, see figure 2-5. The probability that a plasma electron streaming along the magnetic field will be stopped due to collisions is higher near the axis of symmetry of the cloud than near its edge due to the variation of the cloud density with radius. In this case the radial variable is taken to be the distance from the axis of symmetry. This sets up a radial variation of the electrostatic potential in the cloud, which in turn gives rise to a inwardly directed radial electric field within the ablation cloud. When combined with the background

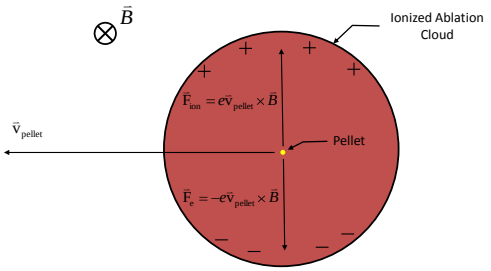

(a) Cloud Polarization

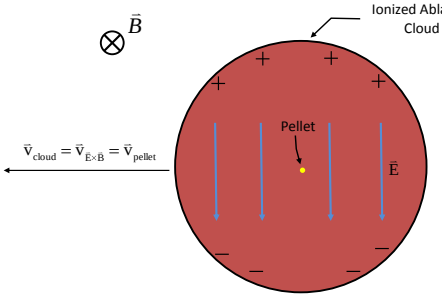

(b) Open circuit

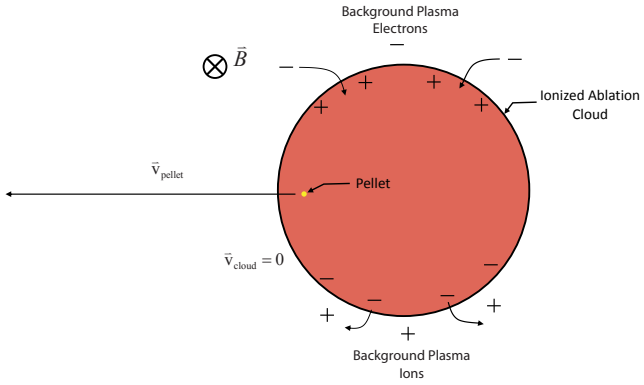

(c) Closed circuit

Figure 2-4: (a) Ion and Electron drift in the ionized portion of the ablation cloud due to the Lorentz force. (b) Open circuit conditions allow charge to accumulate at the upper and lower edge of the ablation cloud, leading to an Electric field and ExB drift of the ablation cloud with the pellet. (c) Under closed circuit condition, accumulating charge in the ablation cloud is neutralized by currents from the background plasma. There is no ExB drift and the ablatant becomes penned to the magnetic field lines as soon as it ionizes.

magnetic field this in turn gives rise to a ExB rotation of the cloud about it axis of symmetry, as shown in figure 2-6.

As it turns out, the shine through electrons are the key element of this instability. If all of the electrons were stopped in the ablation cloud it would charge up uniformly, resulting in a radial electric field that increases in magnitude as $\sim r^2$. This would result in a ExB rotation in the cloud that was not uniform, ie $\omega_{\mathrm{E\,x\,B}} = v_{\mathrm{E\,x\,B}}/r \sim r$. The resulting velocity shear could then potentially stabilize the Rayleigh-Taylor instability [35]. Inclusion of the shine through electrons in the calculation has the effect that the center of the cloud, closest to the axis of symmetry, preferentially charges due to the spatial variation of the cloud density, which is expected to go like $1/r$ due to symmetry considerations. The resulting radial electric field is then proportional to r, which results in a ExB rotation frequency of the ablation cloud is independent of r, $\omega_{\mathrm{E\,x\,B}} = v_{\mathrm{E\,x\,B}}/r \sim Const.$ i.e. the ablation cloud essentially rotates as a rigid body [34]. The overall depth of the potential barrier is a function of the background electron temperature for this determines what depth of potential is required to balance the ion flux. Thus, as the pellet penetrates into hotter plasmas, the potential well deepens, and the rate of rotation of the cloud increases.

The density gradient in the cloud, denser near the axis and more diffuse at the edge, creates the classic situation for a Rayleigh-Taylor instability where the analog of the gravitational force is provided by the centrifugal acceleration of the ablatant in the frame of the rotating ablation cloud, $F_G \sim {}^{v^2_{E\times B}}/_{r_{cloud}}$. As the rate of rotation increases, the "gravitational" force increases until, at a critical rotation frequency, a low order, $(m = 1)$ shift instability sets in.[3] As the mode grows, it eventually displaces the ablation cloud from the pellet, exposing the pellet to the flux of electrons from the background plasma and causing a burst in the ablation rate, which subsequently reestablishes the full shielding of the ablation cloud. The ejected cloud, now free from the dynamics of the pellet, corresponds to the filaments described in references

[3]The $m = 1$ mode, or shift mode, may not be the dominant mode in the Rayleigh-Taylor instability, and higher order modes could exist as well. According to Parks, the $m = 1$ modes was explored because of evidence of its importance from magnetic mirror experiments [36], and because the $m = 1$ mode is the only mode that could displace the cloud from the pellet.

[31, 24], and the variation in shielding to the pellet, caused by the ejection of the ablation cloud, gives rise to observed fluctuations in the ablation rate.

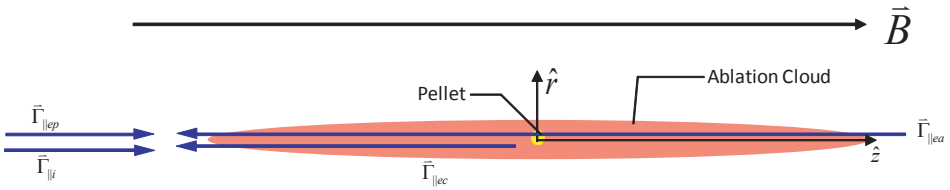

Figure 2-5: Schematic of the ablation cloud, pellet and the relevant fluxes for determining the electrostatic potential in the ablation cloud. $\vec{\Gamma}_{\|i}$:background plasma ions; $\vec{\Gamma}_{\|ep}$:background plasma electrons; $\vec{\Gamma}_{\|ec}$:cloud emitted electrons; $\vec{\Gamma}_{\|ea}$: attenuated shine through electrons from the background plasma.

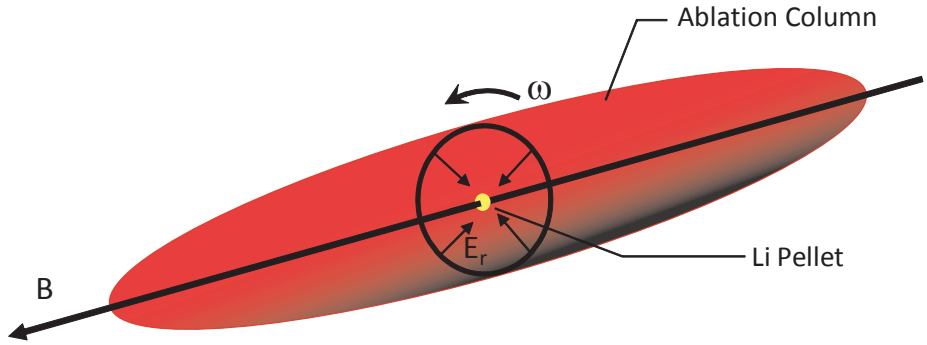

Figure 2-6: Schematic of the ablation cloud, showing the radially directed electric field and the direction of ExB rotation of the ablation cloud.

2.3 Plasma Response

The injection of a solid pellet into a tokamak plasma is associated with a wide array of observed plasma responses. The following survey is intended to provide the reader with a taste of the phenomena which may play a part in the evolution of the pellet material after deposition including temperature and density effects, MHD activity and poloidal rotation.

2.3.1 Temperature and Density Effects

The most obvious result of the injection of a solid pellet into a magnetically confined plasma is the near stepwise increase in electron density and drop in the electron temperature. Shown in figure 2-7 is an example of the time histories of the line integrated density, and electron temperature during a lithium pellet injection in Alcator C-Mod. As can be seen, the injection of the lithium pellet results in an increment in the electron density of approximately a factor of two, with a corresponding drop in the electron temperature [4]. In general, pellet injection is nearly globally adiabatic, meaning that the total thermal energy of the plasma is the same just prior to and just after the injection. As can also be seen in figure 2-7, after the injection the plasma temperature and density return to their nominal values in approximately 100 ms.

Pellet injections are also associated with a non-local plasma response in the form of a cold front which propagates radially in front of the pellet [11]. On Tore Supra the cold front was measured to move ahead of the pellet at a speed of $\approx 25\,{}^{km}/_{s}$ Even more surprising, when the cold front is still outside the $q = 1$ surface, a temperature depression forms on the plasma axis and propagates outward, creating a hollow temperature profile [37]. This behavior is not universally observed, though an increase in the speed of the cold front is often observed as the front passes the $q = 1$ surface [10].

[4] Although the GPC data indicates that the electron temperature drops essentially to zero, this is only a result of the extremely high electron density. The extremely high density causes the plasma frequency to temporarily surpass the local electron cyclotron frequency, and cut off the signal to the GPC. Temperature measurements from Thomson scattering, which has extremely fast time resolution but a low duty cycle, indicate that the temperature drops by approximately a factor of two.

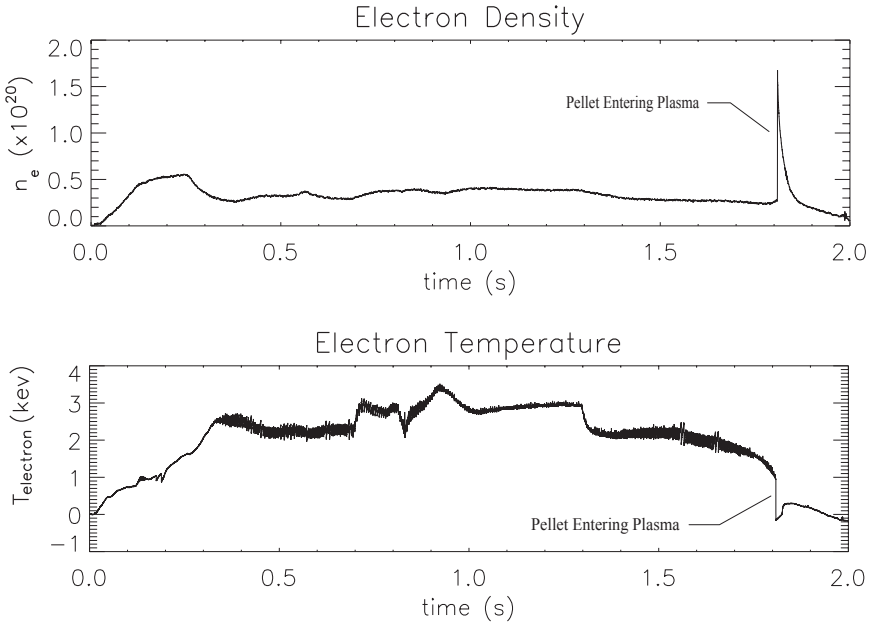

Figure 2-7: Time trace of line integrated electron density from TCI (upper) and electron temperature from GPC. Note the injection of a lithium pellet at $t \sim 1.8$s

2.3.2 MHD Activity

Additionally, it is observed that there is a general increase in the level of MHD activity during a pellet injection. The increase in MHD activity is usually coincident with the arrival of the pellet material at a flux surface, but usually does not persist beyond $\sim 100ms$ after the injection. Simulations have shown that injections on the low field side of the torus tend to be more perturbative than high field side injections because the pressure perturbation caused by the pellet is localized in a region of bad magnetic curvature and thus can give rise to ballooning instabilities [38, 39]. Measurements have also been made indicating that pellets can cause tearing instabilities when the ablatant reaches low order rational surfaces ($q = 2, {}^3/_2$, etc...). One of the more striking effects of pellet injection on MHD concerns the suppression of sawthooth oscillations. Studies on the pellet's interaction with the $q = 1$ surface indicate that pellets that penetrate close to the $q = 1$ surface, but that do not cross it, cause a reduction in sawtooth activity while pellets that penetrate past the $q = 1$ surface can cause the formation of magnetic islands [40]. Additionally, the formation of magnetic islands is also believed to be responsible for the appearance of unusual oscillations in the soft X-ray emissivity, termed *snakes*, seen at the $q = 1$ and $q = {}^3/_2$ surfaces on numerous machines including JET [41], Tore Supra [42], and Alcator C-Mod [43]. The island, which is believed to be formed by localized cooling at the $q = 1$ surface by the pellet, traps a portion of the ionized pellet material, leading to a density perturbation of 25-140% of the background density.

Another feature common during pellet injections into H-mode plasmas is the appearance of Edge Localized modes (ELMS), which are MHD events in the pedestal region of the plasmas [10]. It is most likely that the ELMs are driven unstable by the large pressure perturbation at the edge caused by the pellet. Although the pellet is globally adiabatic, i.e., the integrated plasma pressure over the total volume of the plasma remains constant, there are local variations in the pressure during pellet injection away from the initial plasma pressure profile prior to the injection. When the pellet enters the plasma it causes a large drop in the local plasma temperature

and a massive increase in the plasma density. Differences between the rate of particle and energy transport result in a local non-adiabatic evolution of the plasma pressure, leading to a hollow pressure profile, with larger pressures and pressure gradients at the edge; the ELM is triggered when the pressure gradient exceeds the ballooning limit [10]. Figure 2-8 shows an example of the pressure profile on Alcator C-Mod just before, red, and 40ms after, blue, a pellet injection.

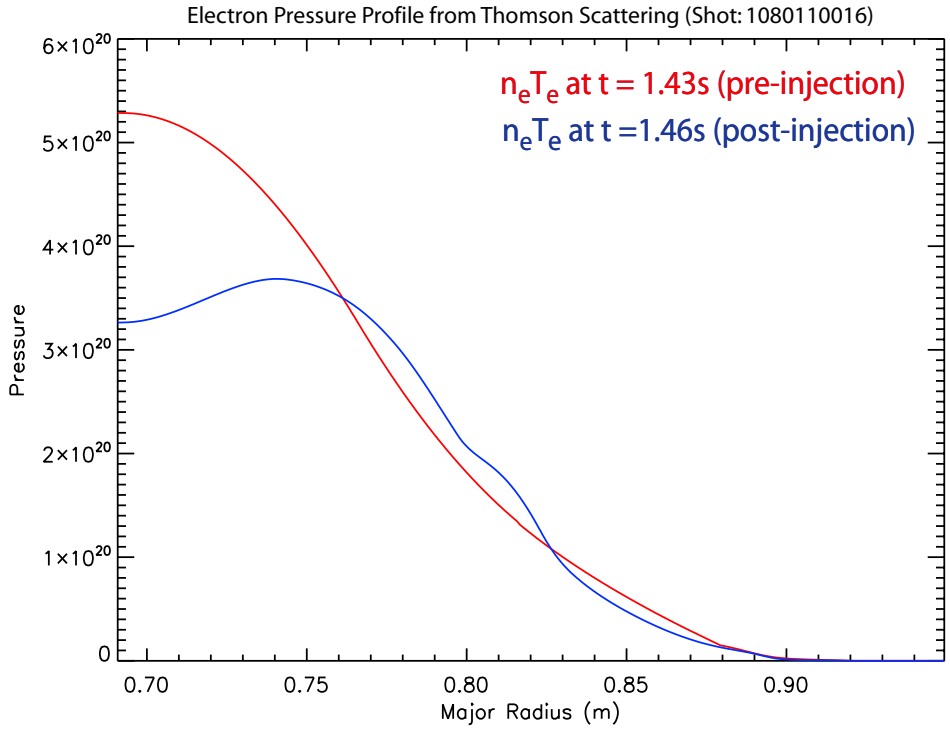

Figure 2-8: Pressure Profiles from Thomson Scattering just prior (red) and just after (blue) a lithium pellet injection on Alcator shot 1080110016. The pressure profile is the product of the Thomson density and temperature profiles

2.3.3 Poloidal Rotation

Numerous pellet injection experiments are accompanied by observations of poloidal rotation within the tokamak. For instance the oscillation of snakes, as described in section 2.3.2, is due poloidal rotation of the magnetic island which has trapped the cold ablatant[40, 41]. Similarly, on Tore Supra, poloidal rotation was shown to be necessary to accurately map the ablation rate onto the time history of the line

integrated density measurements for pellet injection [44]. Uniform rotation such as that mentioned above is believed to be a result of a global modification of the plasma electrostatic potential caused by the pellet. Exactly what is causing the change in potential is a matter of debate, but two opposing mechanisms are believed to play a part. In one, the pellet ablatant acts as an electron sink causing the plasma to acquire a positive charge [34]. Such a positive potential would cause the plasma to rotate in the ion diamagnetic direction. The second mechanism results from the difference in temperature equilibration times between the ions and electrons. The electrons, which equilibrate with the background plasma much more quickly than the ions, heat up and leave the ablatant, causing the plasma to acquire a negative potential[44], which would result in the plasma rotating in the electron diamagnetic direction.

A more puzzling form of rotation is observed on HL-1M [45], ASDEX-U [46], and Alcator C-Mod [31], where poloidal drifts in the pellet ablatant are seen to change direction as a function of space and time. The cause of this rotation has not been previously understood, and as mentioned in chapter 1is the main subject of investigation in this thesis.

Chapter 3

Plasma Flow

The observation of fluctuating poloidal drifts in the filaments formed during pellet ablation as observed on several fusion devices suggests that by studying the evolution of the filaments' motion one could gain insight into the structure and evolution of flows within the tokamak plasma. The subject of plasma flow, the mass weighted average motion of particles in the plasma, is a matter of intense interest in the fusion community due to its capacity to regulate turbulent transport in the plasma. In this chapter I give a brief explanation of the mechanism by which flow can help regulate turbulent transport, outline the mechanisms by which flow can be generated, and finally describe Zonal Flows, an important class of poloidal plasma flow.

3.1 Plasma Flow and Turbulence Suppression

In the early decades of fusion research, plasma confinement, and hence fusion energy production, were severely limited by transport due to small scale turbulent fluctuations [35]. Driven by the temperature and density gradients required for confinement, this transport appeared to pose an unavoidable obstacle to the success of the fusion program. Then, in the early 80's, during high power operation of the ASDEX tokamak [47], the first transport barrier was observed. In the region of the transport barrier, the thermal and particle transport are reduced by orders of magnitude, in some cases down to the minimum level set by collisions. As a result the energy and

particle confinement times increase and the temperature and density profiles steepen. Since their initial discovery, transport barriers have become a ubiquitous feature of fusion research, and have been observed on a wide variety of plasma confinement devices including limited and diverted tokamaks [48], current-less stellarators [49], and mirror machines [50].

Flow shear is believed to be the dominant mechanism in the formation of plasma transport barriers. In particular, poloidal flows have been shown to play an important role in the early stages of the transition to H-mode[51], and magnetic breaking techniques on DIII-D show a clear spatial and temporal correlation between the change in transport and the change in ExB flow shear [52, 51]. Spontaneously induced rotation shear suppresses turbulence leading to a temporary reduction in transport. During this time, the density and temperature profiles steepen until power balance is again reached, resulting in higher pressure gradients and longer confinement times[35]. The shear in flow velocity acts to reduce transport in two basic ways, through the stabilization of the micro-instabilities that give rise to turbulence and through the decorrelation of turbulent flows.

3.1.1 Stabilization of Micro-instabilities

The basic premise behind the notion that sheared flow can stabilize micro-instabilities rests on the idea that the flow distorts the fluid faster than the rate at which energy can be released from the free energy source into the instability. The conventional expression of this condition is,

$$\gamma_{\mathrm{E\times B}} > \gamma_{micro} \tag{3.1}$$

Where $\gamma_{\mathrm{E\times B}} = \frac{r}{q}\frac{\mathrm{d}}{\mathrm{d}r}\left(\frac{qE_r}{rB}\right)$ is the ExB shearing rate and γ_{micro} is the larger of the instability growth rate, and the real frequency of the unstable mode.

An example of this form of turbulent suppression results in the so called Dimits Shift [53]. The onset of ITG turbulence is controlled by the parameter η_i, the ratio of the inverse ion density gradient scale length, $L_{n_i}^{-1} = \frac{\mathrm{d}\ln n_i}{\mathrm{d}r}$, to the inverse ion

temperature gradient scale length, $L_{T_i}^{-1} = \frac{\mathrm{d}\ln T_i}{\mathrm{d}r}$. Numerical studies examining the anomalous thermal diffusivity show the onset of ITG turbulence in the absence of ExB shear occurs at a threshold, $\eta_i^{threshold}$, that is significantly below the threshold, $\eta_i^{\mathrm{E\times B}}$, found in the presence of robust ExB flow shear, thus indicating that the flow shear stabilizes the linear ITG instability [54]. The difference between the threshold in the absence of shear flow, $\eta_i^{threshold}$, and the threshold in the presence of ExB flow, $\eta_i^{\mathrm{E\times B}}$ gives the phenomena its name, Dimits Shift.

Though useful for heuristic arguments concerning the levels at which shear becomes important, calculations have shown that the criteria in equation 3.1 is not, in general, a reliable quantitative threshold for the stabilization of linear instabilities [35].

3.1.2 Decorrelation of Turbulent Flows

The primary mechanism by which shear flow acts to regulate turbulent transport is through the decorrelation of the flows generated by the turbulence. What follows is a heuristic and physically intuitive model as outlined by Terry in reference [35]. For a more in-depth discussion, as well as more rigorous derivations, I direct the reader to that excellent review.

We begin by examining the nature of turbulence. In a neutral fluid the evolution of flow is governed by the Navier Stokes Equation[1] [55].

$$\frac{\partial \vec{u}}{\partial t} + (\vec{u}\cdot\vec{\nabla})\vec{u} = \frac{1}{\rho}\vec{\nabla}p + \mu\nabla^2\vec{u} \tag{3.2}$$

Where $\vec{u}$ is the fluid flow velocity, ρ is the mass density, p is the pressure and μ is the viscosity. Examination of the above equation reveals two time scales, an inertial time scale associated with the advection of the fluid, $\tau_{inertia} \sim l/u$, and a dissipative time scale due to the viscosity, $\tau_{vis} \sim l^2/\mu$, where l is the spatial scale of the turbulent dynamics. Because turbulence has vorticity, $\vec{\omega} \equiv \vec{\nabla}\times\vec{u}$, the turbulent flow can be thought of as a hierarchy of vortices, or eddies, in which the energy of

[1]The evolution of vorticity for the Navier-Stokes equation in two dimensions can be shown to be isomorphic to the evolution of the electrostatic potential in a magnetized plasma [35]

the fluid motion of individual vortices is exchanged through their advection of, and by, other vortices. In numerical simulations of plasma turbulence, eddies appear as radial elongated structures, termed *streamers*, (see figure 3-1).

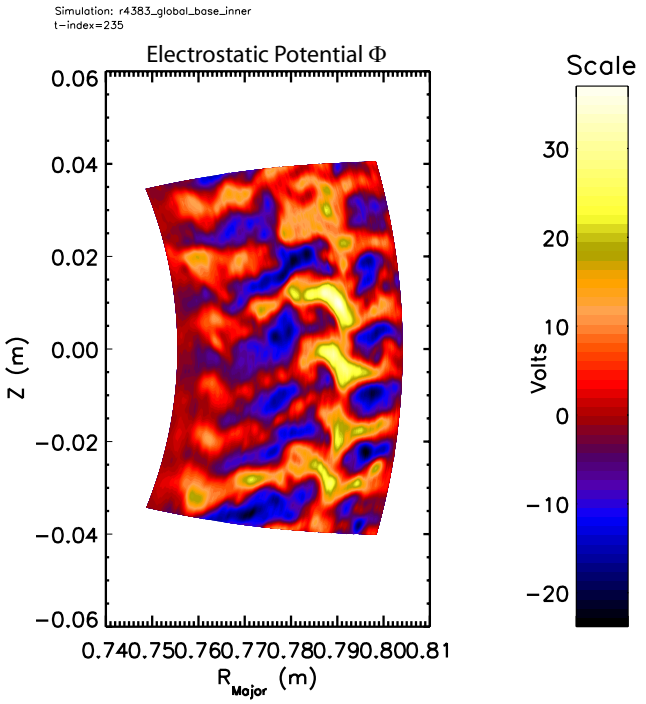

Figure 3-1: Example of streamers-radially elongated structures-in a poloidal cross section of fluctuating potential from a nonlinear global GYRO simulation of a C-Mod plasma. The electric field is perpendicular to contours of constant potential, and the resulting ExB drifts will thus be parallel to the contours. Thus, the streamer is effectively a free path for charged particles to move across the equilibrium flux surfaces.

As the cascade proceeds to smaller scales, the viscous time scale, which goes as l^2, decreases faster than the inertial time scale of the advection, which goes like l. Thus at large scales, the energy cascade essentially proceeds without loss, while at smaller scales energy is drained from the cascade in the form of heat from viscous damping. The scale at which the inertial time is comparable the dissipative time is known as the Kolmogorov Scale. In steady state conditions, energy considerations require that the turbulent cascade adjusts itself so that the energy flow through all scales of vorticity are equal and also equal the dissipation rate at the smallest spatial scales.

Turbulent eddies also act to increase thermal and particle transport by effectively increasing the step size and rate in the diffusive random walk[2] For a plasma, in the absence of turbulence the particle random walk is governed by collisions, and thus the step size is of the order of the Larmor radius at high collisionalities, or the banana orbit width at low collisionalities, and the rate is determined by the collision frequency. In contrast to this, in the presence of turbulent flows, the random walk is determined by the advection of fluid elements in the turbulence. Imagine a cluster of particles in a fluid packet that is part of a turbulent eddy. They will remain part of that eddy until it is advected by another eddy[3], at which time the fluid packet will become part of the new eddy. Thus the effective step size is increased to the eddy width, and the rate is determined by the eddy turn over time-the time an eddy will continue to exist as a coherent structure until advected by another eddy.

The eddy correlation length is the distance over which the eddy flow remains correlated. In turbulent flow, in the absence of mean flow shear, advection by other eddies is the primary cause of decorrelation. The correlation length can thus roughly be thought of as the distance between eddies. As mentioned above, the life time of an eddy is roughly equal to its turn over time, the time it takes to complete one revolution, since this is time that we can expect the eddy to remain correlated before it is decorrelated by interaction with other eddies.

Now imagine that one superimposes a laminar flow, $\bar{u}(y)$, which varies transverse to its direction, on the turbulent eddy, (see figure 3-2). This flow will distort the eddies, causing them to stretch. After a period $\tau_{shear} \sim \delta x/\bar{u}_y \delta y$ the sheared flow will stretch the eddy beyond its correlation length in the direction parallel to the flow, where $\bar{u}_y$ is the spatial derivative of the background flow in the transverse direction, δy is the eddy scale in the transverse direction and δx is the eddy scale length in the direction parallel to the background flow. In the case where the shear time is

[2]Recall that for particles undergoing diffusive random walk, the diffusivity, $\underline{\chi}$, relates the transport flux of a scalar quantity to its gradients. For thermal energy this is $\vec{Q} = -\underline{\chi}\vec{\nabla}p$, where $\vec{q}$ is the heat flux. From the properties of a random walk, we expect that the diffusivity goes like $\chi \propto \lambda^2/\tau$, where λ is the step-size of the random walk, and τ is the time between steps

[3]Advection refers to the process whereby the fluid motion of a nearby eddy destroys the coherent structure of the original eddy.

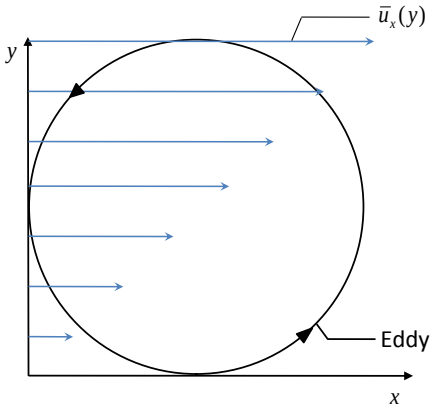

Figure 3-2: Above is shown an eddy in a laminar flow whose velocity varies transverse to the flow direction. The blue arrows represent the mean flow.

shorter than the turnover time, $\tau_{shear} < \tau_{inertial}$, the eddy looses it coherence due to the flow shear before advection from other eddies, (see figure 3-3). The eddy scale in the transverse direction is thus reduced to $\delta y_s \sim \sqrt{\tilde{v}_y^{(s)} \delta x / \bar{u}_y}$, where $\tilde{v}_y^{(s)}$ is the shear modified turbulent flow in the transverse direction. The eddy correlation time is also modified to be consistent with the shear, $\tau_{inertial}^{(s)} \sim \delta y_s \bar{u}_y / \delta x = \sqrt{\tilde{v}_y^{(s)} \bar{u}_y / \delta x}$. Together, these combine to modify the transverse turbulent diffusion coefficient to $D_y^{(s)} \sim {\delta y_s}^2 / \tau_{inertial}^{(s)} = \sqrt{\tilde{v}_y^{(s)} \delta x^3 / \bar{u}_y^3}$. The precise effect of the shear flow on the turbulent diffusion requires a information on the effect of the shear on the turbulent drive, and thus on the transverse turbulent flow $\tilde{v}_y^{(s)}$. Neglecting the shear effect on the transverse turbulent flow, the result is a decrease in the turbulent diffusivity, $D_y^{(s)} \sim \bar{u}_y^{-3/2}$, and a reduction in the heat and particle transport associated with the turbulence.

In unmagnetized fluids, the presence of a strongly sheared flow can drive instabilities, such as the Kelvin-Helmholtz instability, and thus increase turbulent diffusion[4]; in fusion plasmas such flow driven instabilities are stabilized by shear in the magnetic field [56]. In general there are three criteria that must be met for turbulence

[4]The shear driven Kelvin-Helmholtz instability is an example of the caveat mentioned in the previous paragraph regarding the effect of the shear on the turbulent transverse flow, $\tilde{v}_y^{(s)}$.

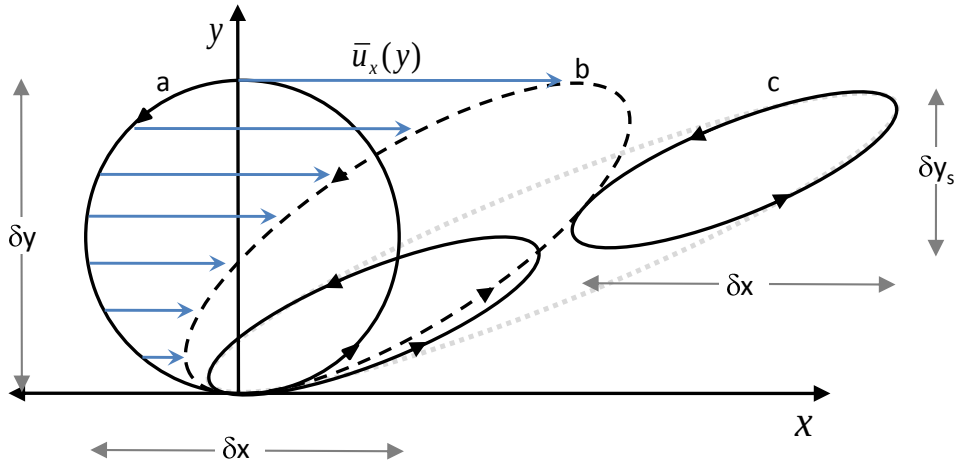

Figure 3-3: The evolution of a turbulent eddy in a sheared flow. Curve a: the original eddy prior to shearing. Curve b: the eddy after some time interval. The blue arrows represent the mean flow, and show the motion of the fluid elements from curve a to b. Curves c: stretched beyond its coherence length, the eddy breaks up into two smaller eddies, whose dimensions are δx and δy_s

to be suppressed by shear flow [35]: the dynamics must be two dimensional[5]; the shear flow must be stable (ie not suffering from flow driven instabilities like K-H); and the turbulence must remain in the domain of the flow shear longer than an eddy turn-over time, so that the flow shear can cause sufficient distortion of the turbulent flow pattern. If these criteria are not met, the flow shear will drive turbulence, rather than suppress it.

3.2 ExB Flow

ExB drifts play a special role in plasma dynamics. Independent of charge and mass, the ExB drifts allow the plasma to flow as a unified body and under most conditions

[5]The requirement for two dimensional dynamics rests on the effects of flows that run parallel to the axis of the vortices, and that increase as you move away from the vortex. The variation in flow causes a stretching of the vortex tube, and, due to conservation of vortex volume, a decrease in the cross-sectional area. For an inviscid flow (one without viscous losses) invariance of circulation, $\oint \mathbf{u} \cdot d\mathbf{l} = Const$, means that the decrease in area requires an concomitant increase in vorticity. This amplification process is three dimensional in nature and not applicable to tokamak plasmas.

ExB drifts represent the only advecting flows in a plasma [35]. Since the magnetic field can be regarded as a known quantity to lowest order, determining the ExB flow revolves around determining the radial electric field inside the plasma[6]. Radial electric fields can generally be determined from the ion radial force balance equation:

$$E_r = \frac{1}{Z_i e n_i}\frac{\partial}{\partial r}p_i + \frac{m_i}{Z_i e}\vec{\nabla}\cdot\left\langle \tilde{\vec{u}}_i \tilde{u}_{ri} \right\rangle - u_{\theta i}B_\varphi + u_{\phi i}B_\theta \tag{3.3}$$

The components of the Reynolds stress, $\left\langle \tilde{\vec{u}}_i \tilde{u}_{ri} \right\rangle$, can be neglected in determining mean flows, but become important when fluctuations are large. This possibility will discussed more in the following paragraphs. Neglecting the Reynolds stress, the radial electric field is determined by the balance between the radial pressure gradient and the poloidal and toroidal flows crossed with the magnetic field.

Equation 3.3 is the fundamental relation for determining the radial electric field, and thus the ExB flow. Understanding the drive behind each of the terms on the right hand side of equation 3.3 require the introduction of additional relations. The pressure gradient term can be understood as a connection to the heat flux through the thermal diffusivity:

$$Q_i = -\chi_i \frac{\partial p_i}{\partial r} \tag{3.4}$$

where Q_i is the radial heat flux, and χ_i is the thermal diffusivity. The steeper density and temperature gradients resulting from turbulence suppression thus result from the decrease in the thermal diffusivity. Similarly, the ion flow velocities can be understood from momentum balance relations. For a species, j, the momentum balance is given by,

$$m_j n_j \left(\frac{\partial}{\partial t}\vec{u}_j + \vec{u}_j\cdot\nabla\vec{u}_j\right) = Z_j e n_j \left(\vec{E} + \vec{u}_j \times \vec{B}\right) - \nabla\cdot\bar{\bar{\mathrm{P}}}_j\vec{R}_j \tag{3.5}$$

where $\vec{R}_i$ is the momentum exchange between species and $\bar{\bar{\mathrm{P}}}_j = \bar{\bar{\Pi}}_i + p\bar{\bar{\mathrm{I}}}$ is the total pressure tensor [6]. Combining the electron and ion equations, to eliminate the

[6]We only need to know the radial component since confinement requires that **B** and the ExB flow lie in a flux surface.

momentum exchange and electric field terms gives:

$$m_i n_i \left(\frac{\partial}{\partial t} \vec{u}_i + \vec{u}_i \cdot \nabla \vec{u}_i \right) + m_e n_e \left(\frac{\partial}{\partial t} \vec{u}_e + \vec{u}_e \cdot \nabla \vec{u}_e \right) = \frac{1}{n_i} \left(J \times B - \nabla p \right) - \frac{\nabla \cdot \bar{\bar{\Pi}}}{n_i} \quad (3.6)$$

where $\vec{J} = e(Z_i n_i - n_e)$. The electron inertial term, $m_e n_e (\frac{\partial}{\partial t} \vec{u}_e + \vec{u}_e \cdot \nabla \vec{u}_e)$, is usually neglected since $m_e/m_i \ll 1$. The physical mechanisms that drive mean flow act through the terms in equation 3.6.

Reynolds stress arises from the advective derivative in equation 3.6. For an incompressible flow with no external currents, the resulting flow equation takes the form [57]:

$$\frac{\partial \langle u_{\theta i} \rangle}{\partial t} = -\frac{\partial}{\partial r} \left[\langle \tilde{u}_{ri} \tilde{u}_{\theta i} \rangle - \frac{1}{m_i n_i \mu_0} \left\langle \tilde{b}_r \tilde{b}_\theta \right\rangle \right] - \mu_\theta \langle u_{\theta i} \rangle \quad (3.7)$$

where μ_θ is the neoclassical poloidal flow damping which results from ion-ion collisions and poloidal variation in the magnetic field[7]. In a torus, with toroidal symmetry, there is no viscous damping of the toroidal flow. The quantity in the square brackets is the generalized Reynolds Stress. From its form, its can be seen that the Reynolds Stress effects the transfer of energy from the chaotic turbulent flows to the equilibrium flow. Furthermore, as can be seen in equation 3.7, in a toroidal plasma the balance between Reynolds stress and viscous damping determines the radial transport of poloidal flow.

In order to understand the mechanism that allows the Reynolds Stress to rearrange momentum, it is helpful to consider an example which is more familiar to fusion researchers, the transport of particles due to electrostatic fluctuations. The radial particle flux can be written $\Gamma_r = n v_r$, where n is the particle density and v_r is the radial flow velocity. We break the density and flow into equilibrium, $\{\langle n \rangle_t, \langle v_r \rangle_t\}$ and

[7]The source of the neoclassical viscosity for poloidal flow can be understood in terms of magnetic pumping due to conservation of the magnetic moment of the ions. As the poloidal flow carries a flux tube from the low field side to the high field side, conservation of magnetic moment, $\mu_B = v_\perp^2/2B$, along with conservation of energy, requires an increase in the perpendicular velocity of the ions. Due to ion-ion collisions, the parallel and perpendicular velocity components rapidly equilibrate, and during this relaxation process, the ordered poloidal motion is converted to the thermal motion of the ions [58]

fluctuating $\{\tilde{n}, \tilde{v}_r\}$ pieces, where $\langle ... \rangle_t$ represents an average over times long compared to the time scale of turbulent fluctuations, but short compared to the dynamical time scale of the system, such that $\langle v_r \rangle_t = 0$, in accordance with radial confinement. In this case the lowest order non-zero time averaged particle flux is given by $\langle \Gamma_r \rangle_t = \langle \tilde{n}\tilde{v}_r \rangle_t$. Using the fact that the perturbed velocity is due to the ExB drift of electrostatic fluctuations, $v_r \simeq E_\theta / B = -i \sum_k k_\theta \tilde{\phi}_k / B$, the particle flux can be rewritten as,

$$\langle \Gamma_r \rangle_t = Re \left[-iB^{-1} \sum_k k_\theta \left\langle \tilde{\phi}_k \tilde{n}_{-k} \right\rangle_t \right] \tag{3.8}$$

This is the familiar result that the particle flux due to electrostatic fluctuations is a function of the amplituds of both the fluctuations in density and potential, and the phase between them, being a maximum when the phase difference is $\pi/2$ and zero when $\tilde{n}_{-k}$ and $\tilde{\phi}_k$ are in phase, or π out of phase [35].

Now consider the role of Reynolds stress in the evolution of the mean flow. First, from its form it is apparent that, like the particle transport mentioned above, the transport due to Reynolds stress depends on correlations between the different components of the flow. Expanding the derivative on the right hand side of equation 3.7, we see that the mean flow goes like,

$$\frac{\partial \langle u_{\theta i} \rangle}{\partial t} \sim \left\langle \tilde{u}_{\theta i} \frac{\partial \tilde{u}_{ri}}{\partial r} \right\rangle + \left\langle \tilde{u}_{ri} \frac{\partial \tilde{u}_{\theta i}}{\partial r} \right\rangle \tag{3.9}$$

The first term on the right hand side of equation 3.9 represents the generation of poloidal flow due to divergence in the radial flow, while the second term represents rearrangement of the poloidal flow due to flows in the radial direction. Given these observations, it is not hard to imagine how correlations between the fluctuating components of the electrostatic potential allow flows in the radial direction to "push" around flows in the poloidal direction, thus transforming the chaotic turbulent flows into coherent flows. As a final note, its important recall from momentum conservation, since the fluctuating flows have zero mean, $\langle \tilde{u} \rangle = 0$, the Reynolds Stress only rearranges flow, and does not contribute any net momentum [35].

Due to its dependence on the correlation between two fluctuating quantities which

are difficult to measure, Reynolds Stress is usually not measured in experiment; however numerical simulations, where Reynolds Stress is easily calculated, imply expected flows of sufficient size to decrease turbulent transport [59].

The fluctuating ExB flows resulting from the electromagnetic fields of radio frequency waves can also generate flows through Reynolds Stress. Observations of reduced ion thermal and particle diffusivity on PBX-M [60], and impurity ion poloidal rotation on TFTR [61] in regions of absorption of ion-Bernstien-Waves is strongly suggestive that this process is able to drive poloidal flow shear, though there were no diagnostics available to measure the poloidal flow in those experiments.

Flux surface charging due to orbit losses can drive ExB flows in the edge [62]. This phenomenon arises due to the difference in the poloidal projection of the ion and electron banana orbits. The orbit width, $\rho_\theta = \frac{2u_\parallel m_j}{|e|B_\theta}$, is proportional to the particle mass, and thus the ions are preferentially lost at the edge, and the plasma becomes negatively charged in this region. Mathematically, orbit loss enters the flow equation, 3.7, through the anisotropic pressure term, $\bar{\bar{\Pi}}$ [35]. This process can only produce a radial electric field within one banana orbit of the edge, and is thus intrinsically an edge effect.

3.3 Stringer Flow Mechanism

Poloidal flows are also believed to arise from asymmetries in transport fluxes. Intuitively, one would expect radial electric fields to be generated due to differences in particle losses between ions and electrons, similar to the fields caused by orbit losses described in the preceding paragraph. Losses due to the effects of magnetic ripple, which would preferentially affect electrons due to their low mass, could give rise to positive bias of the plasma and resulting ExB flow.

Additionally, transport fluxes which are asymmetric with respect to the poloidal angle can give rise to poloidal rotation, such as occurs in the Stringer Spin-up [63]. The mechanism is more complicated than the Reynolds Stress, requiring coupling between particle fluxes, parallel flows and poloidal rotation. The basic physical mech-

anism, elucidated in reference [64], is driven by the effective gravitational force in the outward major radial direction that a density perturbation experiences as a result of the inhomogeneity of the magnetic field in a toroidal geometry (see figure 3-4).

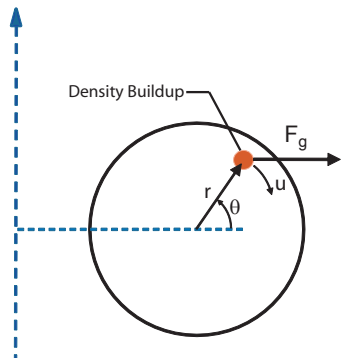

Figure 3-4: A region of excess density feels an outward hoop force F_g, which results in a poloidal flow u.

Neglecting parallel viscosity and diamagnetic effects, it can be shown that a poloidally asymmetric density perturbation, Δn, will evolve in manner similar to the motion of a pendulum, i.e. $\frac{\partial^2 \theta}{\partial t^2} \sim -\frac{2c_s^2}{rR}\left(\frac{\Delta n}{n}\right) sin\theta$, where $c_s = \sqrt{T_e/m_i}$ is the ions sound speed. To understand how this gives rise to a poloidal rotation, consider a poloidally asymmetric density distribution peaked on the low field side of the torus (either from poloidally asymmetric radial transport, or particle source), as shown in figure 3-5. In the absence of other flows, the density buildup will cause diffusive flows parallel to the field in order to smooth out the density distribution. The convergence of the oppositely directed flows will then cause a smaller density buildup on the high field side of the torus.

Suppose this occurs in the presence of a small background poloidal flow. In this case, the poloidal flow will cause the parallel flows, and the resultant high field side density buildup will shift poloidally (see figure 3-6). Regardless of whether the high field side density bulge is pushed above or below the mid-plane, the effective gravitational force exerted on the high field side density buildup will cause it to move along

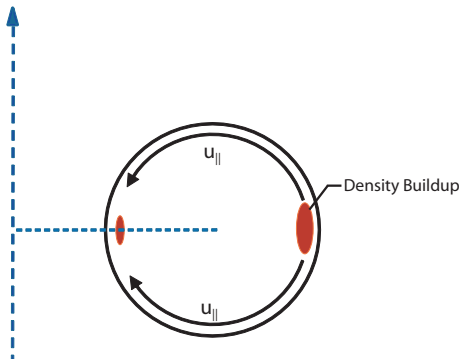

Figure 3-5: Poloidal projection of the parallel flows, $u_{\|}$, resulting from the poloidally asymmetric density distribution.

the flux surface towards the low field side, reinforcing the original poloidal flow.

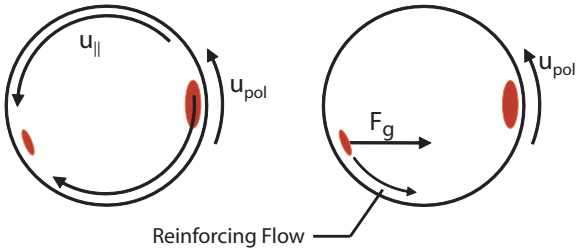

Figure 3-6: Left: Superposition of the background poloidal flow, and the poloidal projection of the parallel flows from the density perturbation. Right: Resulting density perturbation on the high field side, and consequent reinforcing poloidal flow.

3.4 Zonal Flows

In the late 1990's Rosenbluth and Hinton published a landmark paper [65] outlining the existence of a long lived class of $n = 0$ modes. The flows resulting from these modes, termed Zonal Flows, are believed to be the primary regulators of ITG and TEM turbulence in plasmas, which were described in **{introduction }** . They may also play an important role in the L-H transition [66]. These modes come in two

flavors, zero mean frequency (ZMF) modes, for which $\omega \sim 0, n = m = 0$, and finite frequency Geodesic Acoustic Modes (GAM), $n = 0, m = 1$.

3.5 Zero Mean Frequency Zonal Flows

Zero Mean Frequency Zonal Flows are radially localized, poloidally and toroidally symmetric electrostatic fluctuations in the plasma (see figure 3-7). Studies of ITG turbulence have indicated that the radial length of the zonal flows is $\sim 10\rho_i$, though the sensitivity of this to system parameters is not currently understood. As mentioned above, the ZMF spectra consists of a broad peak centered around $\omega_{ZF} = 0$, the width of which indicates a life time of the order $\tau = (\Delta\omega_{ZF})^{-1} \sim \varepsilon\nu_{ii}^{-1}$, where ε is the inverse aspect ratio and ν_{ii} is the ion-ion collision frequency [66]. The magnitude of zonal flows, as predicted from turbulence simulations is typically over the order $10^{-2}\sqrt{\frac{T_i}{m_i}}$ [67].

ZMF Zonal flows are primarily in the poloidal direction with $v_\theta = -E_r/B$, but due to the toroidal geometry of a tokamak plasma, and the resulting inhomogeneity of the magnetic field, an uncompensated poloidal rotation would give rise to plasma compression. In order to relieve this compression, there exists a return flow along the field lines, which gives rise to a toroidal flow $v_\phi \sim 2qE_r \cos\theta/B$.

ZMF are believed play a critical role in the regulation of drift wave turbulence. Observed during numerical simulations of ITG and TEM driven turbulence [68] they are generally considered to be the primary source of ExB flow shear suppression of turbulence[66]. In principle, any low-n modes can shear shorter wavelength turbulence, however, ZMF play a special role because of their properties. First, because they are $n = 0$, $k_\parallel = 0$, ZMF's effective inertia goes like $q_r^2\rho_s^2\tilde{\phi}_q$, as opposed to $(1 + k_\perp^2\rho_s^2)\tilde{\phi}_k$ for general drift waves. Since $q_r\rho_s \sim k_\perp\rho_s << 1$ large flows can be generated in response to even a small drive. This has the consequence that ultimately a significant portion of the available free energy is deposited in the Zonal Flows [66]. Another important property arising from the $k_{parallel} = 0$ condition, is that ZMFs do not suffer from Landau damping and thus collisions are the only linear damping

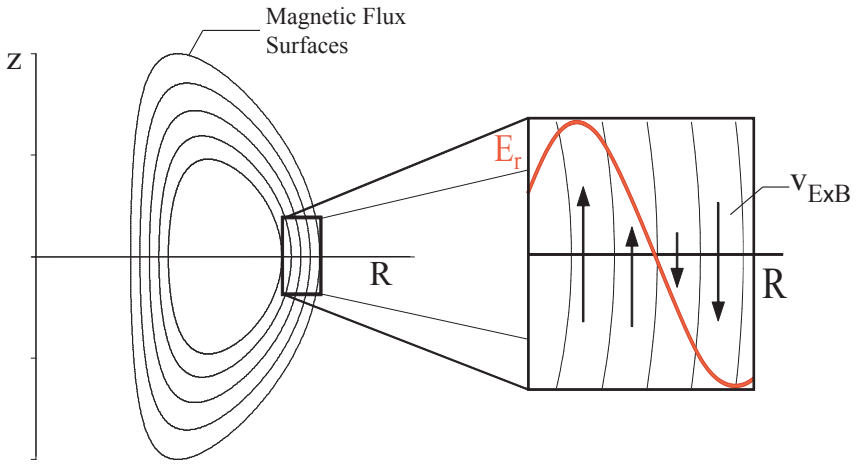

Figure 3-7: Poloidal projection of Zonal Flow. The cut box shows the local variation of the radial electric field and the resulting ExB drifts

mechanism. Finally, due to their toroidal and poloidal symmetry, $\tilde{\phi}_q = \tilde{\phi}_q(r)$, they are intrinsically incapable of driving radial ExB flows.

As a consequence of their poloidal and toroidal symmetry, $n = 0, m = 0$ ZMF can not tap the free energy associated with the temperature and density gradients inside the plasma. Thus ZMF are driven by non-linear interactions that transfer energy from finite-n drift waves.

Rosenbluth and Hinton showed [65] that there exists a component of the axi-symmetric flow that remains undamped by linear collisionless processes. This followed from an analysis of the gyrokinetic equation where the effects of the finite-n drift wave turbulence was treated as a noise source of known properties. The main result is that the initial charge separation that gives rise to the zonal flow potential is partially screened by the polarization of the flux surfaces due to neoclassical effects, in particular the excursions caused by the ion banana orbit. The residual potential, as $t \to \infty$, is given by:

$$\lim_{t\to\infty} \frac{\phi_q(t)}{\phi_q(0)} = \frac{1}{1+\epsilon_{cl}/\epsilon_{neo}} = \frac{1}{1+1.6\varepsilon^{-1/2}q^2} \tag{3.10}$$

where ϵ_{cl} is the classical polarization due to the gyro orbit and ϵ_{neo} is the neoclassical polarization due to the banana orbits. This residual represents the lower limit to which Zonal Flows will decay in a collisionless plasma, not a saturated level they will reach. To determine saturation amplitudes, the only tool currently available is large scale numerical simulation of the gyrokinetic equation, such as GS2 [69, 70] and GYRO [71].

ZMF are believed to exist in a self consistent state with the turbulence that generates them, and which they suppress. This is similar to a predator-prey model, in which the predator both regulates the prey's population, and is in turn regulated by that population. Consider the simplified model of the ZMF-Drift Wave system presented in reference [66], which is absent any form of non-linear damping mechanism for the the ZMF Zonal Flows,

$$\frac{\partial \langle N \rangle}{\partial t} = \gamma_L \langle N \rangle - \gamma_2 \langle N \rangle^2 - \alpha \left\langle U^2 \right\rangle \langle N \rangle \tag{3.11}$$

$$\frac{\partial \langle U^2 \rangle}{\partial t} = \gamma_{damp} \left\langle U^2 \right\rangle + \alpha \left\langle U^2 \right\rangle \langle N \rangle \tag{3.12}$$

where $\langle N \rangle$ & $\langle U^2 \rangle$ are the energy in the Drift Wave spectrum and Zonal Flows respectively, γ_L & γ_2 are the drift wave linear growth rate and non-linear damping rate, γ_{damp} is the Zonal Flow collisional damping rate and the energy exchange between the Drift Waves and Zonal Flow is mediated by the $\alpha \langle U^2 \rangle \langle N \rangle$ term.

Importantly, in the case with moderate collisional damping, $0 < \gamma_{damp} < \alpha\gamma_L/\gamma_2$, as would be expected in high-temperature fusion plasmas, we end up in a state where the zonal flows coexist with the Drift-Wave spectrum, $\langle N \rangle = \gamma_{damp}/\alpha$ and $\langle U^2 \rangle = (\gamma_L - \gamma_2\gamma_{damp}\alpha^{-1})/\alpha$. The level of the drift wave turbulence is set by the collisional damping of the zonal flows, and thus, one might expect that as the collisionality drops, the flow pattern of the plasma will be increasingly dominated by the coherent poloidal flows of the ZMF at the expense of the chaotic flows of the turbulent spectrum. This feature in particular may be important with respect to the drift of filaments formed during lithium pellet injections, since an intact filament that the

result of advection by a coherent flow will probably be easier identify and measure than one which is torn apart by turbulence.

The non-linear damping mechanism of the Zonal Flows is currently a matter of intense research. Strong non-linear damping is probably the reason that the $n = 0$ and $n > 0$ fluctuating components of the electrostatic potential do not usually show the characteristic oscillation of a predator-prey model. If the Zonal Flow amplitude saturates via the non-linear mechanism when there is very little driving turbulence, then a slight drop in drift wave amplitude would not result in a drop in ZMF amplitude. Possible mechanisms for the non-linear saturation include the trapping of drift waves by the zonal flows, excitation of tertiary instabilities which dissipate Zonal Flow Energy, and quenching of zonal flow drive by modification of the drift wave spectrum.

3.6 Geodesic Acoustic Modes

GAMs were first described in late 1960's by Winsor [72], and have since been observed on a large number of plasma containment devices [73, 74, 75]. In the original formulation, GAMs were described as a linear combination of an ion acoustic wave propagating along the magnetic field and an integral of the product of a density fluctuation and the geodesic curvature of the magnetic field on a flux surface. Thus their appellation as an acoustic wave driven by the geodesic curvature. GAMs are a ubiquitous low frequency phenomenon with $n = 0, m = 1, k_{\|} \neq 0$, which arise in toroidal plasmas due to poloidally symmetric fluctuating radial electric fields. Thus GAMs are connected to ZMF Zonal Flows through a coupling between the $m = 0$ ZMF Zonal Flows and $m = 1$ side bands [66]. Because $k_{\|} \neq 0$ GAMs produce electro-static fluctuations along field line, the adiabatic electron response, $\tilde{n}_e = n_0 \frac{e\tilde{\phi}}{T}$, generates large density fluctuations[8], $\sim 25 - 40\%$ [73].

[8]The large density fluctuations produced by GAMs are in stark contrast to the near absence of density fluctuations in ZMF. Because $k_{\|} = 0$ for ZMF, the potential variation caused by the ZMF is uniform along a magnetic field line. The electrons must move across flux surface to respond to the change in potential, and thus are not able to respond rapidly.

The GAM oscillation occurs because the effects of torodicity imply that the plasma can not be symmetric in the poloidal direction, one example is the magnetic field strength on a flux surface, which goes as $B \sim B_0/\left(1+\epsilon\cos\theta\right)$ in a circular plasma. Thus the flows generated by the ZMF mode's poloidally symmetric radial electric field, $\tilde{\mathbf{v}}_\perp = \tilde{\mathbf{E}} \times \mathbf{B}(\theta)/B^2(\theta)$ are not poloidally uniform due to the inhomogeneity of the magnetic field. The divergence of this flow leads to a density accumulation, which goes like $\frac{\partial \tilde{n}}{\partial t} \sim \nabla \cdot \tilde{\mathbf{v}}_\perp$, in turn generating a current, $\tilde{J} = \mathbf{B} \times \nabla \tilde{n}/B^2$, that acts to reduce $\tilde{E}_r$ [72]. Detailed calculations in toroidal geometry yield the GAM frequency:

$$\omega_{GAM}^2 \simeq 2c_s^2/R^2(1+\frac{1}{2q^2}) \tag{3.13}$$

Because of the nonzero component of the wave vector along the field line, GAMs are subject to much stronger damping than ZMF Zonal Flows. The condition for Landau damping on passing particles, whose poloidal transit frequency match the GAMs frequency, implies a resonance condition with the passing ions, $v_\parallel \simeq qR\omega_{GAM}$. The consequence of this resonance condition can be seen by considering the behavior of the q-profile and the distribution of ion velocities. Since the q-profile is usually a monotonically increasing function of minor radius, and the width of the ion distribution function a decreasing function of minor radius, $v_{T_i} = \sqrt{T_i/M_i}$, the number of particles in which to damp decreases with increasing q. The net result is that GAMs are the most weakly damped on the outside edge of the plasma, and hence have the largest amplitude on the low field side of the tokamak. A detailed calculation of the collisionless landau damping rate shows that damping of GAMs goes like $\gamma_{GAM} \sim -\omega_{GAM}\, \mathrm{e}^{-q^2/2}$ [76, 66].

3.7 Conclusion

Is important to remember that the primary goal this thesis is to test the hypothesis that the poloidal drifts observed in the filaments formed during pellet injections are a results of background flows within the plasma. The above mentioned sources of plasma flow, RF driven flows from Reynolds stress, Stringer spin-up, ZMF Zonal

Flows, and GAMs, constitute most probable drivers of poloidal flow and will form the basis of our interpretation of the experiments in the following sections.

Chapter 4

Pellet Imaging Experiment

4.1 Introduction

The following chapter concerns the pellet injection experiments that were used to characterize the properties of the filaments formed during the ablation of lithium pellets injected into Alcator C-Mod. The aim of these experiments were two fold; to determine if the motion of the filaments formed during lithium pellet ablation were indeed moving primarily in the poloidal direction, and to make a broad survey of the trajectories of the filaments under a variety of plasma conditions. The later objective, cataloging the filament trajectories, was compelling in its own right in order to fully document a phenomenon which had remained unexplored up to this point, but also serves as a useful source of information for a comparison of the filament properties with the inferred properties of turbulent ExB flows within the plasma as determined by nonlinear gyrokinetic simulations.

To accomplish these combined objectives, a stereo imaging diagnostic was designed, constructed and installed on B-port of the Alcator C-Mod tokamak. The stereo imaging diagnostic was used in conjunction with a fast framing PSI-IV CCD camera and the lithium pellet injector to obtain detailed measurements of the three dimensional evolution of the trajectories of filaments formed during lithium pellet injection. What follows will include a brief discussion of the experimental setup, including design, calibration and operation of the stereo imaging system, the analysis

techniques using the raw images, an overview of the experimental data set, and results from the analysis.

4.2 Lithium Pellets

Lithium was chosen as the impurity injection species for these experiments due to its physical and atomic properties. Lithium is the lowest Z impurity that can be formed into a solid pellet at room temperature. Lithium's low atomic number ensures that in the post pellet plasma, which is dominated by the injected impurity, the increase in radiated power, which proportional to Z_{eff}, will remain relatively low. Furthermore, lithium is a low-recycling impurity, and is only observed in the plasma immediately following the injection.

Additionally, fabrication of the pellet is facilitated by lithium's extreme softness. The approximately cylindrical pellets are formed by "punching" them out cookie-cutter fashion from a 2.5 mm thick metallic foil using stainless steal hypodermic tubing with an inner diameter of 1 mm. The dimensions of the pellet were chosen such that the pellet would be large enough to penetrate to the plasma axis but small enough not to cause a disruption. A general rule-of-thumb is that the pellet should contain approximately the same number of electrons as the target plasma, which for Alcator C-Mod is $\sim 10^{20}$[77].

4.3 Lithium Pellet Injector

The Lithium Pellet Injector (LPI) used to inject the pellets for these experiments was designed and constructed by Darren Garnier[77]. The injector is a multi-barrel single stage pneumatic gun capable of firing up to three pellets at independent times throughout a single plasma discharge. The hydrogen gas propellant is controlled through a series of high pressure fast valves capable of producing 1 ms bursts at pressures of $300 - 1000$ psi; accelerating a standard sized pellet to velocities of $500 - 1000$ m/s. Except during firing, the entire system is kept under vacuum, to prevent

leakage into the torus, and to protect the lithium pellets stored in the magazine from chemical decomposition.

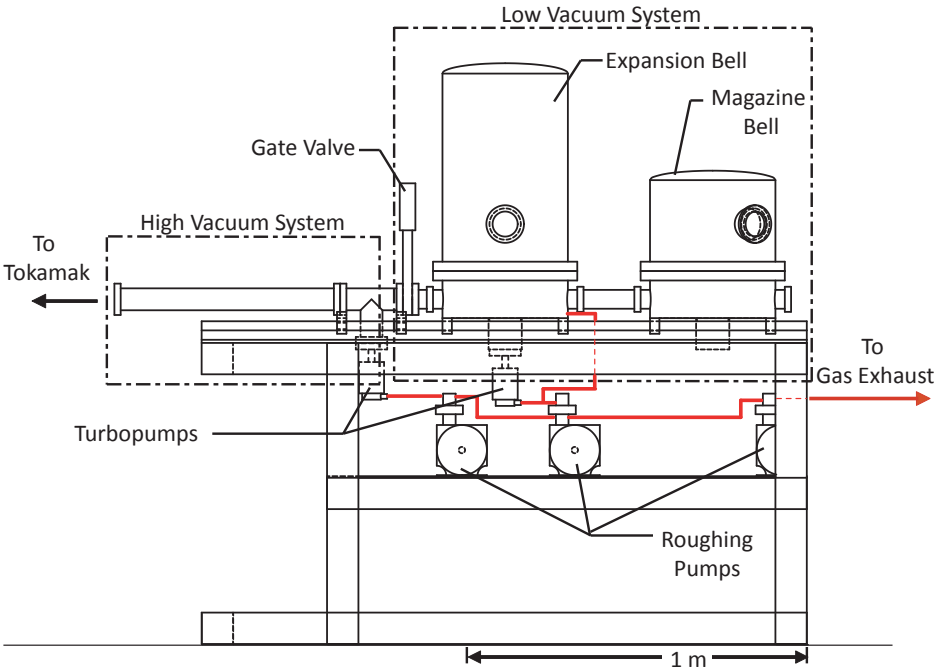

Figure 4-1: Schematic of Lithium Pellet Injector, designed and constructed by Darren Garnier [77]

In order to control the flow of propellant gas during injection, the injector is subdivided into two segments, a low and a high vacuum subsystem. The first segment is low vacuum, base pressure of 10^{-5} Torr, and houses the high pressure fast valves for the propellant, the pellet magazine, and the guide tubes. It acts as an expansion chamber to reduce the pressure of the propellant, which exits the guide tube at a small gap located in the second bell jar, after it has accelerated the pellets. This segment has a total volume of $\sim$ 350 L, and is composed of two stainless-steel bell jar vacuum vessels connected by a small pipe, see figure 4-1. The pressure in the low vacuum segment is maintained by a turbomolecular pump, capable of pumping 210 L/s at the base pressure, backed by a 453 L/s rotary vane roughing pump.

The second segment of the injector is a high vacuum system which acts as a buffer between the injector and the tokamak. This segment is maintained at a base

pressure of approximately 10^{-7} Torr by a 45 L/s turbopump. The high vacuum system interfaces with the previously mentioned low vacuum segment on one end and the tokamak on the other via the pellet guide tubes, which have a very low conductance (< 1 L/s). Additionally, communication between the high-vacuum system and both the low vacuum system and the tokamak can be eliminated by gate valves located between the systems. In standard operation, the gate valves remain closed until just prior to injection. Thanks to the turbopump and the low conductance guide tubes, the high vacuum system can be maintained at a pressure two orders of magnitude lower than that of the low-vacuum system while the gate valves open. Additionally, little or no change ($< 10^{-6}$ Torr) in the torus base pressure can be detected during the injection.

4.4 PSI-IV Fast Framing CCD

The PSI-4 camera, constructed by Princeton Scientific Instruments, is a high speed, solid state digital imaging system capable of rates ranging from $100-500$k frames/sec. This speed is achieved by storing the data on the 18.4×9.2 mm (160×80 pixel) imaging sensor's internal memory array. As the frames are acquired the internal memory array is filled by shifting data packages down the array stack. When the array is filled, the oldest elements are dumped in a first-in first-out manner. For the PSI-4 a total of 28 frames can be held in the internal memory. Acquisition is terminated based on an external signal, in our case a photo-diode filtered to observe neutral lithium emission from the pellet injection, after which the data from the internal array is read out at a much slower rate (~ 3 seconds) to the camera control computer to minimize readout noise. A mechanical optical shutter is used to block light during the readout process. The data acquisition allows from 0 to 28 pre-trigger frames to be retained, giving additional flexibility in capturing the dynamics of the pellet ablation process.

4.5 Pellet Imaging Diagnostic

A schematic of the pellet imaging diagnostic on B-horizontal is shown in figure 4-2. The pellet imaging diagnostic consists of two 24 mm canon lenses mounted approximately 9.5 inches above and below the mid-plane on B-horizontal. The lenses have a field of view of approximately 9°, and are oriented such that their lines-of-site approximately cross at the same location the pellet trajectory crosses the mid-plane. Each lens sits on a kinematic optical mount that gives an additional adjustment of $\pm 2°$ in its orientation. Each lens views the plasma through a 2 inch diameter window mounted in the port. Due to the mounting optics, the lenses sit $\sim$ 2 inches beyond the window through which they view the plasma, but this additional aperture does not limit the field of view of the lens, or cause substantial vignetting of the image. For all experiments the lenses were focused on the inner wall, with the f-stop set at its minimum level. This resulted in a depth of focus sufficient to keep the ablating pellet in focus for the entire time it was within the plasma.

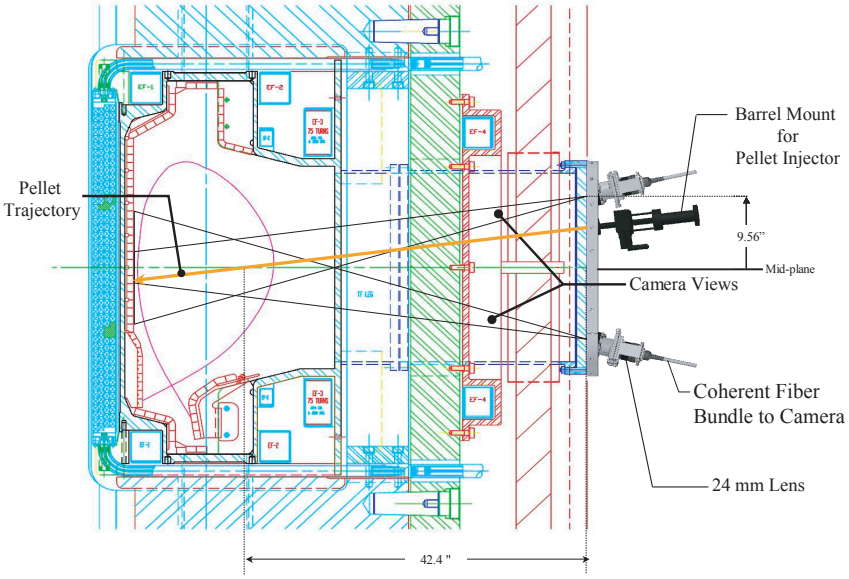

Figure 4-2: Schematic of the Pellet Imaging Diagnostic on B-port. Each lens has a field of view of $\sim$ 9° and is inclined to the horizontal $\sim$ 12°. The barrel mount is connected to the pellet injector via a low throughput guide tube, and the images from the lenses are passed to the CCD camera via the coherent fiber bundles.

The view from each lens is imaged onto one of the arms of a bifurcated 4 mm $\times$ 4 mm image preserving coherent fiber bundle mounted at the focal plane of the lens. The bifurcated fiber bundle consists of two legs, each 152 cm long and carrying a single coherent bundle, and a 25.4 cm common branch joining the two legs side-by-side to form a 8 mm $\times$ 4 mm bundle. The 2-to-1 aspect ratio of bundle is then imaged onto the 160 $\times$ 80 pixel CCD of the fast framing PSI-IV camera as shown in figure 4-3. The choice to image the views from both lenses onto the same CCD was motivated by two factors; first, by transferring the images from the lenses via the fiber bundles, and imaging them on the same CCD, we were assured of simultaneity, a feature that is essential for the success of the stereo imaging procedure to determine three dimensional data; second we only had access to one fast framing camera.

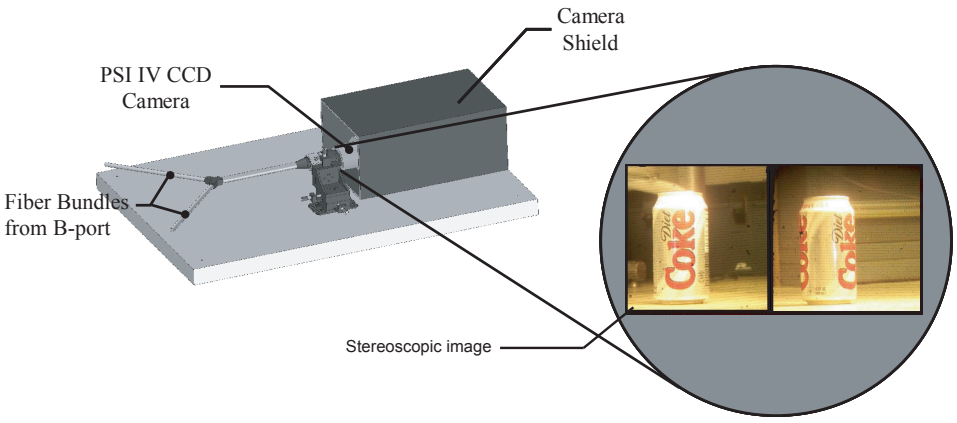

Figure 4-3: Schematic of PSI-IV-fiber bundle interface showing the imaging of two views of a Coke® can. The shown image was not taken using the PSI-IV camera (which only has a resolution of 160 $\times$ 80, but rather was taken using a 5 Mpixel digital camera.

4.5.1 Calibration of Stereo Imaging System

The mechanics behind determining three dimensional positions from stereo images is quite straight forward, the exact details of which can be found in Appendix A.

The method relies on using the views from two well defined reference locations to determine the location of a point of interest. Determining the location of the point of interest is thus dependent upon an exact knowledge of the physical properties of the imaging system. For the our system on Alcator C-Mod, we identified 16 parameters, eight for each view, neccesary to map locations in the two images of the stereo system to locations in the lab. These parameters are the three coordinates associated with the lens' location, $\vec{X}_{lens}$; the three euler angles associated with the lens' orientation, (α, β, γ); and two parameters, (ϵ_1, ϵ_2), respectively characterizing the magnification and distortion of the lens.

In order to minimize systematic errors in the analysis, the calibration of the stereo imaging system was performed *in situ*. In theory, one could determine all sixteen calibration parameters for the stereo imaging system by performing a large least squares regression of known calibration data. Unfortunately, due to the limited spatial extent available to collect calibration data inside the torus, this sort of analysis is almost intractable. For example, in this situation, where there is only $\sim$ 30 cm of depth, it is extremely difficult to distinguish a small horizontal displacement of a lens from a small rotation about the vertical axis. Thus as far as possible the different elements of the stereo imaging were characterized independently.

Lens Position

The most straight forward parameters to determine for the Pellet Imaging Diagnostic were the locations of the top and bottom lenses. Since the position of the port, and the layout of objects on the port are well known, $\vec{X}_T$ and $\vec{X}_B$ were determined by mounting the lenses prior to the port's installation on the machine, and measuring their location relative to the center of the port. Using a simple tape measure $\vec{X}_T$ and $\vec{X}_B$ could be determined to within an accuracy of less than a millimeter.

Characterization of Lenses

The magnification and distortion of the lenses were characterized independently of the other parameters of the imaging system. The setup for the calibration is shown

in figure 4-4b. Reference points were produced from a flat rectangular piece of G-10 which had grid of horizontal and vertical groves cut at 1 inch intervals. A 3×2 inch mirror was then mounted in the center of the calibration grid in order to align the lenses. The lenses were mounted on an optical rail, and adjusted so that the line of site of the lens peered into the alignment mirror, and directly into the center of the mirror's image of the lens, ensuring that the optical axis of the lens was perpendicular to the surface of the mirror and the grid. Using the image of the grid as a reference frame, the location of the intersection of the line of site of the lens with the grid could be determined, as well as the relative orientation of the lens, about its line of site. Together, these two pieces of information, along with the distance of the lens from the grid, could be used to determine the angle subtended from the optical axis of the lens to the intersection of any two grid lines that fell within the view of the lens. Figure 4-4a shows an image taken during the characterization of the bottom lens, including the normalized fiber frame, and the vector δ which points from the origin of the fiber frame to the calibration point depicted in figure 4-4b

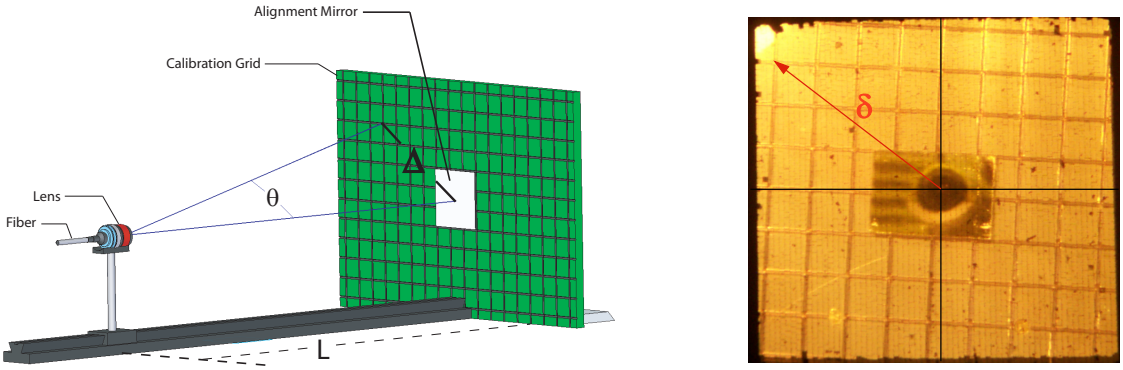

(a) Lens Characterization Setup

(b) Characterization Image

Figure 4-4: (a) Setup for lens characterization. $\tan\theta = \Delta/L$, where L is the distance from the lens to the grid and Δ is the distance on the surface of the grid from the optical axis to the image point, which can be determined from the grid spacing. (b) Sample image from the characterization of the bottom lens. Equation A.7 relates the normalized fiber frame quantity δ to the quantities Δ, L and θ.

By varying the distance between the lens and the calibration grid, a large number of calibration points could be collected in a relatively short period of time. Figure

4-5 shows the resulting analysis for the top and bottom lenses, and the corresponding parameters, $\{\epsilon_1, \epsilon_2\}$ characterizing the lenses.

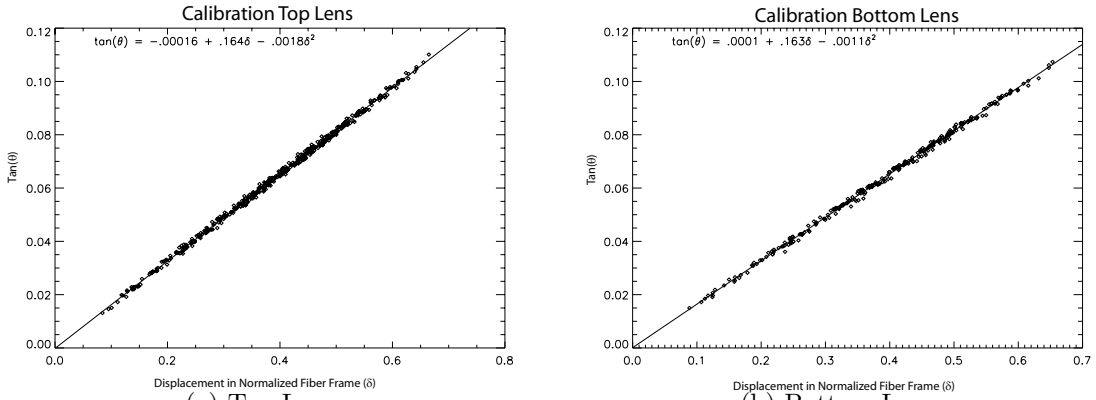

(a) Top Lens (b) Bottom Lens

Figure 4-5: Lens characterization data for top (a) and bottom (b) lenses

In Situ Calibration

The last six parameters of the stereo-imaging system, the Euler angles determining the orientation of the top and bottom lenses, are difficult to measure reliably, and as a consequence were determined through an in-vessel calibration. The calibration consisted of viewing a large number of points of known position through the stereo-imaging system and comparing the measured position of those points in the fiber frame to the calculated positions that would appear for a given set of Euler angles. If we let $\mathbf{X}_i^{exp}$ be the actual measured position in the fiber frame of the i^{th} measured point and $\mathbf{X}_i^{cal}(\alpha, \beta, \gamma)$ be expected location of the point in the fiber frame as calculated from its known position in space and the lens parameters, then a global fit parameter can be defined as the sum of the absolute values of the differences between $\mathbf{X}_i^{exp}$ and $\mathbf{X}_i^{cal}(\alpha, \beta, \gamma)$,

$$\Psi = \sum_{i=1}^{N} \left| \vec{X}_i^{exp} - \vec{X}_i^{cal}\,(\alpha, \beta, \gamma) \right| \tag{4.1}$$

The optimal choices of Euler angles, (α, β, γ), for each lens are those that minimize the fit parameter Ψ.

The calibration apparatus consisted of a 7×7 planar array of red LEDs, with a 1 inch grid spacing and single green LED, to be used as a reference point, at the center. The array was constructed on a movable hanger, which could be attached to a spar that was cantilevered from the inner wall of the tokamak as shown in figure 4-6. The spar was placed on the inner wall in such a manner that the LED array's middle row was at the same elevation as the plasma mid-plane, and the middle column was aligned with the center of B-horizontal. During the calibration the hanger was sequentially moved along the spar from a major radial position of $R = 37.4$ inches to $R = 44.4$ inches in half inch increments. At each position along the spar a digital photograph was taken of the LED array using the stereo-imaging system, which was then used for computer analysis. Figure 4-7 shows an example of the raw images and the resulting calibration data.

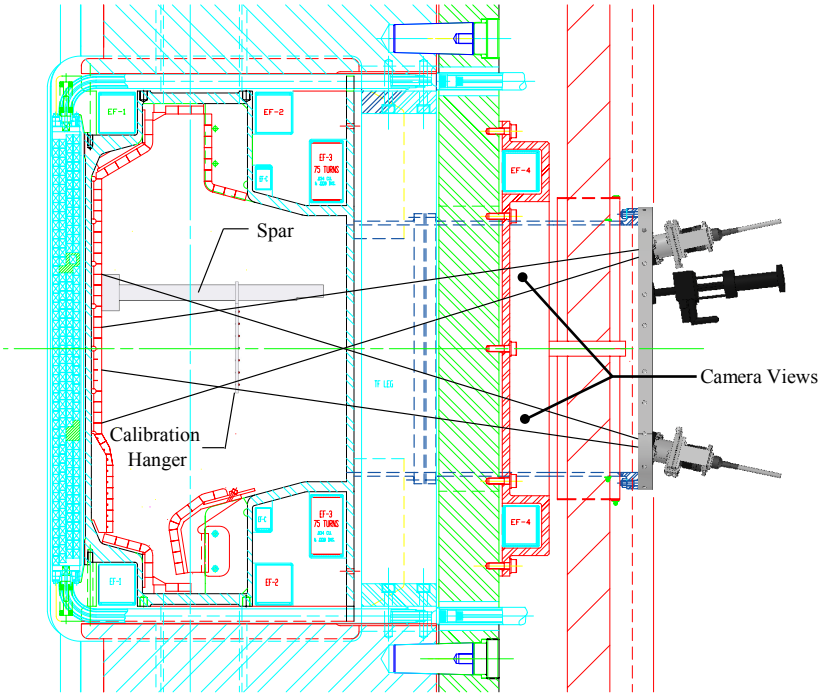

Figure 4-6: Diagram of in vessel calibration of the stereo imaging system.

Since the calibration had to only be done once every campaign, and thus the computational time was not a major concern, minimization of the fit parameter Ψ was effected by scanning the parameters on a regular grid. Ψ was calculated on a

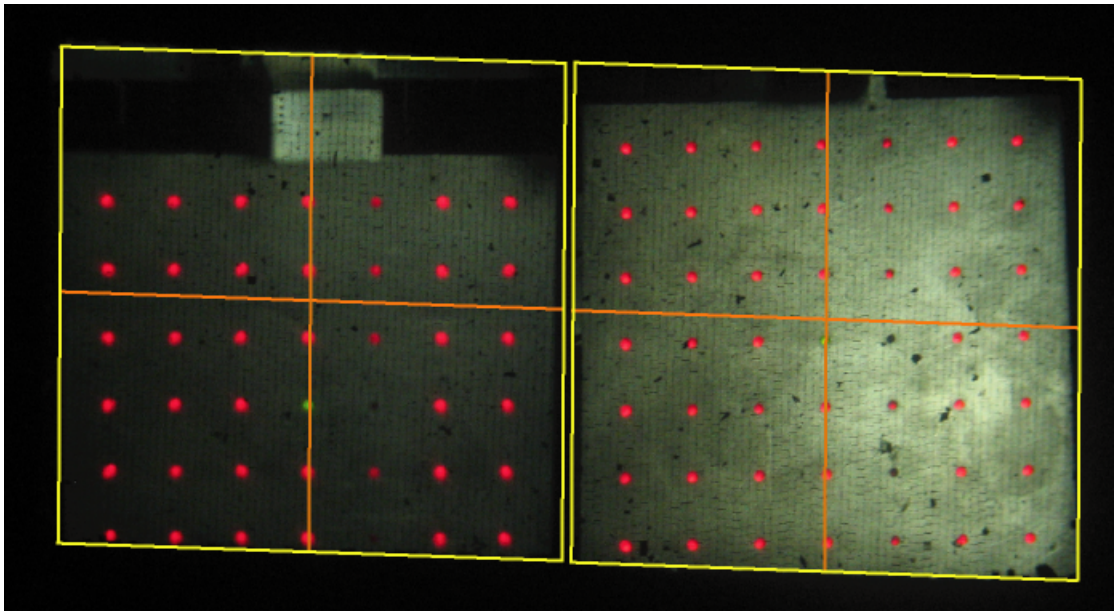

(a) Calibration Image

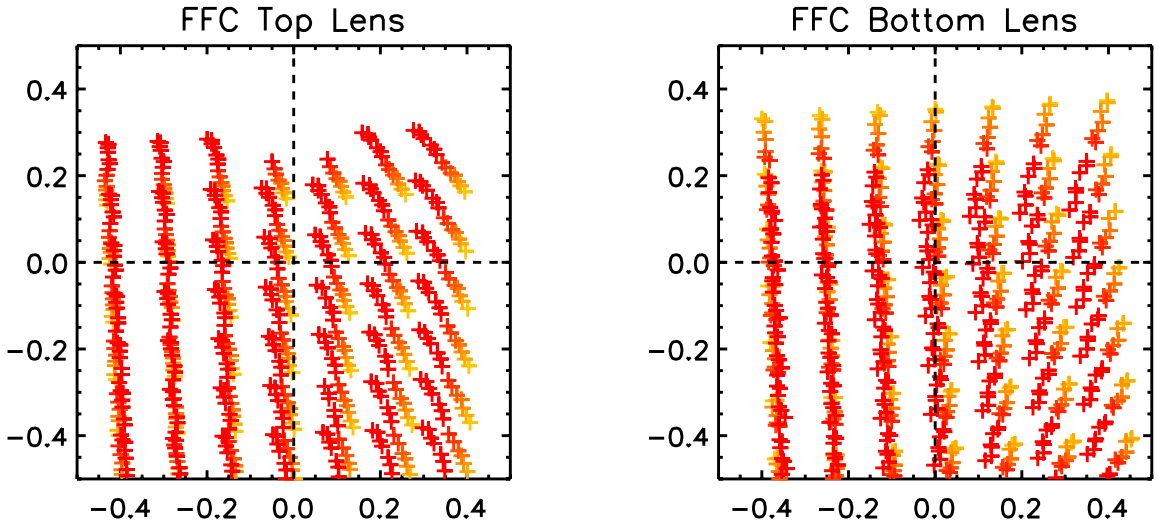

(b) Calibration Data

Figure 4-7: (a) Example of a image from the in-vessel calibration of the PID, taken using a 5 Mpixel digital camera. The yellow lines delineate the edges of the fiber bundles. (b) Cumulative calibration data from the in-vessel calibration on 2.23.07. Points of the same color correspond to data taken from the same image, and hence the same hanger position on the spar.

Table 4.1: Pellet Imaging Diagnostic's Calibration Parameters

Year	**2007 (I)**		**2007 (II)**		**2008**	
Parameter	**Top**	**Bottom**	**Top**	**Bottom**	**Top**	**Bottom**
α	$-10.82°$	$13.74°$	$-10.78°$	$13.74°$	$-10.49°$	$13.79°$
β	$-3.29°$	$-2.90°$	$-3.29°$	$-2.90°$	$-3.14°$	$-3.04°$
γ	$-1.98°$	$-2.88°$	$-0.82°$	$-1.06°$	$-0.52°$	$1.13°$
X (cm)	-6.17	-6.29	-5.47	-6.29	-5.47	-6.29
Y (cm)	26.36	-26.57	26.56	-26.57	26.56	-26.57
Z (cm)	192.70	193.81	193.40	193.81	193.40	193.81
ϵ_1	.164	.163	.164	.163	.164	.163
ϵ_2	-0.002	0.001	-0.002	0.001	-0.002	0.001

rectangular grid in a $500 \times 500 \times 500$ grid in (α, β, γ) space, with a grid spacing of 0.01 degrees. The grid was centered on an initial set of values for α, β & γ which were determined by manually attempting to align the measured positions in the fiber frame coordinates. An example of the results from the scan of parameters are shown in figure 4-8. As can be seen, Ψ is a rather featureless function, i.e., it appears to posses a single minimum which defines the best choice for α, β, and γ. Table 4.1 summarizes the calibration parameters for the 2007 and 2008 campaign.

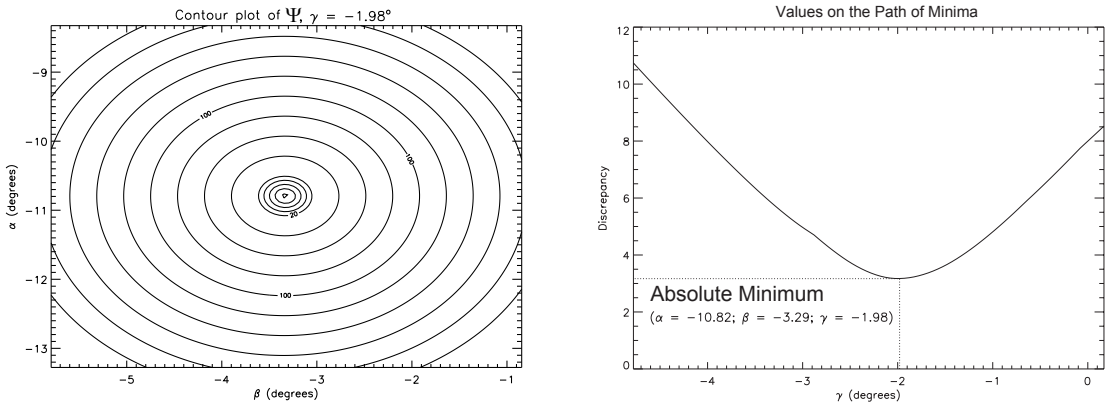

(a) (b)

Figure 4-8: (a) Contour plot of Ψ, as a function of α and β for $\gamma = -1.98°$. (b) Plot of the minimum value of Ψ as determined in the $\alpha - \beta$ scans, as a function of the parameter γ. The absolute minimum shown represents the best choice for the lens parameters. Note, the contours in figure (a) are of the order ~ 100's, whereas the variation along the minimum ranges from 11 to 3.2

4.5.2 Image Analysis

Figure 4-9 is an example of a typical image taken with the stereo imaging system during a pellet injection. As mentioned above, gleaning three dimensional information from the stereo system relies on being able to identify the same point in space in the images from both the top and bottom lenses. The pellet is ideal for this since it is essentially a point source of light easily identifiable in both the top and bottom lenses. In this case the uncertainty is determined by errors in the calibration of the stereo imaging system, the so called cross-eyed error discussed in appendix A, and its position can be determined in absolute terms to within a couple millimeters.

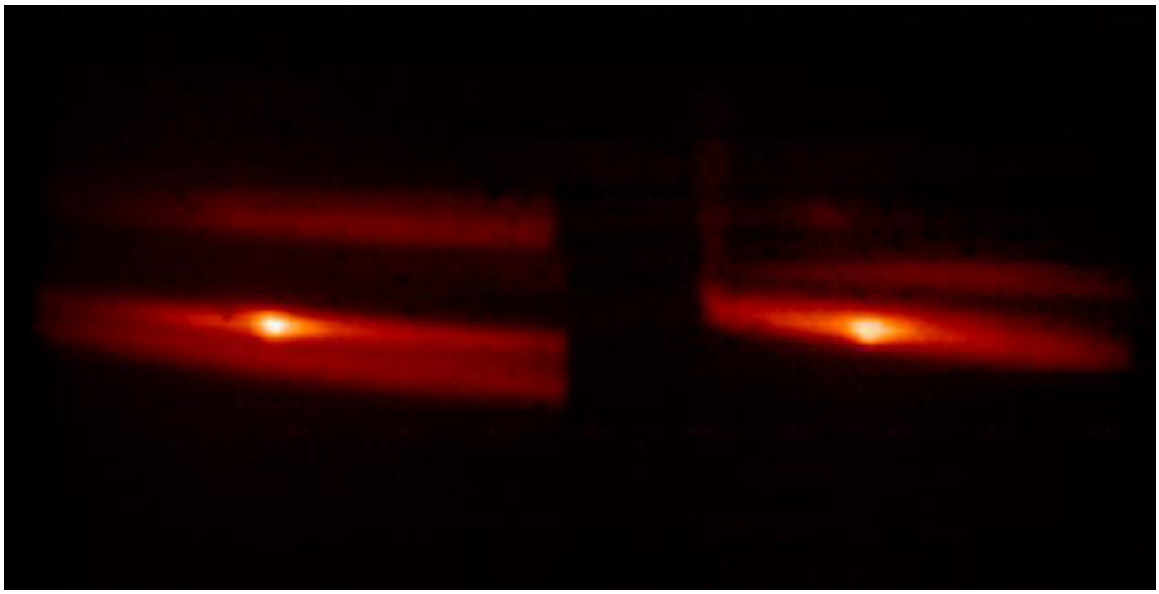

Figure 4-9: Image from shot 1080501011. Image has been processed to bring out its features, in particular what we are seeing is logarithm of the intensity recorded by the CCD above some threshold background value. The display is normalized such that the highest numerical value is represented as white (255) and the lowest as black (0).

The filaments on the other hand, present a much harder problem. First off, the exact geometry of the filaments is not known, and the image is in essence a line integrated measurement of plasma brightness along the line of site of the lens. Figure 4-10 shows an example of the kind of difficulties in that can occur in the interpretation of this kind of measurement. Additionally, the filaments are extended, and largely uniform, along the magnetic field lines making determination of common points in the

different images problematic. In order to treat these difficulties, it was assumed that the filament drift was perpendicular to the local magnetic field direction to lowest order. Thus the filament location can be expressed as its distance from the pellet in a direction perpendicular the local field angle.

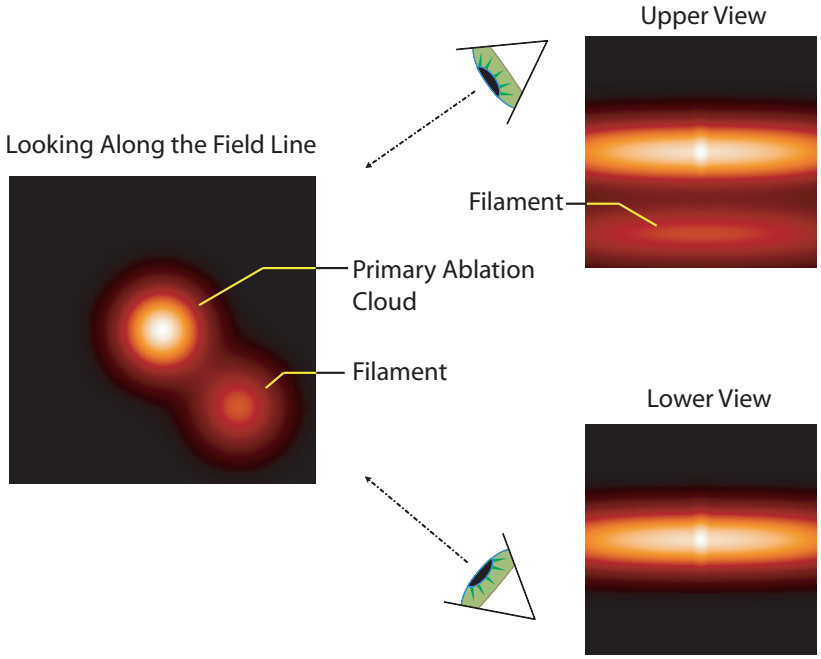

Figure 4-10: Example of the issues with determining the location of the striations. The image on the left is a representation of a filament moving away from the primary ablation cloud in cross section. The images on the right are the resulting views from the top and bottom lens. Because the image is essentially a line integrated measure of the light emission along the line of site of the lens, it is difficult to pinpoint exactly what is a filament, or where it is.

The first step in the analysis is determination of the location of the pellet, which can easily be identified by scanning the image for location of most intense light. The field direction was then determined using a method similar to the maxscan method of reference [46]. Each column of the image was analyzed to determine the location of maximum intensity, which usually occurs at the location of the ionized portion of the ablation cloud. A linear least squares regression was then used to fit these points to a line, the slope of which should be approximately the tangent of the field direction. The image was then rotated by the determined angle about the location

of the pellet so that the ionized ablation cloud and the filament appeared horizontal in the image. The 2D image was then converted to a 1D profile by summing along the rows and subtracting out the background light (ie, subtracting out the constant component from the profile). The profiles were then fitted to a series of Gaussians which matched the intensity profiles of the primary ablation cloud and the filament. The distance between the pellet and the filament in the image, δ, is taken to be the distance between the pellet location in the profile and the centroid of the Gaussian fitted to the filament. The location of the filament is then taken to be the point a distance δ from the pellet perpendicular to the local magnetic field direction, which can be expressed as,

$$(X_{fil}, Y_{fil}) = (X_{pellet} - \delta\cos\theta, Y_{pellet} + \delta\sin\theta) \tag{4.2}$$

where θ is the angle of the local magnetic field in the unrotated image, see figure 4-11

This entire process was automated in order to achieve an acceptable level of objectivity[1] and to vastly decrease the amount of time required for the analysis. Figure 4-11 shows the typical image analysis method for a single lens view. Taken together, the location of the filament in the top and bottom lens yields the measurement of the location of the filament.

Variation of the probable location of the striation on the CCD image, and the resulting variation in the predicted location of the filament in the lab frame, yields a rough estimate of the uncertainty in the location measurement. In the direction perpendicular to the field, and along the magnetic flux surface, the uncertainty runs at approximately 1 cm, but due to the geometry of the stereo imaging system, the shallow angle of convergence of the two views leads to an uncertainty in the radial direction which is ~ 3 cm.

[1]Due to restricted field of view and difficulties with the field of view, the auto-analysis of the images was often over-ridden when obvious errors occurred. In this case quantities like the filament displacement, and the field angle were chosen by hand.

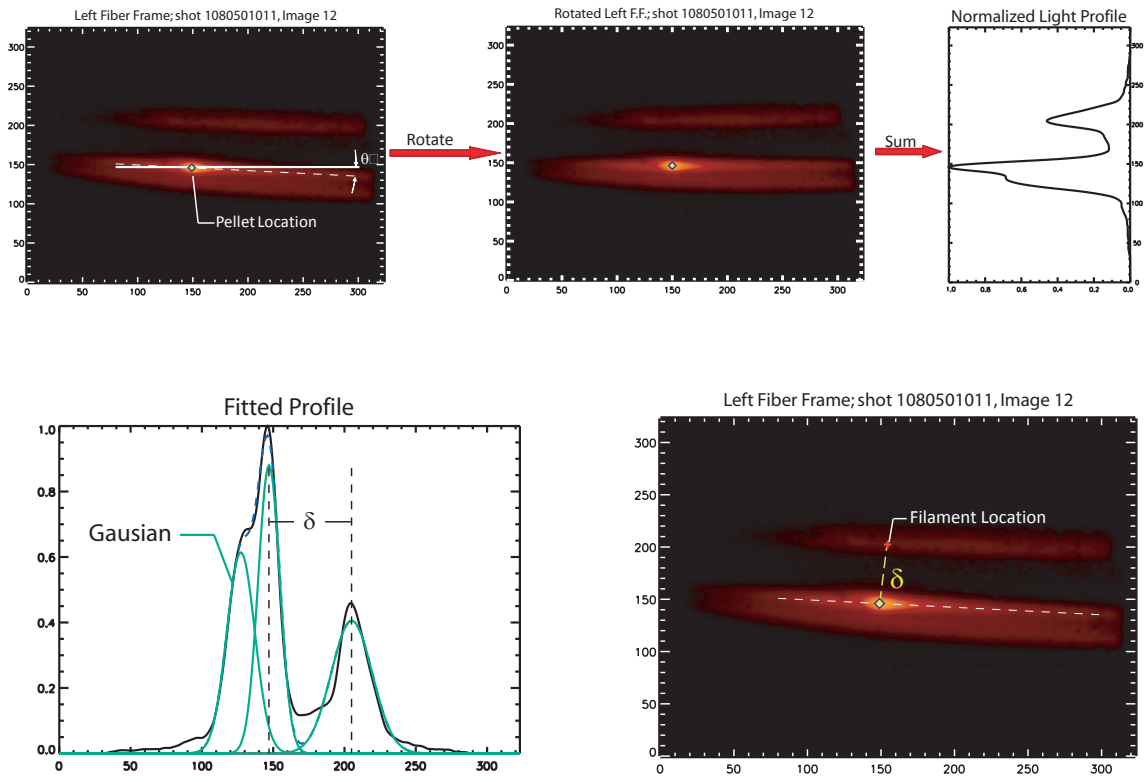

Figure 4-11: Steps in analysis of the ray images. In the top left the pellet location is determined as the brightest spot in the image, and the field angle is determined using the maxscan method [46]. The image is then rotated and summed along the columns to produce a profile of the light intensity on the image. Moving to the lower left, the profile is then fitted using Gaussian to represent the light intensity from the ablation cloud and filament. The distance between the primary ablation cloud and the filament is then taken to be the distance between the centroids of the Gaussians that represent the pellet and the filament of interest. That distance is then used, along with the field angle, to determine the location of the filament as shown in the lower right hand image.

4.6 Experimental Data Set

During the 2007 and 2008 experimental campaigns, images were taken of pellets injected into 122 discharges under a wide variety of plasma conditions. The distribution of the number of filaments observed during each shot is shown in figure 4-12 and ranged from 0 to 10, with an average 2.5 filaments.

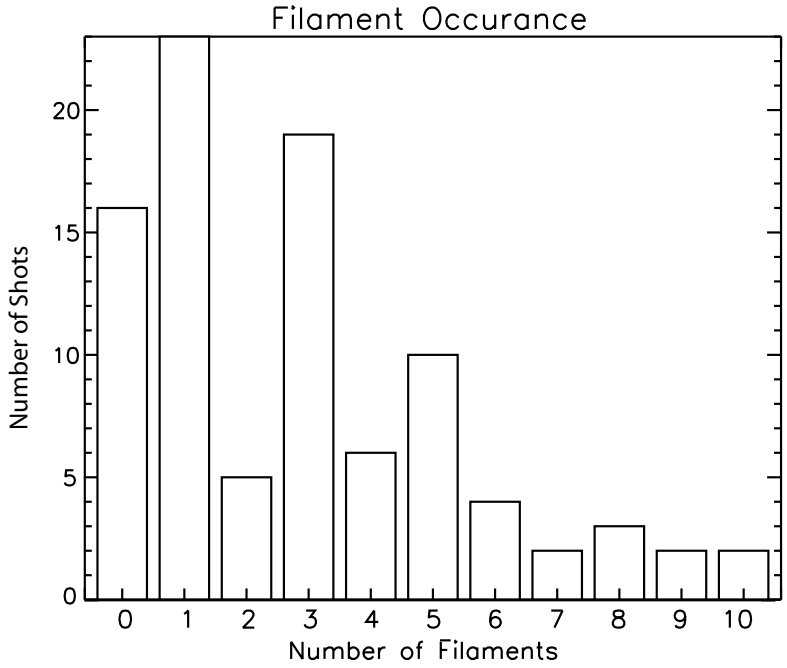

Figure 4-12: Distribution of the number of filaments observed per shot.

Figures 4-13a and 4-13b show an overview of electron temperatures and densities for the data set. Each line segment in the plots indicates electron density, and temperature profiles just prior to the pellet injection as determined by Thomson scattering[2].

From these data, the trajectories of 306 filaments were tracked using the stereo imaging system. Figure 4-14 shows an example of the trajectories determined on a typical discharge where the flux surfaces are determined from an EFIT [78] magnetic reconstruction. The yellow dots represent the location of the pellet in one of the

[2]For discharges in which Thomson scattering was not available, temperatures were taken from ECE and densities were approximated from the line averaged density determined by TCI

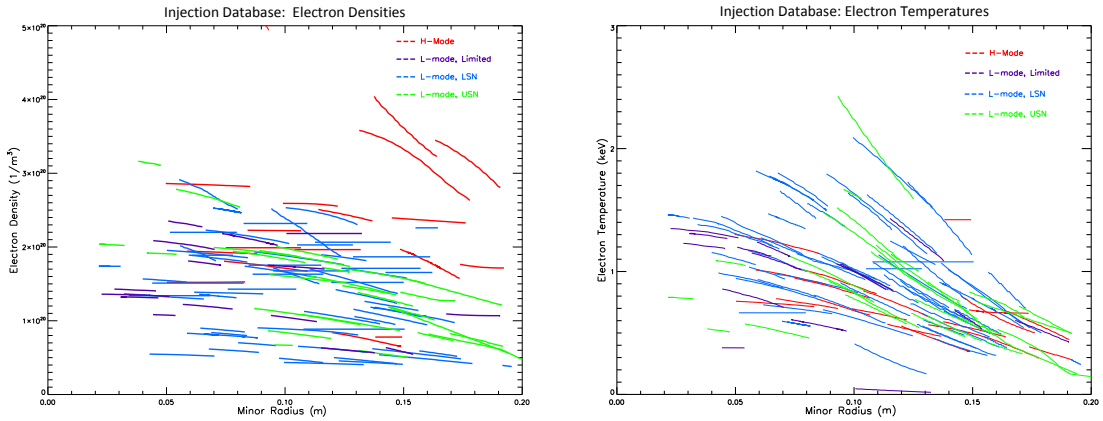

(a) Database Densities

(b) Database Temperatures

Figure 4-13: The complete database of electron densities (a) and temperatures (b) determined using Thomson scatter within 1 ms prior to the injection. Horizontal traces correspond to injections when Thomson data was not available. In these cases the temperature was determined using GPC and the densities are from TCI

28 frames from the PSI-IV camera, and the red crosses represent the locations of the striations. The black arrows, which track the trajectory of the filaments, can be interpreted as follows. The first black arrow in a filament trajectory points from the pellet location in the frame prior to the filament's appearance to the location where the filament first appears. The arrows then point from where the filament appears in an image to where the filament appears in the next image, until the filament disappears, moves out of view of the optics, or the movie ends. The filaments in these two discharges move along the magnetic flux surfaces in accordance with our hypothesis. This is corroborated in figure 4-15, which shows the distribution of the ratio of the filament's poloidal velocity to its total velocity, $|v_\theta|/|v|$, for the entire data set. As can be seen, a majority of the filaments move primarily in the poloidal direction.

4.6.1 Statistical Analysis

As noted in chapter 1, the poloidal motion of the filaments demonstrates a semi-random behavior in L-mode plasmas, where the direction of motion of consecutive filaments in the same discharge showed a predilection for moving in the same direction,

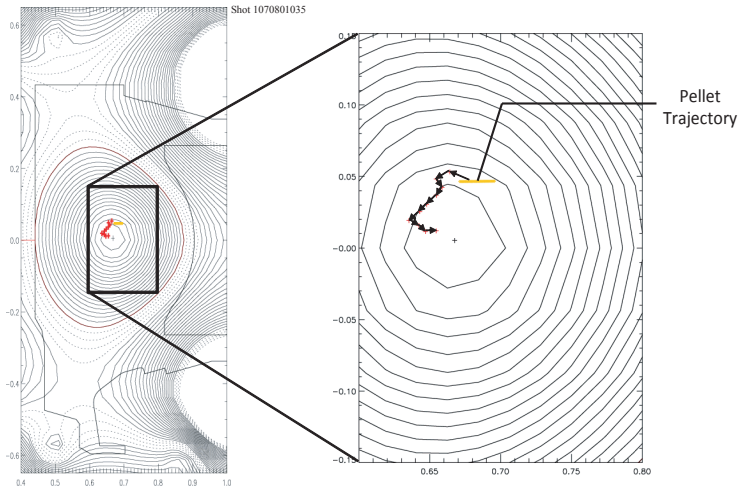

(a) Shot 1070801035

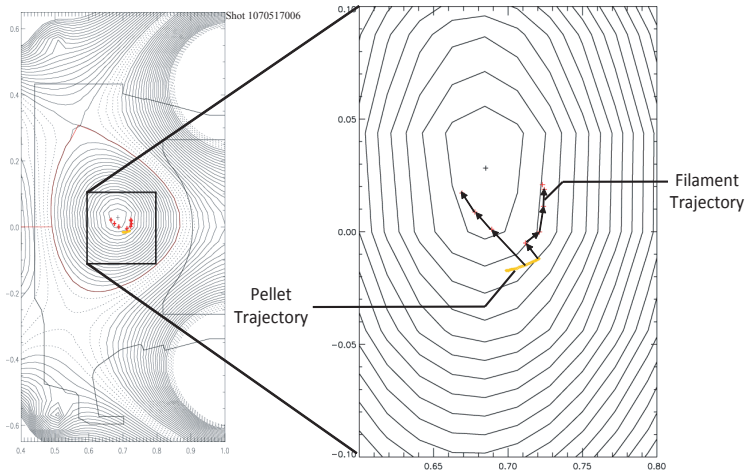

(b) Shot 1070517006

Figure 4-14: Both of the above trajectories observe filaments as the pellet passes above or below a flux surface. In both cases the filaments motion is not strictly vertical or horizontal, but rather they curve around the plasma axis.

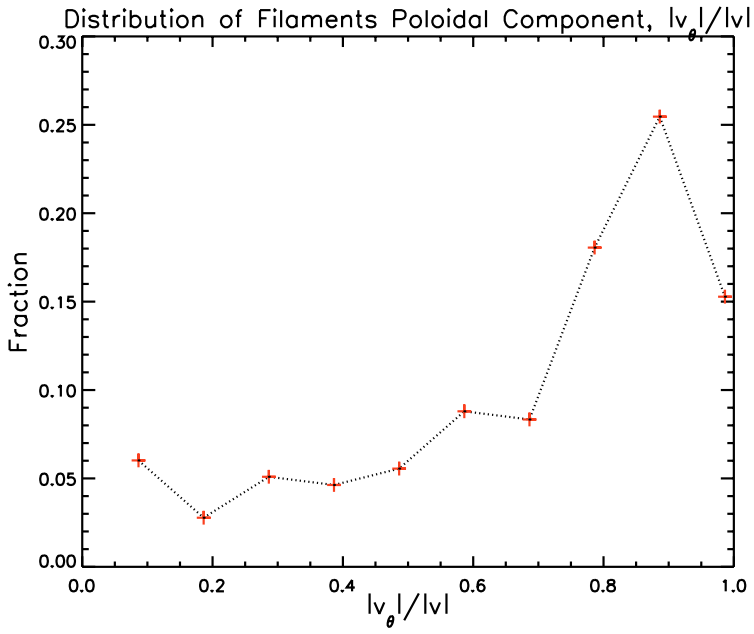

Figure 4-15: Distribution of $|v_\theta|/|v|$ for the filaments in the pellet injection database. The distribution shown above has a binsize of $\Delta|v_\theta|/|v| = .1$, and the velocities are averaged over the total life of the filament.

but there was no correlation in direction between filaments in different discharges[3]. For this reason a statistical approach was employed in our study of the filaments. We compiled our data into filament velocity distributions and tracked the variation in statistical properties, such as the mean and standard deviation, as a function of various local plasma parameters. Our aim was to determine which, if any, parameters influenced the filament behavior[4].

In order to determine the statistical properties of the striations, and their dependence on various plasma parameters, a method of binned histograms was used. As an example consider figure 4-16a which shows the cumulative database for the filament motion plotted as a function of the local safety factor. In order to determine the q-dependence of the filament velocities' the data are separated into bins which are then used to form velocity histograms as shown in figure 4-16b. The histogram acts

[3]This characteristic is also evident in the larger database. There is a 78% chance that a filament will go in the same direction as the one preceding it.

[4]As noted in chapter 1, a systematic variation in filament properties was observed between L-mode and H-mode plasmas

as a estimator of the probability distribution function (PDF) for the velocity of the filaments with a safety factor value equal to that for the center of the bin. Statistical properties, such as the mean velocity and standard deviation, can then be determined from the estimated PDF. If we think of the filament velocity measurements as a randomly sampled measurement of a fluctuating quantity, then we can associate the standard deviation of the PDF with the amplitude of the fluctuations and the mean with the equilibrium value.

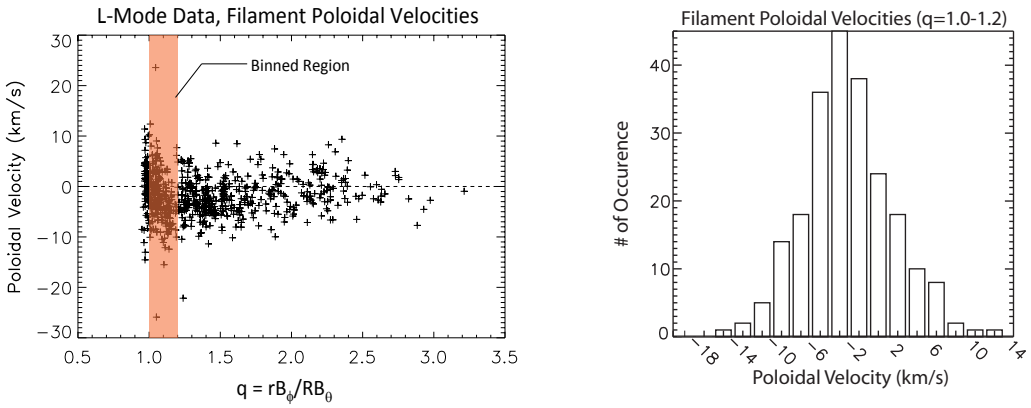

(a) (b)

Figure 4-16: (a) A plot of the velocity of every filament measured during an ohmic L-mode discharge as a function of the local safety factor determined from an E-Fit reconstruction of the magnetic geometry just prior to the injection. (b) Distribution of velocities that occur between $q = 1.0 - 1.2$

Database

In the analysis that follows, only ohmically heated L-mode shots were included. This excludes only a small portion of the data because the filaments formed during H-mode and RF heated plasmas tended to last at most 1 or 2 frames[5], and thus did not provide much data on the filament trajectories. In what follows we present the major results and trends that appear in the statistical study, with a brief discussion of possible implications.

[5]The fact that the filaments were only visible for a few frames after their emission from the ablation cloud was probably a result of the higher electron temperatures and densities in these discharges, which dramatically shortened the ionization time from the first to second charge state, where they would no longer emit light visible to our optics.

Drift Direction and Persistence

Our investigation of the L-mode shots revealed that there exists a preferential drift direction, in the electron diamagnetic direction, similar to what is seen in the H-mode data from 2003-2004, but not as extreme. Figure 4-17 shows the poloidal velocity distribution for the filament drifts for the Ohmic L-mode shots. The mean of the distribution, $-1878m/s$, is almost half of a standard deviation, $4307m/s$, from zero velocity. If we interpret the mean of the distribution as the result of an equilibrium electric field, drifts of this magnitude would imply fields of the order 10kV/m, directed towards the plasma axis. This would be consistent, in magnitude and direction, with electric fields of order 15kV/m inferred from toroidal velocity measurements in L-Mode discharges in Alcator C-Mod [79].

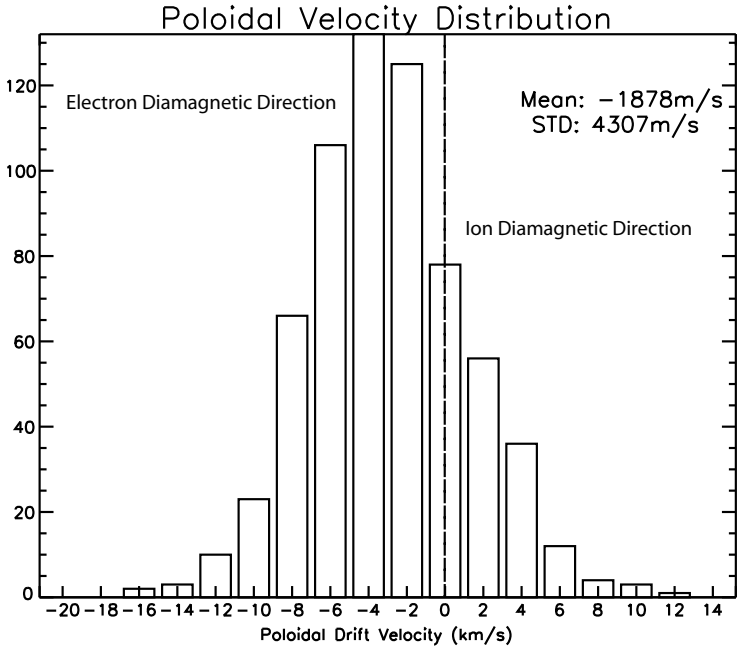

Figure 4-17: Distribution of poloidal velocities for filaments in the injection database. Note that this distribution runs over each velocity measurement of a filament, not just the average of the velocity over the lifetime of the filament.

The expanded injection database allowed us to further test our assertion that the direction of the emission of a filament is not purely random, but rather is correlated with the direction of previous filaments. Figure 4-18 shows the probability, calculated

from the database, that a filament moves in the same poloidal direction as the i^{th} filament proceeding it. For example the red curve at $i = 1$ denotes the fraction of filaments that move in the same direction as the filament that immediately preceded them, $i = 2$ denotes the fraction of filaments that move in the same direction as the filament came two ahead of them, etc... This should be compared to the horizontal blue line, which denotes the probability that the two filaments randomly go in the same direction. Since there is a preferential direction, 29% of the filaments move in the ion diamagnetic direction and 71% move in the electron diamagnetic direction, there is a 58.8% probability that two filaments will go in the same direction purely by chance. The vertical blue lines denote the 5% significance level for each of the measurements. The significance level represents the probability that the deviation of our measurement from the random result is merely due to statistical fluctuation. Thus the interval for the 5% significance level is the region where we would expect 95% of our measurements to lie if the process was truly random. The points at $i = 1$ and $i = 2$ lie significantly outside the 5% significance interval, indicating that there is a preference for the filaments to drift in the same direction as those proceeding beyond the preference for filaments to drift in the electron diamagnetic direction.

Safety Factor, q

As noted in section 3.6, the damping rate of the Geodesic Acoustic mode is expected to have a strong dependence on the local safety factor due to Landau damping on passing particles. Thus if the motion of the filaments is due to flows generated by the GAM potential, we would expect the filament velocities to be larger, with correspondingly broader distributions, at higher values of q where there are fewer resonant particles and hence a lower damping rate. Figures 4-19a and 4-19b show the mean and width of the filament velocity distributions respectively as a function of the local safety factor. As can be seen, the distributions do not increase in width at higher q, but generally drop with increasing q. On the other hand, as can be seen from figure 4-19a, the means of the velocity distributions do not show any systematic behavior as a function of q.

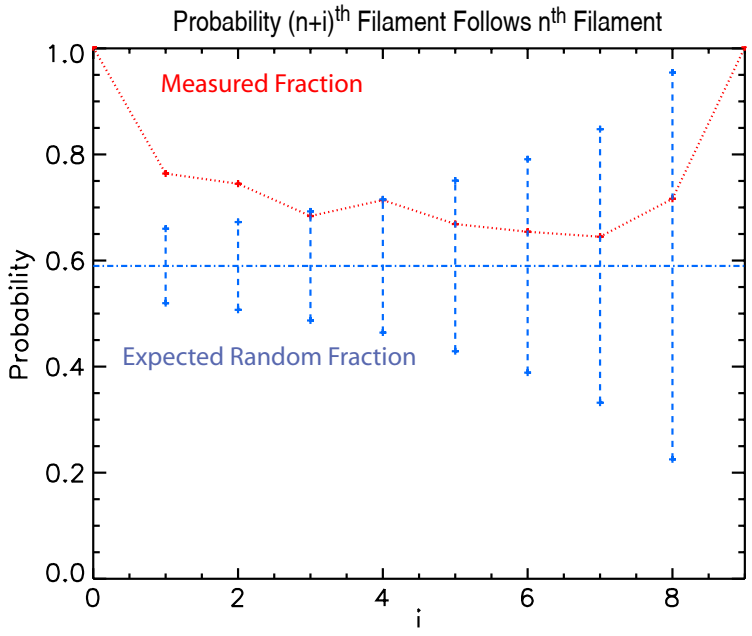

Figure 4-18: The red dotted line denotes the measured probability for filaments to move in the same direction as the i^{th} filament preceding it. The horizontal blue dotted line denotes the probability that filaments move in the same direction by random chance, and the vertical blue lines indicate the 5% significance level for each measurement. The divergence of the significance level as i increases is a consequence of decreasing amount of data available to compute each probability. E.G. one requires shots with 9 filaments to determine the frequency of filaments separated by 8 filaments that move in the same direction.

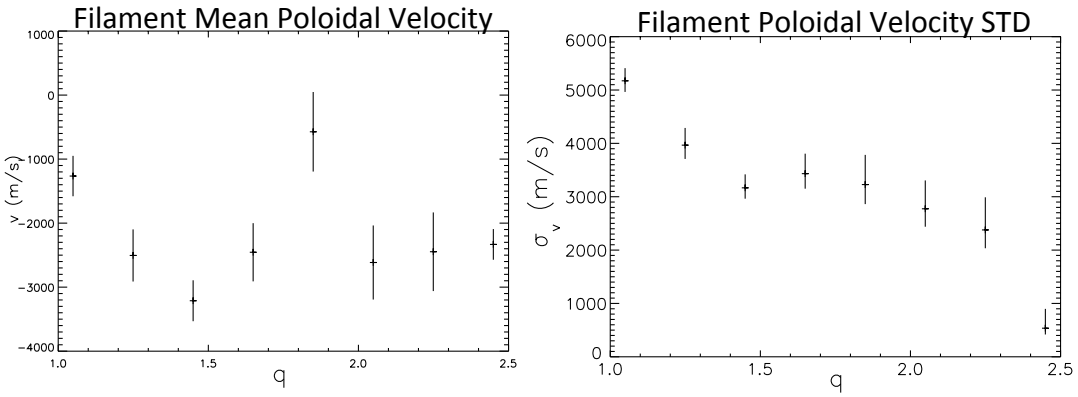

(a) (b)

Figure 4-19: The mean (a) and standard deviation (b) of the filament poloidal velocity as a function of the local safety factor.

Collisionality

As noted in section 3.5, the collisionality should not set the zonal flow amplitude, rather the ZMF zonal flow amplitude should be set by the drive of the drift wave turbulence or the Zonal Flow non-linear saturation mechanism [66]. On the other hand, if the filament drifts were a product of the coherent flows generated by ZMF Zonal Flows, one might expect a dependency on collisionality owing to the nature of our measurement, which relies on the coherent drift of the plasma filaments, At low collisionalities, the self consistent state, composed of both Zonal Flows and driftwave turbulence, is dominated by the Zonal Flows, which one expects would lead to a coherent flow pattern rather than the chaotic pattern one would expect from turbulence [66]. As can be seen from figure 4-20, the width of the velocity distributions shows a complicated dependence on collisionality, increasing up to a point, and then decreasing with increasing collision frequency.

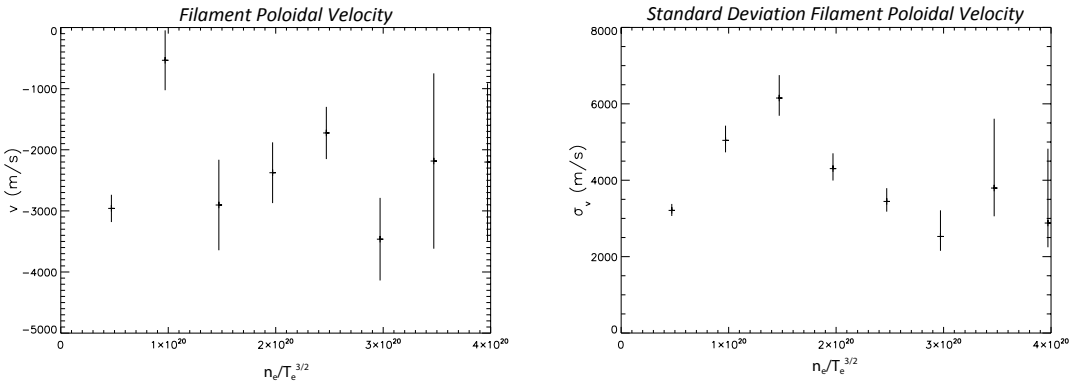

(a) (b)

Figure 4-20: The mean (a) and standard deviation (b) of the filament poloidal velocities as a function of $n_e/T_e^{3/2} \sim \nu_{ie}$. Collisions are the only linear damping mechanism on the Zonal Flows.

Temperature and Density

The dependence of the filament velocity on quantities like the safety factor and the collision frequency immediately suggests that possibly the dependence is actually due

to a more fundamental physical quantity, such as the temperature or density. The collision frequency is a function of only the density and temperature, and similarly, in typical tokamak discharges, there is a correlation between the safety factor, the density and temperature, with all three generally varying monotonically as one moves from the plasma axis to the edge. Figure 4-21 and 4-22 show the variation of the distribution means and widths with the electron temperature and density respectively. The statistical properties of the filament velocities show no obvious dependence on the electron temperature and density.

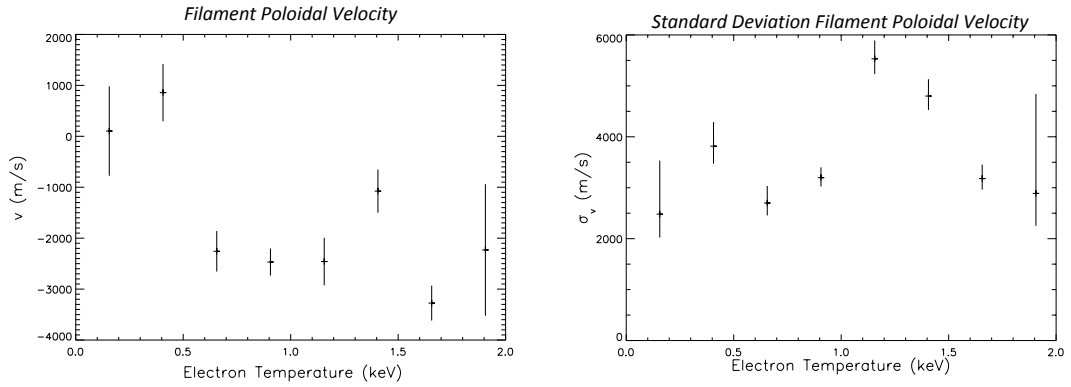

(a) (b)

Figure 4-21: The mean (a) and standard deviation (b) of the filament poloidal velocities as a function of the electron temperature. The lack of any obvious dependence with temperature indicates that filament velocities dependence on safety factor, is not an artifact of the correlation between $T_e$and q.

Magnetic Shear

Additionally, since the q value increases strongly toward the edge of the plasma, one might also suspect that the q dependence is an artifact of the general increase in magnetic shear, $\hat{S} \equiv \frac{r}{q}\frac{\partial q}{\partial r}$ as a function of q, since the magnetic shear is know to have a strongly stabilizing effect on micro-instabilities. Figure 4-23, which shows the variation of the filaments' statistical properties as a function of the magnetic shear, shows that there is little or no apparent dependence of the mean velocity or standard deviation on the magnetic shear.

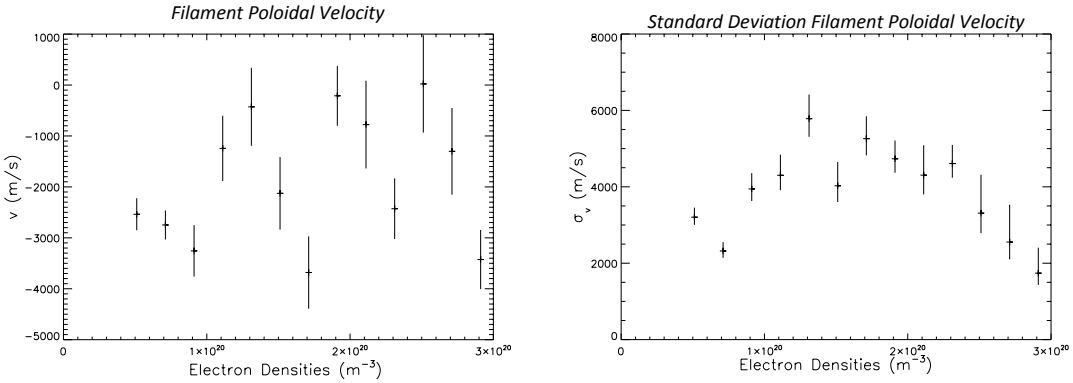

(a) (b)

Figure 4-22: The mean (a) and standard deviation (b) of the filament poloidal velocities as a function of the electron density. As with the temperature, the lack of any obvious dependence with density indicates that filament velocities dependence on safety factor, is not an artifact of the correlation between n_e and q.

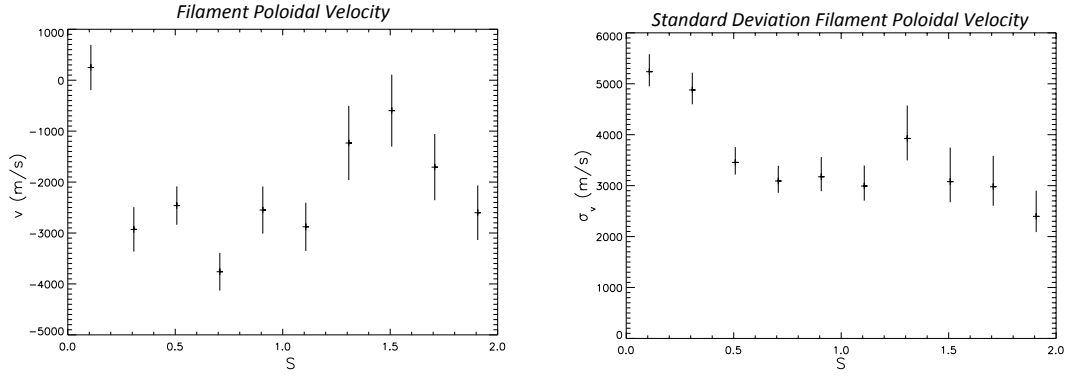

(a) (b)

Figure 4-23: The mean (a) and standard deviation (b) of the filament poloidal velocities as a function of the magnetic shear, $\hat{S} \equiv \frac{r}{q}\frac{\partial q}{\partial r}$. As above, the lack of any obvious dependence with shear supports the hypothesis that the filament velocities dependence on safety factor, is not an artifact of the correlation between q and its derivatives.

Gradients

One might expect that if the filaments' velocities are indeed a product of ZMF zonal flows, then perhaps there would be a dependence on the temperature and density gradient scale lengths. It is believed that ZMF zonal flows are driven by ITG turbulence. The turbulence is driven in turn by the ion temperature gradient, and moderated by the ion density gradient, through the parameter $\eta_i \equiv L_{T_i}/L_{n_i}$. Figure 4-24 shows the dependence of the filament statistical properties with η_e, which we use as a proxy for η_i. Again, there is no obvious dependence. Another plausible candidate source term for ZMF zonal flows are TEM modes, which are driven by the electron density gradient. Figure 4-25 shows the dependence of the filament velocities statistical properties on L_{n_e}, which again shows no apparent dependency. Finally, Figure 4-26 shows the filament's statistical properties as a function of the electron temperature gradient scale length. Again there is no apparent dependence of either the mean filament velocity or the standard deviation in the velocities.

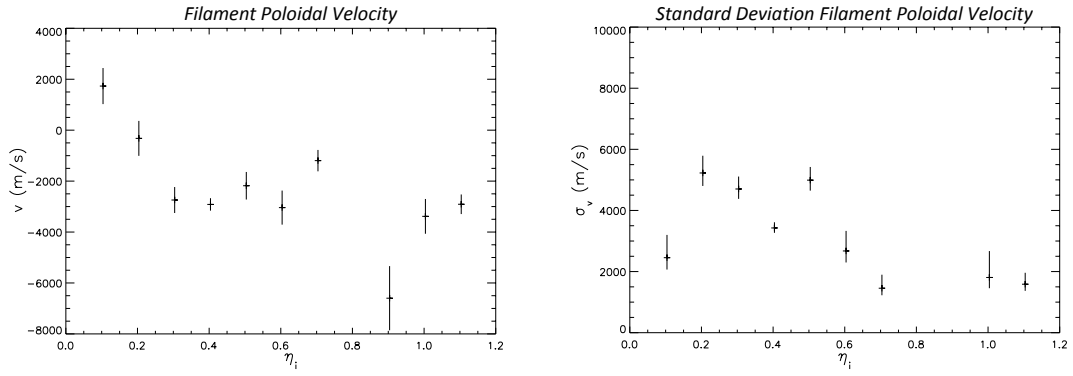

(a) (b)

Figure 4-24: Mean (a) and standard deviation (b) of the filaments' velocity as a function of $\eta_i = L_{T_i}/L_{n_i}$. η_i is believed to play a key role in the onset of ITG turbulence, which is believed to be the primary driver of ZMF Zonal Flows.

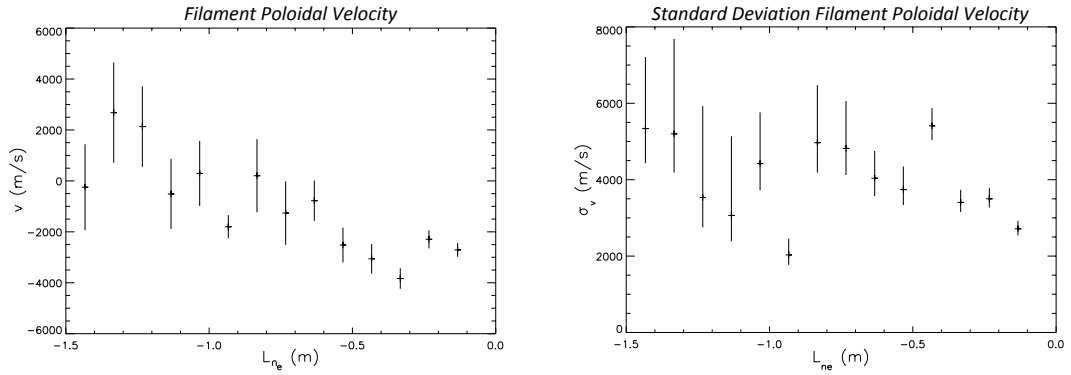

(a) (b)

Figure 4-25: Mean (a) and standard deviation (b) of the filament velocities with respect to the electron density gradient scale length. The electron density gradient scale length is believed to play a key role in driving TEM modes, which in turn are believed to play strong role in driving ZMF Zonal Flows.

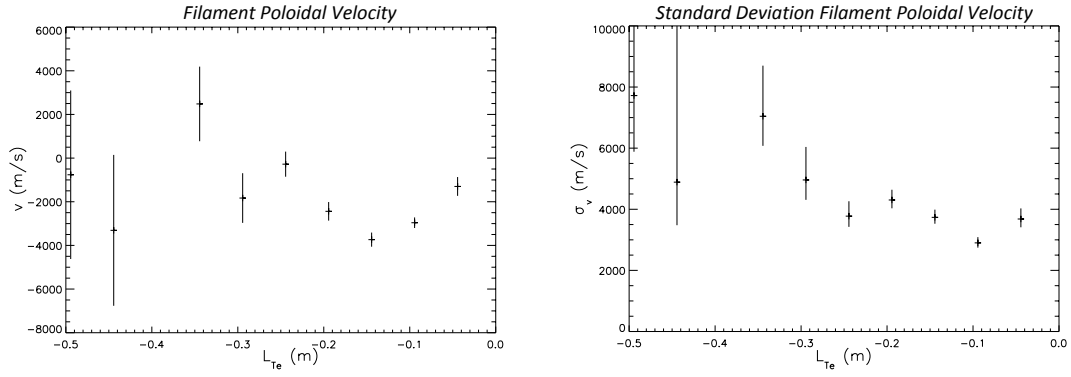

(a) (b)

Figure 4-26: Mean (a) and standard deviation (b) of the filament velocities with respect to the electron temperature gradient scale length, which is standing as a proxy for the ion temperature gradient scale length. The ion temperature gradient scale length is believed to play a key role in driving ITG modes, which in turn are believed to play strong role in driving ZMF Zonal Flows.

It should be noted that the absence of a dependency on the drivers of turbulence is not necessarily an indication that the drifts are not a result of ZMF zonal flows. As mention in section 3.5, the non-linear saturation mechanism of the ZMF zonal flows is not currently understood, and it is possible that it requires very little turbulent drive to push the zonal flows to their saturated state. In that case, we would not expect to see a dramatic change in the zonal flow amplitude as a function of the driving terms of the source turbulence.

Chapter 5

Gyrokinetic Simulations

5.1 Introduction

As mentioned in section 1.5, the most plausible cause for the drift in the filaments formed during lithium pellet injections are radial electric fields within the plasma, including ZMF Zonal Flows and GAMs. Currently, there exists no independent measure of the turbulent electric fields to which we can compare the filament drifts, and for that reason, we turn to non-linear gyrokinetic simulations to make correlations to our experimental data. In particular, we will utilize the electrostatic potential as calculated by the gyrokinetic solver, GYRO, designed and written by Candy and Waltz [71], to serve as the basis for our comparison.

In what follows, we undertook three projects using the GYRO code in an attempt to make comparisons of turbulent flows to the measured drifts of the filaments. In the first project, we explored the background turbulence dependence on the local safety factor in order to compare it to the systematic dependence in the variation in the standard deviation of the filament drift velocity distribution, as shown in figure 4-19b. A lack of correlation of the measured turbulence properties with those of the filaments led us to suspect that the filament drifts might be caused by turbulence that is generated by the large temperature and density gradients associated with the pellet injection itself. The next project was to gauge if these large gradients could indeed change the structure of plasma turbulence on an observable time scale. To

that end we examined the growth rate of turbulent modes under plasma conditions that are similar to those expected to prevail during the pellet injection. The results of these simulations indicated that, indeed, the effects of the pellet fueling could have an appreciable effect on the plasma turbulence. This observation led to the final project, a nonlinear global simulation using our best estimates of the temperature and density profiles during the injection.

The chapter follows the following outline. We begin with a brief discussion of the GYRO code, including its inputs and output, including post processing and analysis. We then cover each of the three sets of simulations, and finish with a summary of the results and their implications.

5.2 GYRO Overview

GYRO uses fixed grid (Eulerian) initial value algorithms to solve the nonlinear electromagnetic, coupled, 5-D Gyrokinetic Maxwell (GKM) equations [80]. The GKM describe the evolution of fluctuations which satisfy the gyro kinetic ordering,

$$\frac{\tilde{h}}{F_0} \sim \frac{e\tilde{\phi}}{T} \sim \frac{\omega}{\Omega} \sim \frac{\rho}{L} \ll 1, \;\; k_\parallel L \sim 1, \;\; k_\perp \rho \sim 1 \tag{5.1}$$

where $\tilde{h}$ is the non-adiabatic portion of the perturbed distribution function, F_0 is the equilibrium distribution function, $\tilde{\phi}$ is the perturbed electrostatic potential, L is the equilibrium scale length, ρ is the thermal gyro radius of the species of interest, and Ω is the cyclotron frequency. From a theoretical point of view, the GKM are believed to contain all the physics necessary for a first principles calculation of anomalous tokamak energy transport due to turbulence [71]. GYRO can be run in either a linear or non-linear mode. Linear simulations are local, all plasma parameters have a single fixed value, and GYRO returns the linear eigen modes and growth rates. For nonlinear simulations GYRO can be run in either a "flux tube" mode, in which the simulation domain has periodic boundary conditions and all parameters, including all scalar quantities and their gradients, are constant across the domain, or in "global" mode with Dirichlet zero value boundary conditions with full profile variation across

the domain. Additionally, GYRO may include experimental or user defined parameters, in realistic toroidal geometries, including, circular $\hat{S} - \alpha$[1], "D" shaped Miller geometries, and an expansion of an arbitrary flux shape.

Information on the plasma conditions, including electron temperature, density, and magnetic geometry are determined from the diagnostic set of Alcator C-Mod described in chapter 1. In the cases of linear and flux tube runs, these parameters can be entered by hand into GYRO's INPUT file, essentially a name list delineating the values of plasma parameters and important specifications for the code. When running in global mode, full profile data is supplied to GYRO via TRGK, which translates the TRANSP output into profile files from which GYRO reads the required plasma information. In this instance, TRANSP only acts to generate unknown profiles, such as the ion temperature, from known quantities, such as the electron temperature , density profile and core neutron rate.

In all of the simulations that follow, the electron temperature and density profiles were taken from curves fitted to data from the Thomson scattering diagnostic, radiated power from the bolometry array, plasma current from magnetics and the flux surface reconstruction from EFIT. The code was run on the Loki cluster, located at MIT's Plasma Science and Fusion Center, and the Kestrel Cluster located at Princeton's Plasma Physics Laboratory. Even given the awesome array of computing power presented by these two clusters, each GYRO simulation required a substantial investment of time. A typical flux tube run required over 5700 CPU hours, and the global runs required substantially longer ($\sim 20,000$ CPU hours).

[1]The $\hat{S} - \alpha$ equilibrium model satisfies the Grad-Shafranov equation (equation 1.15) in the limit that the magnetic pressure is much greater than the kinetic pressure, $\beta \equiv \frac{2\mu_0 p}{B^2} \ll 1$. In this case the flux surfaces are nearly concentric circles. This model gets its name due to its use in analyzing ballooning instabilities. In this simplfied geometry the flux surfaces suceptability to ballooning instabilities can be characterized by two parameters, the flux averaged shear, $s = \frac{r}{q}\frac{\mathrm{d}q}{\mathrm{d}r}$ and a normalized pressure gradient, $\alpha = -\frac{2\mu_0 r^2}{R_0 B_\theta^2}\frac{\mathrm{d}p}{\mathrm{d}r}$ [6]

5.2.1 Convergence and Uncertainty

In this thesis we take the numerical results from the GYRO simulation to be an accurate representation of otherwise unmeasurable plasma phenomena. That this is the case is far from guaranteed. Numerous uncertainties exist which can be general grouped into the following four general categories: 1. Is the gyro kinetic model sufficient to describe the phenomena of interest? 2. Does GYRO properly implement the gyrokinetic model? 3. Is the code completely converged and free of numerical problems? 4. To what extent are the results of your simulation effected by the uncertainties in the input parameters of the simulation? In this section we will address each of these concerns.

The first two concerns, referred to as validation and verification[2] respectively, are a matter of great concern in the nuclear fusion community as numerical simulations play a larger role in the planning and interpretation of experiments.

The GYRO code has undergone extensive verification studies [81, 71, 82], benchmarking the results of standardized base cases against the initial value eulerian flux tube codes GS2 [69], and GENE [83], and the particle-in-cell (PIC) codes GTC [68], PG3EQ [53], and GEM [82]. These verification studies give us confidence that GYRO is properly coded and has correctly implemented the gyrokinetic formalism.

Validation presents a unique challenge for the fusion community due measurement and diagnostic capability on on fusion devices and the complexity of plasma dynamics, such as the non-linearity of turbulence, disparate time scales, bifurcation of equilibrium states and critical gradients[84]. Though the resolution of these issues lies outside the scope of this thesis, I direct the reader to recent articles by Greenwald [85], Terry [84] and Oberkampf [86] discussing the importance of validation, and possible approaches to resolving the above mentioned issues.

In the case of GYRO the results of validation remain ambiguous. Work comparing both the net energy flows and detailed electron density and temperature fluctuation

[2]Validation refers to the process of ensuring that the model you are solving is indeed consistent with the real world, Verification on the other hand refers to the process of ensuring that the code properly implements your physical model.

statistics between a GYRO simulation and a non-sawtoothing L-mode discharge on DIII-D showed excellent agreement at a normalized minor radius of $\rho = 0.5$, but showed significant deviations at $\rho = 0.75$ [87, 88]. In the latter case, at $\rho = 0.75$, GYRO under predicted the net energy flow by a factor of seven and the fluctuation amplitude by a factor of three, though the GYRO was able to reproduce the correct shape of the experimental power spectra. These results undoubtedly create certain skepticism about GYRO's ability to accurately predict the amplitude of the electrostatic fluctuations in Alcator discharges.

Taking for granted that the code is functioning properly, and that it is in fact correctly representing the dynamics of interest, the next issue to address regarding confidence in the accuracy of a simulation falls to the confidence that the simulation is free of numerical problems, and that the simulation has been run through a sufficient number of iterations to be converged.

To ensure stability of the simulation the first parameters that were checked were the courant numbers. In general the courant number is defined as $C_r = u\Delta t/\Delta x$, and represents the ratio of the distance traveled by wave-like features with a velocity u, per time step, Δt, to the radial grid spacing, Δx. A necessary, although not sufficient, condition for the convergence of a numerical solution to a hyperbolic partial differential equation [89], is that $C_r < 1$; for all of the following simulations, the time step and grid spacing were chosen to keep $C_r < .75$.

Another key parameter is the integration error associated Eulerian time advancement. Since the electron dynamics have the shortest time scale, they have the largest integration error in the perturbed distribution function for a time step of a given size. For all simulations, the time step was chosen sufficiently small so that the electron time integration error remained below 10^{-3} throughout the simulation; figure 5-1 shows an example of the time integration error for a GYRO simulation.

In GYRO, in order to limit the computational time and memory requirements of the simulation, only a small subset of possible modes are simulated. For that reason, it is necessary to check the energy diffusion spectrum, to ensure that results of the simulation are not an artifact of the particular modes chosen. An example of

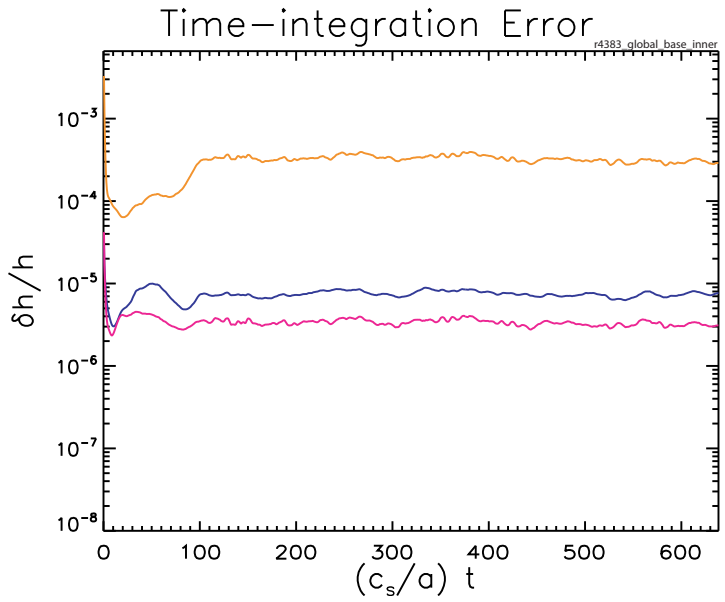

Figure 5-1: Example of GYRO time integration error from r4383_global_base_Inner.

the diffusion spectrum is shown in figure 5-2. It is important that the peak in the spectrum does not occur at the first non-zero value of k. If this is the case, then it is possible that the grid in toroidal mode number is not fine enough, and that a majority of the transport occurs in modes that are below the lowest non-zero mode number. Similarly, it is important that sufficient modes are simulated such that the highest modes transport significantly less energy than the peak mode (this is usually taken to be about a factor of 10), so that we can be confident that we have simulated sufficient modes to account for a majority of the transport. Issues regarding effects related to the precise mode spacing chosen for a simulation are discussed later during uncertainties.

Additionally, GYRO is optimized to deal with ballooning like modes, i.e. modes whose amplitude peaks on the outside mid-plane. Thus a check is made on the spatial structure of the electrostatic modes to ensure that they have the appropriate form. For GYRO, the (n,p) spectrum shows the mode amplitude as a function of the toroidal mode number, n, and the poloidal location[3], p. Appropriate (n, p) spectra

[3]The parameter p is associated with the extended ballooning space representation and represents a poloidal position.

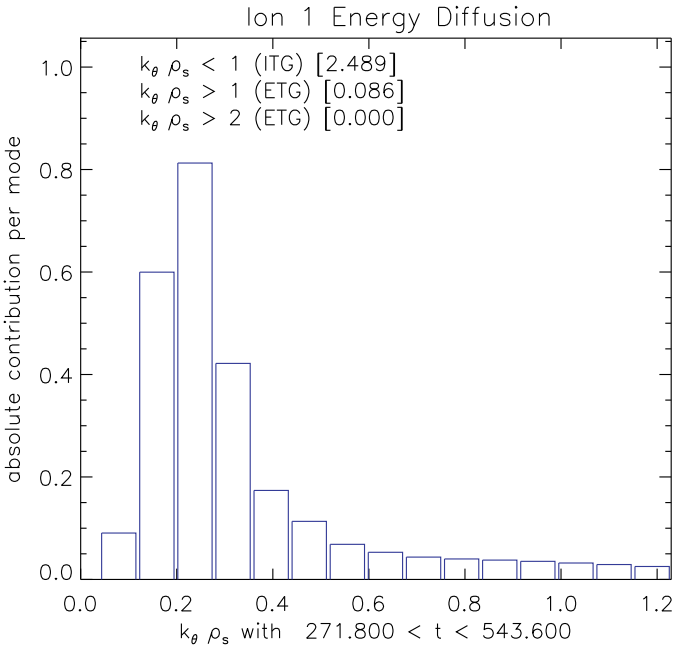

Figure 5-2: Plot each toroidal mode's contribution to energy diffusion. The mode spacing is chosen such that the peak occurs after the first non-zero mode, and the number of modes is chosen to allow significant decay from the peak mode.

have a saddle-like shape, peaked at low n and $p = 0$. Figure 5-3 shows an example of good and bad spectra.

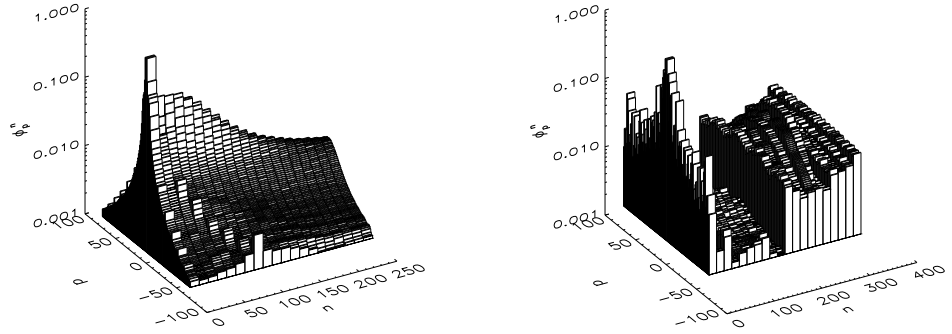

(a) Good (n,p) Spectrum

(b) Bad (n,p) Spectrum

Figure 5-3: a) Good (n,p) spectrum characterized the central peaking in p, and fall off at increasing n. b) Bad (n,p) spectrum indicative of a numerical problem.

As mentioned above, GYRO is an Eulerian initial value code, and thus takes a finite number of time steps to move from its initial value to a limiting state. Because the code does not converge to a stationary value, determining when GYRO has reached a limiting state is performed by considering the time evolution of several key parameters. What follows is an explanation of the parameters we examined, and the factors that were considered, in order to ensure convergence. All these factors had to be satisfied in order for the simulation to be considered converged.

The first parameter we considered was the flux surface average of the root mean squared potentials, as shown in figure 5-4. As can easily be seen, the RMS potentials continue to fluctuate throughout the simulation, but after $\sim 200(c_s/a)$ both the Zonal Flows, $n = 0$, and the turbulence, $n > 0$, stop trending up. Even small trends can lead eventually to large changes in the turbulence. For instance, if the zonal flow potentials are continuing to increase in amplitude, it is possible that the increased ExB shear resulting from the growing zonal flows could eventually lead to a dramatic reduction in the $n > 0$ portion of the turbulent spectrum, and thus a state with different statistical properties.

Two other key parameter that are considered are the electron and ion thermal

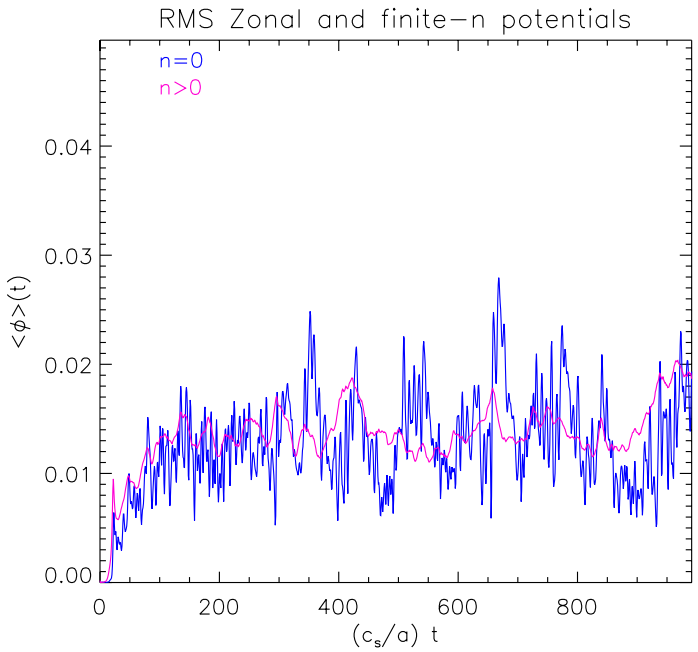

Figure 5-4: Plot of the flux surface averaged root mean squared potentials for the Zonal Flow, $n = 0$, and turbulent modes, $n > 0$ for a non-linear simulation. Note that potentials reach a limiting value after $t \sim 200(c_s/a)$

diffusivities. The diffusivity is dominated by the turbulent transport, and thus dramatic and sustained changes in the ion and electron thermal diffusivity are reflective of changes in either the amplitude or structure of the turbulent spectrum.

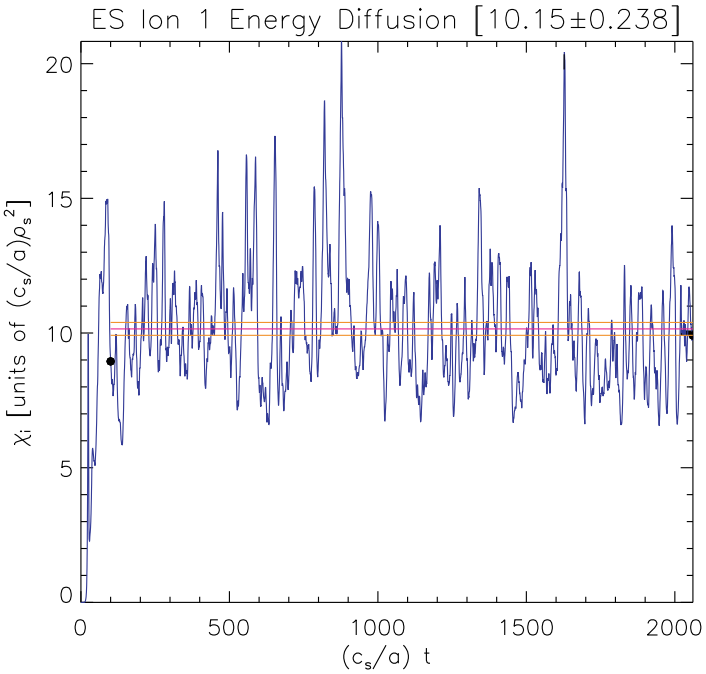

Figure 5-5: Ion thermal diffusivity for a GYRO simulation. The purple horizontal line represents the average, and the orange side bars are the standard deviation.

As a final check on the quality of the simulation the effective thermal diffusivity, $\chi_{eff} = (\chi_e + \chi_i)/2$ for the simulation was compared to the thermal diffusivity calculated by TRANSP using power balance. Figure 5-6 shows an example of such a comparison. The question of, "How good does the agreement have to be to be good enough?" is a current issue in the Fusion community regarding verification and validation, as mentioned at the beginning of this section. For our purposes, we are merely interested in verifying that the simulation is free from catastrophic numerical instabilities and as such simulations where the GYRO and TRANSP diffusivities were within factor of two were deemed acceptable.

The uncertainties in plasma parameters, such as the ion temperature or its gradient, were treated by re-running each simulation numerous times, and on each occasion, changing a single experimental parameter to an extreme consistent with the uncer-

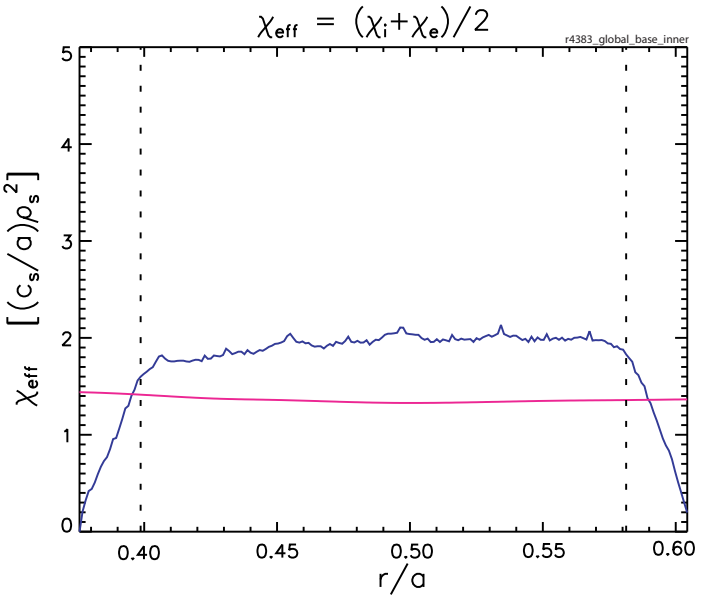

Figure 5-6: Comparison of χ_{eff} as determined by GYRO (blue) and TRANSP (pink) for simulation r4383_global_base_inner.

tainty in its measurement. For example, suppose for a simulation we obtained an electron temperature from Thomson Scattering of $T_e = 1 \pm .2keV$. The equilibrium run would be made with $T_e = 1keV$, and two stability simulations would be run with $T_e = 1.2keV$ and $T_e = .8keV$ to determine the effects of the uncertainty in the electron temperature on the results of the simulation. Additionally, numerical parameters, such as the radial grid spacing and toroidal mode spacing, were varied by small amounts to ensure that the results of the simulation were not artifacts of the numerical choices. For the remainder of the thesis I refer to these additional simulations as the stability runs, since by varying one parameter at a time is analogous to a linear stability analysis.

5.2.2 Post Simulation Processing and Analysis

In order to make meaningful comparisons between the observation from pellet injection experiments and the GYRO simulations, we need to carefully consider what our experimental data is measuring, and to what it should be compared in the simulation. If indeed the filament motion is a result of turbulent ExB drifts in the plasma, then

our filament distributions can be viewed as an estimator for the probability distribution of measuring an electric field of a particular value at a random time and place with respect to the fluctuating fields inside the plasma. The appropriate quantity for comparison in the simulations is thus the distribution of radial electric fields.

Gyro uses the right handed, field-aligned coordinates (ψ, θ, α) together with the Clebsch representation [90] for the magnetic field,

$$\vec{B} = \vec{\nabla}\alpha \times \vec{\nabla}\psi \tag{5.2}$$

where the angle, α, is written in terms of the toroidal and poloidal angle, φ and θ, in such a way that α remains constant on a magnetic field line,

$$\alpha \equiv \varphi + \nu\,(\psi, \theta) \tag{5.3}$$

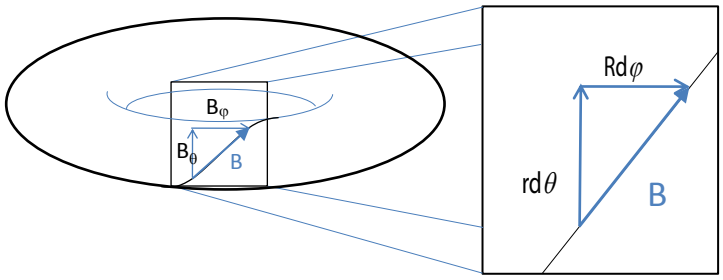

Figure 5-7: Diagram of the θ and φ relationship for a field line. The $rd\theta$-$Rd\varphi$ triangle and the B_θ-B_φ triangles are similar, in a geometric sense, if $\frac{\mathrm{d}\varphi}{\mathrm{d}\theta} = \frac{rB_\varphi}{RB_\theta}$

In a simple circular geometry α is a straight forward function of φ and θ and the safety factor. As can be seen in figure 5-7, to stay on the the same field line, one must increment φ by an amount,

$$\Delta\varphi = \frac{rB_\varphi}{RB_\theta}\Delta\theta \tag{5.4}$$

for each increment in θ. Thus for coordinate α to remain constant on a field line we have,

$$\alpha \equiv \varphi + \nu\left(\psi, \theta\right) = \varphi - q(r)\theta \tag{5.5}$$

For more complicated geometries there is no simple analytic expression for α, but in these cases ν is calculated numerically by the GYRO program. An example of an (r, α) grid from a non-circular geometry is shown in figure 5-8

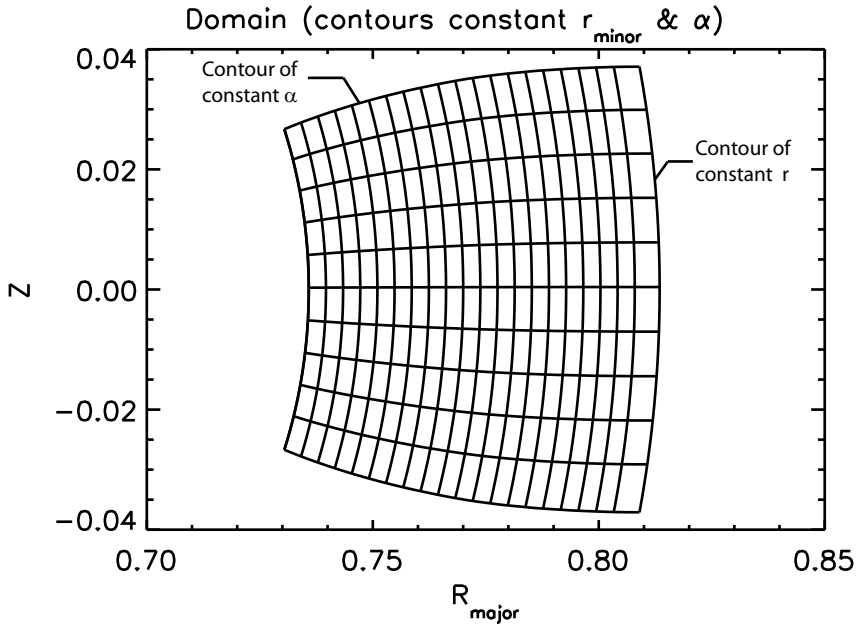

Figure 5-8: Example of an (r, α) grid from GYRO simulation r4383_chili_comb. Note that because the definition of α is dependent on the magnetic field, the grid is different under different field geometries.

All the simulations that follow were run in a Miller geometry [91], where the flux surfaces are defined by,

$$\begin{aligned} R\left(r, \theta\right) &= R_0(r) + r\cos\left(\theta + \sin^{-1}\left(\delta\right)\sin\left(\theta\right)\right) \\ Z\left(r, \theta\right) &= Z_0(r) + \kappa(r) r \sin\left(\theta\right) \end{aligned} \tag{5.6}$$

where κ is the plasma elongation, δ is the triangularity, and r, the minor radius of the flux surface, is defined to be one half the difference between the maximum and minimum major radius of the flux surface on the mid plane (see figure 5-9).

$$r(\psi) \equiv \frac{R_+ - R_-}{2} \tag{5.7}$$

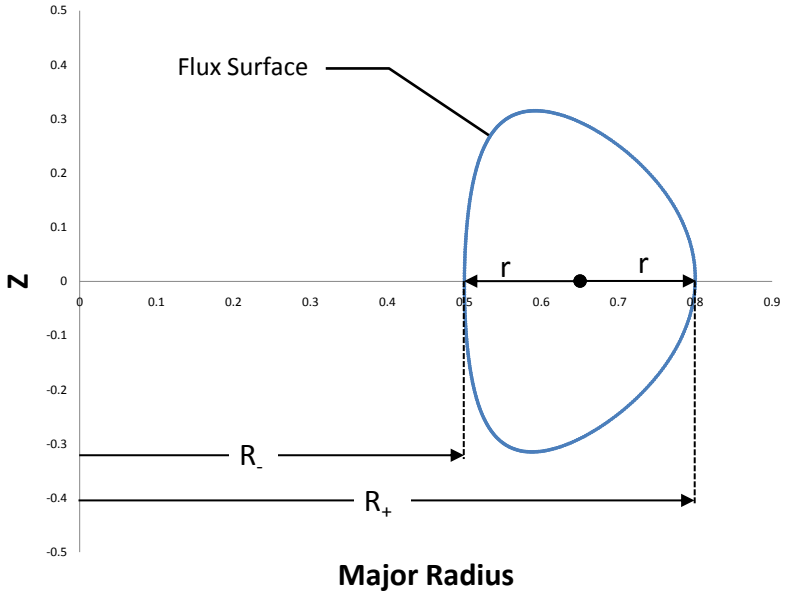

Figure 5-9: Definition of minor radius in GYRO. The dot from which r is measured is the center of the flux surface, $R_0(r)$ in equation 5.6, not the plasma axis.

In GYRO the perturbed quantities, such as the electrostatic potential, and the distribution function are expanded as a Fourier series in the coordinate α. The potential is thus written as [92],

$$\delta\phi\left(r,\theta,\alpha,t\right) = \sum_{j=-N_n+1}^{N_n-1} \delta\phi_n\left(r,\theta,t\right) \mathrm{e}^{-in\alpha} \tag{5.8}$$

where $n = j\Delta n$, and Δn is the spacing between toroidal modes in the simulation[4].

[4]To save time and computational power not every toroidal mode is simulated by gyro. The modes that are simulated by gyro are determined by two parameters, Δn, which determines the spacing between modes, and N_n, which denotes the total number of modes.

The coefficients, $\delta\phi_n(r,\theta,t)$, contain the slow variation of the potential with respect to poloidal angle, θ, where as the rapid spatial variation is contained in the exponentials. For the purpose of our investigation, and to limit the outputs generated by the code, the analysis consisted of the $\delta\phi_n(r,\theta,t)$ components on the outboard mid plane, $\theta = 0$, and an expansion in α in the immediate vicinity. The exact poloidal extent of the domain was determined by the properties of the expansion. Since the components are periodic in α, we chose the poloidal extent of the domain to be the size of the longest wavelength mode. This maximized our use of the available synthetic data and also ensured that every point in the domain was unique. The lowest non-zero mode number occurs for $j = 1$, or for $n = j\Delta n = \Delta n$, and thus the extent of the domain was chosen to be,

$$\Delta\alpha = \frac{2\pi}{\Delta n} \tag{5.9}$$

Using the fact that $\delta\phi$ is real, the Fourier coefficients satisfy the condition $\delta\phi_n^* = \delta\phi_{-n}$, and thus the potential can be written in the form,

$$\delta\phi(r,\theta,\alpha,t) = \delta\phi_0 + 2\sum_{j=1}^{N_n-1}\left[Re\{\delta\phi_n\}\cos(n\alpha) + Im\{\delta\phi_n\}\sin(n\alpha)\right] \tag{5.10}$$

where $\delta\phi_0$ is the toroidally symmetric, $n = 0$, portion of the potential associated with the ZMF zonal Flows and GAMs, and $Re\{\delta\phi_n\}$ and $Im\{\delta\phi_n\}$ are the real and imaginary parts respectively of the $n > 0$ potential in the turbulent spectrum. It should be noted that our initial aim was to consider only the zonal, $n = 0$ components of the potential but a comparison of the relative amplitudes of the $n = 0$ and $n > 0$ components of the field compelled us to consider the full turbulent spectrum. Figure 5-10 shows the typical results of a measure of the relative energy in the $n = 0$ and $n > 0$ fields for our simulations.

In order to make a meaningful comparison between the measurements of the filament drifts and the GYRO simulations, we need to transform the potential from GYRO into the quantity measured during the pellet injection experiments, namely

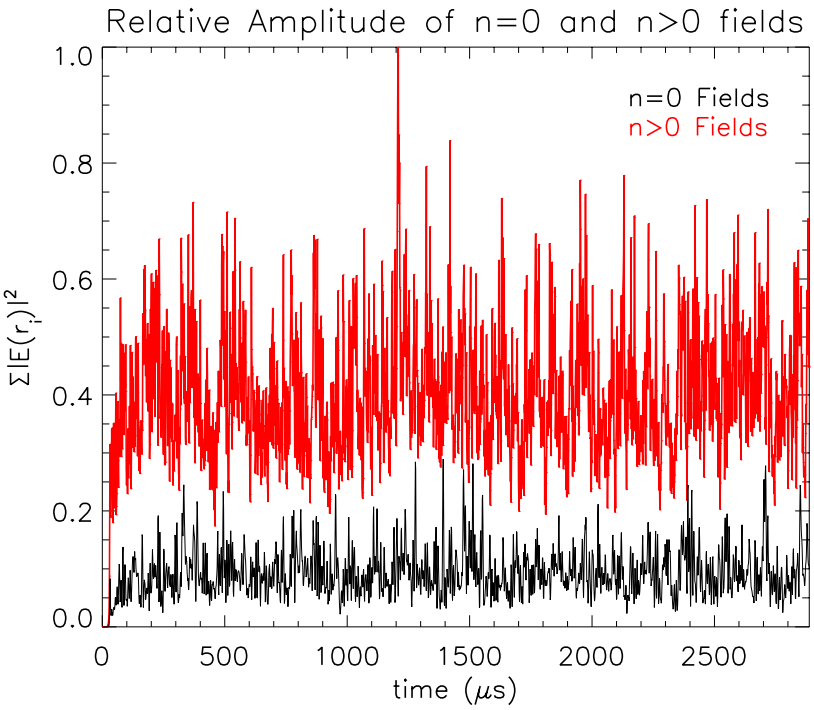

Figure 5-10: Example of the relative amplitude of the $n = 0$ and the $n > 0$ components of the electric field. Shown above is sum of the squares of the components of the electric field, $\sum_i |E(r_i, t)|^2$, as a function of time for the r4132_fv_q225 simulation.

the local poloidal ExB drift velocity. The first step in this process is to convert the potential into an electric field, which is easily done by taking a numerical derivative of the data. As noted in the previous chapter, the pellet imaging device is most sensitive in detecting displacements in the flux surface and perpendicular to the magnetic field,[5] we therefore limited our analysis to the radial component of the electric field which gives rise to drifts perpendicular to the field, $E_r = -\hat{r} \cdot \vec{\nabla}\delta\phi$.

Additionally, to transform the simulation results into a form that is consistent with the pellet imaging diagnostic, the electric field data was boxcar averaged in the spatial and temporal domains. The radial electric field from the simulation was averaged over a temporal domain consistent with the integration time of the PSI-IV camera, $2\mu s$. Similarly, because the filaments are of finite extent in the cross field direction, the E_r data was averaged over a boxcar of $2mm$ in the radial direction, and $1cm$ in the poloidal direction. The radial direction was limited to $2mm$ because we have no information on the radial extent of the filament, and based on maximum velocity of the pellets, $\sim 1000m/s$, $2mm$ is the maximum distance covered by the pellet during the $2\mu s$ integration time. Previous studies from ASDEX [29] and TEXT [7], where the pellet injections are observed from above and below, indicate that the filaments are most likely of similar spatial extent in all directions perpendicular to the magnetic field. Figure 5-11 illustrates the steps in the post simulation processing.

Once the potential data had been processed to make it consistent with the measurements of the pellet imaging diagnostic, it was compiled into a histogram in order to form a distribution function to be compared to the filament distribution functions. For determination of the histogram, each grid-location in the expansion was weighted by its relative area on the entire grid, so that the histogram represents the probability of a measurement at a random location and time which yields a specific electric field. Figure 5-12 shows an example of a distribution calculated from a flux tube run.

In addition to ensuring that the simulations were numerically stable and compu-

[5]Recall that due to the narrow angle of incidence between the two viewing optics the pellet imaging diagnostic was only $1/3^{rd}$ as sensitive in the radial direction, and due to the fact that the filaments are extended and amorphous in the direction parallel to the field, the exact location of the filament in that dimension is difficult to determine.

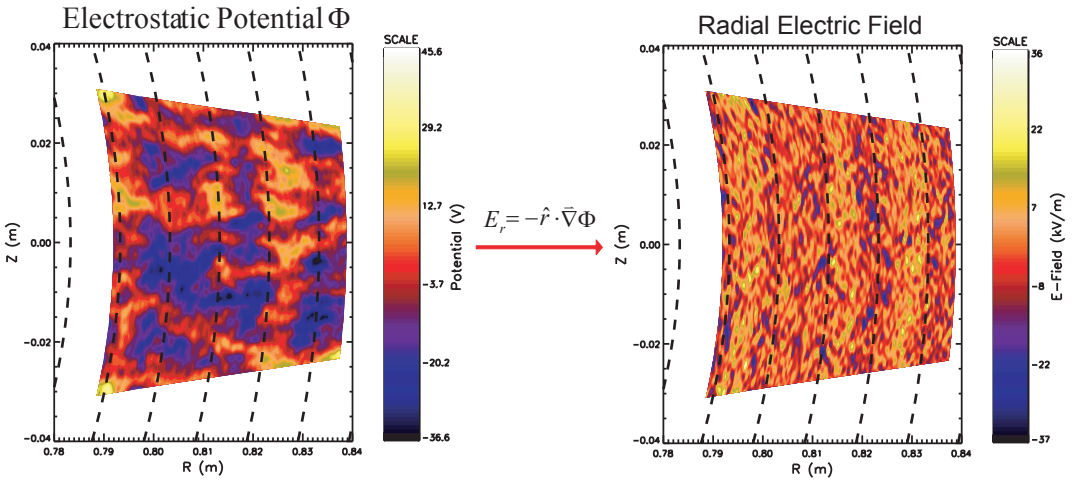

(a) $\Phi \rightarrow E_r$

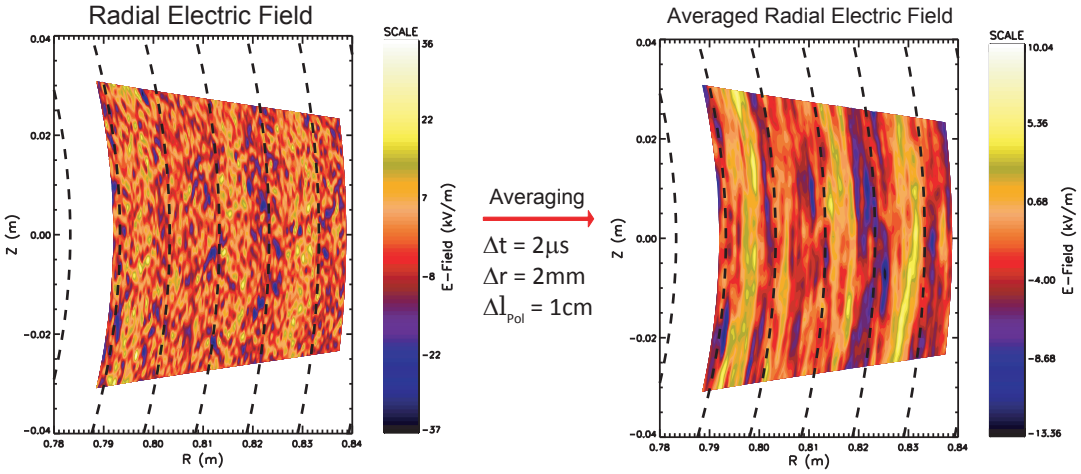

(b) $E_r \rightarrow \langle E_r \rangle_{t,r,\theta}$

Figure 5-11: Example of the post processing that occurs on the electrostatic potential calculated by GYRO (the black dashed lines are the flux surfaces for the discharge as calculated by an EFIT magnetic reconstruction). a) Conversion of the potential to the radial electric field. b) Boxcar averaging of E_r to make it consistent with the capabilities of the pellet imaging diagnostic.

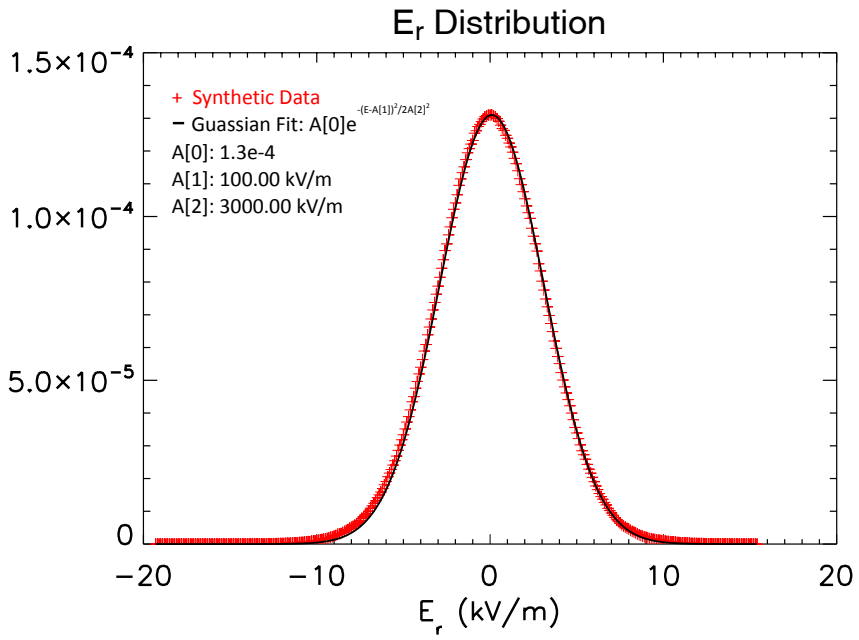

Figure 5-12: Example of the Probability Distribution Function of radial electric fields calculated from a gyro run. Distribution is normalized so that the total area under the curve is one.

tationally converged, it was also necessary to ensure that the simulations were run for a sufficient number of time steps such that the distributions were statistically stationary, i.e. the statistical properties such as mean and standard deviation were no longer changing. To this end studies were performed in which the simulations were run for dramatically longer periods than were necessary for convergence, $\sim 4000\ a/C_s$. These simulations were then broken into bins, which were used to determine electric field distributions. The variations of the statistical properties, as a function of the binsize were then used to guage the length of time necessary to gather a statistically stationary amount of data. Figure 5-13 shows an example of the variation of distribution width as a function of binsize for a simulation. For the simulations in our study it was found that a time interval of approximately 500 a/C_s was appropriate to gather statistical data. Beyond this diminishing marginal gains in variation reduction made extending the run unnecessary.

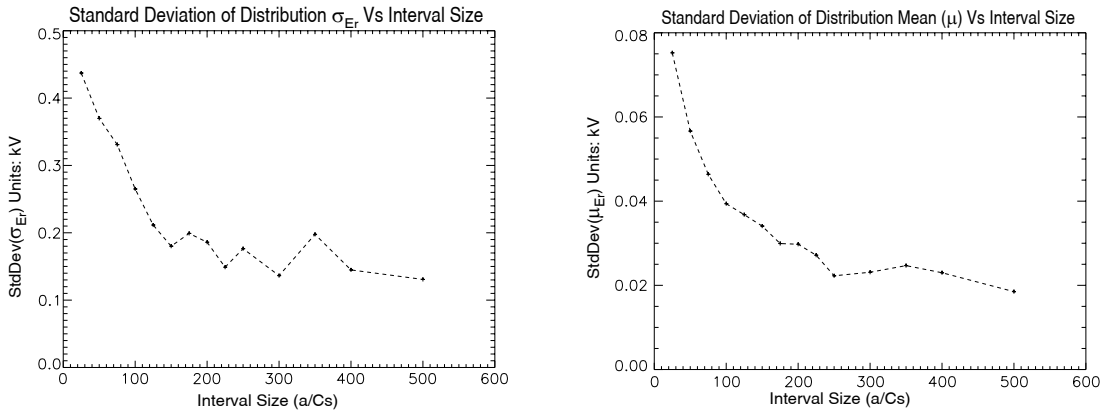

(a) (b)

Figure 5-13: The standard deviation of the distribution standard deviations (a) and means (b) as a function of the size of the interval used to construct the distribution.

5.3 Safety Factor Scan

As a starting place for our comparison of turbulence and the properties of the filaments, we conducted a scan in the local safety factor to test whether the filaments' velocity dependence on q was mirrored in the ExB drifts of turbulence. We chose to

run the code in flux tube mode in this series of simulations because it allowed us to limit the number of external factors that could be causing a variation in the turbulence properties. Recall that flux tube simulations have periodic boundary conditions and all plasma parameters are constant across the entire domain. Every point in the domain is thus effectively identical to every other point in the domain. This means that when we compile the data in order to determine statistical properties, we may use any point in the domain without worrying about how far we are from our typical value of the safety factor, or worry about how variations in other plasma parameters, or nonlocal effects such as turbulence spreading, might affect the results. Furthermore, since all the points are identical, we may use data from the entire domain to compile the distribution.

For model profiles we chose shot 1070821030 at $t = 1.7s$, a Lower Single Null (LSN) ohmic L-mode plasma[6]. Figure 5-14 shows diagnostic traces of the discharge while figures 5-15a and 5-15b show the pre-pellet electron density and temperature profiles, determined from Thomson scattering, used for the simulation in comparison to the rest of the pellet injection database. This shot was chosen because it was, in some sense, representative of the entire database in terms of the temperatures and densities and their gradients. The exact choice of profiles was in some ways quite arbitrary. The formation of the filaments is a ubiquitous phenomena, and thus cannot extremely sensitive to the exact shape of the plasma profiles. Also shown in figures 5-15a and 5-15b, are the radial locations chosen for the flux tube simulations. These locations were chosen to form approximately equidistant intervals in the safety factor (see figure 5-16).

5.3.1 Results From Safety Factor Scan

As an initial check we examined the radial and temporal correlation functions on the mid-plane to verify that the filaments produced fields with structures that were

[6]Prior to the injection, RF-power was used to heat the plasmas, as can be seen by inspection of the diagnostic traces of the shot in figure 5-14. The injection occures $200ms$ after the termination RF heating by which time the plasma has relaxed back to an ohmic state.

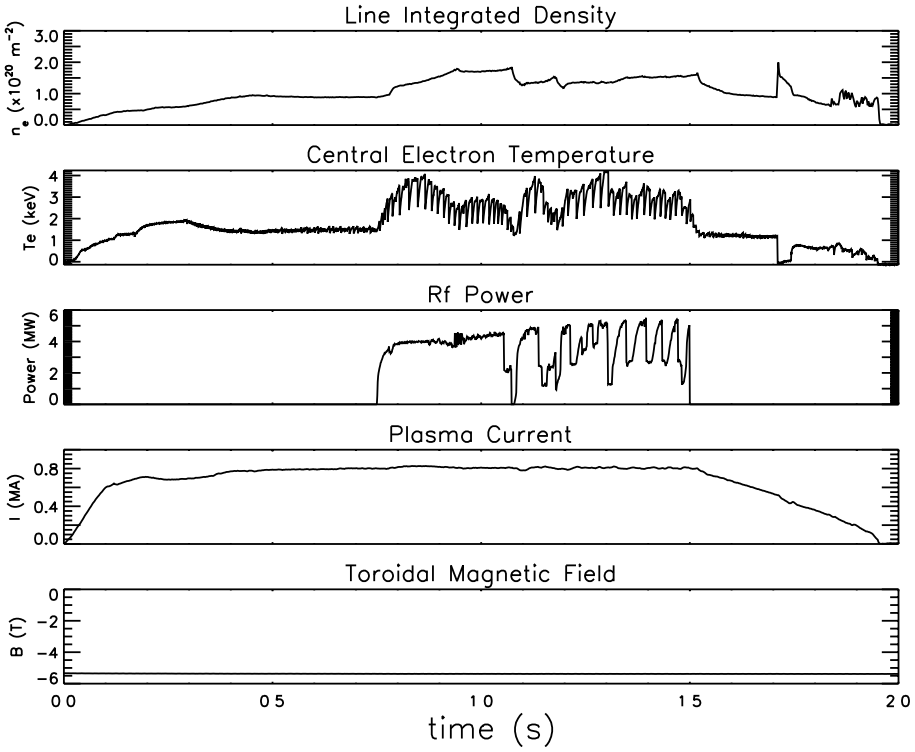

Figure 5-14: Diagnostic Traces Shot:1070821030. From the top down, n_e from TCI, T_e from GPC, RF power, plasma current, toroidal magnetic field on axis.

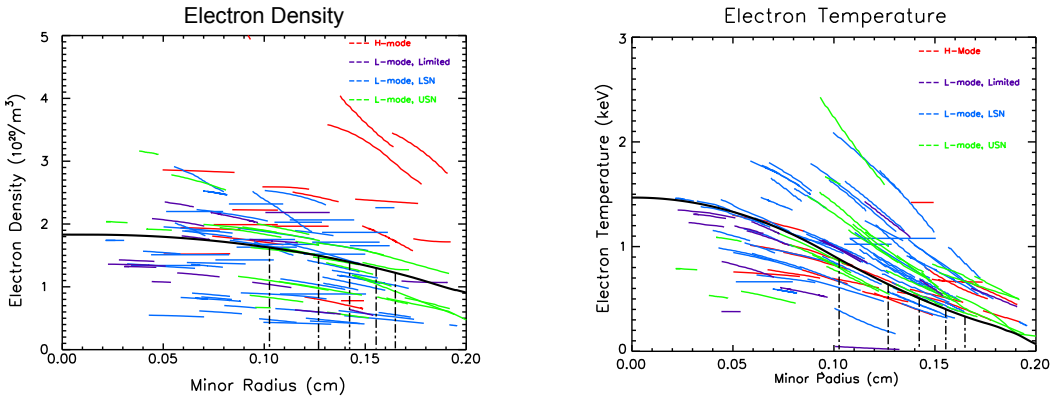

(a) (b)

Figure 5-15: n_e (a) and T_e (b) Profiles for the pellet injection data base. The curves in black are profiles from C-Mod shot: 1070821030, which are the base profiles for the GYRO q-scan.

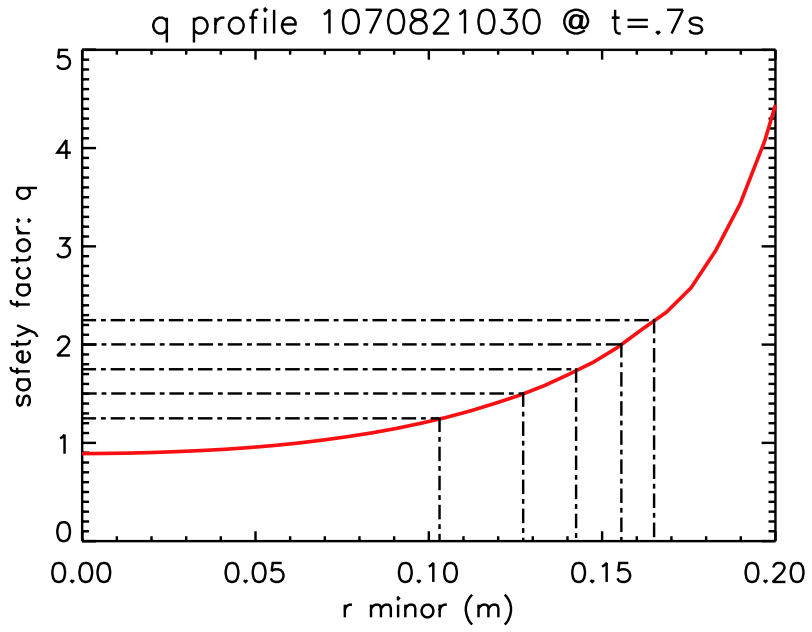

Figure 5-16: q-profile, C-Mod Shot: 1070821030

consistent with our observations of the filaments. We define the temporal correlation function as,

$$C(\tau) = \frac{\langle E_r\left(r, \theta = 0, t\right) E_r\left(r, \theta = 0, t + \tau\right)\rangle_{r,t}}{\langle {E_r}^2\left(r, \theta = 0, t\right)\rangle_{r,t}} \tag{5.11}$$

where $\langle ... \rangle_{r,t}$, denotes an averaging over all times and radii. To avoid artifacts in the correlation functions created by boxcar averaging, the electric field data was taken directly from the radial derivative of the GYRO potential data.

Figure 5-18a shows the temporal correlation functions for the simulations at $q = 1.25, 1.76$ & 2.25. Defining the correlation time as the time required for the correlation function to drop to $1/e \approx .36$, figure 5-18a indicates that the radial electric fields remain correlated for a period of only $3 - 4\ \mu s$. This of the same order as what is observed in the filaments formed during the ablation, which are observed to persist for $\sim 8\ \mu s$, but it too short to be truly consistent. It may be noted that the correlation functions become more sinusoidal at larger q, which is indica-

tive of a coherent fluctuation in the radial electric field. One possible explanation for the coherent fluctuation would be the increased appearance of GAMs which are expected to be stronger at larger safety factor as noted in section 3.6, but the apparent frequency of $\sim 65kHz$, $T \sim 15\ \mu s$, is approximately twice the expected GAM frequency, which using equation 3.13 and the plasma conditions in the q=2.25 simulation, ($C_s = 1.32 \times 10^5\ m/s, R_{maj} = .83\ m$) is calculated to be $\sim 35kHz$

In addition to the standard temporal correlation time, where the electric field is compared at the same spatial location but at two different times, we also considered what may be termed a drift adjusted correlation. In the drift adjusted correlation we compare the electric field at some initial time and location, (r_0, θ_0, t_0), with the field at a later time and different poloidal location, $(r_0, \theta_0 + \Delta\theta, t_0 + \Delta t)$, where the new location is chosen such it is at the place where the a fluid element at the original location would have drifted to in the time Δt, as shown in figure 5-17.

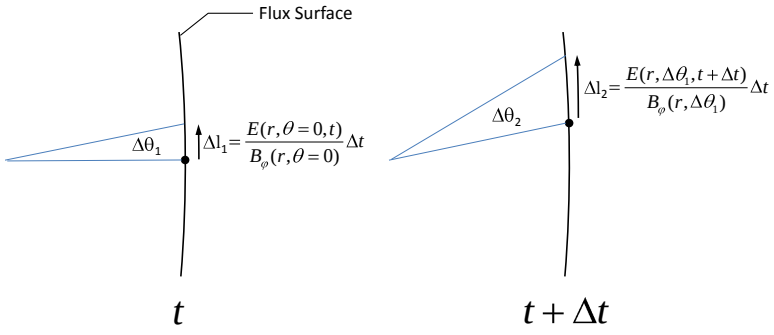

Figure 5-17: Diagram of how the locations are chosen for the drift adjusted correlation time. The location at each time is determined by the drift due electric field at the previous location.

Mathematically we define the drift adjusted correlation function as,

$$C(\tau) = \frac{\left\langle E_r^{\tau}\left(r, \theta = 0, t\right) E_r^{\tau}\left(r, \sum_i^N \Delta\theta_i, t + \tau\right)\right\rangle_t}{\left\langle E_r^{\tau\,2}\left(r, \theta = 0, t\right)\right\rangle_t} \tag{5.12}$$

where $\tau = \sum_i^N \Delta t = N\Delta t$ is the time since the first observation, $\sum_i^N \Delta\theta_i$ is the total poloidal extent traversed since the first observation. $\Delta\theta_i$ is the poloidal distance drifted since the last time step, and is defined as the angle necessary to cover a distance Δl_i defined as,

$$\Delta l_i = \frac{E_r\left(r, \theta_{N-1}, t + (N-1)\Delta t\right) B_\varphi\left(r, \theta_{N-1}\right)}{B^2\left(r, \theta_{N-1}\right)} \Delta t \tag{5.13}$$

where $\theta_{N-1} \equiv \sum_j^{N-1} \Delta\theta_j$.

The fact that we have a finite domain has to be factored into our definition of the adjusted correlation function. For instance, it is possible for fluid elements to drift completely the domain, and for that reason only fluid elements that remained within the domain out to a time, T, were computed in the averaging. We denote these fields as E_r^τ.

The drift adjusted correlation function is more consistent with the experimental data from the pellet injection since we only measure the electric field at the location of the filament. Since the filaments location change with time, so should the location at which we take the correlation function. An additional motivation for this method arises from a visual examination of the GYRO output. When one observes a time sequence of the electric fields generated by GYRO, it is apparent that the structures within the fields drift poloidally, and thus it seems possible that although the filament moves a substantial distance in the poloidal direction, the electric field that causes this motion may not be poloidally elongated.

Figure 5-18b shows the drift adjusted correlation times for $q = 1.25, 1.76$ & 2.25. Comparing with figure 5-18a we see that there is very little difference between the drift adjusted correlation times and the standard correlation times, indicating that the decorrelation of the fields after $3 - 4\mu s$ is a result temporal evolution of the turbulence, and not its spatial evolution.

Turning to spatial correlations, the radial correlation function as,

$$C(R) = \frac{\left\langle E_r\left(r, \theta = 0, t\right) E_r\left(r + R, \theta = 0, t\right)\right\rangle_{r,t}}{\left\langle {E_r}^2\left(r, \theta = 0, t\right)\right\rangle_{r,t}} \tag{5.14}$$

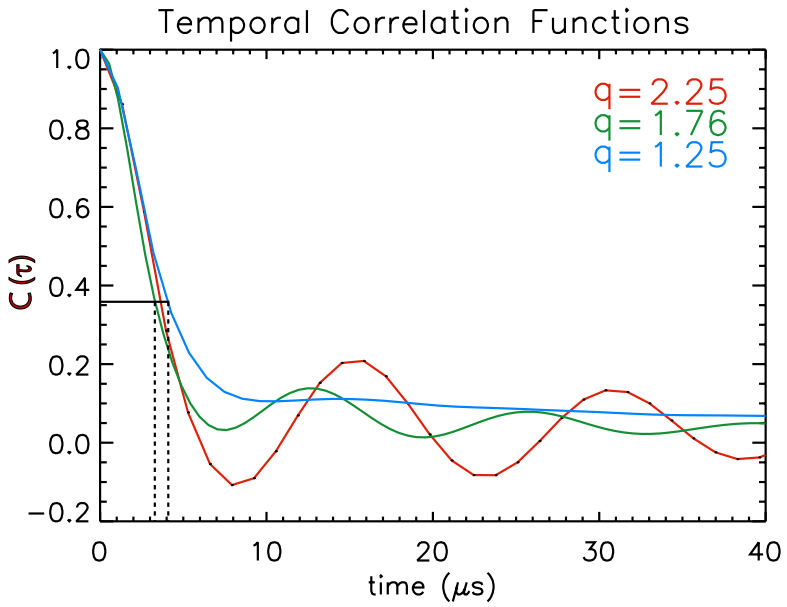

(a)

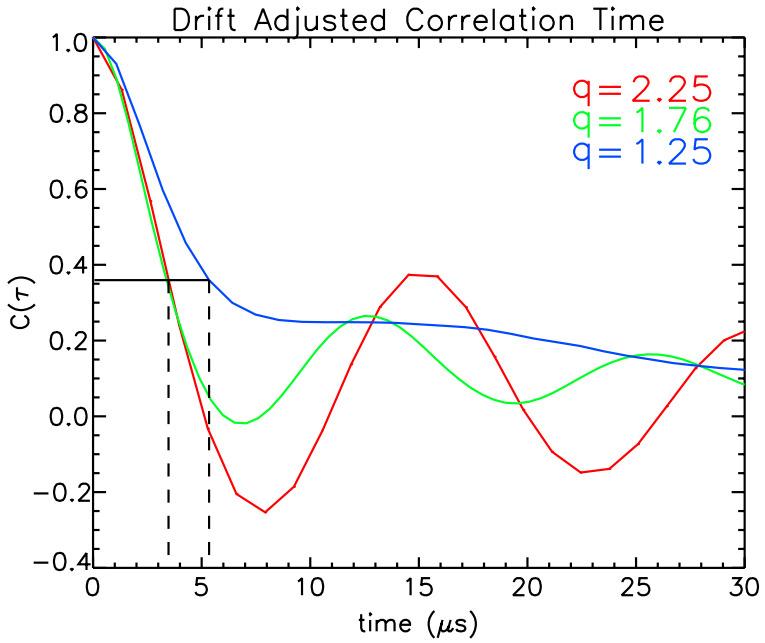

(b)

Figure 5-18: Standard temporal correlation functions (a) and drift adjusted correlation functions (b) for the simulations at $q = 1.25, 1.76$ & 2.25. The Correlation times, taken as τ at the $1/e$ value of the correlation function, range from $3-4\mu s$. Note that the the correlation functions develop a pronounced oscillation as one progresses from lower to higher values of the safety factor.

and the radial correlation lengths for the simulations at $q = 1.25, 1.76$ & 2.25 are shown in figure 5-19. Again taking the distance it takes the correlation function to drop to $1/e$ as the correlation length, we see that the radial electric fields are only correlated over a distance of a few millimeters, which is consistent with our inferred width for the filaments.

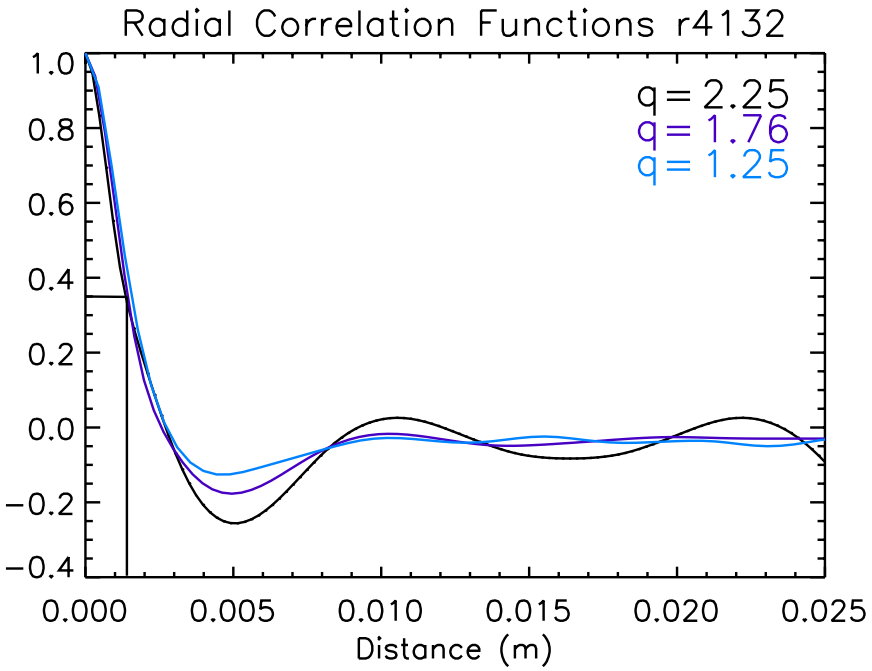

Figure 5-19: Radial correlation functions for the simulations located at $q = 1.25, 1.76$ & 2.25. The Correlation length, taken as R at the $1/e$ value of the correlation functions are all approximately $1.4mm$

Figure 5-20 shows the distribution widths and means of the radial electric fields that resulted from the q-scan with GYRO simulations. These results should be compared to the figures 4-19 from section 4.6.1 detailing to properties of the filament distributions. Since GYRO calculates only the fluctuating components of the potential, the distributions should have zero mean,as is indicated in figure 5-20a.

Figure 5-21 shows a direct comparison of the standard deviation of the inferred ExB drift velocities from GYRO with the standard deviations determined from the filament drift distributions. Several observations warrant discussion. First, the drifts

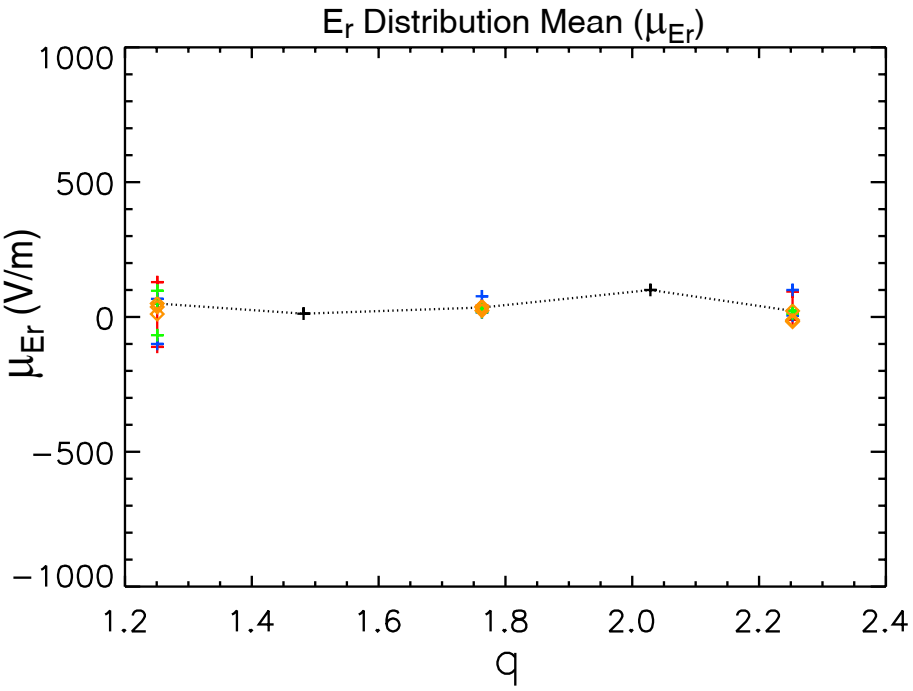

(a)

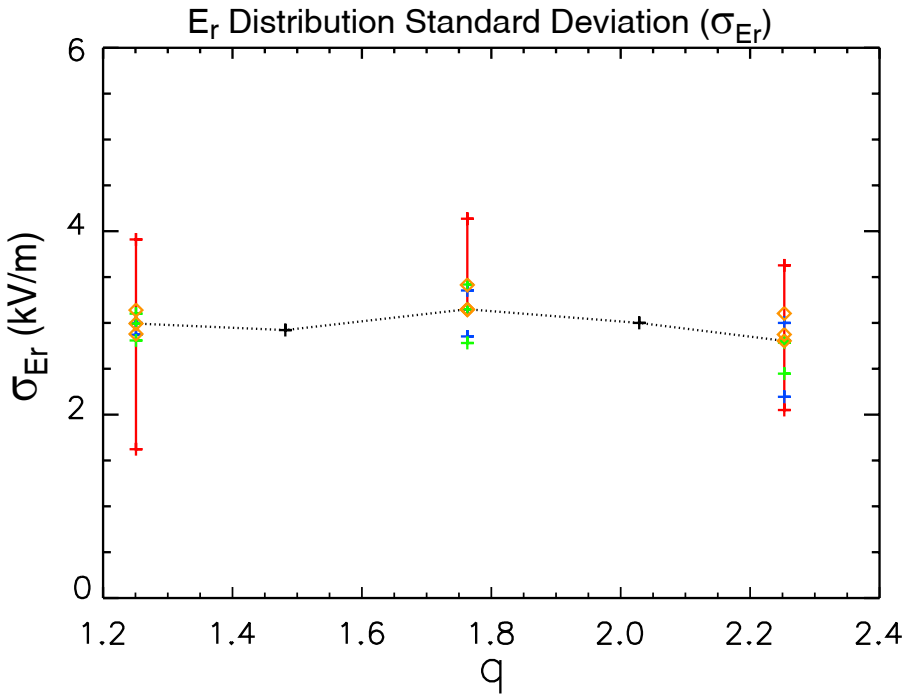

(b)

Figure 5-20: The mean (a) and standard deviation (b) of the E_r distributions from GYRO as a function of the local safety factor. That the means are within the error bars of zero is expected since GYRO returns only the fluctuating components of the electric potential.

that would result from the fields observed during the GYRO simulation are about a factor of $5-10$ smaller than what is necessary to produce the filament drifts observed during the injection experiments. Second, the widths of the distributions determined from the GYRO data does not show the pronounced downward trend with q seen in the experimental filament velocity distributions. Indeed any trend in the GYRO results is small compared to the variation introduced by the uncertainties in the measured plasma parameters, as can be seen by the quoted error bars on the simulation results.

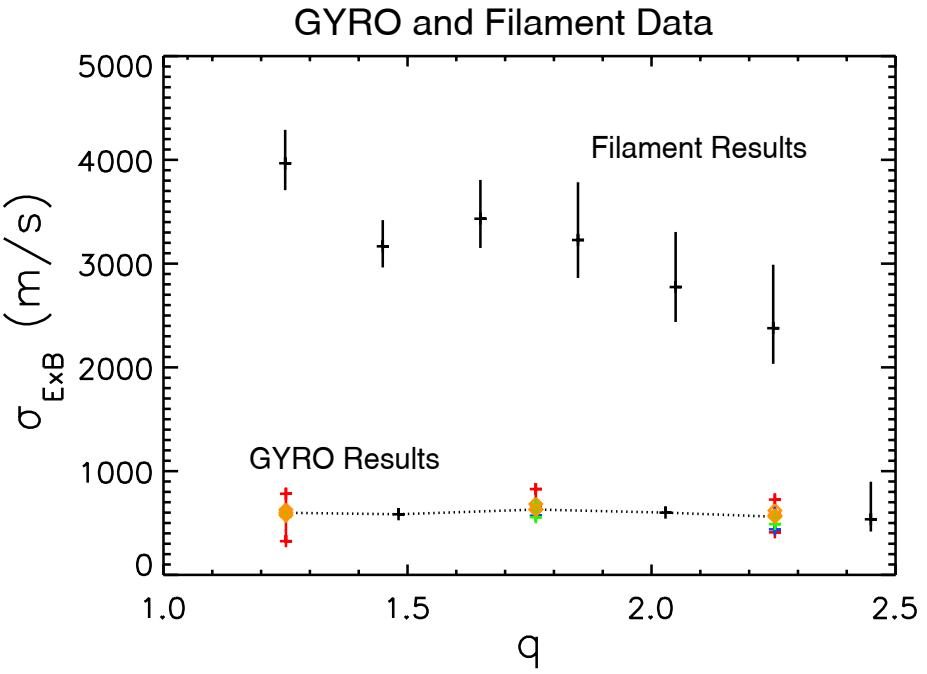

Figure 5-21: Comparison of the standard deviation of the filament velocity distribution and GYRO's radial electric field distribution.

A close inspection of the stability runs shows that the largest source of variation in the GYRO data results from the uncertainties in the ion temperature gradient scale length, L_{T_i}. For the C-Mod shots used in this study, no diagnostic was available to directly measure the ion temperature gradients. The ion temperature profile was inferred by the transport code TRANSP using electron temperature, the electron density and the neutron rate. Experience with the fitting routines used to determine the electron temperature profiles indicate that profiles consistent with the Thomson

data could be generated with gradient scale lengths that differed by as much as 20%. This seems like the most reasonable level to set the uncertainty in the ion temperature scale length, since the electron profiles form the basis of the ion temperature estimate. Figure 5-22a shows the effect on the E_r distribution widths as a function of the inverse ion temperature gradient scale length. It is interesting to note, that although a/L_{T_i} more than doubles as one moves from $q = 1.25 - 2.25$ in a profile consistent manner, the standard deviation of the E_r distributions changes by only about 5%. On the other hand, if only L_{T_i} is changed, holding all other parameters constant, the E_r standard deviation can change by as much as 50%.

Similarly, the ion density gradient scale length, L_{n_i}, had a large effect on the E_r distribution widths, as shown in figure 5-22b. Unlike L_{T_i}, which monotonically increased the distribution width as the temperature gradient steepened, σ_{E_r} appears to peak around a/Ln_i from $0.15 - 0.20$, though more investigation would be required to ensure that this is not a result of a the particular choice of parameters.

5.4 Injection Consistent Profiles

5.4.1 Overview

As noted in chapter 2, it has been observed that the injection of solid pellets into a tokamak discharge is accompanied by dramatic changes in the plasma temperature and density profiles (see figures 5-23a and 5-23b). These changes in the profiles can be expected to significantly change the drivers of plasma turbulence which undoubtedly results in large changes to the turbulence spectrum. This notion is corroborated by the observation of nonlocal response of the plasma electron temperature (see section 2.3.1), which indicates that the injection is accompanied by changes in plasma transport, and by inference in the plasma turbulence. We hypothesize then, that the filament drifts could be the result of the turbulence generated by the injection perturbations.

The next step in our investigation was to use GYRO to simulate plasmas with

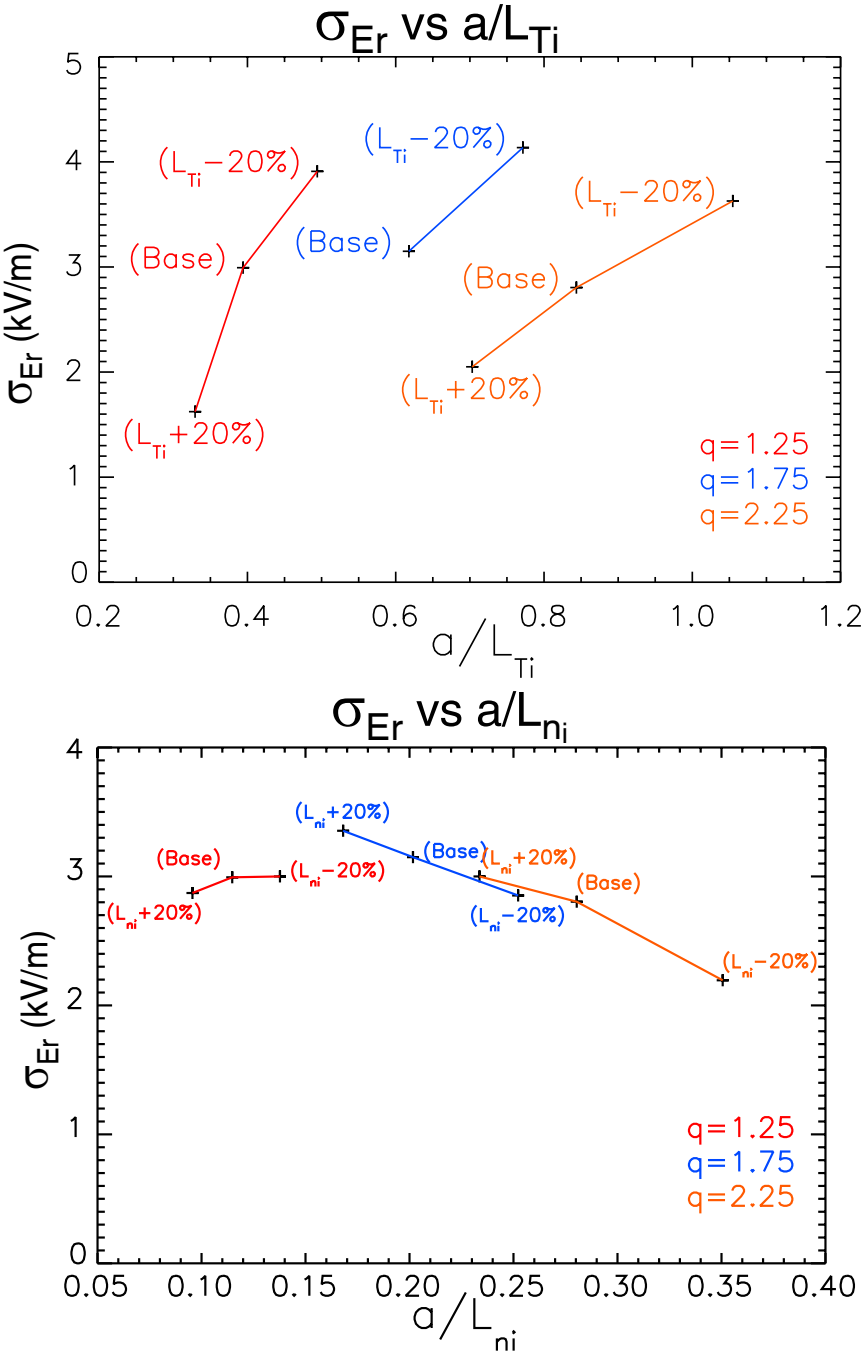

Figure 5-22: Effect of the ion temperature (a) and density (b) gradient on the width of the E_r distribution. The point labeled Base corresponds to the gradient scale lengths taken from TRANSP. The points labeled $L_{T_i/n_i} \pm 20\%$ indicate the results from simulations where all parameters were kept constant except gradient scale length of interest, which was adjusted by $\pm 20\%$.

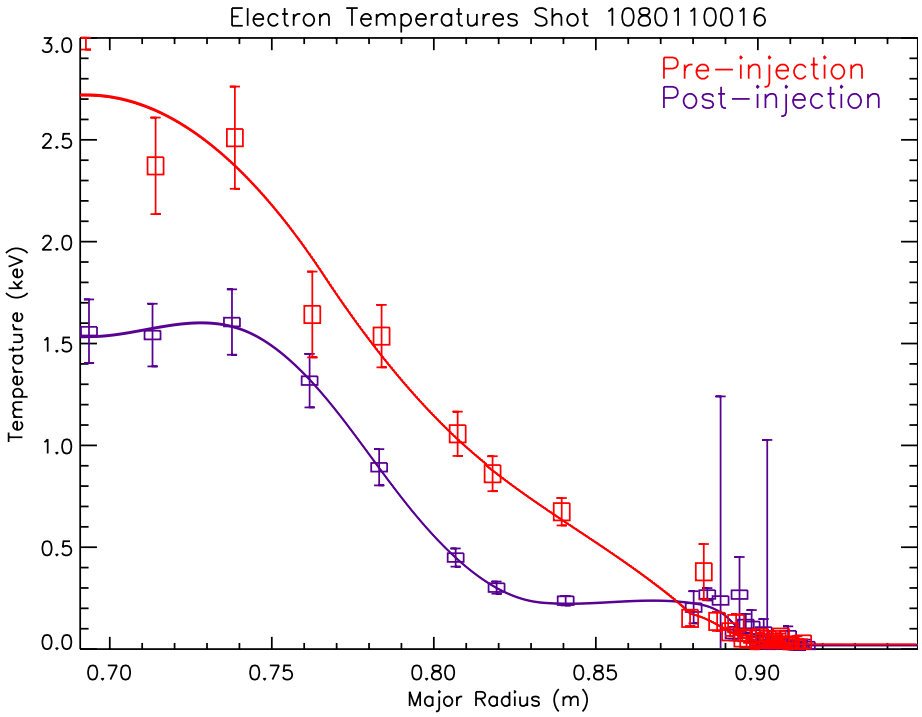

(a)

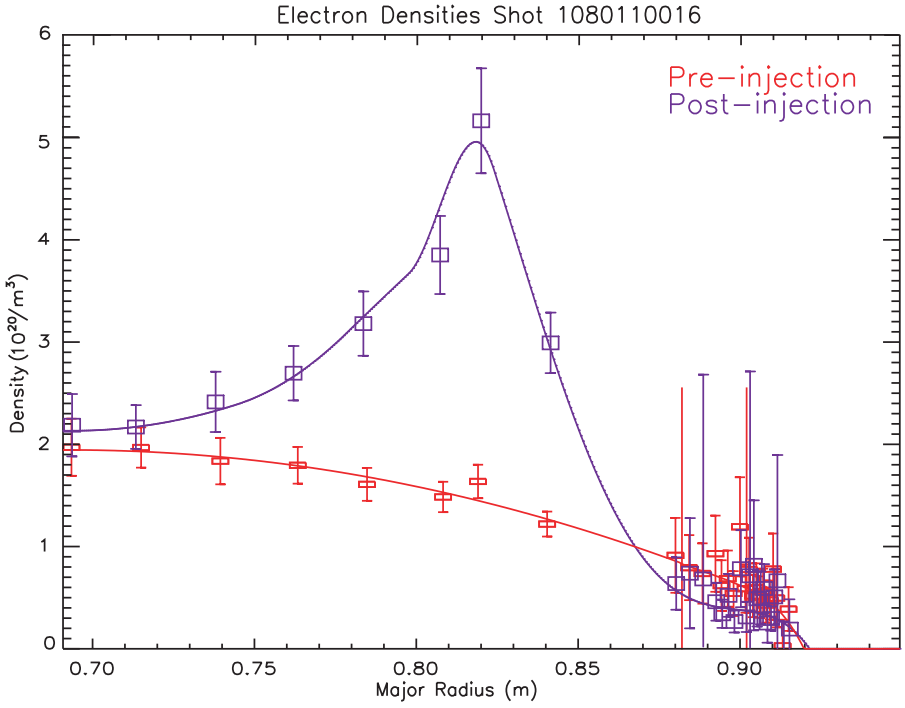

(b)

Figure 5-23: Electron Temperature (a) and density (b) profiles from just prior to (red) and during (blue) the pellet injection.

conditions similar to what should be prevalent during the injection. GYRO calculates turbulence in equilibrium plasma conditions, and does not accurately calculate transient conditions. This means that GYRO's calculation will only be an accurate representation of the plasma turbulence if the plasma conditions are stationary with respect to the relevant turbulent time scales. In light of this, our investigation of the possible effects the pellet injection has on the plasma turbulence proceeded in three steps. The first step was to determine a model that was representative of the plasma conditions during the injection. Once this was done, we used the modeled plasma conditions to calculate the linear growth rate of toroidal modes in the plasma. These growth rates represent the time scale of plasma response to small perturbations, and, in essence, they represent the characteristic timescale for the evolution of the turbulence. This investigation revealed that the turbulence is evolving on time scale that is fast compared to that of the pellet injection, and thus it's plausible that the turbulence remains in a quasi-saturated state throughout the injection. From that point we moved on to the third step and performed a global nonlinear simulation using the plasma profiles modeled on the pellet injection. As might be expected, the pellet consistent profiles produced levels of turbulence significantly larger than the background profiles used for the q-scan.

In the section that follows we briefly describe the model used for the pellet-consistent profiles. We then move on to discuss the parameters for the linear runs, and their results; and conclude with the results from the global nonlinear run.

5.4.2 Pellet Consistent Profiles

Our aim in the choice of model used to generate the pellet consistent profiles was to match the electron temperature and density response, which are the only parameters for which we have good measurements, and make reasonable assumptions about the corresponding response of the lithium and deuterium ions to determine their temperature and density profiles. This model follows the work that was done by Camilo Gomez's [93]. Although the model was developed for frozen hydrogen pellets, it only followed the electron dynamics, which are governed by the spatial and tempo-

ral characteristics of their deposition by the pellet. As mentioned in section 2.1.1, the deposition characteristics are described by the NGS model for all pellets of light nuclei, and thus in this respect the Lithium and Hydrogen pellets should be identical.

The model begins by breaking the electron response into two parts, $\left[\overline{T}_e, \overline{n}_e\right]$ which correspond to the background conditions prior to injection, and $\left[\tilde{T}_e, \tilde{n}_e\right]$ which represent the changes caused by the pellet. Note, there is no restriction on the size of $\tilde{T}_e/\overline{T}_e$ or $\tilde{n}_e/\overline{n}_e$, rather this division is used as a bookkeeping measure. We expect that the background profiles satisfy the full set of transport equations under the conditions that prevailed prior to the injection, and that the evolution of the perturbation profiles will be dominated by the effects of diffusion and collisional energy exchange among species. The model used to generate the pellet-consistent profiles is given by equations 5.15 through 5.20. For a complete discussion of the model, please see appendix C.

$$\frac{\partial}{\partial t}\tilde{n}_e = \frac{1}{r}\frac{\partial}{\partial r} r D_e \frac{\partial}{\partial r}\tilde{n}_e + S_n \tag{5.15}$$

$$\begin{aligned}\frac{\partial}{\partial t}\tilde{T}_e = &- \left(\frac{\overline{T}_e + \tilde{T}_e}{\overline{n}_e + \tilde{n}_e}\right)\frac{\partial}{\partial t}\tilde{n}_e \\ &+ \frac{2}{3r(\overline{n}_e + \tilde{n}_e)}\frac{\partial}{\partial r}\left[r\chi_e\left((\overline{n}_e + \tilde{n}_e)\frac{\partial}{\partial r}\tilde{T}_e + \tilde{n}_e\frac{\partial}{\partial r}\overline{T}_e\right)\right] \\ &+ \overline{\nu}_\epsilon^{ei}(T_i - [\tilde{T}_e + \overline{T}_e]) + \overline{\nu}_\epsilon^{eLi}(T_{Li} - [\tilde{T}_e + \overline{T}_e])\end{aligned} \tag{5.16}$$

$$\frac{\partial}{\partial t} n_i = 0 \tag{5.17}$$

$$\frac{\partial}{\partial t} T_i = \overline{\nu}_\epsilon^{ie}([\tilde{T}_e + \overline{T}_e] - T_i) + \overline{\nu}_\epsilon^{iLi}(T_{Li} - T_i) \tag{5.18}$$

$$3\frac{\partial}{\partial t}n_{Li} = \frac{\partial}{\partial t}\tilde{n}_e \tag{5.19}$$

$$\begin{aligned}\frac{\partial}{\partial t}T_{Li} = &-\left(\frac{T_{Li}}{n_{Li}}\right)\frac{\partial}{\partial t}n_{Li} \\ &+\frac{2}{3rn_{Li}}\frac{\partial}{\partial r}\left[r\chi_{Li}n_{Li}\frac{\partial}{\partial r}T_{Li}\right] \\ &+\overline{\nu}_{\epsilon}^{Lie}([\tilde{T}_e+\overline{T}_e]-T_{Li})+\overline{\nu}_{\epsilon}^{Li\,i}(T_i-T_{Li})\end{aligned} \tag{5.20}$$

where $\overline{\nu}_{\epsilon}^{ij}$ is the energy exchange collision frequency between the i^{th} and j^{th} species, χ_{Li} is the lithium thermal diffusivity, χ_e and D_e are the electron thermal and particle diffusivities, and S_n is the electron source term represented by the pellet. The source term in equation 5.15 is chosen to satisfy three criteria: 1. the particle source is Gaussian in space and moves at the pellet velocity, v_p; 2. the total number of electrons deposited, N_{tot}, is equal to the total number of electrons in the pellet; 3. the electron deposition profile is consistent with the canonical shape of H_α emissions from pellet injection, see figure 5-24. Taken together, this gives the source term the following form.

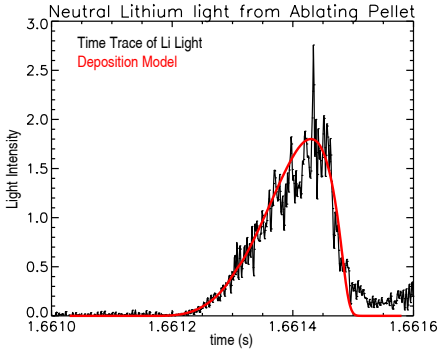

Figure 5-24: Plot of the emitted neutral lithium light on Alcator C-Mod during a lithium pellet injection. The smooth curve is the integrated source term, $\int S_n dr$ from equation 5.21.

$$S_n = \frac{5.28 v_p N_{tot}}{\sqrt{\pi}\sigma L \frac{\partial V_{flux}(r)}{\partial r}} \mathrm{e}^{\frac{-((r_{edge}-r)-v_p t)^2}{\sigma^2}} \left(\frac{v_p t}{L}\right) \sin\frac{\pi v_p t}{L} \tag{5.21}$$

Figures 5-25 and , shows the time evolution of the electron, deuterium, and lithium density and temperature profiles for $\chi_e = 10m^2/s$, $D_e = 10m^2/s$ and $\chi_{Li} = 0m^2/s$. These parameters were chosen such that the evolution of the electron temperature profiles most nearly matched the density and temperature profiles as seen on the Thomson Scattering, see figure 5-23.

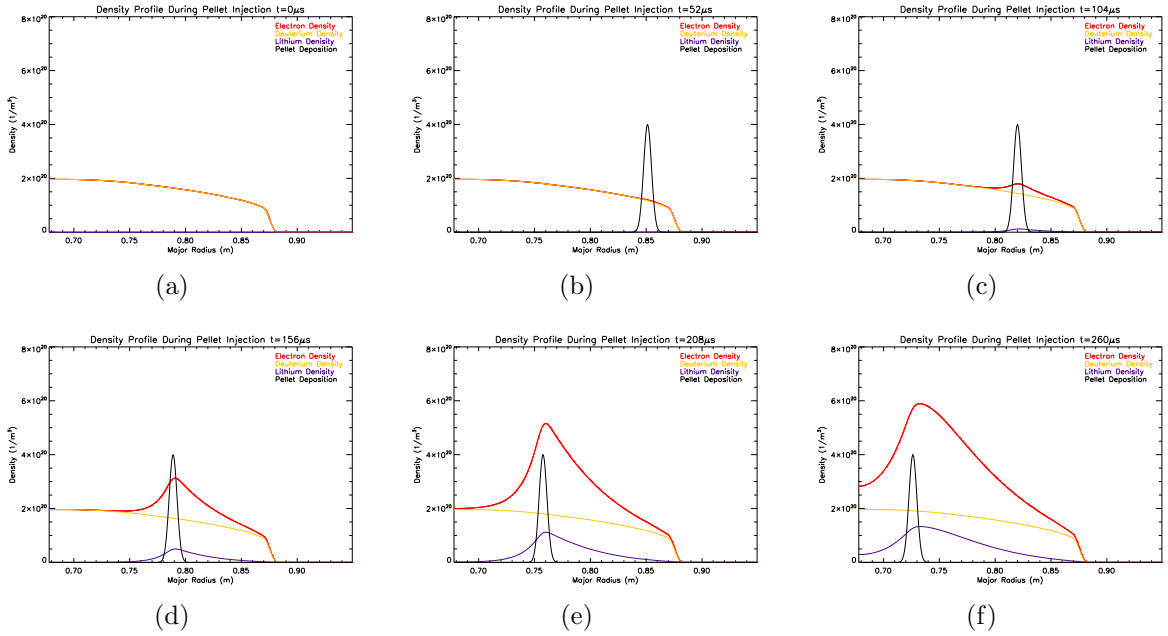

Figure 5-25: Time sequence of density profiles using the model from equations 5.15 through 5.20. Time for each frame: (a) 0μs, (b) 52μs, (c) 104μs, (d) 156μs, (e) 208μs, (f) 260μs

Examining the profiles, there are a few interesting features that result from the model. The first is that, due to diffusion, the plasma is cooled ahead of the pellet, with the result that the region of steepened temperature gradient proceeds the pellet. Additionally, the high electron density leads to a relatively rapid cooling of the ions, on the time scale of the pellet injection, with the effect that the deuterium temperature gradient steepens significantly in the region near the pellet. This creates an interesting situation where the regions with steep gradients in T_e and T_i are separated by a distance of order 10 ion gyro radii.

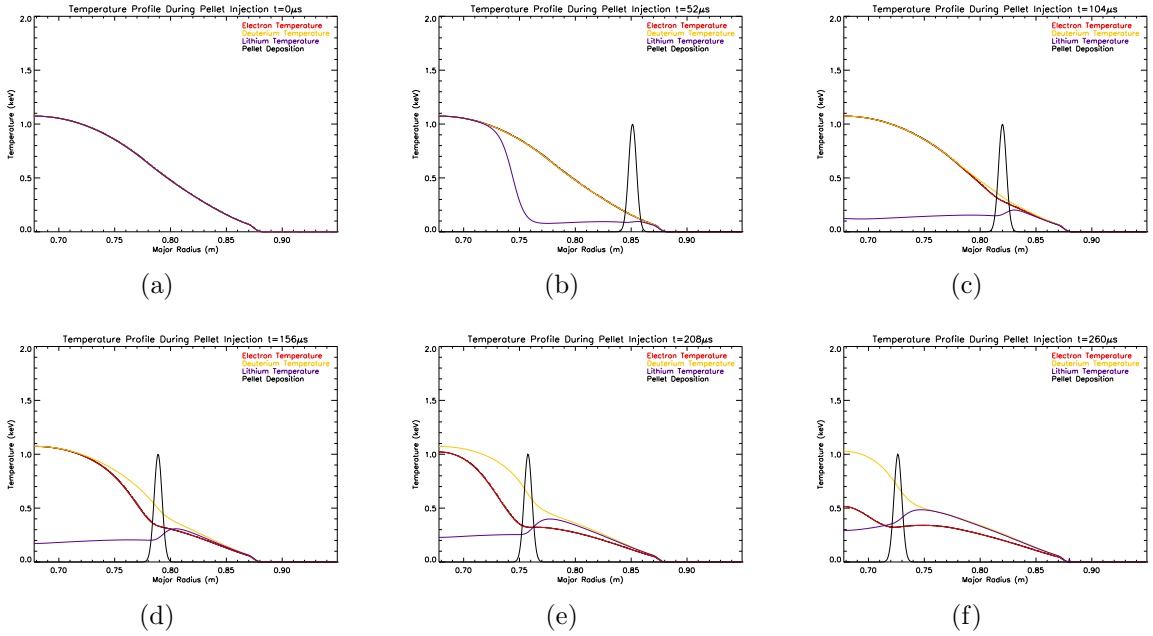

Figure 5-26: Time sequence of temperature profiles using the model from equations 5.15 through 5.20. Time for each frame: (a) 0μs, (b) 52μs, (c) 104μs, (d) 156μs, (e) 208μs, (f) 260μs. Note the spatial separation between the region of steep electron and ion temperature gradients.

5.4.3 Linear Runs

Since GYRO calculates equilibrium turbulence levels, an important issue to be considered is the difference in time scales for the evolution of the plasma turbulence compared to the evolution of the plasma profiles. If the plasma profiles evolve slowly compared to the plasma turbulence, then it is not improbable that the turbulence remains in a quasi-saturated state throughout the injection process, and thus the results of the GYRO simulation can be expected to represent the properties of the plasma turbulence. On the other hand, if the turbulence evolves on a time scale slow compared to the profile evolution, then the plasma could be expected to be in a transient state during the injection, which would make it inappropriate for treatment by GYRO.

In order to address this issue, we examined the linear growth rate of turbulent modes in the pellet consistent profiles. The linear growth rate gives us a rough idea of how rapidly the turbulence will respond to conditions during the injection.

Considering that the pellet moves at a velocity of approximately 1000 m/s, and the ablation affects the profiles on a length scale that is of the order 5cm a head of the pellet then we expect that if the growth rates are much larger than 2×10^4 Hz ($\sim$ 1000 m/s / .05 m) then the plasma turbulence will remain in a quasi-saturated state.

The profiles selected for the GYRO runs are shown in figure 5-27, including black vertical lines which denote the locations chosen for the linear runs. These profiles are taken from 156 μs after the pellet enters the plasma, and the linear runs were chosen to cover a regular grid over the region of temperature and density perturbation caused by the pellet.

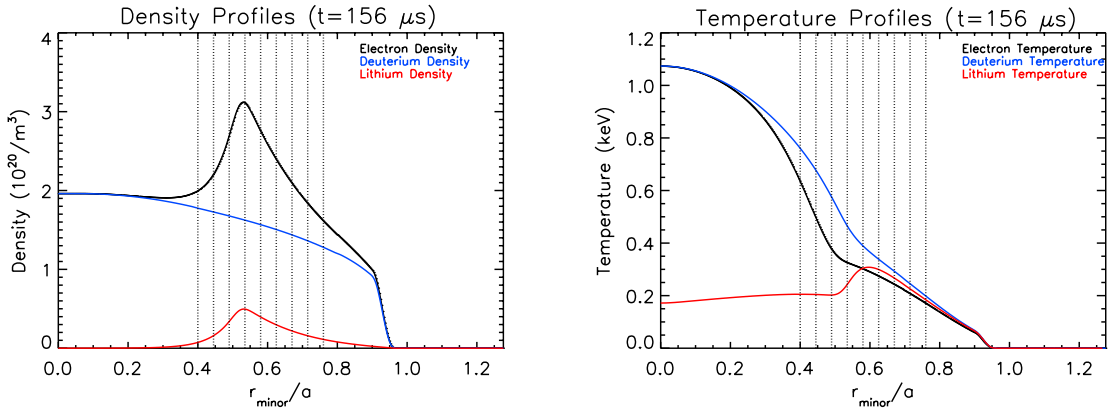

(a) (b)

Figure 5-27: Density (a) and temperature (b) profiles chosen for simulations. The dotted black lines denote the locations chosen for linear simulations.

Figures 5-28 show the linear growth rates as determined by GYRO for various locations for both pre-pellet and post-pellet plasma conditions. The inset in the figure gives the simulation location, the ordinate tracks the mode, in terms of $k_\theta \rho_s$, and the growth rate is plotted on the abscissa. Several key features can be noted, first, the linear growth rates in the region just interior to the pellet are above 400kHz, well above our threshold for stationary turbulence. That the growth rates are large in front of the pellet, along its trajectory, is important because in measuring the filaments we effectively only make measurements of the turbulence properties in a region very near the pellet. Thus so long as the plasma near the pellet is in a quasi-saturated state, GYRO's calculations can be compared to the filament data. Furthermore,

the remarkable change in growth rates between the pre-pellet and post-pellet plasma conditions strongly indicates that we can expect significantly different turbulence in the two cases. Armed with these observations, we conclude that a global non-linear simulation of the post-pellet plasma profiles should provide meaningful results.

We also attempted a rough characterization of the modes in the region just ahead of the pellet, where the linear growth rates are the largest. This was accomplished by performing a series of linear simulations based on the post-pellet profiles in which we varied parameters which are believed to play a role in modifying specific types of turbulence. The results of this investigation suggest that this region is dominated by a mixture of Ion Temperature Gradient (ITG) and Trapped Electron Modes (TEM). ITG modes propagate in the ion diamagnetic drift direction, are driven by the ion temperature gradient, and suppressed by the ion density gradient, whereas TEMs propagate in the opposite direction and are driven by the electron temperature and density gradients [94]. As shown in figure 5-29, the phase velocity of all modes in the region of the positive electron density gradient are in the ion diamagnetic direction[7], which is consistent with ITG modes.

Additionally, figure 5-30 shows the variation of the linear growth rates with a/L_{T_i}. The linear growth rates have a strong positive dependence on ion temperature gradient scale length, which is again consistent with ITGs.

The evidence for TEMs, on the other hand, is a bit ambiguous. The variation of the linear growth rates with the electron temperature gradient scale length, as can be seen in figure 5-31, is very modest except at short wavelengths, $k_\theta \rho_s > 1.0$, in the case where a/L_{T_e} is doubled. In this case dramatic increase in growth rates is most likely the result of Electron Temperature Gradient (ETG) modes driven unstable by the artificial increase electron temperature gradient, and is not representative of the base case. Evidence for the onset of the ETGs can be seen in the abrupt change in the phase velocity from the ion to the electron diamagnetic direction.

Conversely, there is a strong positive dependence on the density gradient scale

[7]In GYRO all wave vector are taken to be positive. The direction of the phase velocity is thus determined by the sign of the real frequency, ω_r, where positive frequencies propagate in the electron diamagnetic direction and negative frequencies propagate in the ion direction.

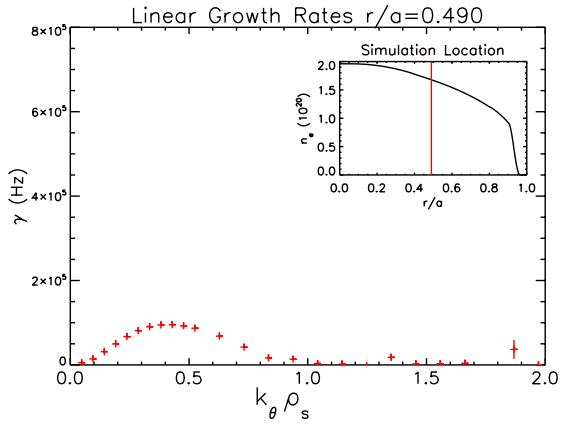

(a) Pre-Pellet

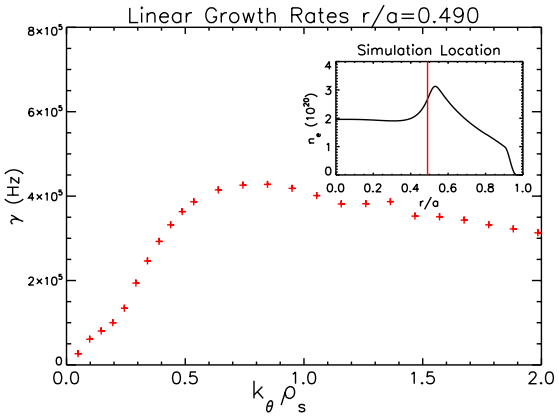

(b) Post-Pellet

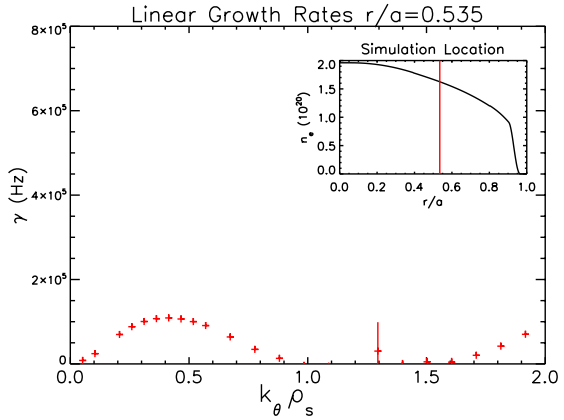

(c) Pre-Pellet

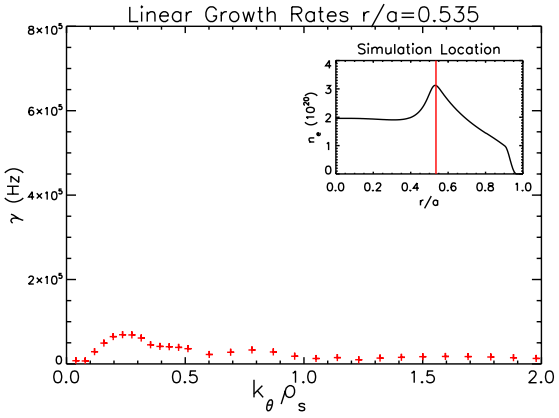

(d) Post-Pellet

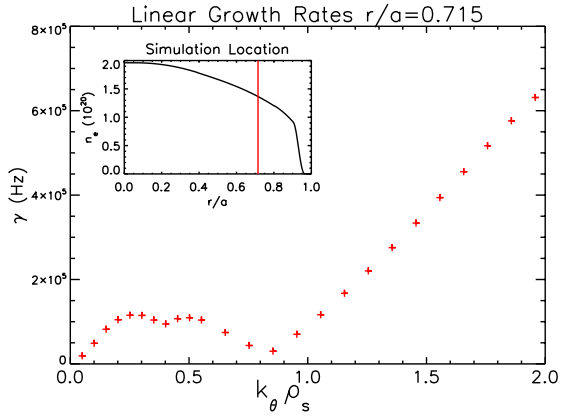

(e) Pre-Pellet

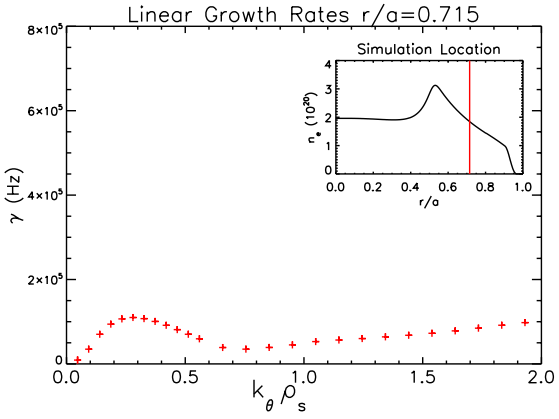

(f) Post-Pellet

Figure 5-28: (a), (c) and (e) show growth rates in pre-pellet plasma conditions. (b), (d) and (f) show growth rates in post plasma conditions. The growth rates in front of the pellet (b) are of the order 10^5 Hz, indicating that the turbulence in this region evolves on a time scale much faster than the profiles are changing.

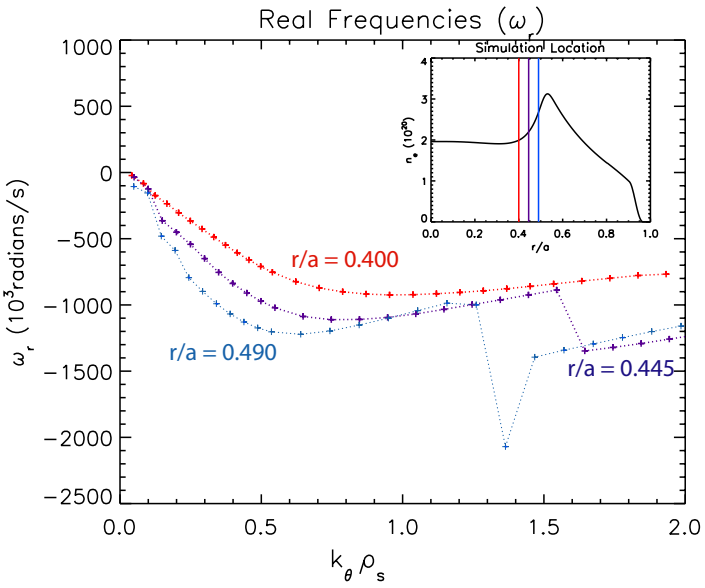

Figure 5-29: Real frequency of modes located at $r/a = 0.400, 0.445\&0.490$. The color of the trace denotes the location of the simulation as marked by the corresponding vertical bar in the inset figure.

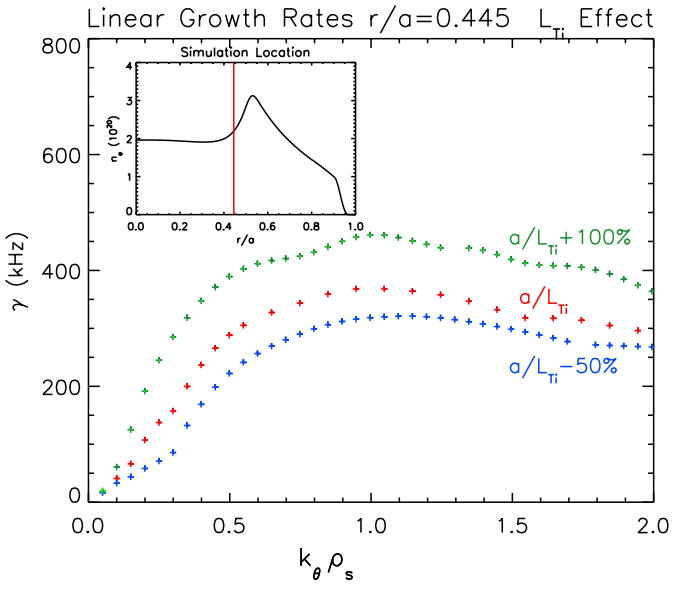

Figure 5-30: Variation of linear growth rates at $r/a = 0.445$ with (a) a/L_{T_i}. The red trace denotes the base case, $a/L_{T_i} = -3.02$, blue denotes simulations where the inverse scale length was decreased by 50%, and green denotes simulations where the inverse scale length was increased by 100%.

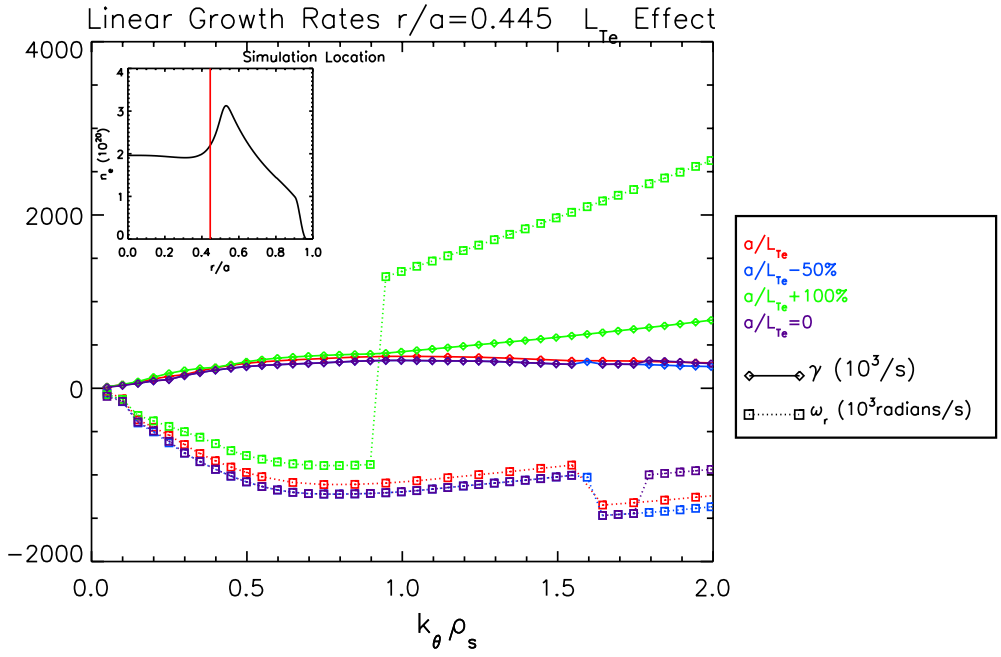

Figure 5-31: Variation of linear growth rates at $r/a = 0.445$ with a/L_{T_e}. The red trace denotes the base case, $a/L_{T_e} = -6.15$, and the purple, blue, and green traces denote simulations where the inverse scale length was decreased by 100%, decreased 50%, and increased by 100% respectively. The growth rates (in units of kHz) for each case are represented by diamonds, and the real frequencies (in units of 10^3 radians/s) are represented by squares.

length, as would be expected from TEMs but not ITG or ETG modes, which appears to saturate at the level of our base case for our model. In addition, the shorter wavelengths also show a negative dependence on collisionality, ν_{ei}, as shown in figure 5-33, which would be consistent with TEMs since an increase in ν_{ei} would reduce the population of trapped electrons.

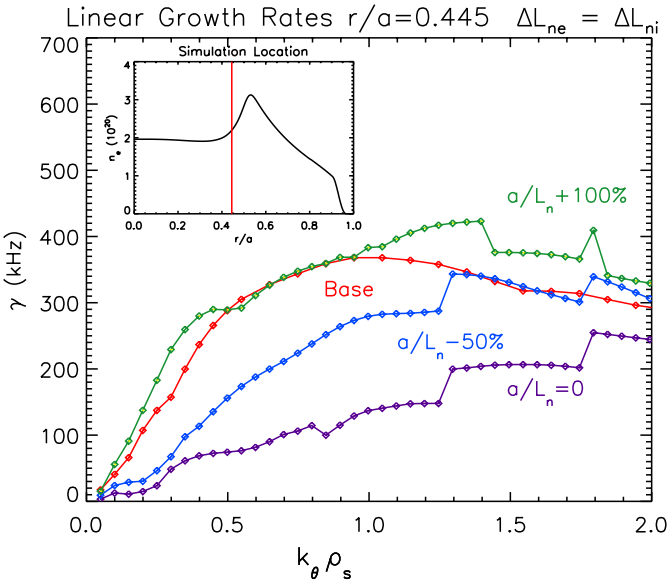

Figure 5-32: Variation of linear growth rates at $r/a = 0.445$ with a/L_n. The red trace denotes the base case, $a/L_n = 3.22$, and the purple, blue, and green traces denote simulations where the inverse scale length was decreased by 100%, decreased 50%, and increased by 100% respectively.

5.4.4 Nonlinear Run

The next step in our investigation was to perform a global non-linear run to investigate the effects of the pellet consistent profiles on the plasma turbulence. A global simulation was chosen for this step in our investigation because the plasma parameters change very rapidly over short spatial scales. Thus it possible that non-local effects resulting from the full profile variation would play an important part in the results. It should be noted that for a global run, GYRO takes the profiles to be poloidally and toroidally symmetric, but as was discussed in chapter 2 we know that the tem-

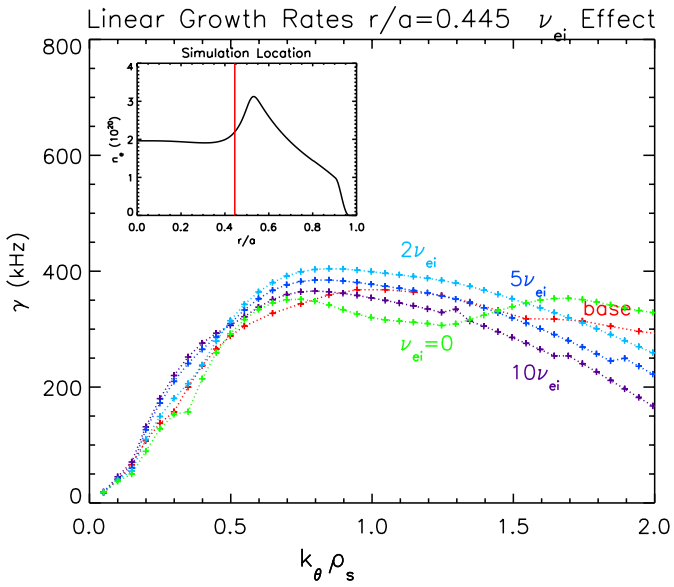

Figure 5-33: Variation of linear growth rates at $r/a = 0.445$ with ν_{ei}. For the base case $\nu_{ei} = 1.05(MHz)$.

perature and density perturbations are not poloidally and toroidally symmetric. In fact, they are not even constant locally on a magnetic field line. Thus the work that follows should be considered as a first order approximation, yielding an indication of the effects of the injection.

In addition to the simulation using pellet consistent profiles, a global simulation was also performed over the same region using the pre-pellet profiles. The purpose of this exercise was to touch base with the previous work done during the flux tube scan in q-space, and to provide a control to compare the results from the simulations with pellet consistent profiles. The domain for the simulation (see figure 5-34) was chosen such that it covered the radial region from the beginning of the increase in the electron temperature gradient until just slightly past the location of the pellet.

Unlike the flux tube runs, in which every point in the radial domain is identical to every other point in terms of plasma conditions and their derivatives, every radial point in a global run is unique. Thus when compiling the probability distributions for the radial electric fields, a distribution was calculated at each radial location. The distributions determined for the simulation with pre-pellet profiles and post-pellet

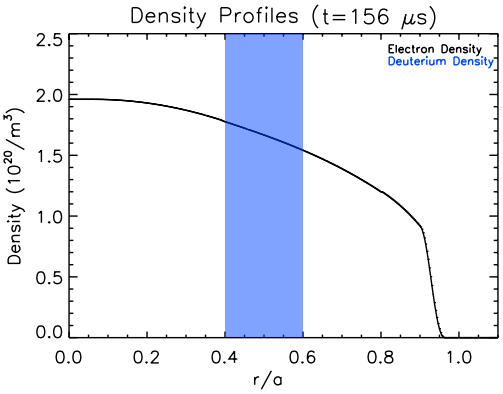

(a) Pre-Pellet

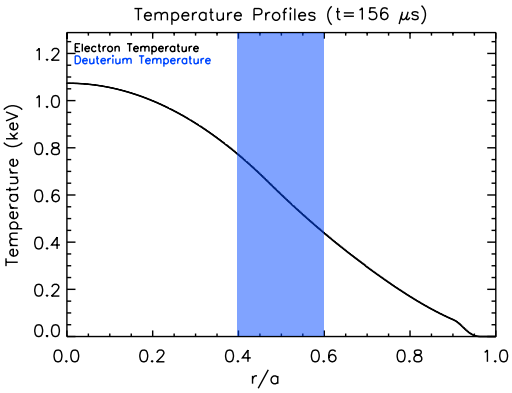

(b) Pre-Pellet

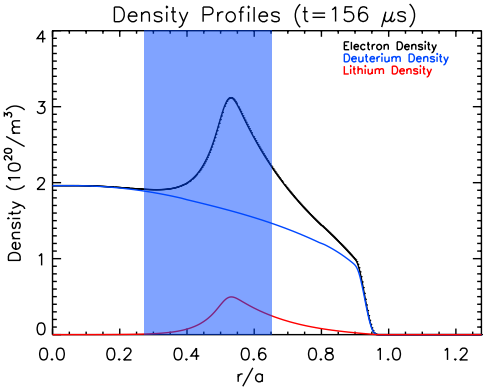

(c) Post-Pellet

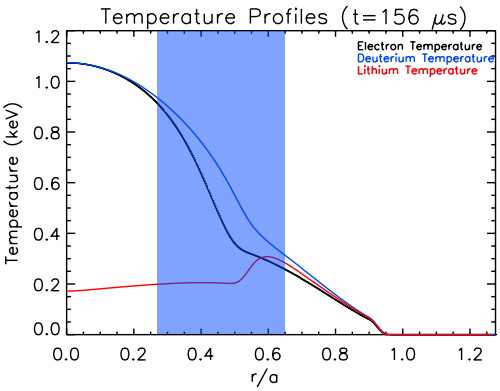

(d) Post-Pellet

Figure 5-34: The blue band marks the simulation domain for the pre-pellet, (a) & (b), and post-pellet, (c) & (d), simulations.

profiles are shown as surface plots in figures 5-35a and 5-35b.

The distribution at each radial location was fitted to a Gaussian function, and standard deviations of the distributions are shown in figures 5-36a and 5-36b. There is a significant difference between the widths of the distributions taken from the pre-pellet and post-pellet simulations. The pre-pellet simulations have ExB drift distribution standard deviations that range from 400 - 600 m/s, similar to what was observed in the flux tube simulations. The post-pellet profiles have a much larger standard deviation, up to 1500 m/s, in the region of inverted density profiles and steepened temperature profiles. Velocities of this magnitude are of the same order as those seen experimentally in the drift of the filaments measured in chapter 4.

Figure 5-37a and 5-37b show the temporal correlation functions at numerous radii for both the pre and post-pellet plasma conditions. Comparing the pre-pellet correlation functions from figure 5-37a with the correlation functions from the flux tube runs in figure 5-18a, it's interesting to note that the global simulation produces correlation times that are approximately twice that of the flux tube runs at $4.5 - 8.5\mu s$, and they do not show the tendency towards oscillations at larger minor radii (which corresponds to large values of the safety factor q). Examining the temporal correlation functions from the post-pellet plasma conditions (figure 5-37b) we see that the correlation times in the region of steepened temperature gradients and inverted density gradients, $r/a = .35 - .5$, the correlation times are approximately $3\mu s$, but in the outer region of the domain, where again the density is monotonically decreasing and the electron temperature gradient returns to values more like those of the pre-pellet plasma conditions, the correlation times larger, $\sim 8\mu s$.

As was done during the q-scan, the drift adjusted temporal correlation function was computed for the pre-pellet, figure 5-38a, and post-pellet, figure 5-38b, profiles. As was the case with the q-scan, adjusting for the drift caused a modest increase in the temporal correlation functions. For the pre-pellet simulation, the correlation times remained between $4.5 - 8.5\mu s$. For the post-pellet simulation the correlation times in the regions with the steepest temperature gradient increased by $2 - 3\mu s$ out to $4.5 - 6.5\mu s$, while in the outer region of the domain the correlation times increased

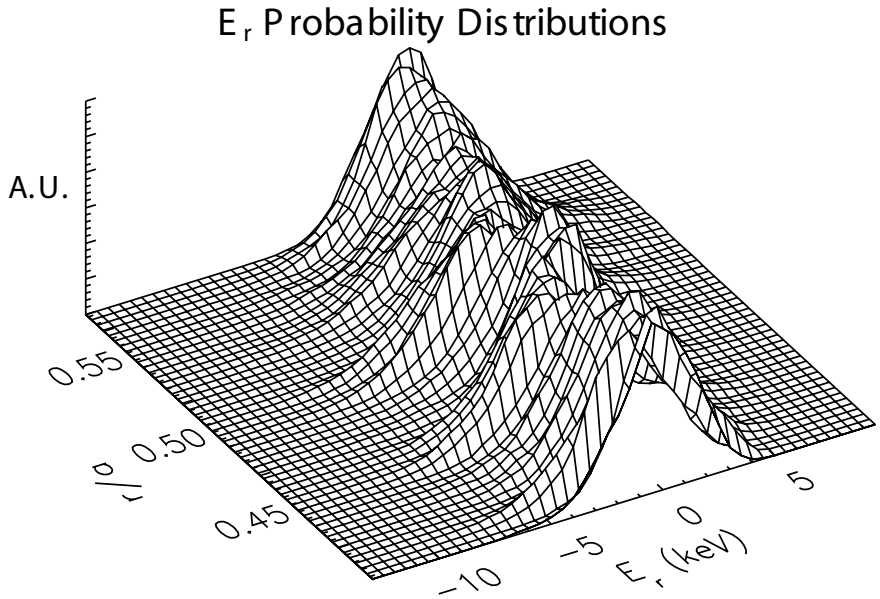

(a) Pre-pellet

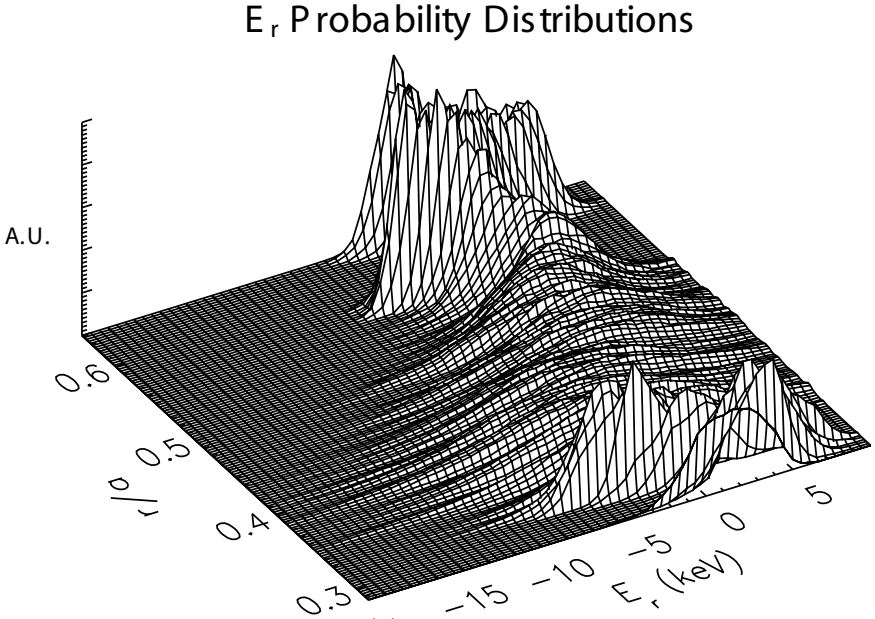

(b) Post-Pellet

Figure 5-35: Surface plots of the E_r probability distribution function as function of minor radius for the pre-pellet (a) and post-pellet (b) conditions. Note the region of wider distributions between $r/a = .06 - .11$ in the post-pellet conditions.

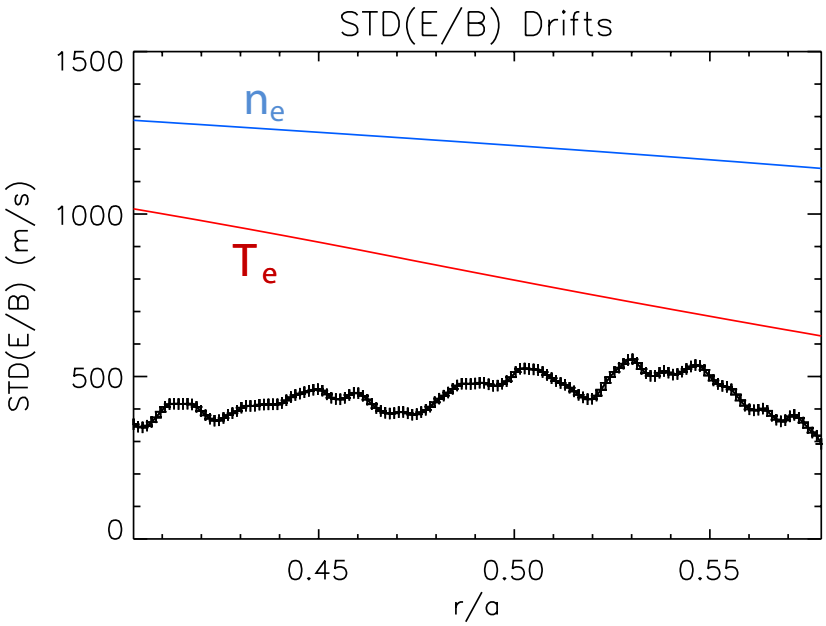

(a) Pre-pellet

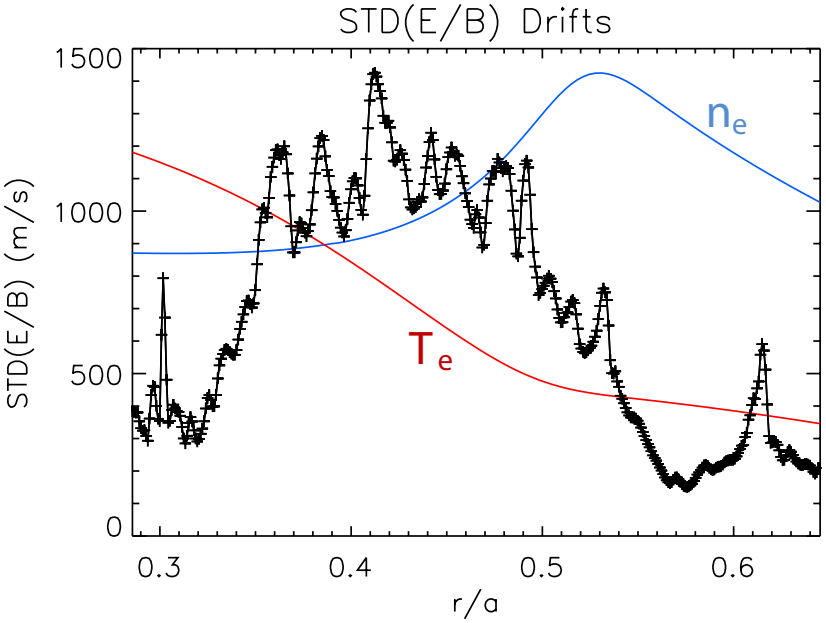

(b) Post-Pellet

Figure 5-36: Standard deviation in the inferred ExB drifts from the E_r distributions for the pre-pellet (a) and post-pellet (b) conditions. Shown in the background of each plot are the electron temperature (red) and density (blue) normalized to fit on the graph. Note that for the simulation with post-pellet conditions, the increase in distribution widths occurs in the same region as the steepened $\vec{\nabla}T_e$ and inverted $\vec{\nabla}n_e$.

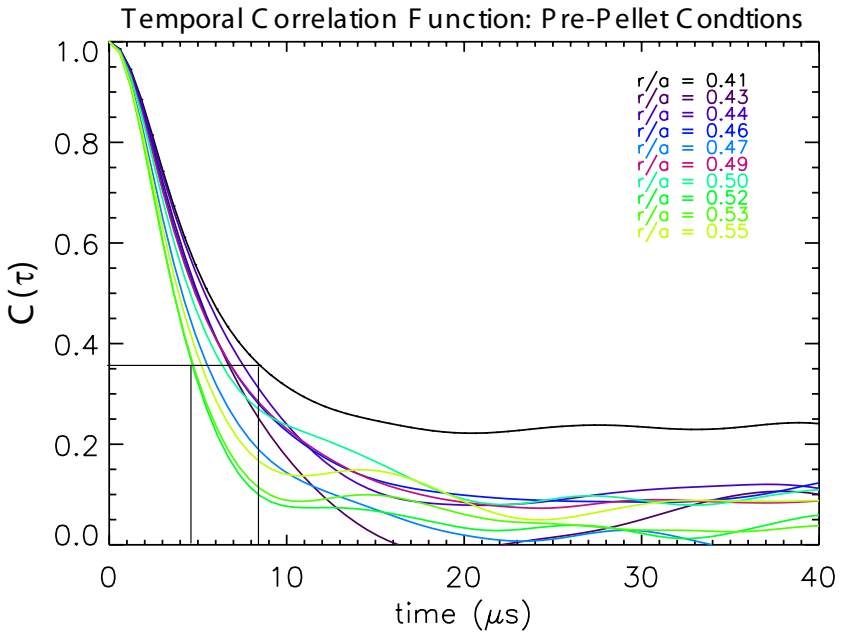

(a) Pre-pellet

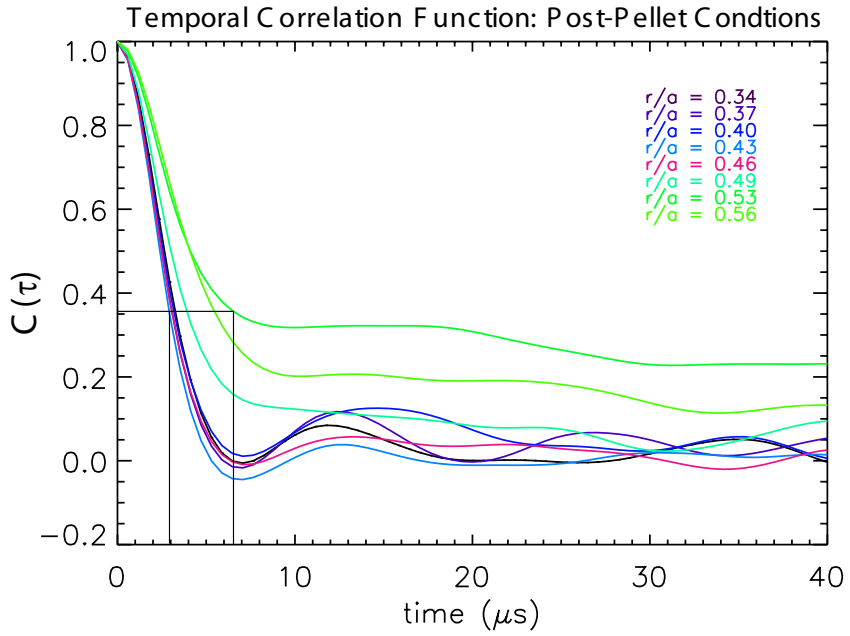

(b) Post-Pellet

Figure 5-37: Temporal correlation functions at various minor radii for the pre-pellet (a) and post-pellet (b) plasma conditions.

to greater than $15\mu s$.

Turning now to the spatial correlations, the radial correlation functions for the pre-pellet and post-pellet plasma conditions are remarkably similar, with radial correlation lengths of $\sim 1-2mm$ as shown in figures 5-39a and 5-39b. Figure 5-40a and 5-40b show colorized contours plots of the the poloidal correlation function. Every point in the plot is determined as the correlation the radial electric field at that point with the point at the midplane with the same minor radial location. Mathematically this is defined as,

$$C\left(r,\theta\right)=\frac{\left\langle E_r\left(r,\theta=0\right)E_r\left(r,\theta\right)\right\rangle_t}{\left\langle E_r\left(r,\theta=0\right)^2\right\rangle_t} \tag{5.22}$$

where we assume the system is ergodic and time average, $\langle ...\rangle_t$, is equivalent to an ensemble average. In the pre-pellet simulations, radial electric fields are highly correlated, $C(r,\theta)\sim .8$, over the entire poloidal extent of the domain. In the post-pellet simulations the radial electric fields remain correlated over a much shorter poloidal distance, ~ 1 cm, in the region of steepened gradients, but regain a extended character outside this region.

5.5 Results

The results of the GYRO simulations indicate that the turbulent ExB flows during standard operation are inconsistent with the experimentally measured drifts in the ablation filaments. Although the radial and temporal correlation length of the fields are consistent with the filament data, the correlation time is relatively short compared to what is observed in with the filaments, $\sim 3\mu s$. Additionally, the simulations from the q-scan produced distributions of radial electric fields with standard deviations of $\sim 3\mathrm{k}V/m$, which would generate flows with a standard deviation of approximately $600m/s$, a factor of 10 smaller than the $3-5$ km/s observed in the filament drifts.

Global simulations using pre and post-pellet profiles indicate conditions in the post-pellet plasma are more consistent with the observed filament behavior. As ex-

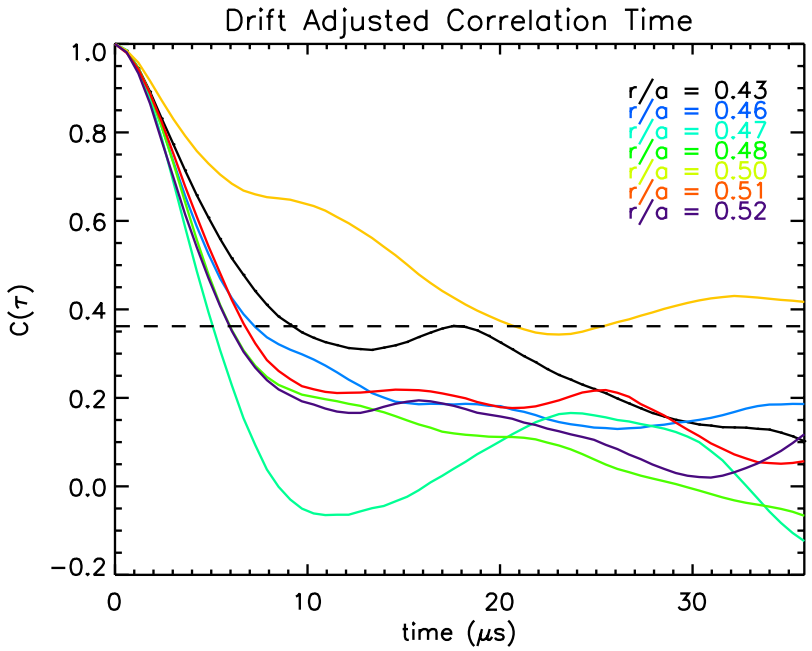

(a) Pre-pellet

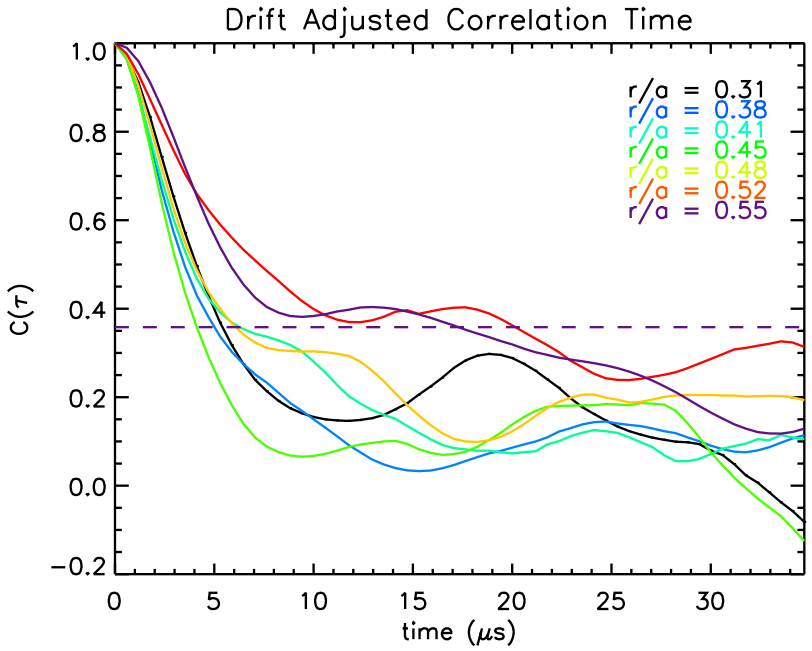

(b) Post-Pellet

Figure 5-38: Drift adjusted temporal correlation functions for pre-pellet (a) and post-pellet (b) plasma conditions.

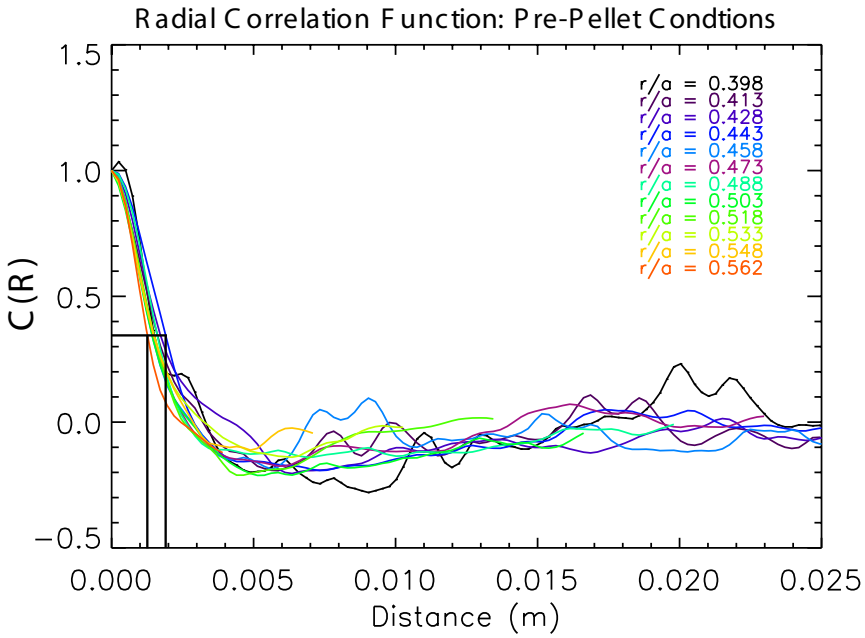

(a) Pre-pellet

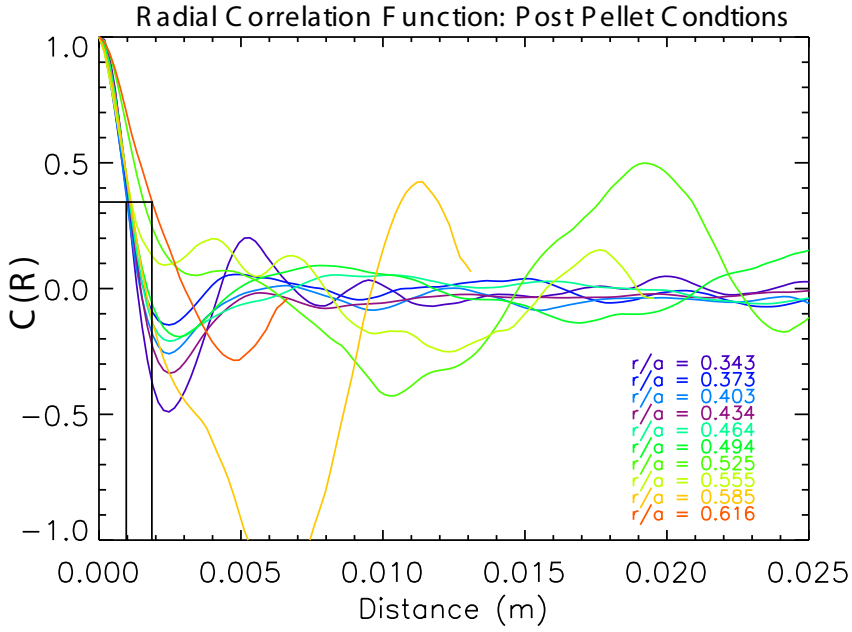

(b) Post-Pellet

Figure 5-39: Radial correlation functions at various minor radii for the pre-pellet (a) and post-pellet (b) plasma conditions.

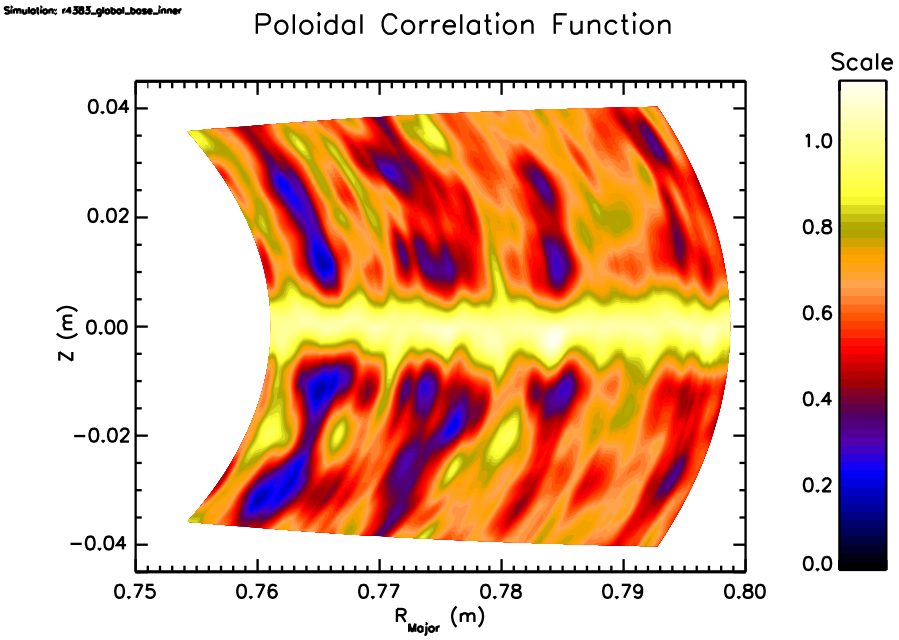

(a) Pre-pellet

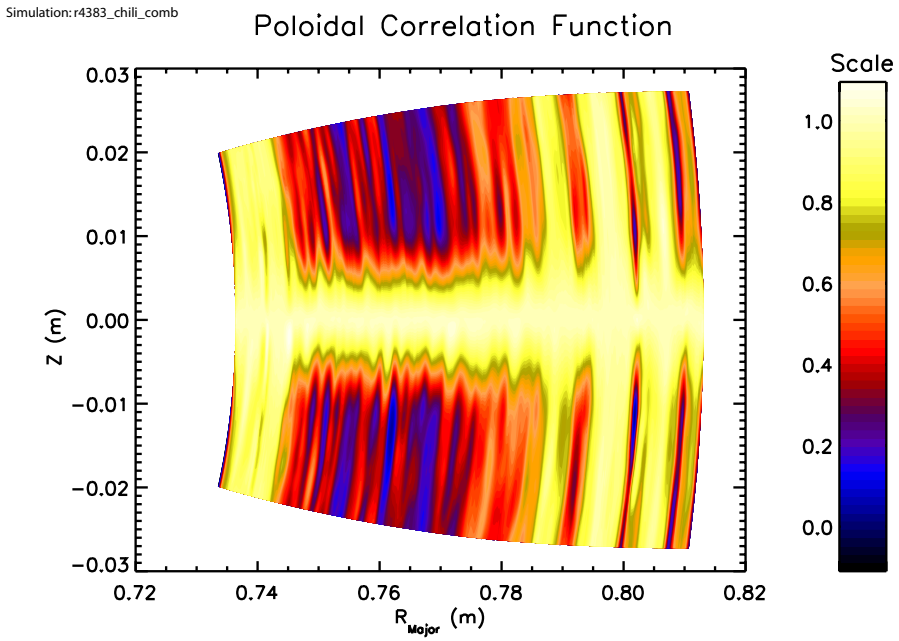

(b) Post-Pellet

Figure 5-40: Poloidal correlation functions at various minor radii for the pre-pellet (a) and post-pellet (b) plasma conditions.

pected the pre-pellet simulation produced results that were very similar to the flux tube scan in q with respect to correlation times, lengths and ExB flows. On the other hand, the electric field distributions from the post-pellet simulations have standard deviations that would produce ExB drifts of up to 1.5km/s, only a factor of $2-3$ smaller than the magnitude of the drifts experimentally observed in the filament data. Furthermore, the drift adjusted correlation time of the electric field in the post-pellet simulation is more consistent with the drift time observed in the filaments. Adjusting the observation point for the correlation function to move with the ExB drift of the plasma generates correlation times of $\sim 15\mu s$ in the region just past the pellet, where one would observe the filaments.

It is also interesting to note that the increase in the distribution widths for the post-pellet simulation is accompanied by a shortening of the poloidal correlations in the radial electric field. Fields in the pre-pellet simulations are correlated on a length scale greater than the poloidal extent of the domain, $>$ 4 cm, while the fields in the regions of the largest gradients in the post-pellet simulations, the correlation length is much shorter, $\sim$ 1 cm. Interestingly, the region with the largest correlation time in the post-pellet simulations occurs behind the pellet at $r/a > .5$ which corresponds to a major radius of $78cm$. If one examines figure 5-40b they can see that this is the region where the poloidal correlation length begins to recover to pre-pellet values.

It should also be noted that although the post-pellet simulations produce results that are consistent with the drift of a single filaments, the radial correlation length and standard correlation time are not consistent with the propensity of successive filaments to drift in the same direction as previous filaments. In this case, one would expect correlation lengths of the order 2-3 cm, and standard correlation times of the order 20-30μs.

Thus it seems that the post-pellet simulations have many of the key features of the filament drifts, but not off them, and not all in same location at the same time. This could be the result of the fact that we are simulating the plasma as stationary, and the turbulence as saturated, while in actuality they are both continually evolving through out the injection process. Even our linear growth rates only indicate that

the time scale for the evolution of the turbulence was much short than the time scale for the evolution of the plasma in the region in front of the pellet. It is possible that region behind the pellet is not in a fully saturated state, and thus may retain some of the features of the turbulence in front of the pellet. Furthermore, the post-pellet simulations treated the pellet perturbation as toroidally and poloidally symmetric, a fact we know to be false, and it is possible that correctly treating this asymmetry could bring the simulation and experiment into better agreement.

Chapter 6

Conclusions and Future Work

The primary aim of this work was to study the properties of filaments formed during the ablation of injected lithium into Alcator C-Mod and explore any connections between the filament evolution and ExB flows generated by plasma turbulence. Our initial hypothesis was that the filaments might represent the direct measurement, and perhaps a future diagnostic, of plasma turbulence, especially for GAMs and ZMF Zonal Flows, a set of modes believed to play an important role in transport suppression. In this work, the three dimensional trajectories of ablation filaments are measured for the first time using an ultra-high-speed stereo imaging system, and a survey was made of filament evolution under a variety of plasma conditions to study the statistical properties of filaments. These observations are compared with turbulent ExB flows calculated with the non-linear gyrokinetic solver GYRO, where it was found that the statistical characteristics of the filament drifts are more consistent with the turbulence during the injection than with the turbulent conditions that prevail just prior to the injection.

Experimentally, this study required the design, construction and calibration of a stereo imaging system on Alcator C-Mod. This system incorporated an innovative design, whereby the views from two different lenses were imaged onto a single CCD by way of a bifurcated coherent fiber bundle . This approach ensured simultaneity of the measurements, a condition that is required for reconstructing three dimensional information from the images.

This diagnostic system was used to analyze the filament evolution from 122 pellet injections. These showed convincingly that our initial observations in 2003-2004 were correct, that the filaments move primarily along the flux surfaces, and that there is a predilection for filaments to move in the same poloidal direction as preceeding filaments. Additionally, the cumulative set also revealed that there exisists a preferred drift direction, the electron diamagnetic direction, in L-mode. Data on the filament positions and velocities were compiled into a statistical database whereby it was observed that the width of the filament velocity distribution was a decreasing function of the local safety factor, q. This observation suggests that the filament drift is not a result of GAMs, whose amplitude should increase with q. Essentially no dependence was found on pre-pellet quantities that play roles in plasma turbulence, such as the ion temperature and density scale length or the magnetic shear.

To test our hypothesis that the filament drifts were related to pre-pellet plasma turbulence, we applied the non-linear gyrokinetic solver, GYRO. Using the electrostatic potential computed by GYRO to calculate the ExB flows that would result from this plasma turbulence, we performed a series of studies of their statistical properties. The first study used a series of flux tube runs to examine the turbulence under background, ohmic L-mode, plasma conditions prior to any pellet injection, as a function of the local safety factor. These investigations revealed that although the poloidal ExB flows were sufficiently well correlated in time and space to be consistent with the drift of a filament, the distributions were a factor of 10 smaller than those of the filament drifts, and did not show a clear dependence on the local safety factor.

The next step in our investigation was to explore the possible effects that the injection process itself might have on the turbulence. To this end we developed a numerical model to estimate the effects of the pellet injection on the density and temperature profiles of the various plasma species, electrons as well as deuterium and lithium ions. We then used the profiles calculated from this model as input to a series of linear simulations to determine the expected linear growth rates of a spectrum of toroidal modes, and thereby guage the characteristic response time of the turbulence to changes in the profiles. These studies indicate that the turbulence

should adjust on a time scale much shorter than the time scale for the evolution of the profiles themselves, and thus, that turbulence should remain in a quasi-saturated state during the pellet injection.

Given these results for the expected response time of the turbulence, we felt that it would be illuminating to perform global non-linear simulations using both the pre-pellet and post-pellet profiles. The pre-pellet simulation served the purpose of making contact with the previous results from the flux tube runs, and indeed, produced similar results. The post-pellet simulations on the other hand showed an increase in the width of the turbulent ExB distributions to 1.5km/s, within a factor of 2 of the experimentally observed drift velocities of the filaments. Additionally, the drift adjusted correlation time for the turbulent fields is of the order $10\mu s$, which is more consistent with the duration of the filament drifts.

Given the similarities between the results of the post-pellet simulations, and the statistical properties of the filament drifts, it seems likely that the drifts are a result of turbulence response to the pellet modified profiles. Having said this, there are features regarding the spatial scale of the ExB flows generated by GYRO that are not consistent with the properties of the filaments. It was observed in the experimental filament data that successive filaments have a tendency to drift in the same direction as the previous filament, over a time scale of $20 - 30\mu s$. Considering that the pellet moves at $\sim 500m/s$, this would indicate poloidal flows correlated over a distance of $1 - 1.5cm$, while the pre and post-pellet simulations yield expected radial correlation lengths that are at most a few millimeters. It is possible that if the density and temperature perturbations were properly treated as being localized toroidally and poloidally, this might lead to radial correlation lengths consistent with the filament drifts, although intuitively one expects that turbulence levels would go up and correlation lengths down as the perturbation became more asymmetric.

One logical extension of this work would be to expand the pellet injection database and to improve on our models for the plasmas response to the pellet injection. Although the current database contains 122 injections, tracking 306 filaments, questions arise as to whether this is sufficient to make a proper statistical study. More injec-

tions into H-mode and RF-heated plasmas are also needed, to verify the preferential drift of the filaments, as observed during the 2003-2004 campaign (see section 1.5), and identify if this results from the H-mode profiles, or perhaps from flows driven by the RF via Reynolds stress.

Numerically improving on the models for the plasma response to the injection will likely be a much more challenging project. The gyrokinetic formalism which has been so successful in advancing our understanding of plasma turbulence breaks down in the limit that the variation in the perturbation along the field line is large. From the ordering in equation 5.1, gyrokinetics requires $k_{\|}L \sim 1$, while for the density perturbations resulting from the injections we have $k_{\|}L \gg 1$. Thus better modeling would require more than just an extension of the GYRO code; it will require an entirely new formalism. For example, one possible mechanism which cannot be treated by the GYRO code would be the Stringer Spinup mechanism discussed in section 3.3, which is driven by a poloidally asymmetric density perturbation. This mechanism could act to amplify the pre-existing flows, such as the ZMF zonal flows, resulting in radial correlation scale lengths which might be consistent with our filament observations.

Additionally, further investigations should be made of the effects of the electrostatic perturbation caused by the pellet. As noted in section 2.3.3, the injection of a pellet is often accompanied by an observed modification of the plasma potential measured at the edge. This is consistent with the theoretical formalisms invoked to explain the plasma response to the pellet, or the formation of the ablation filaments, which predict potential modifications due to either absorption or emission of electrons by the ablation cloud. The internal instability model presented in section 2.2.1 predicts that the ablation cloud acquires an electrostatic potential that is of the order $\sim 0.1T_e/e$ [34], where T_e is the background plasma electron temperature. If we consider that the ablation cloud is approximately $1cm$ in diameter, for electron temperatures of order 1keV this would lead to electric fields of the order $10\mathrm{k}V/m$. Furthermore, since the pellet is moving at $\sim 500m/s$, this perturbation would appear to a stationary observer to have a frequency of $\frac{500m/s}{.01m} = 50\mathrm{k}Hz$. It is interesting to note, that these fields would produce ExB drifts of the correct order to explain the

drifts of the filaments, and have similar time and spatial scales to features that were observed in the $n = 0$ components determined from the GYRO simulations. Figure 6-1 shows the radial and temporal correlation function for the $n = 0$ and $n > 0$ components of the field, taken on the outboard midplane, for one of our flux tube simulations (q=2.25). As can be seen, these oscillations, most likely GAM oscillations, have a wavelength of approximately $1cm$ and period of approximately $15\mu s$, corresponding to a frequency of 67kHz. It should also be noted, that the perturbation from the pellet, localized on the outboard midplane, would have a strong m=1 character, like the Geodesic Acoustic Mode. It would be interesting to see if a simulation which incorporated the full spatial and temporal variation of the electrostatic perturbation produced interactions with low order modes in the plasma, such as the GAM.

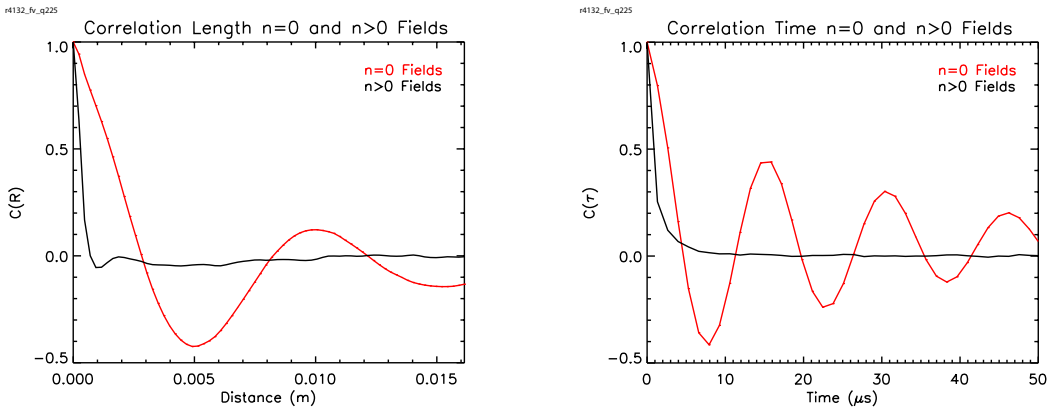

(a) (b)

Figure 6-1: Radial (a) and temporal (b) correlation functions for the $n = 0$ (red) and $n > 0$ (black) components of the radial electric field.

Appendix A

Stereo Imaging Mechanics

Although the mechanics behind determining three dimensional location of an object from stereo images is quite straight forward, the details can be a bit involved. The derivation that follows outlines the method that was implemented for all of the work in this thesis.

Suppose that there exists two well defined reference positions in space, $\{\vec{X}_T, \vec{X}_B\}$, which in our case would be the location of the top and bottom viewing optics respectively. If one also knows the unit vectors, $\{\hat{\xi}_T, \hat{\xi}_B\}$, which point from the reference points towards a third point **O**, the location of point **O** can be determined by the intersection of the projections of $\hat{\xi}_T$ and $\hat{\xi}_B$, see figureA-1.

In the real world, because of errors and calibration uncertainties, the projections of $\hat{\xi}_T$ and $\hat{\xi}_B$ don't quite intersect, so instead we take the center of the line of closest approach as our best guess at the location of point **O**. To determine where this point is, first define the vector that points to the point where the projection of $\hat{\xi}_T$ most closely approaches the projection of $\hat{\xi}_B$.

$$\vec{C}_T \equiv \vec{X}_T + \lambda_T \hat{\xi}_T \tag{A.1}$$

where λ_T is the distance from $\vec{X}_T$, the top lens, to the point of closest approach. Similarly, define the vector that points to the point where the projection of $\hat{\xi}_B$ most closely approaches the projection of $\hat{\xi}_T$ as,

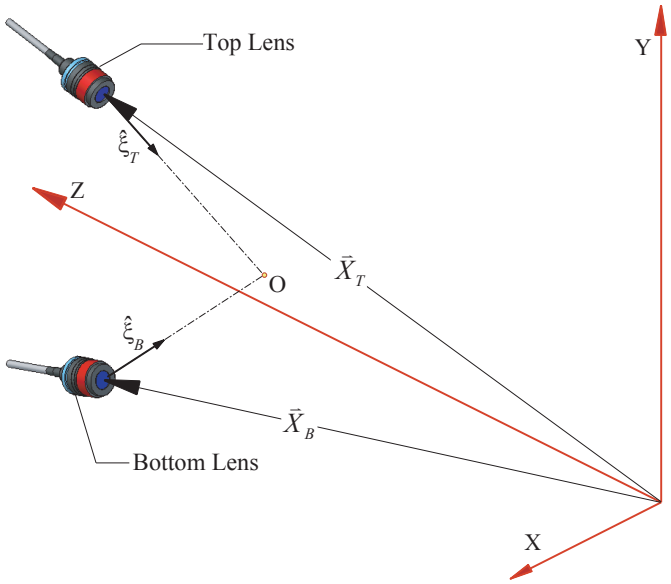

Figure A-1: The object point **O** can be determined from the vectors $\{\vec{X}_T, \vec{X}_B\}$, which point to the top and bottom lens respectively, and the unit vectors $\{\hat{\xi}_T, \hat{\xi}_B\}$, which indicate the directions from the lenses to the object point.

$$\vec{C}_B \equiv \vec{X}_B + \lambda_B \hat{\xi}_B \tag{A.2}$$

The center of the line of closest approach is thus the average of these two position vectors, $\vec{C}_O = \frac{\vec{C}_B + \vec{C}_T}{2}$. Determining the location of point **O** thus reduces to finding λ_T and λ_B, which can be accomplished by considering the fact that the vector connecting the two points of closest approach should be perpendicular to both $\hat{\xi}_T$ and $\hat{\xi}_B$. Stated another way,

$$\begin{aligned} \left(\vec{C}_T - \vec{C}_B\right) \cdot \hat{\xi}_T = 0 \\ \left(\vec{C}_T - \vec{C}_B\right) \cdot \hat{\xi}_B = 0 \end{aligned} \tag{A.3}$$

Solving these equations simultaneously we get the relations,

$$\lambda_T = \frac{\left(\vec{\triangle}\cdot\hat{\xi}_B\right)\left(\hat{\xi}_T\cdot\hat{\xi}_B\right) - \vec{\triangle}\cdot\hat{\xi}_T}{1-\left(\hat{\xi}_T\cdot\hat{\xi}_B\right)^2}$$

$$\lambda_B = \frac{\vec{\triangle}\cdot\hat{\xi}_B - \left(\vec{\triangle}\cdot\hat{\xi}_T\right)\left(\hat{\xi}_T\cdot\hat{\xi}_B\right)}{1-\left(\hat{\xi}_T\cdot\hat{\xi}_B\right)^2} \tag{A.4}$$

Where $\vec{\triangle} \equiv \vec{X}_T - \vec{X}_B$. Substituting the relations for λ_T and λ_B into the expression for the object point $\vec{C}_O$ we get the expression.

$$\vec{C}_O = \frac{\vec{X}_T+\vec{X}_B}{2} + \frac{\left[\vec{\triangle}\cdot\hat{\xi}_B - \left(\vec{\triangle}\cdot\hat{\xi}_T\right)\left(\hat{\xi}_T\cdot\hat{\xi}_B\right)\right]\hat{\xi}_B - \left[\vec{\triangle}\cdot\hat{\xi}_T - \left(\vec{\triangle}\cdot\hat{\xi}_B\right)\left(\hat{\xi}_T\cdot\hat{\xi}_B\right)\right]\hat{\xi}_T}{1-\left(\hat{\xi}_T\cdot\hat{\xi}_B\right)^2} \tag{A.5}$$

As a convenient measure of the uncertainty in this determination we can use the "cross-eyed" error, which is the just the length of the line of closest approach. Using the expressions for $\vec{C}_T$ and $\vec{C}_B$, the cross-eyed error is given by,

$$\begin{aligned}\delta_O &\equiv |\vec{C}_T - \vec{C}_B| \\ &= |\vec{\triangle}|\left[1 - \frac{\left(\hat{\triangle}\cdot\hat{\xi}_T\right)^2 + \left(\hat{\triangle}\cdot\hat{\xi}_B\right)^2 - 2\left(\hat{\triangle}\cdot\hat{\xi}_T\right)\left(\hat{\triangle}\cdot\hat{\xi}_B\right)\left(\hat{\xi}_T\cdot\hat{\xi}_B\right)}{1-\left(\hat{\xi}_T\cdot\hat{\xi}_B\right)^2}\right]^{1/2}\end{aligned} \tag{A.6}$$

Where $\hat{\triangle} \equiv \vec{\triangle}/|\vec{\triangle}|$. Figure shows histograms of the cross-eyed error in the major radial and Z direction resulting from determination of the pellet's location during pellet injection experiments.

Determining the unit vectors $\hat{\xi}_T$ and $\hat{\xi}_B$ from the stereo images is most easily done in the frame of the viewing optics. Consider the situation depicted in figure A-3, where we define a coordinate system on the face of each the left and right fiber bundle. For simplicity, the units in the fiber frame are normalized to the dimensions of the fiber, i.e. a distance of 1 in the fiber frame coordinates is equal to the mean of the horizontal and vertical dimension of the fiber. The vector pointing from the center of the lens to the object point's position in space can be determined from the

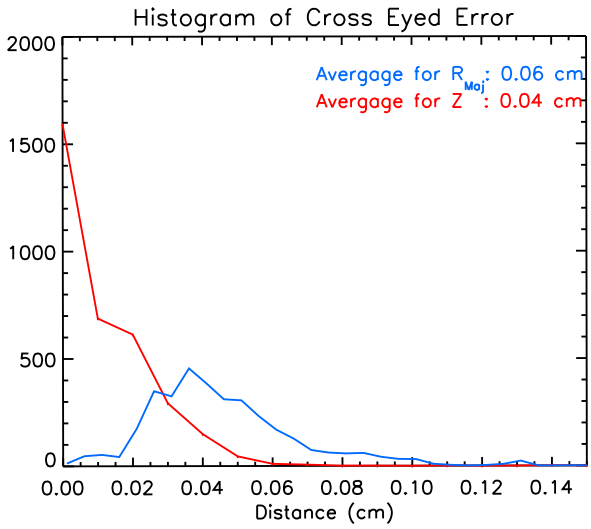

Figure A-2: Histogram of cross-eyed errors from the determination of the location of lithium pellets on Alcator C-Mod.

image point on the fiber by considering the geometric properties of the lens system.

The distance of the image point from the optical axis of the lens can be related to the angle subtended from the object point to the lens's optical axis via the relation, see figure A-3.

$$\tan\theta = \epsilon_1\delta + \epsilon_2\delta^2 \tag{A.7}$$

Where δ is the distance in the image from the optical axis to the image point, $\epsilon_1 \sim 1/f$, where f is the focal length of the lens system, ϵ_2 accounts for non-linear distortion effects of the lens, and we restrict $\theta \in [0, \pi/2]$. Additionally, the angle, φ, which the object point makes with the x-axis of the fiber frame is the same as the angle subtended by the projection of $\hat{\xi}$ in the x,y plane of the lens system, establishing the relation between the x and y components. The final multiplicative factor is determined by the requirement that $\hat{\xi}$ is a unit vector and therefor must have a magnitude of one. Taking all of this into account, we arrive at an expression for the components of $\hat{\xi}$ in the frame of the lens composed of quantities that can be measured in the fiber frame.

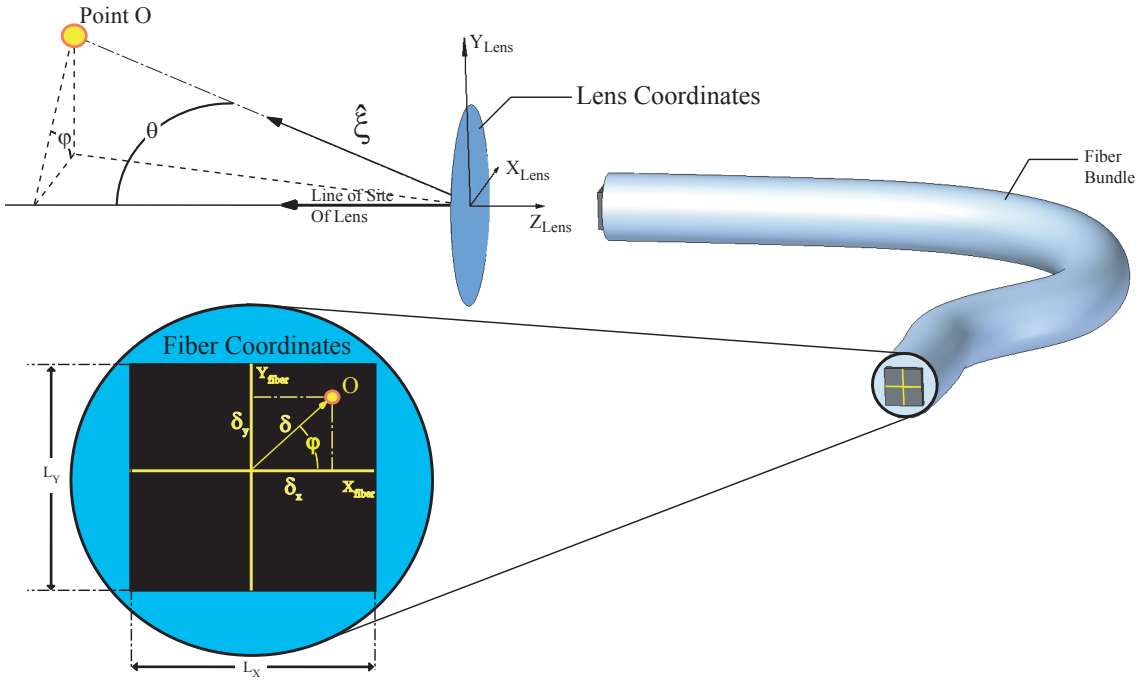

Figure A-3: Above is a schematic of the relation between the three dimensional lens coordinate system and the two dimensional fiber frame coordinate system. The unit vector pointing towards the object point **O** is represented as its projection on the (x, y) in the fiber frame. All distance in the fiber frame are normalized to $(L_x + L_y)/2$.

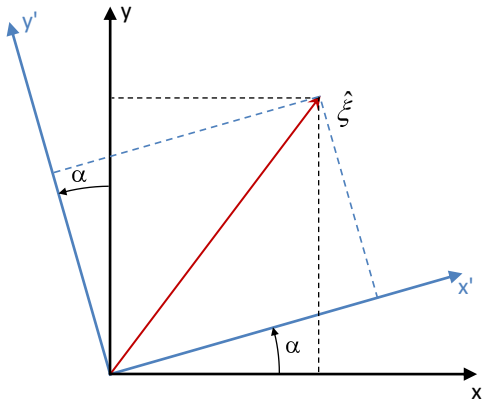

Figure A-4: Components of $\hat{\xi}$ in $R = \{x, y\}$ and $R' = \{x', y'\}$

$$\hat{\xi} = \begin{bmatrix} \cos\varphi \sin\theta \\ \sin\varphi \sin\theta \\ -\cos\theta \end{bmatrix} = \begin{bmatrix} \frac{\delta x}{\delta} \sin\theta \\ \frac{\delta y}{\delta} \sin\theta \\ -\cos\theta \end{bmatrix} \tag{A.8}$$

Where $\tan\varphi = \frac{\delta x}{\delta y}$, and $\{\delta x, \delta y\}$ are the x and y components respectively of δ in the lens frame, and $\sin\theta$ and $\cos\theta$ are determined from relation A.7.

Once we have the components of $\hat{\xi}$ in the lens frame, its a small matter to transform these to the lab frame. The usual method for this kind of transformation is the use of Euler angles, which relate the orientation of any two reference frames. Consider the situation shown in figure A-4, where the unprimed coordinate system,$\{x, y\}$ labeled R, is related to the primed coordinate system, $\{x', y'\}$ labeled R', by a rotation α about the origin.[1] The components of the vector $\hat{\xi}^R$, where the subscript R labels the reference frame that the vector is represented in, can be related to the components of $\hat{\xi}^{R'}$ in the R' coordinate system via the rotation matrix, $\bar{\bar{\mathrm{R}}}_{z'}$

[1]In order to maintain consistency, all rotations will be measured as positive when the rotation about an axis sweeps the other axis towards their cyclic partners. i.e., a rotation about $\hat{z}$ is positive if it sweeps $\hat{x}$ into $\hat{y}$.

$$\hat{\xi}^R = \bar{\bar{\mathrm{R}}}_{z'}(\alpha)\,\hat{\xi}^{R'}$$

$$\hat{\xi}^R = \begin{bmatrix} \cos\alpha & -\sin\alpha & 0 \\ \sin\alpha & \cos\alpha & 0 \\ 0 & 0 & 1 \end{bmatrix} \hat{\xi}^{R'} \tag{A.9}$$

Similarly, we could move back another step, and relate the components of $\hat{\xi}^{R'}$ from some previous coordinate system R'' via a rotation about some axis in the R'' coordinate System. Upon some reflection one can convince themselves that orientation of any two reference frames can be thus related via three such rotations (corresponding to the three rotational degrees of freedom). Thus we may construct our expression for $\hat{\xi}$ in the lab frame, $\hat{\xi}^{Lab}$, from the components in the lens frame by three appropriately chosen rotations.

The choice of angles is depicted in figure A-5, α, β, γ, which represent rotations about the $x, y'\mathrm{and}z''$ axis respectively. These were chosen due to the ease of relating them to known quantities during the calibration of the stereo-imaging system. Thus the final expression of $\hat{\xi}^{Lab}$ is given by...

$$\hat{\xi}^{Lab} = \bar{\bar{\mathrm{R}}}_x(\alpha)\,\bar{\bar{\mathrm{R}}}_{y'}(\beta)\,\bar{\bar{\mathrm{R}}}_{z''}(\gamma)\,\hat{\xi}^{Lens}$$

$$\hat{\xi}^{Lab} = \begin{bmatrix} 1 & 0 & 0 \\ 0 & \cos\alpha & -\sin\alpha \\ 0 & \sin\alpha & \cos\alpha \end{bmatrix} \begin{bmatrix} \cos\beta & 0 & \sin\alpha \\ 0 & 1 & 0 \\ -\sin\alpha & 0 & \cos\alpha \end{bmatrix} \begin{bmatrix} \cos\gamma & -\sin\gamma & 0 \\ \sin\gamma & \cos\gamma & 0 \\ 0 & 0 & 1 \end{bmatrix} \hat{\xi}^{Lens} \tag{A.10}$$

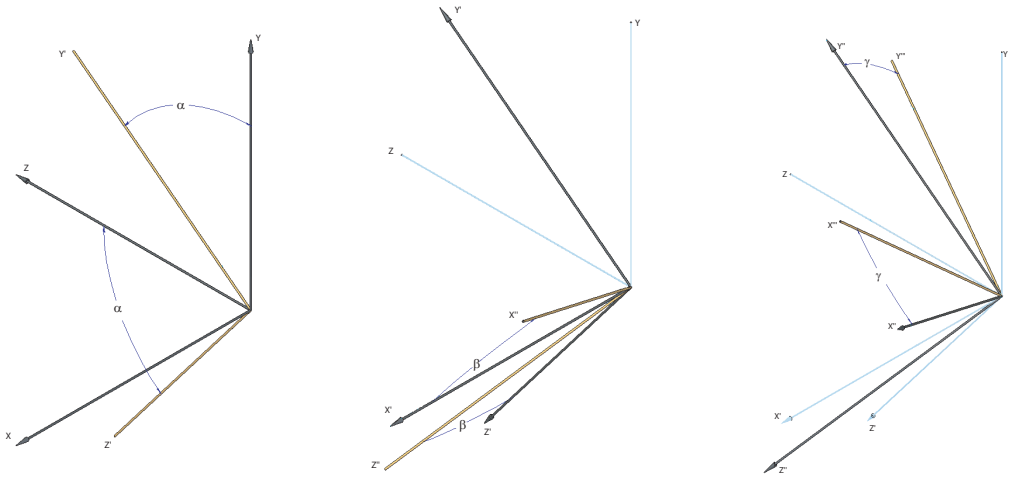

(a) α Rotation (b) β Rotation (c) γ Rotation

Figure A-5: (a) The first rotation is about the original X-axis by an amount γ. (b) The second rotation is about the new Y' axis by an amount β. (c) The final rotation is about the new Z" axis by an amount γ.

$$\hat{\xi}^{Lab} = \begin{bmatrix} \cos\beta & -\sin\gamma\cos\beta & \sin\beta \\ (\cos\alpha\sin\gamma+\sin\alpha\sin\beta\cos\gamma) & (\cos\alpha\cos\gamma+\sin\ \sin\beta\sin\gamma) & -\sin\alpha\cos\beta \\ (\sin\alpha\sin\gamma-cos\alpha\sin\beta\cos\gamma) & (\cos\alpha\cos\gamma+\sin\alpha\sin\beta\sin\gamma) & -\cos\alpha\cos\beta \end{bmatrix} \hat{\xi}^{Lens}$$

Thus, given the location of an object in both the top and bottom fiber bundle one can use equations A.7 and A.8 to determine $\hat{\xi}^{Lens}$, then use equation A.10 to transform the components of $\hat{\xi}^{Lens}$ to $\hat{\xi}^{Lab}$, and finally, using equation A.5 with the vectors from the top, $\hat{\xi}^{Lab}_T$, and bottom, $\hat{\xi}^{Lab}_B$, views one arrives at an expression for the location of the object in the lab frame. All one needs is the physical parameters that characterize the the lens system. Namely, the three components of the lens position, $\vec{X}_{T,B}$, the three Euler angles defining their orientation $\{\alpha,\beta,\gamma\}_{T,B}$ and parameters characterizing the magnification and distortion of the lenses $\{\epsilon_1,\epsilon_2\}_{T,B}$. Sixteen parameters in all.

Appendix B

Statistical Uncertainties

With regards to the statistical studies in this thesis, a certain amount of attention needs to be paid to the uncertainties that are quoted regarding the mean and width of the velocity distributions. As a brief reminder, let us consider the statistical properties of a random variable x whose mean, μ_x, and standard deviation are given by equations B.1 and B.2, where $\langle ... \rangle$ denotes an ensemble average. The mean represents the average value of x, while the standard deviation represents the amount that we can expect x to deviate from its mean.

$$\mu_x = \langle x \rangle \tag{B.1}$$

$$\sigma_x = \sqrt{\langle (x - \mu_x)^2 \rangle} \tag{B.2}$$

Of course, unless you know the probability distribution function for the random variable you can't never really know the actual mean and standard deviation. Rather, you approximate these statistical measures using a finite data set. It can be shown that the appropriate unbiased estimator of the mean, μ_x and standard deviation, σ_x are given by,

$$\bar{x} = \frac{1}{N} \sum_{i=1}^{N} x_i \tag{B.3}$$

$$s_x = \sqrt{\frac{1}{N-1}\sum_{i=1}^{N}(x_i - \bar{x})^2} \tag{B.4}$$

where $\bar{x}$ and s_x are referred to the sample mean and sample standard deviation respectively, and N is the number of measurements. The uncertainties in these estimators can be determined by considering the extent to which we can expect them to differ from the true mean and standard deviation of the distributions.

To address the uncertainty in the mean, we calculate the standard deviation of the sample mean, e.g. the standard deviation of a large number of determinations of $\bar{x}$. This can be expressed as,

$$\begin{aligned}\sigma_{\bar{x}}^2 &= \left\langle (\bar{x} - \mu_x)^2 \right\rangle = \frac{1}{N^2}\sum_{i,j}\left\langle (x_i - \mu_x)(x_j - \mu_x)\right\rangle \\ &= \frac{1}{N^2}\sum_{i=1}^{N}\left\langle (x_i - \mu_x)^2\right\rangle = \frac{\sigma_x^2}{N}\end{aligned} \tag{B.5}$$

where we have used the fact that $\langle (x_i - \mu_x)(x_j - \mu_x)\rangle = 0$ if $i \neq j$.

Thus the appropriate estimator for the standard deviation of $\bar{x}$ is the standard error, defined as $s_{\bar{x}} = s_x/\sqrt{N}$. This is the value which we quote as the uncertainty in the mean. Since $\bar{x}$ is composed many measurements of the random variable, x, the distribution of $\bar{x}$ is almost certainly Gaussian[1], regardless of the distribution for x. Thus our error bars represent a confidence interval of 68%, that is there is a 68% chance that the true mean lies within the error bars.

The quoted uncertainties for the distribution widths are determined assuming a χ^2 distribution for the estimated standard deviations. To understand why this is so, consider the form of the sample standard deviation.

[1]The central limit theorem holds that the probability distribution function resulting from the convolution of large number of independent random variables nearly always approaches a normal distribution, regardless of the form the probability distribution functions governing the random variables.

$$s_x^2 = \frac{1}{N-1}\sum_{i=1}^{N}(x_i - \bar{x})^2 = \frac{\sigma_x^2}{N-1}\sum_{i=1}^{N} z_i^2 = \frac{\sigma_x^2}{N-1}\chi_{N-1}^2 \tag{B.6}$$

Where $\chi_{N-1}^2 \equiv \sum_{i=1}^{N-1} z_i^2$ is a χ^2 random variable with $N-1$ degrees of freedom, and $z_i \equiv (x_i - \bar{x})/\sigma_x$ is a zero mean random variable, with a unit standard deviation. Thus we see that if x_i is a random variable, then the sample standard deviation, s_x^2, behaves as a χ^2 distributed random variable. Rearranging this a bit we get,

$$\chi_{N-1}^2 = \frac{(N-1)s_x^2}{\sigma_x^2} \tag{B.7}$$

In the language traditionally used for the χ^2 distribution, the value $\chi_{n;q}^2$ is defined such that there is a probability, q, that a given measure of the random variable χ_n^2 has a value greater than or equal to $\chi_{n;q}^2$, or stated another way,

$$q = \int_{\chi_{n:q}^2}^{\infty} p\left(\chi_n^2\right) d\chi_n^2 \tag{B.8}$$

Consider the interval bounded by $\left[\chi_{N-1;(1+P)/2}^2, \chi_{N-1;(1-P)/2}^2\right]$, where P is some probability less than 1. According to equation B.8, there is a probability $(1-P)/2$ that a measurement of χ_{N-1}^2 is above $\chi_{N-1;(1-P)/2}^2$. Similarly, there is a probability $(1-P)/2$ that a measurement of χ_{N-1}^2 lies below $\chi_{N-1;(1+P)/2}^2$, see figure B-1. Taken

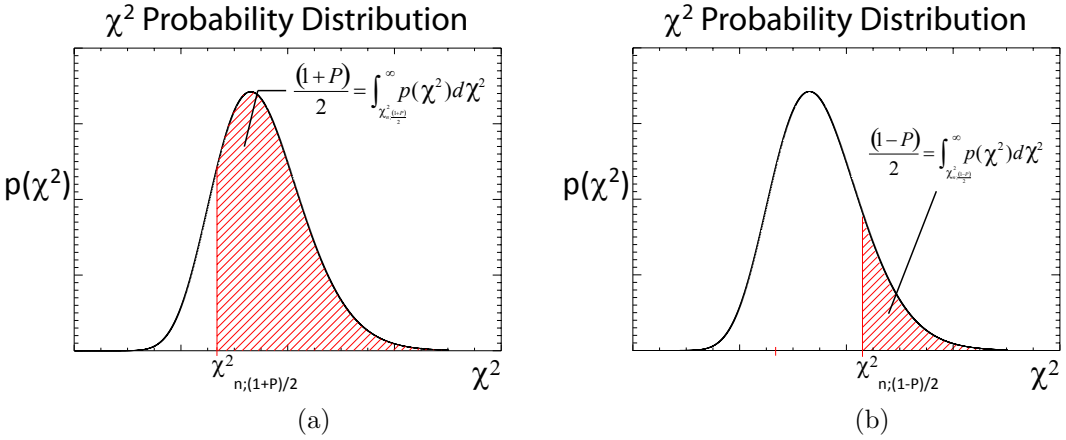

Figure B-1: Definition of (a) $\chi_{N-1;(1+P)/2}^2$ and (b) $\chi_{N-1;(1-P)/2}^2$ which define the upper and lower edge of the confidence interval respectively.

together, we see that there is a probability P that a measurement of χ^2_{N-1} falls within the interval $\left[\chi^2_{N-1;(1+P)/2}, \chi^2_{N-1;(1-P)/2}\right]$. Rearranging this, using equation B.7, we get that there is a probability, P, that the true standard deviation, σ_x lies within an interval of our sample standard deviation, s_x, defined by,

$$\left[\frac{(N-1)s_x^2}{\chi^2_{N-1;(1-P)/2}} \leq \sigma_x^2 \leq \frac{(N-1)s_x^2}{\chi^2_{N-1;(1+P)/2}}\right] \tag{B.9}$$

For the results in this thesis the confidence interval, **P**, is taken to be 68% to be consistent with the one standard deviation error bars of means of the velocity distributions.

Appendix C

Pellet Deposition Model

The purpose of this exercise is to generate density and temperature profiles that are consistent with what we know about the plasma during the pellet injection. We will begin with a basic model governing the evolution of the electron temperature and density, and then elaborate on this model to account for the effects of the Lithium ions and the response of the Deuterium. These profiles will then be used with GYRO to study the turbulence during a pellet injection.

C.1 Basic Model

The model is based off the thesis of Camilo Gomez [93] who studied electron temperature and density evolution during the injection of frozen hydrogen pellets in Alcator C. We start out by assuming that during the injection the evolution of the electron density and temperature profiles are dominated by diffusion and a density source term representing the pellet. We neglect convection and ohmic heating due to large gradients and short time scales involved. This leads to the following set of dynamic equations.

$$\frac{\partial}{\partial t} n_e = \frac{1}{r} \frac{\partial}{\partial r} r D_e \frac{\partial}{\partial r} n_e + S_n \tag{C.1}$$

$$\frac{3}{2} \frac{\partial}{\partial t} n_e T_e = \frac{1}{r} \frac{\partial}{\partial r} r n_e \chi_e \frac{\partial}{\partial r} T_e \tag{C.2}$$

Where S_n is the pellet source term, and χ_e and D_e are constant thermal and particle diffusivities for the electrons. Next we break up the density and temperature into an equilibrium $[\overline{n}_e, \overline{T}_e]$ and fluctuating part $[\tilde{n}_e, \tilde{T}_e]$, where the equilibrium parts represent the profiles prior to the injection, and the fluctuating parts are modifications due to the injection. When we plug these expressions into eq:C.2 and eq:C.1 all the terms that contain only equilibrium quantities are assumed to balance on the right and left hand side with terms in the full transport equations that act on longer time scales. Thus, these terms are dropped from the short time scale equations and the model becomes,

$$\frac{\partial}{\partial t}\tilde{n}_e = \frac{1}{r}\frac{\partial}{\partial r} r D_e \frac{\partial}{\partial r}\tilde{n}_e + S_n \tag{C.3}$$

$$\frac{\partial}{\partial t}\tilde{T}_e = -\left(\frac{\overline{T}_e + \tilde{T}_e}{\overline{n}_e + \tilde{n}_e}\right)\frac{\partial}{\partial t}\tilde{n}_e + \frac{2}{3r(\overline{n}_e + \tilde{n}_e)}\frac{\partial}{\partial r}\left[r\chi_e\left((\overline{n}_e + \tilde{n}_e)\frac{\partial}{\partial r}\tilde{T}_e + \tilde{n}_e\frac{\partial}{\partial r}\overline{T}_e\right)\right] \tag{C.4}$$

Where the first term on the right hand side of eq:C.4 describes the adiabatic response of the electrons and the second term represents the diffusive response.

A Gaussian source term is used to represent the pellet. The properties of the source term are chosen such that it deposits the appropriate number of electrons over the life of the pellet, and has an amplitude whose integrated shape is consistent with the measured light emission from the neutral Lithium during injections and a width consistent with the measured extent of the neutral cloud. This leads to a density source term of the form.

$$S_n = \frac{5.28 v_p N_{tot}}{\sqrt{\pi}\sigma L \frac{\partial V_{flux}(r)}{\partial r}} \mathrm{e}^{\frac{-((r_{edge}-r)-v_p t)^2}{\sigma^2}} \left(\frac{v_p t}{L}\right) \sin\frac{\pi v_p t}{L} \tag{C.5}$$

where r_{edge} is the minor radius of the last closed flux surface, σ is the ablation width, L is total penetration depth of the pellet, v_p is the pellet velocity, N_{tot} is the total number of electrons in the pellet, and V_{flux} is the volume of the flux surface. Figure C-1 (a) shows the model deposition profile and (b) shows the measured H_α light from a frozen hydrogen pellet injected into Alcator C.

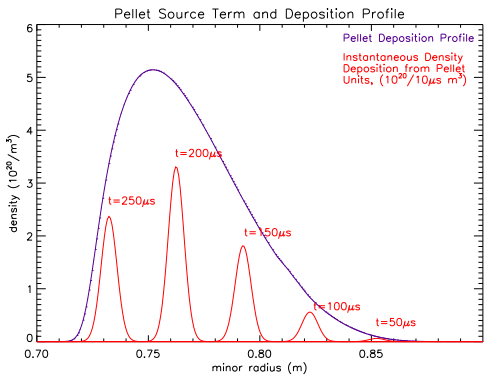

(a)

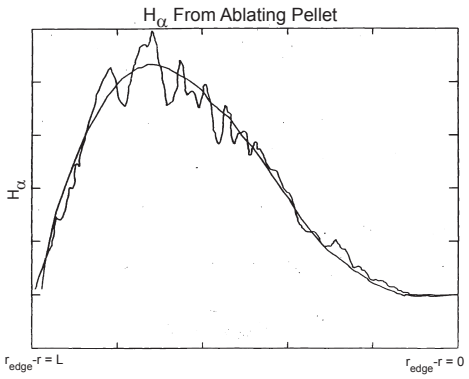

(b)

Figure C-1: (a) Example of deposition profile from model source S_n, σ = .5cm, $N_{tot} = 1 \times 10^{20}$, L=15cm, $v_p = 500\frac{m}{s}$, $r_{\text{edge}} = 88cm$, $r_{\text{plasma axis}} = .67cm$. The curves in red represent the instantaneous deposition rate, scaled to fit on the plot, at the time indicated. (b)Plot of the emitted H-alpha light on Alcator C. Taken From [93].

C.2 Diffusive Model With No Ions

Following the work done by Gomez, we tested the model with a thermal diffusivity of $\chi_e = 30m^2/s$ and a particle diffusivity of $D_e = 9m^2/s$. In this version of the model, the lithium and deuterium ions are left out completely. Figure C-2 and C-3 show the results from this model.

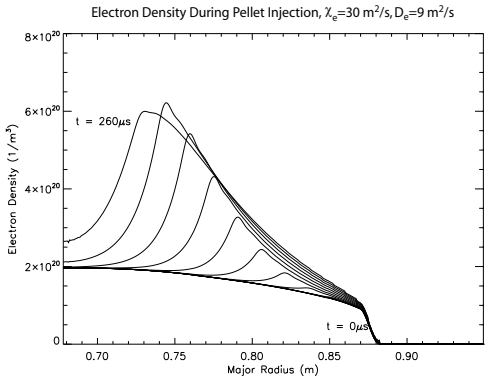

(a)

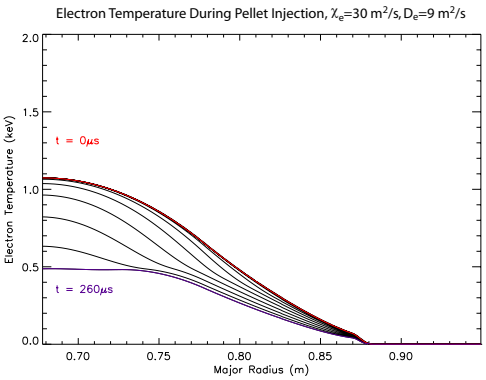

(b)

Figure C-2: Electron density (a) and temperature (b) profiles from model, $D_e = 9m^2/s$, $\chi_e = 30m^2/s$

These results compare very well with the electron temperature, density profiles

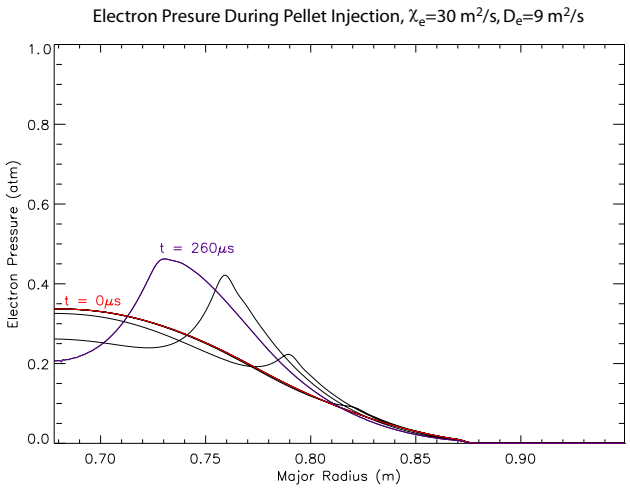

Figure C-3: Electron pressure profiles from model, $\chi_e = 30m^2/s$, $D_e = 9m^2/s$

and pressure profiles taken from C-Mod shot 1080110016, which occurred during the pellet injection. The upper trace in figure C-4 shows the line integrated electron density from TCI, in which the pellet injection time can be clearly seen as a nearly stepwise increment in the line averaged density. The lower figure shows a blow up of a high speed diode recording the intensity of light emission from neutral lithium, which we use as a proxy for the ablation rate. These signals indicate that the pellet entered the plasma at 1.4593s and that the ablation was essentially complete by 1.4595. According to the time stamp of the Thomson data, the Thomson profiles were taken at 1.46025s, or $\sim 525\mu s$ after the injection. The post-pellet Thomson profiles, figure C-5, indicate a steep drop in the temperature profile and an off axis peaking of the density profile. Further more, the pressure, figure C-6, is distinctly hollow, in a manner similar to the model profiles in figure, C-3.

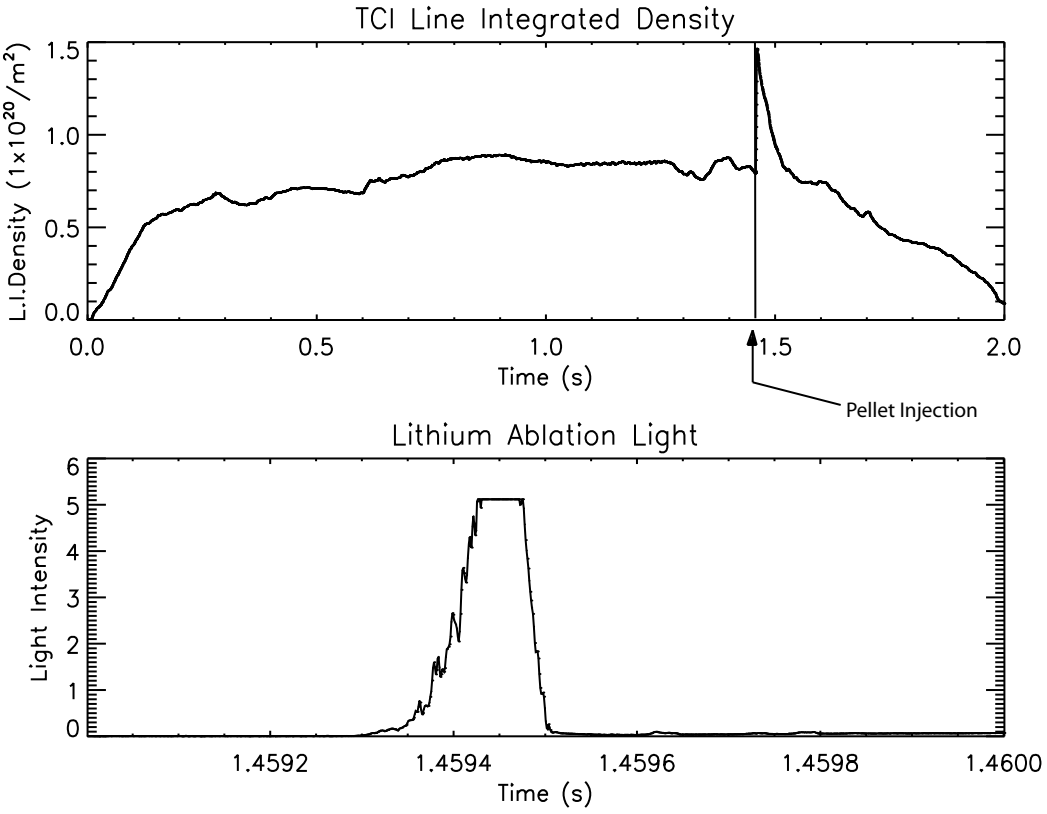

Figure C-4: Top: Trace of the line integrated electron density for shot 1080110016. The step increase at 1.46s is the pellet. Bottom: Trace of the emission from neutral lithium (λ=548.5nm), which is used as a proxy for the ablation rate. Signal saturates at 5.

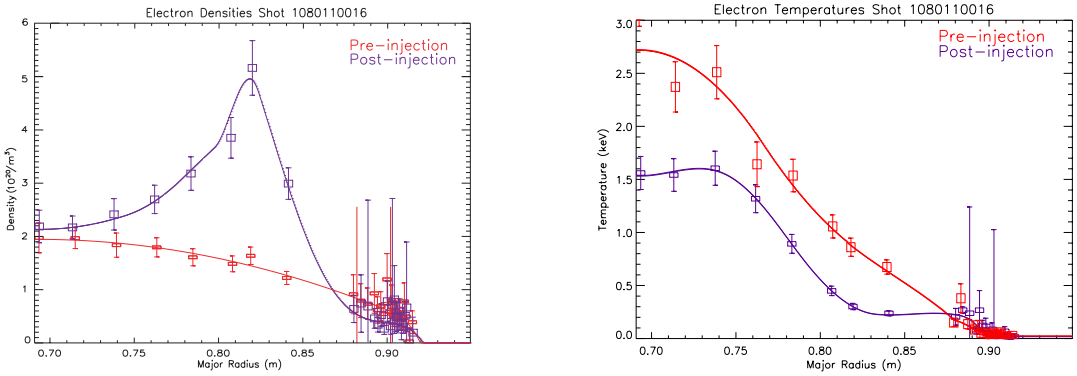

Figure C-5: Profiles, (a) density, (b) temperature, from just prior, and just after (500μs) the injection.

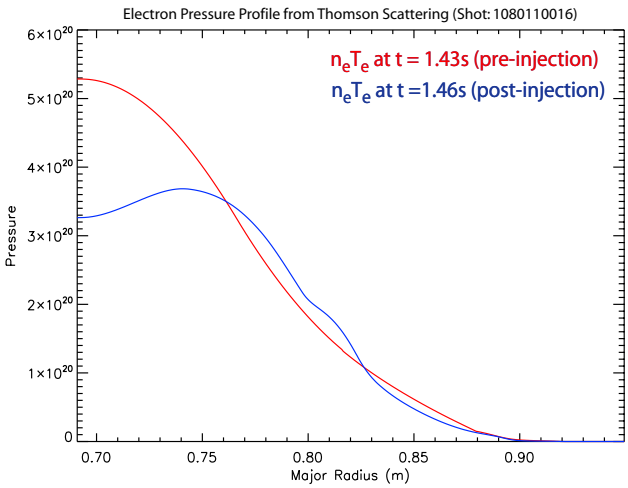

Figure C-6: Pressure Profiles from Thomson Scattering just prior (red) and just after (blue) the pellet injection.

C.3 Energy Exchange Between Species

The next step in the development of this model was to verify that it was appropriate to treat the cold electrons from the ablation cloud and the hot electrons from the plasma as a single species in a gyro-kinetic simulation. A sufficient criteria to treat the plasma and pellet electrons as a single species would be that the the cold electrons from the ablation cloud and the hot electrons from the plasma thermalize on a time scale short compared to our observations. In this case, the residence time of the pellet, moving at $500m/s$, with an ablation cloud $\sim 1mm$ in diameter, would also be approximately $2\mu s$. Using the expression for temperature equilibration from the NRL plasma formulary (pg. 34), the instantaneous rate of change of the temperature of population α due to the population β is given by,

$$\frac{\mathrm{d}T_\alpha}{\mathrm{d}t} = \sum_\beta \overline{\nu}_\epsilon^{\alpha\beta}(T_\alpha - T_\beta) \tag{C.6}$$

$$\overline{\nu}_\epsilon^{\alpha\beta} = 1.8 \times 10^{-19} \frac{(m_\alpha m_\beta)^{1/2} Z_\alpha^2 Z_\beta^2 \lambda_{\alpha\beta}}{m_\alpha T_\beta + m_\beta T_\alpha} sec^{-1} \tag{C.7}$$

Where $\lambda_{\alpha\beta}$ is the coulomb logarithm, and ranges from between 7 and 15. Figure C-7 shows two cases for the temperature evolution of a cold and hot population of

electrons. The two cases demonstrate the thermalization time for plasma electrons with a temperature of 1keV and density of $1\times10^{20}\,{}^{1}/_{m^3}$ in the presence of two different population of cold electrons. One population has a density of $1\times10^{22}\,{}^{1}/_{m^3}$, which is representative of the electron density in the ablation cloud. The second population of cold electrons has a lower density of $5\times10^{20}\,{}^{1}/_{m^3}$, which is consistent with peak flux surface averaged electron density during the injection. The cold electrons start with a temperature of 10eV, which is consistent with the measured temperature of the ablation cloud. These calculations indicate that the two populations of electrons will come to equilibrium within 60ns-1μs, which justifies treating the cloud and plasma electrons as a single species.

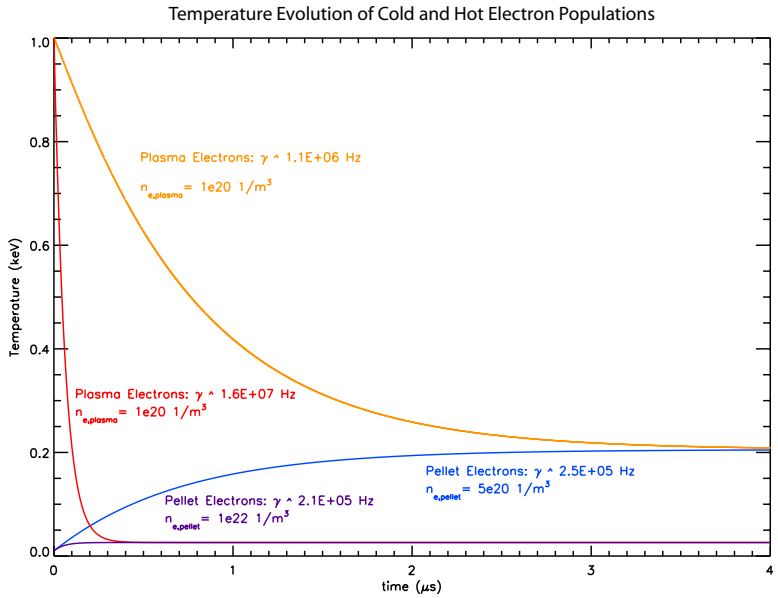

Figure C-7: Evolution of hot and cold electron population. Equilibration times range between 60-1000ns.

We next consider the effect that the hot deuterium and cold lithium ions have on the electron temperature, and vice versa. Since the filaments observed during the ablation form and evolve on a time interval of around 10μs, we need to account for any variations in the temperature profiles that occur on similar time scales. Shown below are the results of calculations for the equilibration time between the cold electrons and the deuterium, figure C-8, the cold lithium and the hot electrons, figure C-10, and the

hot deuterium and cold lithium ions, figure C-9. The results of these calculations show that all of these mechanisms could have a significant effect on the final temperature profiles. For instance, the deuterium-electron thermalization times, ranging from 300ns-3μs, indicate that the deuterium and electron temperature profiles will affect each other within the interval of interest. What is a bit more surprising is that cold lithium ion can effect the effect the electrons, even though their equilibration time is of the order of a millisecond. This occurs because the thermalization time for the lithium and deuterium ions is short, from 4-70μs, and thus it is possible for the lithium ions to effect the electrons by first cooling the deuterium, which then cools the electrons.

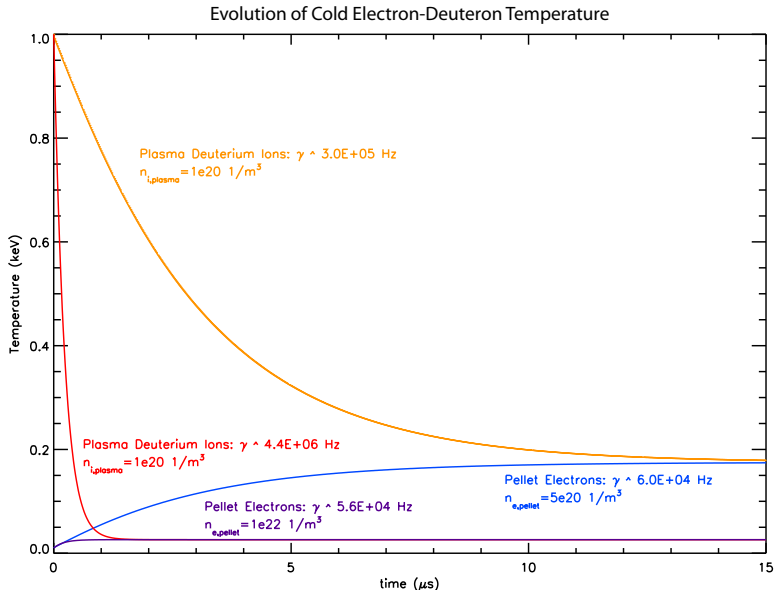

Figure C-8: Thermal evolution of cloud electrons and deuterium ions. Equilibration times range from 300ns-3μs

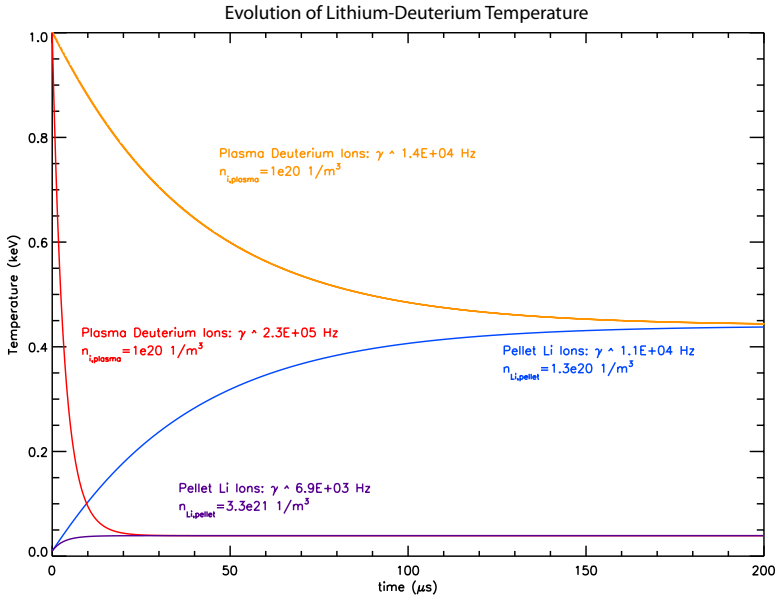

Figure C-9: Thermal evolution of hot deuterium and cold lithium ions. Equilibration times range from 4-70μs

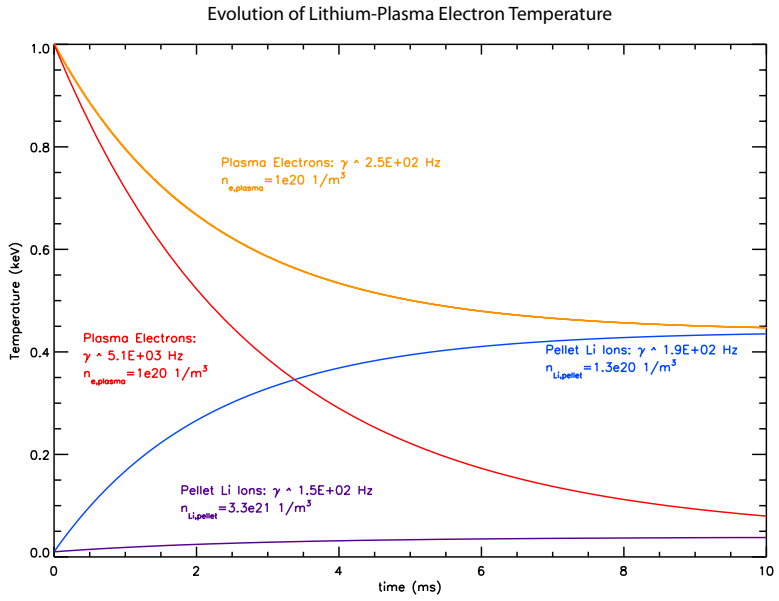

Figure C-10: Thermal evolution of cold lithium ions and hot electrons. Equilibration times range from 0.7-4ms

C.4 Energy Exchange Between Species

To explore the effects if the energy exchange on the profiles, we incorporated the energy exchange terms in our model, set the electron thermal and particle diffusivity to zero, but retained the adiabatic effect of the source term on the electrons giving the following model.

$$3\frac{\partial}{\partial t}n_{Li} = \frac{\partial}{\partial t}\tilde{n}_e = S_n \tag{C.8}$$

$$\frac{\partial}{\partial t}\tilde{T}_e = -\left(\frac{\overline{T}_e + \tilde{T}_e}{\overline{n}_e + \tilde{n}_e}\right)\frac{\partial}{\partial t}\tilde{n}_e + \overline{\nu}_\epsilon^{ei}(T_i - [\tilde{T}_e + \overline{T}_e]) + \overline{\nu}_\epsilon^{eLi}(T_{Li} - [\tilde{T}_e + \overline{T}_e]) \tag{C.9}$$

$$\frac{\partial}{\partial t}T_i = \overline{\nu}_\epsilon^{ie}([\tilde{T}_e + \overline{T}_e] - T_i) + \overline{\nu}_\epsilon^{iLi}(T_{Li} - T_i) \tag{C.10}$$

$$\frac{\partial}{\partial t}T_{Li} = -\frac{T_{Li}}{n_{Li}}\frac{\partial}{\partial t}n_{Li} + \overline{\nu}_\epsilon^{Lie}([\tilde{T}_e + \overline{T}_e] - T_{Li}) + \overline{\nu}_\epsilon^{Lii}(T_i - T_{Li}) \tag{C.11}$$

Shown below are a sequence of density (figure C-11), temperature (figure C-12), and pressure (figure C-13) profiles from using the above model. The black guassian denotes the location of the pellet and ablation cloud. The most obvious result from these plots is a separation between the region of steep electron temperature gradients and the region of steep ion temperature gradient, see figure C-12. There also results a hump in the electron pressure profile which is due to reheating by the ions.

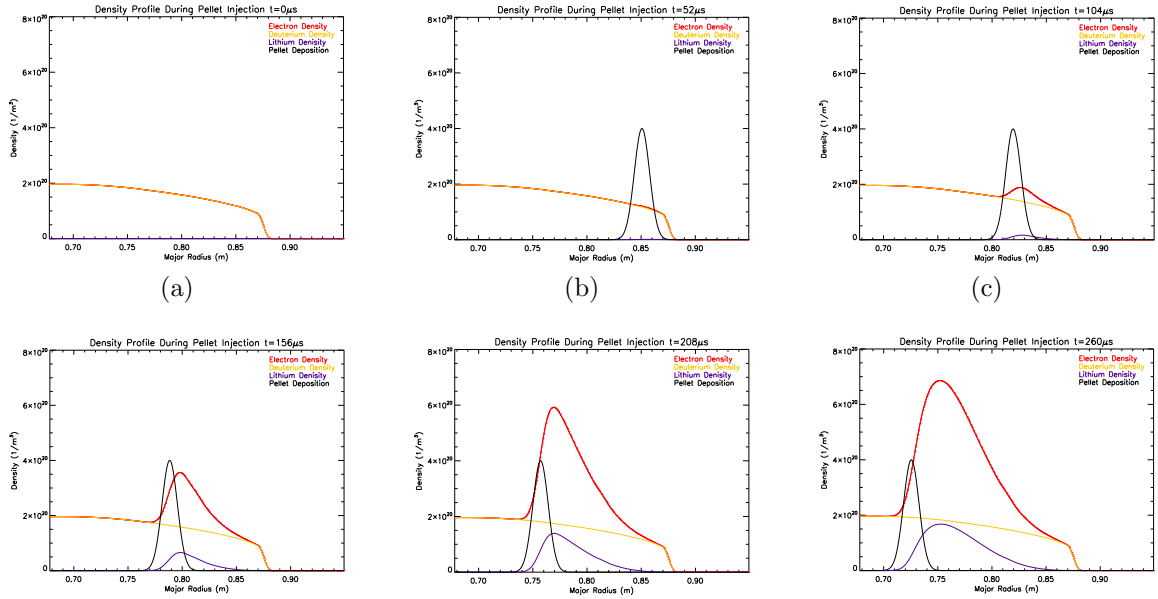

Figure C-11: Time sequence of density profiles for the adiabatic addition of electrons and lithium ions during pellet ablation with energy exchange between the species. Time after pellet enters plasma. 0μs(a), 52μs(b), 104μs(c), 156μs(d), 208μs(e), 260μs(f)

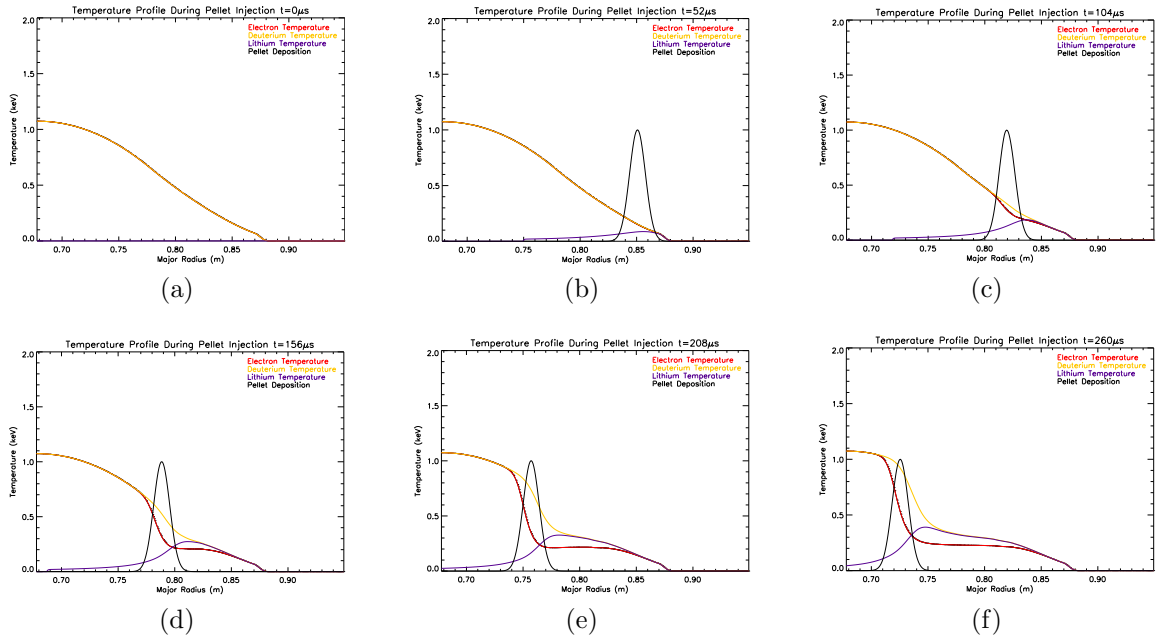

Figure C-12: Time sequence of temperature profiles. Note the spatial separation between the region of steep electron and ion temperature gradients.

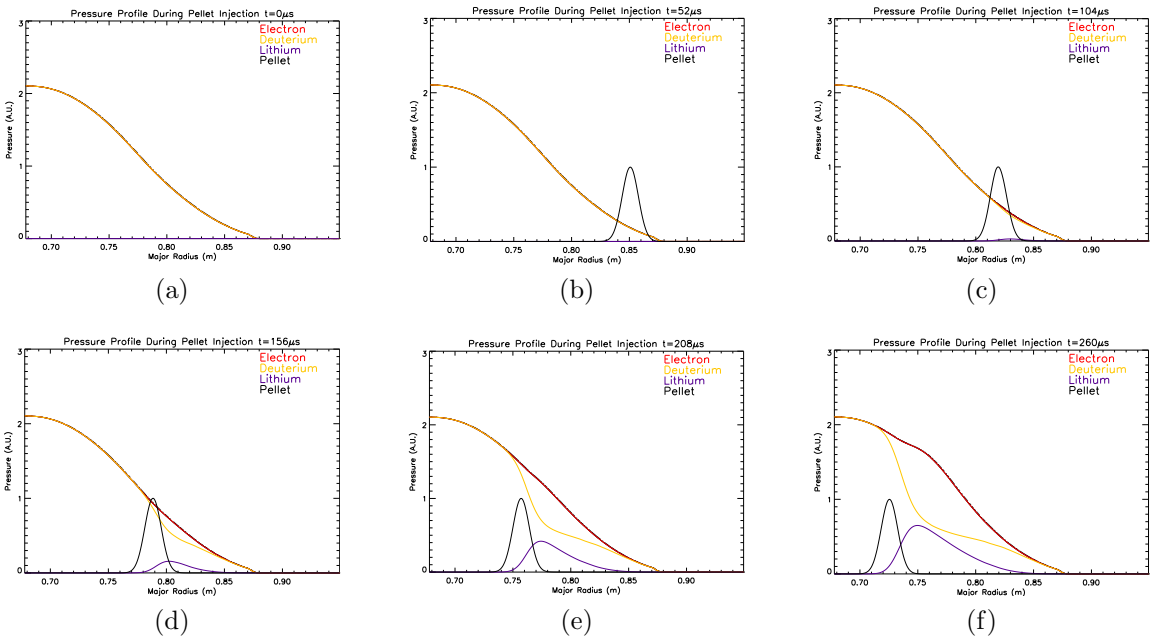

Figure C-13: Time sequence of pressure profiles

C.5 Diffusive Model With Energy Exchange

To complete the model we needed to make some assumption as to the spatial distribution of the lithium ions. To that end it was decided to implement a model where the electrons are allowed to diffuse according to eq:C.3, and the lithium ion density is redistributed to enforce quasi-neutrality. Though it may seem counter intuitive to, in effect, allow lithium ions to be pulled around by electrons, who weigh a factor of 1.25×10^4 less, but this solution was chosen for the following reasons. First, we expect that on the time scale for the evolution of the ablatant that quasi-neutrality will be valid. Second, considering that the pellet is introducing perturbations to the electron and lithium density, we expect that the effect on the deuterium density will smaller and slower to develop than the changes to the electrons and lithium ions. Finally, experimentally we only have direct information from Thomson scattering on the electron density and temperature. Thus any model we postulate to govern the evolution of the lithium density will have to both obey quasi-neutrality, and produce a perturbation in the electron density similar to what is seen in the Thomson data. Therefore, any tractable model we could introduce to govern the evolution of lithium

density would be forced to result in profiles that are extremely similar to what we get by tying the lithium ions to the electron evolution. Thus, using thermal model similar to the electrons, and including collisional energy exchange between the species, we have the following equations to govern the lithium profiles.

$$3\frac{\partial}{\partial t}n_{Li} = \frac{\partial}{\partial t}\tilde{n}_e \tag{C.12}$$

$$\frac{\partial}{\partial t}T_{Li} = \frac{2}{3rn_{Li}}\frac{\partial}{\partial r}\left[r\chi_{Li}n_{Li}\frac{\partial}{\partial r}T_{Li}\right] + \overline{\nu}_{\epsilon}^{Lie}([\tilde{T}_e + \overline{T}_e] - T_{Li}) + \overline{\nu}_{\epsilon}^{Lii}(T_i - T_{Li}) - \left(\frac{T_{Li}}{n_{Li}}\right)\frac{\partial}{\partial t}n_{Li} \tag{C.13}$$

Thus our final becomes,

Electrons

$$\frac{\partial}{\partial t}\tilde{n}_e = \frac{1}{r}\frac{\partial}{\partial r} r D_e \frac{\partial}{\partial r}\tilde{n}_e + S_n \tag{C.14}$$

$$\begin{aligned}\frac{\partial}{\partial t}\tilde{T}_e = &- \left(\frac{\overline{T}_e + \tilde{T}_e}{\overline{n}_e + \tilde{n}_e}\right)\frac{\partial}{\partial t}\tilde{n}_e \\ &+ \frac{2}{3r(\overline{n}_e + \tilde{n}_e)}\frac{\partial}{\partial r}\left[r\chi_e\left((\overline{n}_e + \tilde{n}_e)\frac{\partial}{\partial r}\tilde{T}_e + \tilde{n}_e\frac{\partial}{\partial r}\overline{T}_e\right)\right] \\ &+ \overline{\nu}_\epsilon^{ei}(T_i - [\tilde{T}_e + \overline{T}_e]) + \overline{\nu}_\epsilon^{eLi}(T_{Li} - [\tilde{T}_e + \overline{T}_e])\end{aligned} \tag{C.15}$$

Deuterium Ions

$$\frac{\partial}{\partial t}n_i = 0 \tag{C.16}$$

$$\frac{\partial}{\partial t}T_i = \overline{\nu}_\epsilon^{ie}([\tilde{T}_e + \overline{T}_e] - T_i) + \overline{\nu}_\epsilon^{iLi}(T_{Li} - T_i) \tag{C.17}$$

Lithium Ions

$$3\frac{\partial}{\partial t}n_{Li} = \frac{\partial}{\partial t}\tilde{n}_e \tag{C.18}$$

$$\begin{aligned}\frac{\partial}{\partial t}T_{Li} = &- \left(\frac{T_{Li}}{n_{Li}}\right)\frac{\partial}{\partial t}n_{Li} \\ &+ \frac{2}{3rn_{Li}}\frac{\partial}{\partial r}\left[r\chi_{Li}n_{Li}\frac{\partial}{\partial r}T_{Li}\right] \\ &+ \overline{\nu}_\epsilon^{Lie}([\tilde{T}_e + \overline{T}_e] - T_{Li}) + \overline{\nu}_\epsilon^{Li\,i}(T_i - T_{Li})\end{aligned} \tag{C.19}$$

Bibliography

[1] John Wesson. *Tokamaks 3rd Edition*. Oxford University Press, 2004.

[2] N.P. Basse *et al*. Diagnostic systems on alcator c-mod. *Fusion Science and Technology*, pages 476–507, 2007.

[3] I. H. Hutchinson. *Principles of Plasma Diagnostics*. Cambridge University Press, 2002.

[4] T.H. Stix. *Waves in Plasmas*. AIP Press, 1992.

[5] C. Fiore. Unknown title, 2010.

[6] J. Freidberg. *Ideal Magnetohydrodynamics*. Springer, 1987.

[7] R.D. Durst *et al*. Experimental observations of the dynamics of pellet ablation on the texas experimental tokamak (text). *Nuclear Fusion*, 30:3–9, 1990.

[8] L.L. Lengyel. Pellet injection and toroidal confinement. *Nuclear Fusion*, 29:325–341, 1989.

[9] C.T. Chang. Pellet plasma interactions in tokamaks. *Physics Reports*, 206(4):143–196, 1991.

[10] Pégourié B. Review: Pellet injection experiments and modelling. *Plasma Physics and Controlled Fusion*, 49:87–160, 2007.

[11] S.L. Milora, W.A. Houlberg, L.L. Lengyel, and V. Mertens. Review paper pellet fuelling. *Nuclear Fusion*, 35:657–754, 1995.

[12] D.H. McNeill *et al*. Spectroscopic measurements of the parameters of the ablation clouds of deuterium pellets injected into tokamaks. *Physics of Fluids B*, 3:1994–2009, 1991.

[13] D.H. McNeill, G.J. Greene, and D.D. Schuresko. Parameters of the luminous region surrounding deuterium pellets in the princeton large torus tokamak. *Physical Review Letters*, 55(13):1398–1401, 1985.

[14] P.B. Parks and R.J. Turnbull. Effects of transonic flow in the ablation cloud on the lifetime of a solid hydrogen pellet in a plasma. *Physics of Fluids*, 21:1737–1741, 1978.

[15] P.B. Parks, J.S. Leffler, and R.K. Fisher. Analysis of low z impurity pellet ablation for fusion diagnostic studies. *Nuclear Fusion*, 28:477–490, 1988.

[16] A. Canton *et al.* Analysis of pellet ablation and density build-up in the rfx reversed-field pinch. *Nuclear Fusion*, 19:1061, 1979.

[17] L.R Baylor *et al.* An international pellet ablation database. *Nuclear Fusion*, 37:445–450, 1997.

[18] P.B. Parks, R.J. Turnbull, and C. A. Foster. A model for the ablatin rate of a solid hydrogen pellet in a plasma. *Nuclear Fusion*, 17, 1977.

[19] P.B. Parks *et al.* Model of ablation flow near light atom pellets with surface boundary conditions. *Nuclear Fusion*, 34:417–427, 1994.

[20] R. Ishizaki *et al.* Fluid simulation on pellet ablation with atomic process. *Journal of Nuclear Materials*, 313-316:579–583, 2003.

[21] F.S. Felber *et al.* Effects of atomic processes on fuel pellet ablation in a thermonuclear plasma. *Nuclear Fusion*, 19:1061, 1979.

[22] D.K. Mansfield *et al.* Local-density increment from an ablated deuterium pellet in the tftr tokamak. *Physical Review Letters*, 66(24):3140–3143, 1991.

[23] H.W. Müller *et al.* High-β plasmoid drift during pellet injection into tokamaks. *Physical Review Letters*, 83(11):2199–2202, 1999.

[24] H.W. Müller *et al.* High β plasmoid formation, drift and striations during pellet ablation in asdex upgrade. *Nuclear Fusion*, 42:301–309, 2002.

[25] L.R. Baylor *et al.* Pellet fuelling deposition measurements on jet and tftr. *Nuclear Fusion*, 32(12):2177–2187, 1992.

[26] L.R. Baylor *et al.* Improved core fueling with high field side pellet injection in the diii-d tokamak. *Physics of Plasmas*, 7(5):1878–1885, 2000.

[27] J. de Kloe *et al.* Fast backward drift of pellet ablatant in tokamak plasmas. *Physical Review Letters*, 82(13):2685–2688, 1999.

[28] Parks P.B., W.D. Sessions, and L.R. Baylor. Radial displacement of pellet ablation material in tokamaks due to the grad-b effect. *Physics of Plasmas*, 7(5):1968–1975, 2000.

[29] G.A. Wurden *et al.* Pellet imaging techniques in the asdex tokamak. *Review of Scientific Instruments*, 11(61), 1990.

[30] Foster. Solid hydrogen pellet injection into the ormak tokamak. *Nuclear Fusion*, 17:1067–1075, 1977.

[31] J.T. Terry *et al.* High speed movies of turbulence in alcator c-mod. *Review of Scientific Instruments*, 75(10):4196–4199, 2004.

[32] V. Waller *et al.* Investigatiion of current-density modification during magnetic reconnection by analyss of hydrogen-pellet deflection. *Physical Review Letters*, 91(20), 2003.

[33] B Pégourié and M.A. Dubois. Magnetic surfaces and striations during pellet ablation. *Nuclear Fusion*, 29:745–751, 1989.

[34] Parks P. Theory of pellet cloud oscillation striations. *Plasma Physics and Controlled Fusion*, 38:571–591, 1996.

[35] P.W. Terry. Suppression of turbulence and transport by sheared flow. *Reviews of Modern Physics*, 72(1):109–162, 2000.

[36] M Wickham and G Vandergrift. Curvature-induced interchange mode in an axisymmetric plasma. *Physics of Fluids*, 25:52–58, 1982.

[37] LIU Wangdong and M. Talvard. Rapid global response of the electron temperature during pellet injection on tore supra. *Nuclear Fusion*, 34(3):337–347, 1994.

[38] H.R. Strauss *et al.* 3d mhd simulations of pellet injection and disruptions in tokamak plasmas. *Nuclear Fusion*, 39(11Y):2069–2076, 1999.

[39] H.R. Strauss and W. Park. Pellet driven disruptions in tokamaks. *Physics of Plasmas*, 7(1):250–257, 1999.

[40] E. Giovannozzi *et al.* Magnetic island structures and their rotation after pellet injections in ftu. *Nuclear Fusion*, 44:226–231, 2004.

[41] A. Weller *et al.* Persistent density perturbatioins at rational-q surfaces following pellet injection in the joint european torus. *Physical Review Letters*, 59(20):2303–2306, 1987.

[42] A.L pecquet *et al.* Snake-like phenomena in tore supra following pellet injection. *Nuclear Fusion*, 37(4):451–466, 1997.

[43] I.H. Hutchinson *et al.* First results from alcator c-mod. *Plasma Physics*, 5(1):1511–1516, 1994.

[44] B. Pégourié and J.M. Picchiottino. Plasma density buildup after pellet injection. *Physics of Plasmas*, 12(3):4594–4605, 1996.

[45] Dong Jia-Fu, Wang Shi-Qing, and Li Wen-Zhong. Observation of hydrogen pellet ablation material flow by tomography. *Chinese Physics*, 15(10):2368–2373, 2005.

[46] H.W. Müller *et al.* Improvement of q-profile measurement by fast observation of pellet ablation at asdex upgrade. *Review of Scientific Instruments*, 11(68):4051–4060, 1997.

[47] F. Wagner *et al.* Regime of improved confinement and high beta in neutral-beam-heated divertor discharges of the asdex tokamak. *Physical Review Letters*, 49(19), 1982.

[48] K.H. Burrell *et al.* Confinement physics of h-mode discharges in diii-d. *Plasma Physics and Controlled Fusion*, 31(10), 1989.

[49] V. Erkmann textitet al. H mode of the w 7-as stellerator. *Physical Review Letters*, 70(14), 1993.

[50] O. Sakai, Y. Yasaka, and R. Itatani. High radial confinement mode induced by dc limiter biasing in the hiei tandem mirror. *Physical Review Letters*, 70(26), 1993.

[51] K.H. Burrell *et al.* role of the radial electric field in the transition from l (low) mode to h (high) mode to vh (very high) mode in the diii-d tokamak. *Physics of Plasmas*, 1(5):1536–1544, 1994.

[52] R.J. Haye *et al.* Core flow shear as the cause of very high confinement in the diii-d tokamak. *Nuclear Fusion*, 35(8):988–993, 1995.

[53] A.M. Dimits *et al.* Scalings of ion-temperature gradient-driven anomalous transport in tokamaks. *Physical Review Letters*, 77(1):71–74, 1996.

[54] J.E. Kinsey, R.E. Waltz, and J. Candy. The effect of plasma shaping on turbulent tranport and exb shear quenching in nonlinear gyro-kinetic sumulations. *Physics of Plasmas*, 14, 2007.

[55] G.K. Batchelor. *An Introduction to Fluid Dynamics*. Cambridge Mathematical Library, 2000.

[56] K.H. Burrell. Effects of exb velocity shear and magnetic shear on turbulence and transport in magnetic confinement devices. *Physics of Plasmas*, 4(5):1499–1518, 1996.

[57] G.G. Craddock and P.H. Diamond. Theory of shear suppression of edge turbulence by externally driven radio-frequency waves. *Physical Review Letters*, 67(12):1535–1538, 1991.

[58] A.B. Hassam and R.M. Kulsrud. Time evolution of mass flows in a collisional tokamak. *Physics of Fluids B*, 12(21):2271–2279, 1978.

[59] C. Holland *et al.* Zonal-flow-driven nonlinear energy transfer in experiment and simulation. *Physics of Plasmas*, 14, 2007.

[60] B LeBlanc *et al.* Active core profile and tranport modificationby application of ion bernstein wave power in the princeton beta experiment-modification. *Physics of Plasmas*, 2, 1995.

[61] B LeBlanc *et al.* Direct observation of ion-bernstein-wave-induced poloidal flow in tftr. *Physical Review Letters*, 82(2), 1999.

[62] K.C. Shaing and E.C. Crume Jr. Bifurcation theory of poloidal rotation in tokamaks: A model for the l-h transition. *Physical Review Letters*, 63(21):2369–2372, 1989.

[63] T.E. Stringer. Diffusion in toroidal plasmas with radial electric field. *Physical Review Letters*, 22(15):770–774, 1969.

[64] A.B Hassam and J.F. Drake. Spontaneous poloidal spin-up of tokamak plasmas: Reduced equations, physical mechanism, and sonic regimes. *Physics of Fluids B*, 5(11):4022–4029, 1993.

[65] M.N. Rosenbluth and F.L. Hinton. Poloidal flow driven by ion-temperature-gradient turbulence in tokamaks. *Physical Review Letters*, 80(4), 1998.

[66] P.H. Diamond *et al.* Zonal flows in plasma-a review. *Plasma Physics and Controlled Fusion*, 47, 2005.

[67] T.S. Hahm *et al.* Zonal flow measurement concept i. *Plasma Physics and Controlled Fusion*, 42:205–210, 2000.

[68] Z. Lin *et al.* Turbulent tranport reduction by zonal flows: Massively parallel simulations. *Science*, 281:1835–1837, 1998.

[69] W. Dorland *et al.* Electron temperature gradient turbulence. *Physical Review Letters*, 85(26):5579–5582, 2000.

[70] M Kotschenreuther, G. Rewoldt, and W.M. Tang. Comparison of initial value and eigenvalue codes for kinetic toroidal plasma instabilities. *Computational Physics Communications*, 88:128–140, 1995.

[71] J. Candy and R.E. Waltz. An eulerian gyrokinetic-maxwell solver. *Journal of Computational Physics*, 186:545–581, 2003.

[72] N. Winsor, J.L. Johnson, and J.M. Dawson. Geodesic acoustic waves in hydromagnetic systems. *Physics of Fluids*, 11(11), 1968.

[73] G.R. McKee *et al.* Observation and characterization of radially sheared zonal flows in diii-d. *Plasma Physics and Controlled Fusion*, 45, 2003.

[74] P.M. Schoch *et al.* Zonal flow measurements using a heavy ion beam probe. *Review of Scientific Instruments*, 74(3), 2003.

[75] G.D. Conway *et al.* Direct measurement of zonal flows and geodesic acoustic mode oscillations in asdex upgrade using doppler reflectometry. *Plasma Physics and Controlled Fusion*, 47, 2005.

[76] H. Sugama and T.H. Watanabe. Collisionless damping of geodesic acoustic modes. *Journal of Plasma Physics*, 72, 2006.

[77] D. Garnier. *Lithium Pellet Injection Experiments on the Alcator C-Mod Tokamak*. PhD thesis, The Massachusetts Institute of Technology, 1996.

[78] L.L. Lao *et al.* Reconstruction of current profile parameters and plasma shapes in tokamaks. *Nuclear Fusion*, 25:1611–1622, 1985.

[79] A. Ince-Cushman *et al.* Spontaneous core toroidal rotation in alcator c-mod l-mode, h-mode and itb plasmas. *Plasma Physics and Controlled Fusion*, 50, 2008.

[80] E.A. Frieman and L Chen. Non-linear gyrokinetic equations for low-frequency electromagnetic waves in general plasma equilibrium. *Physics of Fluids*, 25(3):502–508, 1982.

[81] J Candy, R.E. Waltz, and W. Dorland. The local limit pf global gyrokinetic simulation. *Physics of Plasmas*, 11(4):L25–L28, 2004.

[82] W.M. Nevins *et al.* Verification of gyrokinetic δf simulatioins of electron temperature gradient turbulence. *Physics of Plasmas*, 14:084501:1–4, 2007.

[83] F. Jenko *et al.* Electron temperature gradient driven turbulence. *Physics of Plasmas*, 7(5):1904–1910, 2000.

[84] P.W. Terry *et al.* Validation in fusion research: Towards guidelines and best practices. *Physics of Plasmas*, 15:062503:1–12, 2008.

[85] M. Greenwald. Beyond benchmarking-how experiments and simulations can work together in plasma physics. *Computer Physics Communications*, 164:1–8, 2004.

[86] W. Oberkampf and T. Trucano. Verification and validation in computational fluid dynamics. *Aerospace Sciences*, 38:209–272, 2002.

[87] C. Holland *et al.* Implementation and application of two synthetic diagnostics for validating simulations of core tokamak turbulence. *Physics of Plasmas*, 16:052301, 2009.

[88] C. Holland *et al.* Validating simulations of core tokamak turbulence: Current status and future directions. *Journal of Physics: Conference Series*, 125:012043, 2008.

[89] R. Courant, K. Friedrichs, and H. Lewy. On the partial difference equations of mathematical physics. *IBM Journal*, pages 215–234, 1967. English tranlation of the 1928 original in ber die partiellen Differenzengleichungen der mathematischen Physik.

[90] M.D. Kruskal and R.M. Kulsrud. Equilibrium of a magnetically confined plasma in a toroid. *Physics of Fluids*, pages 213–220, 1958.

[91] R.L. Miller *et al.* Noncircular, finite aspect ratio, local equilibrium model. *Physics of Fluids*, 5(4):973–978, 1998.

[92] J Candy. Gyro technical guide. Technical report, General Atomics, 2009.

[93] C.C. Gomez. *Study of Electron Temperature Evolution During Sawtoothing and Pellet Injection Using Thermal Electron Cyclotron Emission in the Alcator C Tokamak*. PhD thesis, Massachusetts Institute of Technology, 1986.

[94] T. Dannert and F. Jenko. Gyrokinetic simulation of collisionless trapped-electron mode turbulence. *Physics of Plasmas*, 12(7):072309, 2005.